Technical University of Crete

School of Environmental Engineering

DOCTORAL THESIS

A study of the effects of high-end climate change scenarios on the global hydrological regime

Lamprini Papadimitriou

Chania, September 2017

DOCTORAL THESIS

A study of the effects of high-end climate change scenarios on the global hydrological regime

PhD Disseratation Committee:

1. Professor Dr. I. Tsanis , Technical University of Crete (Supervisor)
2. Professor Dr. G. Karatzas, Technical University of Crete (member of Supervising Committee)
3. Professor Dr. M. Lazaridis, Technical University of Crete, (member of Supervising Committee)
4. Professor Dr. T. Tsoutsos, Technical University of Crete
5. Associate Professor Dr. D. Kolokotsa, Technical University of Crete
6. Dr. A. Koutroulis, Technical University of Crete
7. Professor Dr. A. Loukas, University of Thessaly

Doctoral thesis: A study of the effects of high-end climate change scenarios on the global hydrological regime

Abstract

In recent years, there has been a strong consensus on the changes in climate caused by increased concentrations of anthropogenic greenhouse gas emissions. Global CO_2 emission rates have been following high-end climate change pathways leading to a future global temperature that is likely to surpass the target limits of $+1.5^oC$ and $+2^oC$, and reach levels of $+4^oC$ and higher at the end of the 21st century. Freshwater availability under such conditions is a key issue of concern and thus, scientific research has focused on estimating the range of changes in the future climate and the effectiveness of different adaptation strategies. The main tool for the investigation of future climate is the utilization of global climate models (GCMs). GCMs are based on physical principles that describe the components of the climate system. The next step for hydrological impacts' assessments is to force global hydrological models (GHMs) or land surface models (LSMs) with GCM outputs. Due to the systematic biases they feature, GCM outputs need some kind of bias correction prior to their application as forcing to impact models, especially for hydrological studies. Most bias correction techniques focus mainly on the variables of precipitation and temperature. However most state-of-art hydrological models require more forcing variables, additionally to precipitation and temperature, such as radiation, humidity, air pressure and wind speed. The biases in these additional variables can hinder hydrological simulations, but the effect of the bias of each variable is unexplored.

In the present thesis, a methodological framework of a multi-faceted assessment of the effects of high-end climate change on the global hydrological regime is presented. The tool for the hydrological simulations in our study is the LSM JULES, a physically based model operating at the global scale. The first component of our methodological framework is the evaluation of the model for a historical period and the assessment of the model's sensitivity to input forcing. A runoff routing algorithm is designed and implemented, to allow the comparison of the model output with discharge measurements. The second part of the methodological framework aims to assess the effect of the GCM biases on the performed runoff simulations, with the scope of deciding on the meteorological variables that should be included in bias correction. To this end, a methodology for the classification of the effect of biases in four effect categories (ECs), based on the magnitude and sensitivity of runoff changes, is developed and applied. The final part of the methodological framework of this thesis is the assessment of hydrological climate change impacts under high-end

warming scenarios. Assessment of impacts focuses on water availability and droughts at the global, European, regional and basin scale, employing a number of different and complementary methods. Climate change impacts are examined for different levels of warming (+1.5, +2 and +4°C) and the uncertainty in the projected changes is assessed throughout this analysis.

The results of this study could assist scientists make informed decisions on variables and methods that should be considered in future climate change impacts' studies, focusing on the uncertainty component of the impact analysis, by examining a wide range of "hydrologically opposing" future climates. The results of the present study could also be useful for policy makers, who need information relevant to this thesis, in order to decide on planning and legislations regarding climate change adaptation and mitigation.

Περίληψη

Τα τελευταία χρόνια έχει επιτευχθεί μια μεγάλη ομοφωνία της επιστημονικής κοινότητας ως προς τις αλλαγές του κλίματος που οφείλονται στην αυξημένη συγκέντρωση εκπομπών ανθρωπογενών αερίων του θερμοκηπίου. Οι εκπομπές του διοξειδίου του άνθρακα σε παγκόσμιο επίπεδο, ακολουθούν τα πιο ακραία σενάρια κλιματικής αλλαγής, οδηγώντας σε μελλοντικές παγκόσμιες θερμοκρασίες που πιθανώς να ξεπεράσουν τα όρια-στόχους των +1.5ºC και +2ºC, και να φτάσουν σε επίπεδα των +4ºC ή και ακόμα μεγαλύτερης υπερθέρμανσης στα τέλη του 21ου αιώνα. Η διαθεσιμότητα υδατικών πόρων υπό αυτές τις συνθήκες, είναι ένα ζήτημα εξαιρετικής σημασίας, γεγονός που έχει στρέψει την επιστημονική έρευνα στην εκτίμηση του εύρους των αλλαγών υπό πιθανά μελλοντικά κλιματικά σενάρια και της αποτελεσματικότητας διαφόρων στρατηγικών προσαρμογής στην κλιματική αλλαγή. Το βασικό εργαλείο για την μελέτη του κλίματος είναι η χρήση των παγκόσμιων κλιματικών μοντέλων (GCMs). Τα GCMs βασίζονται σε φυσικούς νόμους που περιγράφουν τα συστατικά μέρη του κλιματικού συστήματος. Το επόμενο βήμα για την μελέτη επιπτώσεων στην υδρολογία είναι η εισαγωγή των δεδομένων από GCMs σε παγκόσμια υδρολογικά μοντέλα (GHMs) ή μοντέλα προσομοίωσης διεργασιών επιφανείας (LSMs). Εξαιτίας των μεροληπτικών σφαλμάτων που εμφανίζουν, τα δεδομένα των GCMs χρειάζονται κάποια είδους διόρθωση πριν χρησιμοποιηθούν ως δεδομένα εισόδου για τα μοντέλα εκτίμησης επιπτώσεων, ιδιαίτερα για μελέτες υδρολογικού χαρακτήρα. Οι περισσότερες τεχνικές διόρθωσης των μεροληπτικών αυτών σφαλμάτων, εστιάζουν στις παραμέτρους της βροχόπτωσης και της θερμοκρασίας. Τα περισσότερα όμως υδρολογικά μοντέλα προηγμένης τεχνολογίας, χρειάζονται πιο πολλές παραμέτρους εισόδου, επιπρόσθετα από την βροχόπτωση και την θερμοκρασία, όπως η ακτινοβολία, η υγρασία, η πίεση και η ταχύτητα του ανέμου. Αν και τα σφάλματα σε αυτές τις επιπρόσθετες παραμέτρους μπορεί να προκαλέσουν προβλήματα στις υδρολογικές προσομοιώσεις, τα χαρακτηριστικά της επίδρασης του μεροληπτικού σφάλματος κάθε παραμέτρου, μεμονωμένα, δεν έχουν μελετηθεί.

Στην παρούσα εργασία, παρουσιάζεται ένα μεθοδολογικό πλαίσιο μια πολύπλευρης εκτίμησης των επιπτώσεων ακραίων σεναρίων κλιματικής αλλαγής στο παγκόσμιο υδρολογικό καθεστώς. Το εργαλείο που χρησιμοποιείται για τις υδρολογικές προσομοιώσεις είναι το μοντέλο επιφανειακών διεργασιών JULES, ένα μοντέλο βιοφυσικής βάσης που λειτουργεί σε παγκόσμια κλίμακα. Το πρώτο κομμάτι του μεθοδολογικού πλαισίου είναι η αξιολόγηση των αποτελεσμάτων του μοντέλου

για μια πρόσφατη ιστορική περίοδο και η εκτίμηση της ευαισθησίας του στις παραμέτρους εισόδου. Για τη σύγκριση των προσομοιώσεων με μετρήσεις παροχής, σχεδιάστηκε και εφαρμόστηκε ένας αλγόριθμος διόδευσης της απορροής. Το δεύτερο κομμάτι του μεθοδολογικού πλαισίου στοχεύει στην εκτίμηση της επίδρασης των μεροληπτικών σφαλμάτων των GCMs στις προσομοιώσεις της απορροής, ούτως ώστε να ποσοτικοποιηθεί η ευαισθησία και να επιλεχθούν οι μετεωρολογικές παράμετροι που θα πρέπει να ενταχθούν στη διαδικασία διόρθωσης μεροληπτικού σφάλματος. Μια μεθοδολογία για την κατηγοριοποίηση των επιδράσεων των σφαλμάτων σε τέσσερις κατηγορίες, με βάση το μέγεθος και την ευαισθησία των αλλαγών στην απορροή, αναπτύχθηκε και εφαρμόστηκε για τους παραπάνω σκοπούς. Το τελευταίο κομμάτι του μεθοδολογικού πλαισίου της παρούσας διατριβής είναι η εκτίμηση υδρολογικής φύσεως επιπτώσεων ακραίων σεναρίων κλιματικής αλλαγής. Η εκτίμηση των επιπτώσεων εστιάζει στην διαθεσιμότητα υδατικών πόρων και στις συνθήκες ξηρασίας, σε παγκόσμια, Ευρωπαϊκή και τοπική κλίμακα καθώς και σε επίπεδο λεκάνης απορροής, χρησιμοποιώντας πληθώρα διαφορετικών και συμπληρωματικών μεθόδων. Οι επιπτώσεις της κλιματικής αλλαγής εξετάζονται για διάφορα επίπεδα θέρμανσης (+1.5ºC, +2ºC και +4ºC) ενώ παράλληλα γίνεται και εκτίμηση της αβεβαιότητας στις προβαλλόμενες αλλαγές.

Τα αποτελέσματα της παρούσας εργασίας αποσκοπούν να βοηθήσουν την επιστημονική κοινότητα στην λήψη ενημερωμένων αποφάσεων σχετικά με παραμέτρους και μεθόδους που θα πρέπει να ληφθούν υπόψη σε μελλοντικές μελέτες επιπτώσεων της κλιματικής αλλαγής, εστιάζοντας στην αποφυγή της υπερβολικής βεβαιότητας εξετάζοντας μια πληθώρα «υδρολογικά αντιφατικών» κλιματικών προσομοιώσεων. Τα αποτελέσματα της παρούσας εργασίας είναι επίσης χρήσιμα στους φορείς χάραξης κεντρικής πολιτικής σε διακρατικό επίπεδο, καθώς οι τελευταίοι χρειάζονται σχετικές με την παρούσα εργασία πληροφορίες ώστε να αποφασίσουν σε σχέδια και νομοθεσίες σχετικά με την προσαρμογή και την μετρίαση της κλιματικής αλλαγής.

Acknowledgements

First and foremost I would like to thank my supervisor, Professor Ioannis Tsanis, for trusting me with the subject of this thesis and for giving me the chance to work in his lab. It has been an honor to be a PhD student under his supervision. I appreciate all his contribution of time, ideas, and funding to make my PhD experience productive and stimulating. I am also thankful for the excellent example he has provided as a successful professor and researcher.

I am grateful to the members of the Scientific Committee, and especially the members of the Supervising Committee, for their constructive comments and for spending time and effort to evaluate my thesis.

I would also like to warmly thank all the present and past members of the laboratory for their personal and professional support through these years of collaboration. I am deeply grateful to Dr. Aristeidis Koutroulis and Dr. Manolis Grillakis for all the scientific and technical advice, counseling and help they have provided and for all the ideas, plans, discussions and moments of creativity we have shared throughout the past four years. I would also like to deeply thank Kostas Seiradakis for his valuable help with technical issues. Many thanks to Dr. Ioannis Daliakopoulos for the inspiring scientific discussions and to Vasiliki Iordanidou for the programming advice and the exciting moments we had sharing the same office for three years. Special thanks to Irini Vozinaki for providing scientific, and most importantly personal, support and advice. I am also grateful to my colleagues Sotiris Tsitsilonis, Evdokia Tapoglou and Dimitris Alexakis for all the collaboration, ideas and moments we shared during my PhD journey.

Last but certainly not least, I would like to express my deep thankfulness to my parents and my sister for supporting me through this PhD pursuit, and through all my other pursuits, and especially thank them for being always close to me mentally, even though I was far from them physically.

…Dedicated to my parents Amalia and Vasilis,

with love, respect and gratitude

List of publications

Results of the present thesis were published in the following journal publications:

- **Papadimitriou, L. V**., Koutroulis, A. G., Grillakis, M. G., and Tsanis, I. K.: The effect of GCM biases on global runoff simulations of a land surface model, _Hydrology and Earth System Sciences_, 21, 4379-4401, https://doi.org/10.5194/hess-21-4379-2017, 2017.

- **Papadimitriou, L.V**., Koutroulis, A.G., Grillakis, M.G. and Tsanis, I.K., 2016, Hotspots of sensitivity to GCM biases in global modelling of mean and extreme runoff. _Hydrology and Earth System Sciences Discussions_

- **Papadimitriou, L.V.**, Koutroulis, A.G., Grillakis, M.G. and Tsanis, I.K., 2016. High-end climate change impact on European runoff and low flows-exploring the effects of forcing biases. _Hydrology and Earth System Sciences_, _20_(5), p.1785.

- Grillakis, M.G., Koutroulis, A.G., **Papadimitriou, L.V.**, Daliakopoulos, I.N. and Tsanis, I.K., 2016. Climate-Induced Shifts in Global Soil Temperature Regimes. _Soil Science_, _181_(6), pp.264-272.

- Koutroulis, A.G., Grillakis, M.G., Tsanis, I.K. and **Papadimitriou, L.**, 2016. Evaluation of precipitation and temperature simulation performance of the CMIP3 and CMIP5 historical experiments. _Climate Dynamics_, _47_(5-6), pp.1881-1898

Other publications relevant to the results and/or subject of this thesis that were authored during the preparation of the present thesis are the following:

- A. G. Koutroulis, **L. V. Papadimitriou**, M. G. Grillakis, I. K. Tsanis, Wyser, R. A. Betts, 2017, Freshwater vulnerability under high end climate change. A pan-European assessment., _Science of the Total Environment_, 613-614, pp. 271-286.

- Richard A. Betts, Lorenzo Alfieri, John Caesar, Jinfeng Chang, Philippe Ciais, Luc Feyen, Pierre Friedlingstein, Laila Gohar, Aristeidis Koutroulis, **Lamprini Papadimitriou**, Ioannis Tsanis, Klaus Wyser, 2017, Changes in climate extremes, large-scale hydrology and vegetation productivity projected at 1.5°C and 2°C global warming with higher-resolution global climate models, (submitted for publication to Phil. Trans. R. Soc. A – Issue).

Table of Contents

List of Figures

List of Tables

Chapter 1. Introduction

1.1. The climate and its basic mechanisms

1.1.1. Climate definition and components

Climate is generally defined as the description, in terms of the mean and variability, of relevant atmospheric variables such as temperature, precipitation and wind. Climate can thus be viewed as an aggregate of weather, or more precisely, as the probability distribution of possible weather states (Goose et al., 2010; Ridgwell and Valdes, 2009). Thus, the depiction of the climate of a specific region has to involve analysis of mean conditions, seasonality and of the probability of extremes (such as severe storms and heat waves). The World Meteorological Organisation (WMO), suggest a time period of thirty years for analysing climate statistics**.**

The climate system is comprised of the following components (Goose et al., 2010):

i.   The atmosphere: dry air is composed of nitrogen (~78 % v/v), oxygen (~21 % v/v) and other trace gases such as argon, carbon dioxide, neon, helium, methane, and krypton. Water vapour constitutes around 0.25 % of the mass of the atmosphere on average, but this fraction is highly variant, ranging from around 0 % in the coldest parts of the atmosphere to 5 % for areas of high temperature and humidity.

ii.   The ocean: covers about 71 % of the Earth's surface and is composed of 96.5 % water, 3.5 % dissolved salts, particles, gases, and organic matter.

iii. The cryosphere: is the portion of the Earth's surface where water is encountered in solid form. The cryosphere includes sea ice, lake ice, river ice, snow cover, glaciers, ice caps, ice sheets, and frozen ground.

iv.   The land surface and terrestrial biosphere: climate is influenced by the distribution and topography of the land surface and by the presence of terrestrial vegetation.

1.1.2. Energy balance of the climate system and the greenhouse effect

The climate system receives energy in the form of electromagnetic radiation by the Sun. In an equilibrium climate, the temperature of the system is constant, meaning that the input energy from

1

the Sun is balanced by an equivalent energy loss by the climate system. Outgoing energy is the radiation emitted by the Earth. The average temperature of the Earth is the result of the balance between the incoming solar energy absorbed by the Earth and the radiation emitted by the Earth into space. As radiations emitted by the Earth are of a longer wavelength compared to solar radiation, the term longwave radiation is used for Earth's radiation and shortwave radiation describes input solar radiation (Goose et al., 2010). As shown in Figure 1, solar radiation can be reflected by clouds and aerosols or be absorbed in the atmosphere. Radiation that is transmitted through the atmosphere will be reflected or absorbed by the land surface and will contribute to sensible and latent heat fluxes. After the absorption of shortwave radiation, the land surface emits longwave radiation, a fraction of which escapes to space while another fraction is absorbed by the atmosphere and re-emitted back to the land surface.

The latter mechanism is the basis of the "greenhouse effect", a term used to describe the increase of the Earth's temperature due to re-emission of longwave radiation by atmospheric aerosols and gases. Specific atmospheric gases (called greenhouse gases – GHGs) are nearly transparent to incoming shortwave radiation but almost opaque to outgoing longwave radiation. This way they prevent the longwave radiation from exiting the atmosphere, causing increased energy in the system and thus increased temperature (Bowman, 1990; Jain, 1993). Natural GHGs are water vapour and ozone (O_3). Other GHGs whose concentrations have been increased due to anthropogenic activities are: carbon dioxide (CO_2), methane (CH_4), nitrous oxide (N_2O) and chlorofluorocarbons (CFCs).
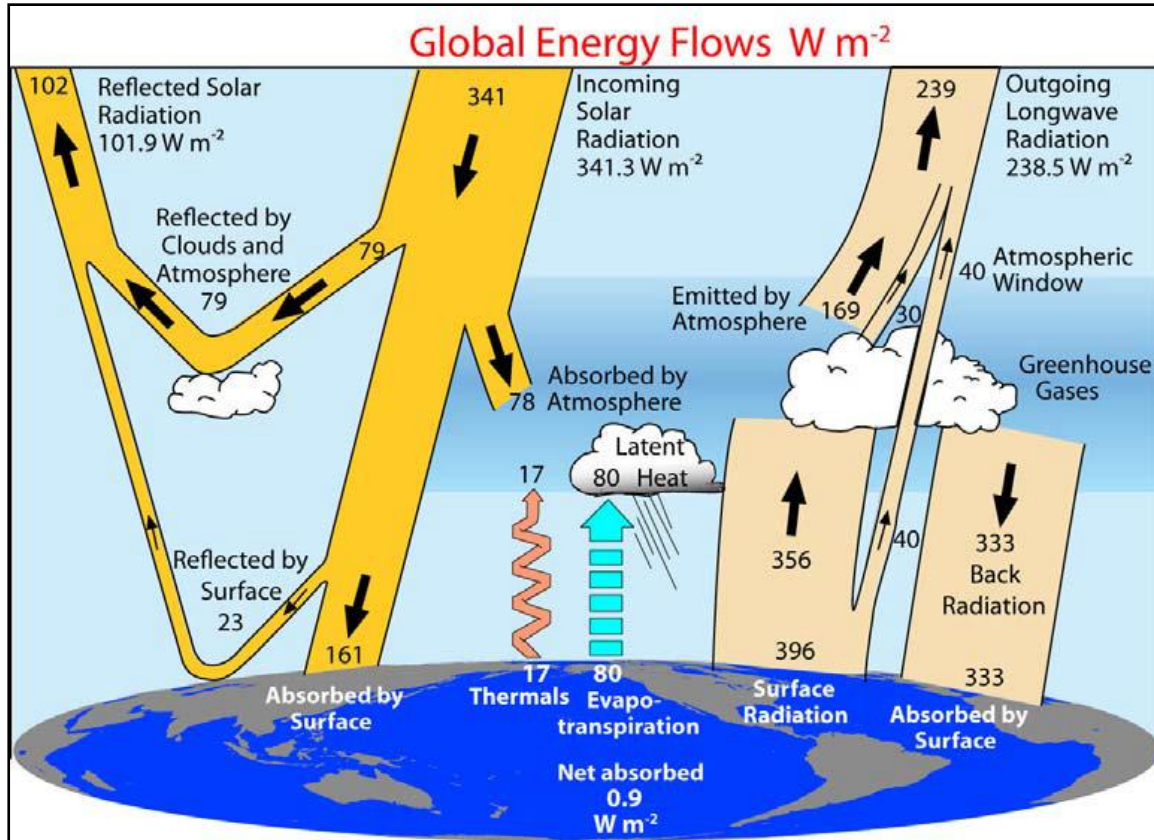
Figure 1. The Earths's global annual mean energy budget (W/m^2). The broad arrows indicate the schematic flow of energy in proportion to their importance (Trenberth et al., 2009).

The energy balance at the land surface is described by equation (1):

$$(1-a) \cdot S_{w\downarrow} + L_{w\downarrow} = L_{w\uparrow} + H_s + \lambda E + G \qquad (1)$$

Where a [-] is the albedo of the surface, $S_{w\downarrow}$ [W/m^2] is the downward shortwave radiation, $L_{w\downarrow}$ [W/m^2] is the downward longwave radiation, $L_{w\uparrow}$ [W/m^2] is the upward longwave radiation, H_s [W/m^2] is sensible heat flux from the surface, λE [W/m^2] is latent heat flux from the surface and G [W/m^2] is heat conducted away from the surface.

Net radiation is defined by equation (2):

$$R_n = (1-a) \cdot S_{w\downarrow} + (L_{w\downarrow} - L_{w\uparrow}) \qquad (2)$$

Based on net radiation, the surface energy balance can be simplified to equation (3):

$$R_n = H_s + \lambda E + G \tag{3}$$

This equation describes the balance of net radiation by sensible, latent and conduction heat fluxes.

1.1.3. Hydrological cycle

Water and energy cycles are tightly connected. Water vapour is the most important GHG and thus poses a significant effect on radiative balance. The hydrological cycle is driven by the incoming solar energy, which causes the vertical transfer of water from Earth to the atmosphere through the process of evapotranspiration (evaporation from surfaces and loss of water from plant leaves – transpiration). Moreover, water plays a dominant role in energy transfers between the land surface and the atmosphere. Latent heat is released during water vapour condensation and sensible heat is transferred along with water vapour in the atmosphere and water in the ocean. The largest water reservoirs are the oceans, followed by the cryosphere (Figure 2). A relatively small fraction of the global water budget corresponds to storage in the atmosphere. If the stored atmospheric water precipitated at once, the precipitation would correspond to only 2.5 % of global annual precipitation (Goose et al., 2010). Thus, the atmospheric water is quickly replaced through evaporation and transpiration. Most of the water evaporated from the ocean will precipitate back to the ocean (and respectively for the land surface). At the same time, around 35 % of total precipitation over land corresponds to water precipitated from the ocean. This ocean to land water transfer is balanced by the surface flow of water (mainly river flow) from the land back to the ocean.
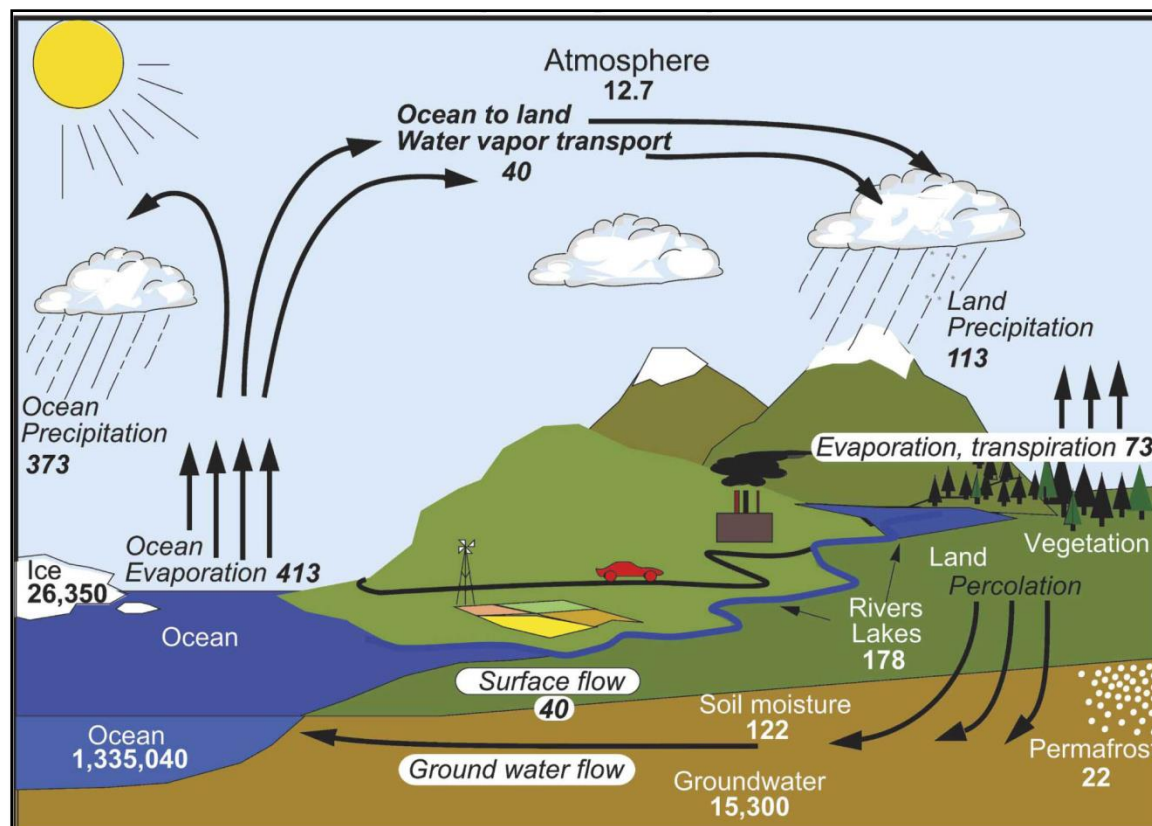
Figure 2. The long-term mean global hydrological cycle. Estimates of the main water reservoirs in plain font (e.g. soil moisture) are given in $10^3\,km^3$ and estimates of the flows between the reservoirs in italic (e.g. *Surface flow*) are given in $10^3\,km^3$/year. Figure from Trenberth et al., (2007) who provide information about the sources used to estimate the magnitude of the elements of the cycle and about the uncertainties of the various terms.

At the hydrological basin scale, the hydrological budget describes the balance between hydrological inputs and outputs. For a specific basin, the water balance is described by equation (4):

$$\Delta S = P - ET - Q + G_{in} - G_{out} \qquad (4)$$

Where ΔS is the change in storage in the basin over some period of time, P is precipitation, ET is evapotranspiration, Q is discharge, and G_{in} and G_{out} are groundwater inflows and outflows from the basin. Storage and groundwater inflows and outflows can be considered as negligible, and the water balance equation is simplified to equation (5):

$$P = ET + Q \qquad (5)$$

5

Where precipitation expresses the water that enters the basin system and evapotranspiration and discharge the water leaving the basin.

1.1.4. Carbon cycle

The carbon cycle is important for the climate as it involves changes in the atmospheric concentration of two important GHGs: carbon dioxide and methane. Carbon in the Earth system is stored in the following main reservoirs: i) in the biosphere – as organic molecules in living and dead organisms, ii) in the atmosphere – as gas carbon dioxide, iii) in soils – as organic matter, iv) in the lithosphere – as fossil fuels and sedimentary rock deposits, v) in the oceans – as dissolved atmospheric carbon dioxide and as carbonate shells in marine organisms. Various processes govern the exchange of carbon between the active carbon pools. Such processes, for example, are photosynthesis and respiration for the land surface and the atmosphere, and dissolution and diffusion between the ocean and the atmosphere.

At the pre-industrial period (before 1750), the exchanges of carbon between the different pools were close to equilibrium. In the last 150 years, anthropogenic activity related to fossil fuel combustion, deforestation and agricultural processes has resulted in a dramatic increase in the carbon flux into the atmosphere (Figure 3). Around 45 % of the anthropogenically released carbon dioxide remains in the atmosphere, while the remaining fraction has been absorbed by the ocean (~30 %) or the terrestrial biosphere (~25 %) (Goose et al., 2010). In the atmosphere, the concentration of carbon dioxide has increased from around 280 ppm in 1800, to 384 ppm in 2007, while it exceeded 400 pm during 2017 (Figure 4).
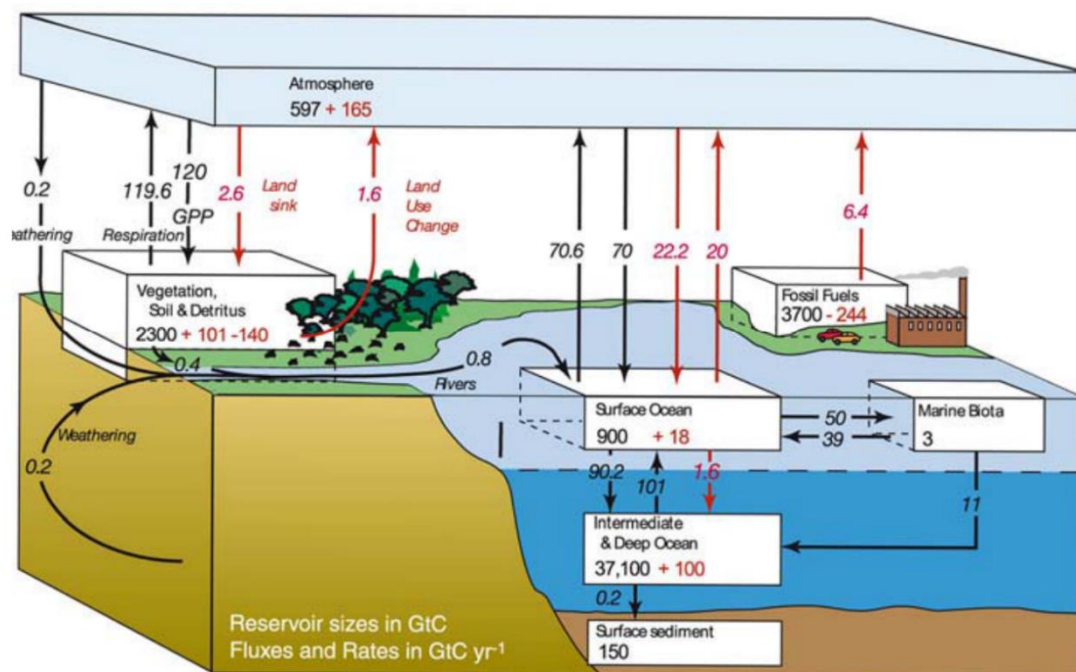
Figure 3. The global carbon cycle for the 1990s, showing the main annual fluxes in GtC yr^{-1}: pre-industrial "natural" fluxes are shown in black and "anthropogenic" fluxes in red (Denman et al., 2007).
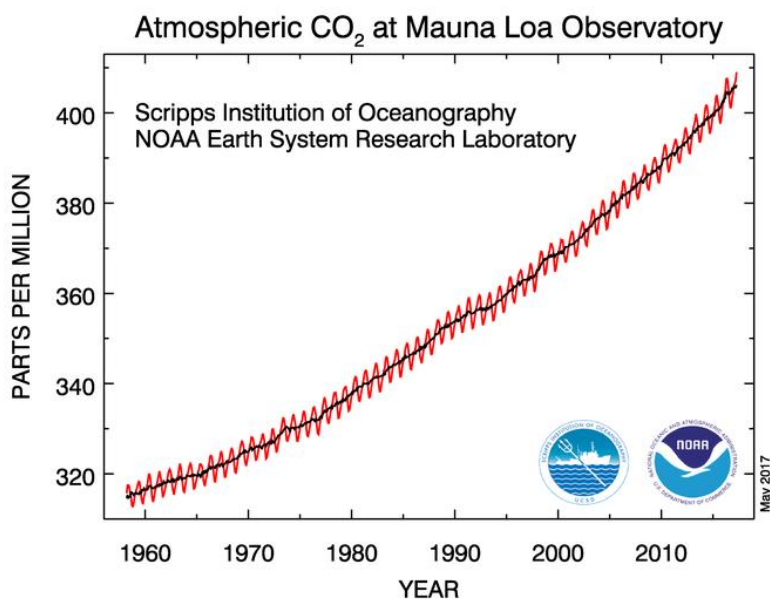
Figure 4. Monthly mean atmospheric carbon dioxide at Mauna Loa Observatory, Hawaii (in ppm). The red curve is the monthly measurement of carbon dioxide on Mauna Loa, expressed as the mole fraction in dry air. The black curve represents the seasonally corrected data smoothed with a 6-month window. Source: NOAA/ESRL (https://www.esrl.noaa.gov/gmd/ccgg/trends/full.html).

1.1.5. Enhancement of the natural greenhouse effect

The increased amounts of carbon dioxide and other GHGs that humans have released into the Earth's atmosphere since the industrial revolution, have resulted in an enhancement of the natural greenhouse effect. With higher concentrations of GHGs, additional heat is retained in the climate system, causing an increase in global temperature. The enhanced greenhouse effect is also referred to as global warming or anthropogenic climate change.

1.2. Studying climate and climate change

1.2.1. Modelling the climate system

Climate models

Climate models are of the most essential tools for studying and understanding climate and climate change. Climate models are mathematical representations of the climate system, based on physical, biological and chemical principles that describe each component of the system and their complex interactions. The equations that describe the system are discretized in space and time, in order to be solved numerically.

The main types of climate models, from lower to higher complexity are: energy balance models (EBMs), Earth system models of intermediate complexity (EMICs) and global climate models (GCMs). EBMs simulate the energy balance of the climate system as a whole, without accounting for the components of the system and the Earth's geography. EMICs include a representation of the Earth's geography, in a relatively coarse and simplified manner. GCMs are the most precise and complex tool for the simulation of the climate system. GCMs have higher resolution compared to the other climate model types and represent explicitly a wide range of atmospheric and oceanic processes. The typical spatial resolution of the GCMs is in the order of 100 to 300 km. Moreover, state-of-the-art GCMs include biogeochemical processes of the climate system (Earth system models – ESMs) (Katzav and Parker, 2015).

Regional Climate Models

Complementary to GCMs, regional climate models (RCMs) have higher resolution and allow a more detailed representation of regional scale processes. However, RCM domain covers only a portion of the globe (at continent or sub-continent level). RCMs run over a specified region, using boundary conditions from GCMs.

Parameterizations in GCMs

Even for the highest resolution GCMs, there are still important processes of the climate system, such as cloud phenomena and ocean eddies, that are related to more detailed spatial scales. Moreover, some phenomena have not been understood in a degree that would allow their explicit representation in a model. Consequently, parameterizations of these physical processes are designed and implemented in the models in order to approximate certain phenomena. As there is not a definite way to be followed for the construction of parametrizations, the latter constitute a considerable source of uncertainty in GCMs.

1.2.2. Climate change scenarios

Changes in climate are largely related to changes in external forcing. IPCC has employed the concept of radiative forcing to quantify the effect posed on climate by changes in parameters that affect the equilibrium of the climate system (such as the concentration of GHGs in the atmosphere). According to the IPCC 5th Assessment Report: " Radiative forcing is a measure of the net change in the energy balance of the Earth system in response to some external perturbation, with positive radiative forcing leading to a warming and negative radiative forcing to a cooling".

By inserting estimates of the changes in radiative forcing in climate models, "predictions" (scientifically termed as projections) of the future climate are produced. Changes in radiative forcing are described through different emission scenarios for GHGs, various pollutants, land use change, etc. The latest set of scenarios includes four representative concentration pathways (RCPs), which cover a wide range of future changes in radiative forcing (van Vuuren et al., 2011). The four RCPs, RCP2.6, RCP4.5, RCP6, and RCP8.5, are named after the value of radiative forcing in the year 2100 relative to pre-industrial values (+2.6, +4.5, +6.0, and +8.5 W/m^2, respectively). The

trends in radiative forcing, carbon dioxide and methane for the different RCPs are shown in Figure 5.
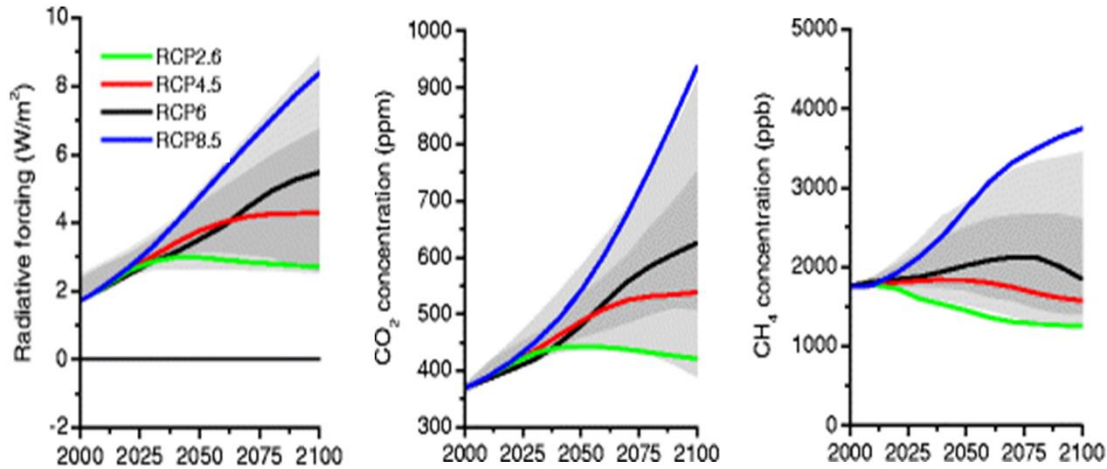
Figure 5. Trends in radiative forcing (left), carbon dioxide (middle) and methane (right) (adapted from van Vuuren et al., 2011).

1.2.3. Impact models

In order to assess climate change impacts for different sectors, climate model outputs based on an emission scenario are used to force respective impact models, specifically designed to represent the examined sector (e.g. water, biophysical, energy, health). For hydrological purposes, the most important tools for examining the impacts of climate change at the global scale are two model categories: global hydrological models (GHMs) and land surface models (LSMs).

GHMs describe the lateral transfer of water and are focused on water resources (Haddeland et al. 2011) while LSMs focus on flux exchanges mainly at the vertical direction, simulating the energy, water and carbon exchanges between the land surface and the atmosphere (Zulkafli et al. 2013), as they were originally developed to provide the lower boundary for climate models. GHMs aim at analysing global water resources and operate at a daily or monthly time-step. The processes typically described within GHMs are: evaporation, soil moisture, river flow, irrigation demands, reservoir operation, and water extraction. On the other hand, LSMs usually employ an hourly time-

step and represent the following processes: surface energy balance, photosynthesis and carbon fluxes, soil temperature and moisture, and river flow.

It should be noted however that for some models, their classification in one of the two categories cannot be definitive, and they have been reported in the literature both as GHMs and as LSMs. According to the classification proposed by Haddeland et al. (2011), the models that solve the water balance are considered as GHMs and the models that solve both the water and energy balance are categorized as LSMs.

1.2.4. Biases in climate modeling

Apart from the spatial resolution issue discussed above, GCM uncertainty can stem from uncertainties regarding the boundary and initial model conditions (Bromwich et al., 2013), and from misrepresentations of physical atmospheric processes (Maraun, 2012). These uncertainties result in GCM biases that express as deviations of the modelled climate variables from respective historical observations. As a result, outcomes of hydrological climate change impact studies have been reported to become unrealistic without a prior adjustment of climate forcing biases (Ehret et al., 2012; Hansen et al., 2006; Harding et al., 2014; Sharma et al., 2007). To overcome this limitation, various bias correction techniques have been developed to post-process climate model data to statistically match observations. Bias correction methods are calibrated based on a historical time-period for which observations are available. The adjustment is then applied to both modelled historical period and to the period beyond the time-frame of the observations.

Bias correction procedures have mainly focused on adjusting the biases of precipitation and/or temperature (Christensen et al., 2008; Li et al., 2010; Miao et al., 2016; Photiadou et al., 2016; Piani et al., 2010). These variables have traditionally been prioritized for bias correction as they are considered the most important driving variables of hydrological processes in modelling applications -even though from a physical perspective radiation is the driving force of the hydrological cycle. However, many state-of-the-art regional models, GHMs, and LSMs, require - apart from precipitation and temperature- additional meteorological forcing, such as solar radiation, air humidity, surface air pressure and wind speed (a summary of the input variables needed by various hydrological models can be found in the Supplement of Hattermann et al. (2017). For this reason, biases in variables like radiation, humidity and wind speed can hinder the representation of

hydrological fluxes such as runoff, evapotranspiration (ET), snow accumulation and snowmelt by the impact models (Haddeland et al., 2012; Hagemann et al., 2011a), indicating that bias correction should be extended to include more input variables.

Bias correction itself also has limitations, as it is a demanding process, both in terms of computational cost and of the involved methodological development. Moreover, the use of bias correction is challenged by conceptual pitfalls such as the disruption of the physical consistency of climate variables, the mass/energy balance and the omission of correction feedback mechanisms to other climate variables (Ehret et al., 2012). For these reasons, it is worth examining whether the effect of biases of input variables on hydrological outputs justifies the use of bias correction. Even though this information would be key for making informed decisions on the variables that should be bias corrected for a specific model application, few relevant studies can be found in literature. Some insight is given by Haddeland et al. (2012), who investigates the combined effect of bias correcting radiation, humidity and wind speed in addition to precipitation and temperature on hydrological simulations. However, the extent to which individual forcing variable biases affect hydrological simulations and the way that this effect varies spatially are important research questions that remain open.

1.2.5. The modelling "chain"

The tools and methods employed for climate and climate change impacts' studies constitute a modelling "chain", which is summarized in Figure 6. Scenarios of future GHG emissions are used to drive GCMs, which produce simulations of the future climate. GCM output can be used directly as forcing to impact models. Alternatively, the steps of downscaling with the used of RCMs and/or correction for systematic GCM biases with bias correction can intervene to improve the representation of observed climate by the GCMs. The impact model output is used to produce the final climate change impacts' assessment for the examined sector (e.g. freshwater, agriculture, biomes, energy, health, etc.).
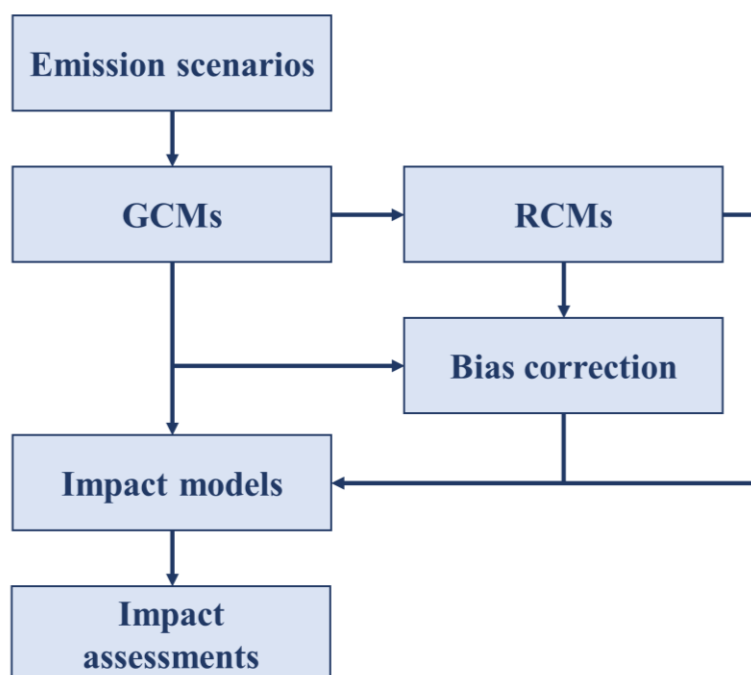
Figure 6. Climate change impacts' assessment modelling chain.

1.3. The need for climate change impact studies

With the Paris Agreement in 2016, the United Nations Framework Convention on Climate Change, decided to pursue efforts to limit global warming to well below +2°C. The increasing trajectory of GHG emissions up to present day however, constitute the accomplishment of the above target increasingly difficult. Global CO_2 emission rates have been following high-end climate change pathways leading to a future global temperature that is likely to surpass the target limit of +2°C, and reach levels of +4°C and higher at the end of the 21st century. Currently, global mean temperature has increased by 0.85°C relative to pre-industrial and already 18 % of the moderate daily precipitation extremes is attributed to this warming. At +2°C, the fraction of the global warming driven precipitation extremes is projected to rise up to 40 % (Fischer and Knutti, 2015).

By the end of the 21st century, the seasonality of river discharge is expected to get more pronounced for one-third of the global land surface, which translates to increased high flows and decreased low flows (Van Vliet et al., 2013). By the mid-century, the hydrological regime is projected to change considerably for a significant part of the global land surface (Arnell and Gosling, 2013).

In this context, information on future climate conditions is of paramount importance for policy makers at the national and international level, in order to plan actions and adaptation strategies to climate change under higher levels of warming. International climate policy often views climate change as levels of warming compared to pre-industrial conditions, and require information on the impacts of different levels of warming in order to decide on the target of warming that is set.

1.4. Hydrological impacts under a changing climate

Especially for water resources, the effect of global warming raises serious concerns on future water availability, especially under the pressure of the growing global population and the consequent increased food production needs. It is projected that the number of people coping with significantly reduced water availability will increase by 15 % globally due to climate change, while the percentage of the global population living under conditions of absolute water scarcity is also projected to increase (Schewe et al., 2014).

Moreover, under global warming, hydrological extremes –such as droughts and floods- are expected to become more often and destructive. Drought events affect millions of people each year and constitute one of the most disruptive natural events for the environment, the society and even the economy (Carrão et al., 2016). Drought is an extreme hydrological event affecting land areas, characterized by periods of below normal precipitation over a period of months to years. Drought is defined as a dry period compared to normal conditions of a region, and in that sense is different from aridity which is a permanent condition that characterizes a region (Dai, 2011). Droughts can be classified into three categories (Dai, 2011; Mishra and Singh, 2011): i) *Meteorological drought,* which is period of months or years with below normal precipitation, triggered by anomalies in large-scale atmospheric circulation patterns, ii) *Hydrological drought,* which is related to river discharge and water storages (e.g. lakes and reservoirs) that have fallen below their long-term mean

level, and iii) *Agricultural drought*, which is a period of reduced soil moisture, caused by a sustained lack of precipitation and/or increased evapotranspiration. A meteorological drought can evolve into an agricultural or hydrological drought, but other factors (such as soil moisture stores, temperature, water management, soil erosion) can enhance or moderate the progression of meteorological drought into the other categories.

The runoff production is the component of the hydrological cycle most representative to describe freshwater availability, as it expresses the amount of available water after the evapotranspiration and infiltration losses and before any stream formation process intervenes. Furthermore, ensembles of mean annual and seasonal runoff can provide information about the climate change impact on river flows (Döll and Schmied, 2012). Studies have shown that changes in runoff are not linearly correlated with changes in global mean temperature (Arnell and Gosling, 2013), neither are meteorological with hydrological droughts (van Huijgevoort et al., 2013), concluding that for climate change impact assessments it is fundamental to use an impact model to translate the precipitation derived signal into runoff.

A substantial number of recent large-scale climate change impact studies examine the future hydrological state analysing projections of runoff or river flow. Fung et al. (2011) compared the projected future water availability under $+2^{\circ}C$ and $+4^{\circ}C$ of global warming, forcing the MacPDM GHM with twenty-two GCMs from the CMIP3 experiment. Arnell & Gosling (2013) performed a global assessment of the climate driven changes in runoff based hydrologic indicators in mid-21st century, using multiple scenarios derived from the CMIP3 experiment. Schneider et al. (2013) focused on the impacts of climate change for the European river flows, using data from three bias corrected GCM scenarios. Van Vliet et al. (2013) performed a global assessment of future river discharge and temperature under two climate change scenarios, forcing a GHM with an ensemble of bias corrected GCM output. They found that the combination of lower low flows with increased river water temperature can lead to water quality and ecosystem degradation in south-eastern United States, Europe, eastern China, southern Africa and southern Australia. An investigation of the future trends in flood risk at the global scale was performed by Dankers et al. (2014) and for the European region by Alfieri et al. (2015). Betts et al. (2015) performed a global assessment of the impact posed on river flows and terrestrial ecosystems by climate and land use changes described by four RCPs. Various multi-model hydrological simulations have been also performed,

in an attempt to quantify the climate change analysis' uncertainty resulting from the impact model (Hagemann et al., 2013; van Huijgevoort et al., 2013; Dankers et al., 2014).

Significant climate change induced alterations are projected for the flow regime in Europe, with the most pronounced changes in magnitude projected for the Mediterranean region and the northern part of the continent (Schneider et al., 2013). Moreover, considering that southern Europe is identified as a possible hotspot where the fraction of land under drought will increase substantially (Prudhomme et al., 2014), along with global temperature rise exceeding +2°C, concerns for future water availability in Europe are raising. Prolonged water deficits during long-term droughts surpass the resilience of the hydrological systems and are a significant threat to water resources security in Europe (Parry et al., 2012). In the Euro-Mediterranean regions the severity of droughts has increased during the past fifty years, as a consequence of greater atmospheric evaporative demand resulting from temperature rise (Vicente-Serrano et al., 2014). Besides southern European areas, north-western and central-eastern regions appear more drought prone than the rest of Europe (Bonaccorso et al., 2013). Streamflow projections indicate more severe and persistent droughts in many parts of Europe due to climate change, except for northern and north-eastern parts of the continent. The opposite is projected for the middle and northern parts with a highly significant signal of reduced droughts that may be reversed due to intensive water use (Forzieri et al., 2014). Consequently European cropland affected by droughts is projected to increase seven-fold (up to 700,000 km^2/year) at about +3°C of global warming (Ciscar et al., 2014) compared to the situation of the last decades. Similarly, under the same warming level, European population affected by droughts is expected to increase by a factor of seven, overcoming the 150 million/year.

1.5. Scope of the present dissertation

The present dissertation focuses on providing a detailed and multi-faceted assessment of the effects of high-end climate change on hydrological resources at the regional, continental and global scales based on a wide range of "hydrologically opposing" future climates. In pursuit of the above scope, the following objectives have been set:

- Set up and validate a hydrological impact model, which serves as the tool for the performed hydrological climate change impact assessment.
- Better understanding of historical hydrological regimes at the regional and global scale.

- Understand the extent and the effect of GCM biases on historical hydrological simulations.

- Development of a methodology for the quantification of the effect of GCM biases on historical hydrological simulations.

- Provide simulations of future water availability and droughts, using state-of-the-art climate model outputs, under scenarios of high-end climate change.

- Combination of methods for the analysis of water availability and droughts at the regional, European and global scale.

1.6.   Points of innovation

The innovative points of this thesis concern the sectors of basic science, applied science, and information technology development as follows:

Basic science:

- Coupling of a routing algorithm with the output of the hydrological model, to allow model validation.
- Development of a new methodological framework for the categorization of the effects of GCM biases.
- Combination of methods for the analysis of runoff regimes and drought events.

Applied science:

- Hydrological simulations at the global scale.
- Evaluation of the hydrological model for a historical period. Assessment of the role of the forcing dataset.
- Processing and analysis of state-of-the-art GCM outputs and hydrological outputs, extraction of climatic trends.
- Drought analysis under different methods, for droughts of different types and durations.
- Study of climate change impacts on mean and extreme hydrological regimes.

Information technology development:

- Development of a routing application in MATLAB.
- Development of the application for the categorization of the effects of GCM biases in MATLAB.

- Development of applications for the analysis of NetCDF type GCM output data in MATLAB.

- Development of applications for the analysis of NetCDF type hydrological model outputs in MATLAB.

1.7.   Outline

Up to this point, the theoretical background on climate and its basic mechanisms and on the science of studying the climate and climate change have been presented. Moreover, the need for climate change impact studies -which is the rationale of the present thesis-, has been advocated and a literature review on hydrological climate change impacts has been presented. The points of innovation of the thesis are also included in this first Chapter.

In the second Chapter, the various datasets used in the thesis are presented, starting from forcing datasets (observational and GCM outputs) and continuing with runoff and discharge data along with other datasets employed for the purposes of this thesis.

Chapter 3 includes the description of the model JULES, which was used to perform the hydrological simulations analysed in the present thesis. Moreover, Chapter 3 includes descriptions of the developed methodologies of runoff routing and categorizing the bias correction effects. Finally, the methodologies employed for bias correction and for climate change impact assessment are also included in Chapter 3.

In Chapter 4, the regions and hydrological basins selected for regional analysis are presented.

Chapter 5 includes the results of this study. Firstly, the historical model evaluation results are presented, followed by an analysis of the effect of GCM biases on runoff at the global scale. Afterwards, the projections of hydrological impacts under high-end climate change for the European region and for the global scale are analysed and inter-compared.

In the final Chapter 6, the findings of the thesis are summarized, conclusions are drawn and suggestions for future research are proposed.

Chapter 2. Datasets

2.1. Observational forcing datasets

State-of-the-art meteorological datasets based on observations have been developed by different institutes, in response to the needs of global impact modelling. They have been designed to provide input for land surface water and energy balance simulations. Typically, they are provided at the global scale, covering an extended historical period of at least thirty years and include near surface values for various meteorological variables commonly required by the impact models (e.g. precipitation, temperature, radiation, humidity, pressure, wind speed). Typical steps for the derivation of observational datasets is some kind of interpolation of station and/or satellite data, elevation adjustments of the variables and corrections of the extracted meteorological variables against observations. The datasets are all based on weather models but employ different analysis methodologies (e.g. for interpolation or bias correction) and observation data.

WATCH Forcing Data Methodology Applied to ERA-Interim Reanalysis (WFDEI): The WFDEI dataset (Weedon et al., 2014) was developed within the Integrated Project Water and Global Change (WATCH). The WFDEI dataset is based on its predecessor WFD (WATCH Forcing Data; Weedon et al. 2010), which was derived from the ERA-40 reanalysis product (Uppala et al., 2005) based on gridded station observations of the Climate Research Unit (CRU) and the Global Precipitation Climatology Centre (GPCC). WFDEI data span from 1979 to 2012, with three-hourly and daily time-steps. For detailed information on the derivation of the WFDEI dataset the reader is referred to Weedon et al. (2014).

Princeton Global Meteorological Forcing Dataset version 2 (PGFv2): PGFv2 is an updated version of the dataset developed by Sheffield et al. (2006), and spans from 1901 to 2012, with three-hourly and daily time steps. PGFv2 combines global observation-based datasets from stations and satellites with the National Centers for Environmental Prediction-National Center for Atmospheric Research (NCEP-NCAR) reanalysis.

Global Soil Wetness Project Phase 3 (GSWP3): GSWP3 (http://hydro.iis.u-tokyo.ac.jp/GSWP3/) is the latest version of the GSWP dataset (Dirmeyer, 2011; Dirmeyer et al., 2006). It covers the time-period from 1901 to 2010, with a daily time-step. GSWP3 is derived based on the 20th Century

Reanalysis (20CR) using the NCEP atmosphere land model. The correction of the variables was based on observational data from GPCC and CRU.

2.2. GCM datasets

Climate data from multiple GCMs of the latest Climate Model Inter-comparison Project (CMIP5, Taylor et al., (2012)) were used in this study. CMIP5 constitutes the state-of-the-art experiment for the climate science at the global scale. In total, three different GCM ensembles were formed: one for the European domain and two for the global scale. For all the ensembles, the members were selected so as to cover a wide range of climate sensitivities and thus explore a wide range of model uncertainty.

For the European domain, regionally downscaled CMIP5 climate data from the Coordinated Downscaling Experiment – European Domain (EURO-CORDEX, Jacob et al., (2014)) were used. The CORDEX experiments are coordinated by the World Climate Research Programme (WCRP) and aim at the production of downscaled climate simulations, mainly at the continent level. For the European domain, the EURO-CORDEX climate simulations are produced at the spatial resolution of 0.44º while for fewer models there are also simulations of higher resolution (0.11º, or ~12km). The time period covered by the EURO-CORDEX simulations extends from 1951 to 2100. For the purposes of this study, five EURO-CORDEX models run under the RCP8.5 emission scenario and with a spatial resolution of 0.44º were selected (Table 1). This set of GCMs is referred as EURO-CORDEX ensemble throughout this study.

Table 1. List of EURO-CORDEX models used in this study and time-slices of SWL2 and SWL4 according to the RCP8.5 emission scenario.

	RCM	Driving GCM	Time-slices (RCP8.5)	
			SWL2	SWL4
1	SMHI-RCA4	GFDL-ESM2M	2040-2069	2071-2100 (+3.2 ºC)
2	SMHI-RCA4	NorESM1	2036-2065	2071-2100 (+3.75 ºC)
3	SMHI-RCA4	MIROC5	2037-2066	2071-2100 (+3.76 ºC)
4	SMHI-RCA4	IPSL-CM5A	2018-2047	2055-2084
5	SMHI-RCA4	HadGEM2-ES	2024-2053	2060-2089

The first model ensemble for the global scale is comprised of three CMIP5 GCMs, under RCP8.5 (Table 2). The second global scale ensemble includes thirteen members (Table 3). Two high resolution GCMs (EC-EARTH and HadGEM) in Atmospheric General Circulation Model (AGCM) mode, are run using boundary conditions of sea surface temperature (SST) of multiple CMIP5 GCMs. The CMIP5 members used to provide SST forcing were selected as representative of a wide range of outcomes for future climate change, as they include models of both low and high sensitivity and with various global patterns of precipitation change. The produced high-resolution climate simulations span from 1971 to 2100 and beyond, have a spatial resolution of 0.5º and follow the RCP8.5 emission scenario. This latter sets of GCMs is referred as HELIX ensemble throughout this study.

Table 2. List of non-downscaled CMIP5 models used in this study, and their original spatial resolution.

No	GCM	ºLon x ºLat
1	IPSL-CM5A-LR	3.75 x 1.88
2	MIROC-ESM-CHEM	2.81 x 2.81
3	GFDL-ESM2M	2.50 x 2.00

Table 3. List of high-resolution CMIP5 models used in this study and time-slices of SWL1.5, SWL2 and SWL4 according to the RCP8.5 emission scenario. The driving GCM provides boundary conditions to the high-resolution GCM.

High-resolution GCM	Driving GCM	Time-slices (RCP8.5)		
		SWL 1.5	SWL2	SWL4
ECEARTH - R1	IPSL-CM5A-LR	2010-2039	2021-2050	2059-2088
ECEARTH - R2	GFDL-ESM2M	2023-2052	2039-2068	
ECEARTH - R3	HadGEM2-ES	2006-2035	2020-2049	2060-2089
ECEARTH - R4	EC-EARTH	2013-2042	2028-2057	2075-2104
ECEARTH - R5	GISS-E2-H	2016-2045	2032-2061	
ECEARTH - R6	IPSL-CM5A-MR	2009-2038	2023-2052	2057-2086
ECEARTH - R7	HadCM3LC	2011-2040	2025-2054	2073-2102
HADGEM-R1	IPSL-CM5A-LR	2009-2038	2020-2049	2056-2085
HADGEM-R2	GFDL-ESM2M	2021-2050	2036-2065	
HADGEM-R3	HadGEM2-ES	2004-2033	2018-2047	2056-2085
HADGEM-R6	IPSL-CM5A-MR	2008-2037	2021-2050	2054-2083
HADGEM-R8	MIROC-ESM-CHEM	2005-2034	2017-2046	2053-2082
HADGEM-R9	ACCESS1-0	2011-2040	2025-2054	2066-2095

2.3. Other datasets

2.3.1. Global gridded runoff data

The University of New Hampshire (UNH)/Global Runoff Data Centre (GRDC) composite runoff dataset (Fekete and Vorosmarty, 2011) includes gridded monthly runoff values spanning from 1986 to 1995. This dataset is one of the products of the International Satellite Land-Surface Climatology Project, Initiative II (ISLSCP II) data collection. UNH/GRDC Composite Monthly Runoff is derived by combining water model runoff estimates with measured river discharge. It is described as a data assimilation application on water balance, which is done by preserving the spatial specificity of the water balance calculations while also constraining them by the more accurate discharge measurements.

2.3.2. Discharge measurements

Discharge measurements from the GRDC database were used in this study. The GRDC database (http://www.bafg.de/GRDC/EN/02_srvcs/21_tmsrs/riverdischarge_node.html) has collected data from thousands of stations worldwide. For this work, data for twenty-one stations were obtained, corresponding to the different study basins, listed in Table 4. Each station was selected based on two criteria: data availability and minimum distance from the actual basin outlet. Discharge data were obtained in daily and monthly time resolution, according to availability.

Table 4. Numbers of the GRDC station numbers used in this study.

Basins	GRDC station number
Amazon	3629001
Congo	1147010
Nile	1362100
Mississippi	4127800
Parana	3265601
Lena	2903430
Yangtze	2181900
Niger	1734500
Volga	6977100
Murray	5404270
Indus	2335950
Ganges	2646200
Orange	1159100
Danube	6742900
Huang He	2180800
Saskatchewan	4213551
Rhine	6335020
Elbe	6340110
Oder	6357010
Guadiana	6116200
Kemijoki	6854700

2.3.3. E-OBS

E-OBS is a gridded dataset of precipitation and temperature for the European land region (Haylock et al., 2008). E-OBS is derived from station observations in Europe, after interpolation procedures. It has a spatial resolution of 0.25° and covers the period from 1950 to 2006 with a daily time-step.

2.3.4. Total Runoff Integrating Pathways (TRIP)

TRIP (Oki and Sud, 1998) is a global gridded data set providing information on the lateral water movement over land, following the paths of river channels. The dataset was originally derived with a spatial resolution of 1°, but the latest version employed for this study provides information on the 0.5° grid. The TRIP component used here is the flow direction, which is an ASCII file that provides for each grid-box a number that indicates the outflow direction from the grid-box.

2.3.5. ISIMIP runoff simulations

Runoff simulations produced by the JULES model are obtained from the server of the ISIMIP project (Inter-Sectoral Impact Model Intercomparison Project, https://www.isimip.org/). The simulations span from 1971 to 2099 and are forced by five GCMs, listed in Table 5. This set of simulations will be referred to as ISIMIP ensemble.

Table 5. List of ISIMIP simulations used in this study and time-slices of SWL2 and SWL4 according to the RCP8.5 emission scenario.

	ISIMIP ensemble		RCP8.5	
	GCM	SWL 1.5	SWL 2	SWL 4
1	GFDL-ESM2M	2040	2055	[2113]
2	NorESM1	2035	2052	-
3	MIROC-ESM	2023	2035	2071
4	IPSL-CM5A-LR	2015	2030	2068
5	HadGEM2-ES	2027	2039	2074

Chapter 3. Methods

3.1. The JULES land surface model

3.1.1. Overview

JULES is a physically based, fully distributed land surface model established in 2006. It is comprised of two parts: the Met Office Surface Exchange Scheme (MOSES; Cox et al., 1998) and the Top-down Representation of Interactive Foliage and Flora Including Dynamics (TRIFFID; Cox, 2001) component. MOSES is an energy and water balance model which is JULES' forerunner, and TRIFFID is a dynamic global vegetation model (Best et al., 2011; Clark et al., 2011; Cox, 2001). In our model application for this study, we do not examine vegetation dynamics and thus we are focusing on the MOSES component of JULES.

The meteorological forcing data required for running JULES are: precipitation rate, air temperature, downward shortwave and downward longwave radiation, wind-speed, air pressure and specific humidity (Best et al., 2011). Other data required by the model are ancillary soil and land use data as well as information on the grid setup (land mask).

JULES has a modular structure, which makes it a flexible modelling platform, as there is the potential of replacing modules or introducing new modules within the model. The physics modules that comprise JULES include the following themes: surface exchange of energy fluxes, snow cover, surface hydrology, soil moisture and temperature, plant physiology, soil carbon and dynamic vegetation (Best et al., 2011), with the latter being disabled for this application.

The plant physiology component of JULES includes the plant response to atmospheric CO_2. Elevated atmospheric CO_2 causes the plant stomata to close, which generally means that the plant becomes more water efficient and evapotranspiration losses are reduced, leaving more water available as runoff. This feature is of particular importance for climate change impact studies and is usually omitted from the standard hydrological models.

In JULES, each grid-box is represented with a number of surface types, each one represented by a tile. JULES recognises nine surface types (Best et al., 2011), of which five are vegetation surface types (broadleaf trees, needleleaf trees, C3 (temperate) grasses, C4 (tropical) grasses and shrubs) and four are non-vegetated surface types (urban, inland water, bare soil and ice). A full energy balance equation including constituents of radiation, sensible heat, latent heat, canopy heat and ground surface heat fluxes is calculated separately for each tile and the average energy balance for the grid-box is found by weighting the values from each tile (Pryor et al., 2012). In JULES, the default soil configuration consists of four soil layers of thicknesses 0.1 m, 0.25 m, 0.65 m and 2.0 m. This configuration however can be altered by the user. JULES simulates the energy, water and carbon fluxes at the vertical direction and does not account for possible exchanges and transfers between the different grid-boxes.

The JULES science modules and their linkages, along with a typical JULES grid-box and soil layers are shown in Figure 7. In the following sections, the different science modules will be briefly described. The definitions for the symbols in the equations to follow are tabulated in Appendix A, for clarity and space-saving reasons.
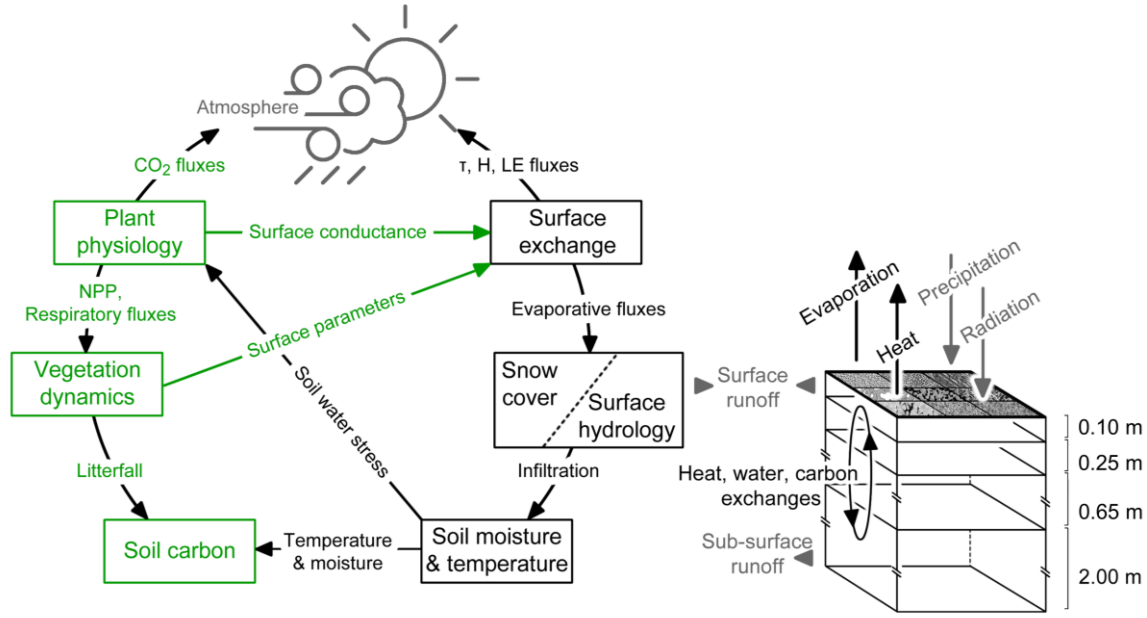
Figure 7. (Left) Graphical description of the main processes and fluxes modelled by JULES (Best et al., 2011, modified) and (Right) a typical JULES grid-box and underlying soil layers

3.1.2. Surface exchanges

The energy balance and the surface fluxes of heat and moisture are calculated in the surface exchange module of JULES. The surface related parameters (such as albedo), are treated differently for vegetated and non-vegetated surfaces. For non-vegetated surfaces these parameters are set by the user, while for vegetation surface types they are calculated in the model from the structure of the vegetation (e.g. based on leaf area index, canopy height, etc.).

The typical energy balance equations for the land surface have been extended to include additional physical processes: thermal inertia -coupled to the underlying soil and coupling of vegetation to the soil through radiative fluxes and heat conduction. The extended surface energy balance in the model is described by equations (6-9):

$$C_s \frac{\delta T_*}{\delta T} = (1 - a) S_{w\downarrow} + \epsilon L_{w\downarrow} - \sigma \epsilon (T_*)^4 - H_s - L_c E - G \qquad (6)$$

Where:

$$H_S = \frac{\rho \, c_p}{r_a}(T_* - T_A) \tag{7}$$

$$E = \frac{\rho}{r_a + r_s}(H_{sat}(T_*) - H_1) \tag{8}$$

$$G = v\left[\sigma\epsilon\epsilon_s(T_*)^4 - \sigma\epsilon\epsilon_s(T_{s1})^4 + \frac{\rho c_p}{r_{a_{can}}}(T_* - T_{s1})\right] + (1-v)\lambda_{soil}(T_* - T_{s1)} \tag{9}$$

The surface heat capacity C_s is prescribed for non-vegetation surfaces, but for vegetation types is calculated based on leaf and woody biomass, accordant to equation (10):

$$C_s = C_L \, B_L + C_W \, B_W \tag{10}$$

Larger heat capacity corresponds to larger thermal inertia of the surface.

3.1.3. Evaporative fluxes

Evaporation in JULES can stem from different sources, depending on the examined surface type. Firstly, possible sources of evaporation are evapotranspiration (water extraction from the soil through vegetation) and bare soil evaporation. Both fluxes depend on a surface resistance representing the restrictions in water availability. For bare soil, the surface conductance g_{soil}, which is the inverse of resistance, is calculated based on the moisture content of the top soil layer, based on equation (11):

$$g_{soil} = \frac{1}{100}\left(\frac{\theta_1}{\theta_c}\right)^2 \tag{11}$$

For vegetative surfaces, the resistance is determined using a photosynthesis model, which links the stomatal conductance g_s to net photosynthetic uptake A via the CO_2 diffusion equation (12):

$$A = g_s \, (C_c - C_i)/1.6 \tag{12}$$

Other sources of evaporation are freely evaporating moisture stores, for which resistance is zero. These sources include evaporation from open water surfaces, evaporation from water held in vegetation canopy and snow sublimation.

Water in the plant canopy is freely evaporated and can thus be depleted. In this case, possible additional evaporation will happen through the evapotranspiration mechanism, with an according stomatal or surface resistance. When snow is present on a surface type, it is treated as a moisture store with zero surface resistance. Snow sublimation from the surface snow store can deplete the snow mass, accordingly to canopy water.

3.1.4. Snow

In JULES, snow in a tile can be stored on the ground or be partitioned between snow intercepted in the plant canopy and snow on the ground. Surface resistance for sublimation is zero for snow on the ground but is determined according to equation (13) for snow on the canopy:

$$r_s = \frac{\rho_i \, r^2}{0.03 \, D_f (1.79 + 3 \, W^{\frac{1}{2}})} \left(\frac{I}{I_{max}}\right)^{0.4} \tag{13}$$

Where:

$I_{max} = 4.4L$, is the snow interception capacity for a canopy with leaf area index L

r=0.5 mm is a nominal grain radius for intercepted snow

In the snow model, the thermal conductivity and density of snow are set by the user. Heat capacity of snow is considered negligible, but the bulk thermal conductivity of the surface changes due to the presence of snow. If the snow depth is less than half the surface soil layer thickness (Δz_1), the thermal conductivity used in the surface energy balance is modified to account for the effect of snow insulation according to equation (14):

$$\lambda = \lambda_{soil} \left[1 + \frac{2 \, d_s}{\Delta z_1} \left(\frac{\lambda_{soil}}{\lambda_{snow}} - 1 \right) \right]^{-1} \tag{14}$$

For deeper snow, the surface conductivity is set equal to snow conductivity.

In the presence of snow on the ground, the surface skin temperature cannot exceed 0ºC. The heat flux used to melt the snow is accounted for in the surface energy balance as a residual. The snow water that melts leaves the snowpack, and is partitioned into soil infiltration and runoff.

3.1.5. Surface hydrology

Within the surface hydrology module, rainfall rate is assumed to fall on a fraction ϵ_r of the grid-box (typically set to a value of 0.3), to account for the size of convective storms compared to grid size. From the precipitating water, the amount of water that reaches the soil surface depends on the surface type. For non-vegetated surfaces, all the precipitation water reaches the land surface. For non-vegetation surfaces, some water is intercepted in the plant canopy. The capacity of the canopy to hold intercepted water, C_m, is defined in equation (15):

$$C_m = A_m + B_m\, L \tag{15}$$

Throughfall is the water that reaches the soil surface in case of vegetated surfaces, and depends on canopy water holding capacity and precipitation rate, as show in equation (16):

$$T_F = P\left(1 - \frac{C}{C_m}\right)exp\left(-\frac{\epsilon_r\, C_m}{P\, \Delta t}\right) + P\,\frac{C}{C_m} \tag{16}$$

Throughfall reduces the canopy water in the next computation time-step. Changes in canopy water can also result from dewfall (downward surface moisture fluxes), which increases canopy water and by evaporation, which decreases the water held in the canopy. With a similar mechanism, snow cover can be increased with frost deposition (modelled as dewfall at surface temperatures below freezing).

The water that reaches the surface infiltrates the soil at a rate K, equal to the saturated soil conductivity modified due to the presence of vegetation. If the throughfall rate exceeds the infiltration rate there is surplus water on the surface and surface runoff is produced. Throughfall can be different for different surface types in a grid-box but infiltration is the same as there is not sub-grid-box heterogeneity for soil in JULES. Therefore, calculation of runoff at the grid-box requires the combination of the grid-box mean infiltration and the grid-box aggregate of infiltration. The runoff calculation equation is shown in equation (17):

$$RF_s = \begin{cases} P \dfrac{C}{C_m} \exp\left(-\dfrac{\epsilon_r\, K\, C_m}{P\, C}\right) + P\left(1 - \dfrac{C}{C_m}\right)\exp\left(-\dfrac{\epsilon_r\, C_m}{P\, \Delta t}\right) & K\, \Delta t \leq C \\[3mm] Pexp\left[-\dfrac{K\, \Delta t + C_m - C}{P\, \Delta t}\right] & K\, \Delta t > C \end{cases} \tag{17}$$

Where:

$K = \beta_s\, K_{hs}$, where β_s [-] is an enhancement factor and K_{hs} [m s^{-1}] the saturated hydraulic conductivity

The water balance for the land surface is described by equation (18):

$$W_0 = \sum_j v_j\left(T_{F_j} + S_{m_j} - RF_{s_j}\right) \tag{18}$$

Where:

W_0 is infiltration flux into the soil [kg m^{-2} s^{-1}]

3.1.6. Soil temperature

The temperatures in the different soil layers are calculated using a finite difference form of the heat diffusion equation, accounting for the latent heat fluxes of solid-liquid phases of water. For the kth soil layer, equations (19-21) describe the soil temperature calculations:

$$C_a\, \Delta z_k\, \frac{dT_{sk}}{dt} = G_{k-1} - G_k - J_k \Delta z_k \tag{19}$$

Where the fluxes are calculated as:

$$G = \lambda_{soil}\frac{\partial T_s}{\partial z} \tag{20}$$

$$J = C_{water}\, W'\frac{\partial T_s}{\partial z} \tag{21}$$

z is the vertical coordinate

C_a is the volumetric heat capacity of the soil, including the effect of phase changes [J m^{-3} K^{-1}]

The top boundary condition for equation (19) is the surface heat flux calculated by the surface exchange module and the lower boundary condition is a zero flux boundary.

3.1.7. Soil water fluxes

The amount of soil moisture accessible by vegetation for extraction depends on plant root density, which is modelled with the assumption of exponential distribution with depth. The fraction of roots in soil layer k extending from depth z_{k-1} to z_k is shown in equation (22):

$$r_k = \frac{e^{-2\,z_{k-1}/d_r} - e^{-2\,z_k/d_r}}{1 - e^{-2\,z_t/d_r}} \qquad (22)$$

Soil water contents are updated using a finite difference form of the Richards equation. The moisture content of each layer is updated as shown in equation (23):

$$\frac{d\theta_k}{dt} = W'_{k-1} - W'_k - ET_k \qquad (23)$$

Where

W'_{k-1} and W'_k are the vertical fluxes of soil water flowing in from the layer above and out to the layer below respectively [kg m^{-2} s^{-1}]

ET_k is the evapotranspiration extracted by plant roots in the layer (and bare soil evaporation from the top soil layer)

The vertical fluxes follow Darcy's law in equation (24):

$$W' = K_h\left(\frac{\partial \Psi}{\partial z} + 1\right) \qquad (24)$$

The top boundary condition for equation (23) is the infiltration of water at the soil surface and the lower boundary condition is drainage, which contributes to sub-surface runoff. Sub-surface runoff is assumed to depend only on the soil moisture content, in contrast to surface runoff, which depends on the canopy throughfall and snowmelt rate, and is a relatively slow process. The relationship between soil water content, suction and hydraulic conductivity can be described either by the

Brooks and Corey relationship (Brooks and Corey, 1964), or by the van Genuchten relationship (Van Genuchten, 1980).

3.1.8. Carbon

The surface fluxes of CO_2 associated with photosynthesis and plant respiration are determined in the physiology component of JULES. The photosynthesis model is based on the biogeochemistry of plant photosynthesis at the leaf scale. These processes are then scaled up to the canopy scale through different methods (big leaf or multi-layer approach). Photosynthesis is calculated in terms of three potentially limiting factors: the Rubisco-limited rate, light-limited rate and rate of transport of photosynthetic products.

3.1.9. Applications of the JULES model

JULES has been used in many recent studies as a tool for evaluating the exchange of water, energy and carbon fluxes between the land surface and the atmosphere. Van den Hoof et al. (2013) assessed JULES' performance in simulating evaporative flux (and its partitions) and carbon flux in temperate Europe. Marthews et al. (2012) implemented JULES in tropical forests of Andes-Amazon to simulate all components of carbon balance and study possible flux variations between sites of different altitude. Zulkafli et al. (2013) implemented JULES in a humid tropical mountain basin of the Peruvian Andes-Amazon. MacKellar et al. (2013) evaluated JULES, implemented in a region of Southern Africa, concerning its ability to simulate the catchment streamflow. In the study of Bakopoulou et al. (2012), the sensitivity of the JULES outputs to the soil parameters of the model at a point scale was estimated. Dadson et al. (2010) sought to quantify the feedback between wetland inundation and heat and moisture fluxes in the Niger inland delta by adding an overbank flow parameterization into JULES. Burke et al. (2013) used JULES to simulate retrospectively the pan-arctic changes in permafrost and Dankers et al. (2011) assessed JULES' performance in simulating the distribution of surface permafrost in large-scale catchments. In a study by Jiménez et al. (2013), soil moisture modelled with JULES is evaluated against satellite soil moisture observations.

Other studies give insight into the hydrological performance of JULES specifically. Blyth et al. (2011) extensively evaluated the JULES model for its ability to capture observed fluxes of water

and carbon. Concerning discharge, their findings suggest that for the European region seasonality is captured well by the model. For temperate regions (like most of central Europe), the model exhibited a tendency towards underestimating river flows due to overestimation of evapotranspiration. Prudhomme et al. (2011) assessed JULES' ability in simulating past hydrological events over Europe. In general, the model was found to capture the timing of major drought events and periods with no large-scale droughts present were also well reproduced. The model showed a positive drought duration bias, more profoundly present in northwest Spain and east Germany-Czech Republic. Prudhomme et al. (2011) argue that this feature is related to overestimation of evaporation by the model. For regions where droughts tend to last longer, JULES exhibited a better ability of reproducing the drought events' characteristics. Gudmundsson et al. (2012) compared nine large-scale hydrological models, and their ensemble mean, based on their skill in simulating the inter-annual variability of observed runoff percentiles in Europe. According to the overall performance (accounting for all examined percentiles and evaluation metrics), JULES was ranked third best out of the ten models, after the multi-model ensemble mean and the GWAVA model. For low and moderately low flows, expressed as 5th and 25th percentile respectively, JULES is also in the top three models regarding the representation of inter-annual variability in runoff. In the study of Gudmundsson et al. (2012b), where an ensemble of hydrological models is evaluated for their ability to capture seasonal runoff climatology in three different hydro-climatic regime classes in Europe, JULES exhibits a good performance, comparable to that of the best performing multi-model ensemble mean. In other studies employing multi-model ensembles, focusing on the whole European region (Gudmundsson and Seneviratne, 2015) or a single basin in Europe (Harding et al., 2014; Weedon et al., 2015) JULES' simulations also correspond with these of the other models.

3.1.10. Technical information

JULES operates on UNIX systems. The user interface of JULES consists of several files with the extension .nml containing Fortran namelists. The model parameters, switches of different science options, and specification of inputs and outputs are all included in the various namelists. JULES can be run for a number of grid-boxes from one upwards. JULES inputs and outputs are in NetCDF format files, which is also the file format used for meteorological gridded datasets (observational and GCM outputs). Meteorological input files have a 2D gridded structure (for the x and y

dimension). In terms of outputs, JULES supports both 2D and 1D outputs. The 1D output is a land-points-only grid, supplied as a vector of land points. This option limits the size of the output file, as it does not store unnecessary information on sea points that are not being processed. For this reason, the 1D output option was used in this study. Due to this, a post-processing step was required in order to present outputs in a grid and thus look at the global scale patterns. Each grid-box of the 1D output was placed on its respective position on the 2D grid, based on the latitude and longitude information of each grid-box, which is included in the model output. The post-processing step to re-grid the 1D JULES output was performed with a relative algorithm, developed and run with the MATLAB software.

3.2. Development of a routing algorithm for historical model evaluation

JULES simulates the energy, water and carbon fluxes at the vertical direction for each grid-box and does not account for possible transfers between the different grid-boxes. For hydrological applications, this means that the model calculates the runoff produced in each grid-box at each time step. In physical systems, the produced runoff moves and accumulates through the river network and is converted to river discharge. The lack of such a mechanism in the model does not limit its applicability for hydrological climate change impact studies, for which runoff production can serve as a good indicator of freshwater availability. However, it hinders the evaluation of the model, as the model output cannot be compared to measured discharge. The transformation of runoff production to discharge requires a river routing scheme. Until recently (February 2015) the standard version of the JULES model did not account for a routing mechanism. To overcome this model limitation, a routing algorithm was developed and applied to the model's runoff output.

3.2.1. The routing algorithm

The developed routing algorithm is conceptual, based on the concept of time of concentration (TOC). It is a semi-distributed model, which routes the water with a source-to-sink approach.

TOC is the time that runoff needs to travel from its origin grid-box (source) to the outlet of a basin. TOC is defined as in equation (25):

$$TOC = L/V \qquad\qquad (25)$$

Where L [m] is the flow length, and V [m/s] is the flow velocity.

The concept of the routing algorithm is to find the time (day) that runoff from each grid-box of a basin contributes to discharge at the outlet. Then, discharge at the basin outlet can be calculated as the aggregation of runoff from the contributing grid-boxes, delayed by the adequate number of days depending on the TOC of each grid-box. As each grid-box has a different distance from the outlet, and thus a different flow length, the TOC is calculated for each contributing grid-box separately. Flow velocity V is treated as a calibration parameter of the model, which is the same for all the grid-boxes of a basin but different for each basin.

The algorithm is described by equation (26):

$$Q_t = \sum_{i=1}^{n} q_i^{(t-TOC_i)} \qquad\qquad (26)$$

Where Q_t [m^3/s] is discharge at the basin outlet at time t, n is the number of grid-boxes contributing to the specific basin, q_i [m^3/s] is discharge contribution of grid-box i, produced at the time-step *t-TOC$_i$* . q_i is calculated from the runoff output [kg m^{-2} s^{-1}], by dividing with the density of water and multiplying with the grid-box area.

As the output of the model has a daily time-step, the algorithm also operates daily, resulting in daily time series of discharge at the outlet of a study basin.

In order to implement the algorithm we need to identify the grid-boxes that contribute to a specific basin, as well as their distance from the outlet (flow length). This is done with a GIS application and the TRIP river routing dataset. In ArcGIS, the Hydrology toolbox is used to set the location of the GRDC gauging station of a study basin as the basin pour point, define the basin contributing grid-boxes and calculate their flow length.

The routing methodology is applied to historical runoff simulations for 16 basins, for which observations of daily discharge were available. The implementation of the developed routing algorithm allows the comparison of JULES simulated discharge with discharge measurements,

essentially providing a way to assess the model performance for a historical period at the basin scale.

3.2.2. Evaluation metrics

For the evaluation of JULES' hydrological performance for the historical period, three widely used evaluation metrics were employed: Nash-Sutcliffe efficiency (NSE), Percent bias (PBIAS) and the coefficient of determination (R^2). The formulas for the calculation of NSE and PBIAS are given in equations (27) and (28):

$$NSE = 1 - \left[\frac{\sum(Q_{sim} - Q_{obs})^2}{\sum(Q_{obs} - Q_{mean})^2} \right] \tag{27}$$

$$PBIAS = \left[\frac{\sum(Q_{sim} - Q_{obs}) * 100}{\sum Q_{obs}} \right] \% \tag{28}$$

where Q_{sim} is simulated discharge, Q_{obs} is observed discharge and Q_{mean} is the mean of observed discharge data. Discharge observations were obtained from the Global Runoff Data Centre (GRDC) database for 16 large-scale basins.

Calibration of flow velocity, *V,* was done using the NSE index and daily data. For the historical model evaluation, the metrics are calculated based on monthly data, based on the period 1981 to 2010. The time-periods missing from the observed discharge time-series were neglected from the calculation of the evaluation metrics.

3.3.   Bias correction methods

3.3.1. Multi-segment Statistical Bias Correction (MSBC)

The MSBC method (Grillakis et al., 2013) follows the principles of quantile mapping correction techniques and was originally designed and tested for GCM precipitation adjustment. According to the method, the Cumulative Distribution Function (CDF) space is split into discrete segments and then the individual quantile mapping correction is applied on each segment, achieving better fit of the parametric equations on the data and thus better correction, especially on the CDF edges. The

optimal number of segments is estimated by the Schwarz Bayesian information criterion to balance between complexity and performance. MSCB is used for precipitation correction while a modification of the methodology is used for bias adjustment of the rest of the meteorological variables required as input by JULES. For the other variables, the methodology is modified to use linear functions instead of the gamma that were used in the original methodology. This change allows for the facilitation of negative variable values that the gamma functions cannot simulate. Hence, the methodology becomes more universal and adequate to use in different variable types and distributions. An additional methodological change is performed to the edge segments correction, which are explicitly corrected using only the difference between the historical period model data and the observations. This provides rigidity to the correction, avoiding unrealistic temperature values at the edges of the corrected data CDF. This choice costs to the methodology the persistence of a small portion of the bias in the corrected data.

The EURO-CORDEX data (Table 1) were corrected with the MSBC method against the WFDEI dataset. Additionally, they were corrected against the E-OBS dataset, in order to assess the effect that the use of different observational dataset during bias correction of GCM outputs can have for hydrological simulations.

The three-member ensemble of CMIP5 models (Table 2) was corrected with the MSBC method against the WFDEI dataset.

3.3.2. Trend preserving bias correction

The trend preserving bias correction method (Hempel et al., 2013) is designed to preserve the absolute changes in monthly temperature, and relative changes in monthly values of precipitation. The methodology was applied for the correction of all the variables required as input by JULES.

The high-resolution GCM data of the HELIX ensemble (Table 3) were corrected with the trend preserving method, against the PGFv2 dataset.

3.4. Assessment of the effect of GCM biases on runoff simulations

3.4.1. Experiment description

In order to examine the effect of each forcing variable's bias on runoff we designed and implemented an experiment comprised of two parts (bias assessment and partial correction bias assessment) and nine sets of JULES' runs in total. A graphical description of the performed experiment is shown in Figure 8. Climate data from three GCMs and the WFDEI dataset are used as JULES' forcing. The sets of runs forced with GCM data, include three model runs –one per GCM. Then the analysis progresses using the ensemble mean. The time span of this analysis is the historical period 1981-2010. This is also the time span of the period used for bias correction of the GCM output.
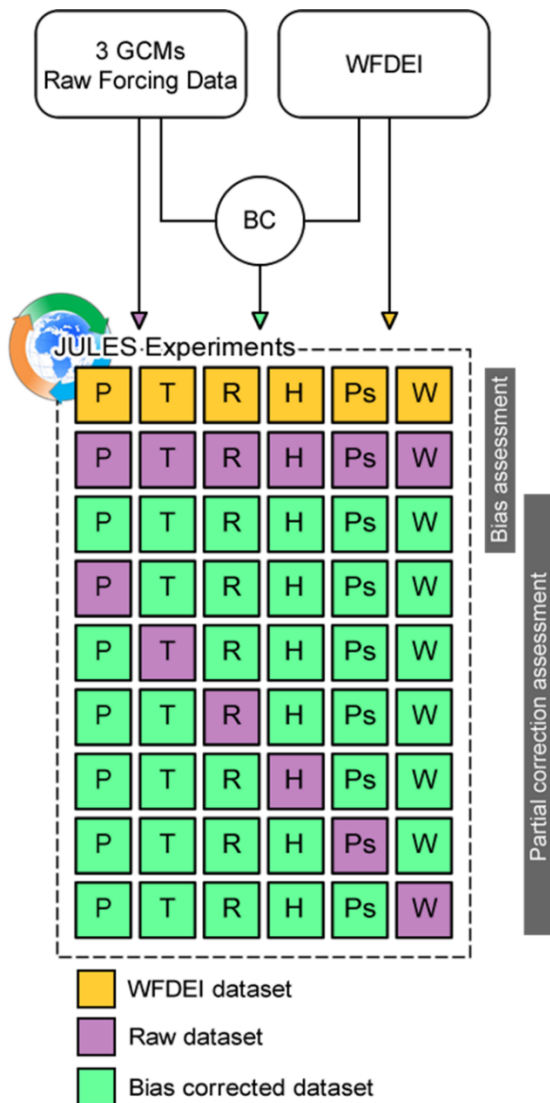
Figure 8. Graphical description of the experiment performed for the assessment of the effect of GCM biases on runoff simulations.

The first part of the experiment is the bias assessment. In this first part of the experiment, the aim is to assess initial and remaining biases in the forcing data and in simulated runoff. Initial bias refers to the difference between raw GCM variables and the respective WFDEI variables. Remaining bias is the bias in the forcing variables after the bias correction, i.e. the difference between bias corrected GCM variables and the respective WFDEI variables. Referring to runoff, "initial" and "remaining" biases are defined as the difference between runoff simulations forced with raw and bias corrected forcing respectively from simulations forced with the WFDEI dataset. This definition is employed

to shorten and simplify the expressions used in the text of this thesis (i.e. "initial bias in runoff" instead of "the difference between runoff forced with raw GCM data and WFDEI data"). In this part of the experiment, three sets of JULES' runs were conducted:

i.   forced with WFDEI (WFDEI);

ii. forced with uncorrected climate data (raw); and

iii. forced with bias corrected climate data (BC).

The second part of the experiment is the partial correction bias assessment. For this, six more sets of JULES' runs were performed. In each of these runs, one of the six forcing variables (precipitation, temperature, radiation, humidity, surface pressure and wind speed) is used in its raw form while the rest of the input forcing is bias corrected. The partial correction assessment runs are symbolized as NobcV (NOt Bias Corrected variable V), where V is one of the six forcing variables: precipitation (P), temperature (T), radiation (R), specific humidity (H), surface pressure (Ps) and wind (W). It has to be noted here that -longwave (Rl) and shortwave (Rs) were examined together, hence in respective NobcR run, both shortwave and longwave radiation were forced in uncorrected form. Partial correction assessment is composed as a tool to quantify the individual effect of each forcing variable on runoff but is not designed to suggest and assess run formats.

The simulated runoff of each partially corrected input is compared to the respective simulation in which all input variables are bias corrected (denoted BC). This comparison allows us to assess the "loss" of the performance of simulations when a variable is neglected from the bias correction procedure. It must be noted however that the "loss of performance" concept bears the assumption that the BC simulation is closer to the WFDEI simulation comparing to a partially corrected set.

3.4.2. A new framework for the categorization of the effect of GCM biases

A new framework for the classification of the effects of forcing variables' biases on modelled runoff is developed and implemented. The classification employs the comparison of the bias in each forcing variable (ΔV) and the corresponding relative effect in simulated runoff (ΔRF), discretizing four different categories (Figure 9). To facilitate the comparison among the different forcing variables, ΔV and ΔRF are expressed as percentages. More specifically, ΔV and ΔRF are defined as follows.

ΔV is the difference between the raw and the bias corrected variable value, divided by the bias corrected variable value. ΔV is estimated by equation (29).

$$\Delta V = (\text{Raw variable} - \text{BC variable}) / (\text{BC variable}) * 100\% \qquad (29)$$

As an exception, for temperature ΔV refers to the absolute difference between raw and bias corrected temperature (in K).

ΔRF expresses the effect of a variable's bias on runoff and is calculated from the difference between runoff forced with all bias corrected variables except for the examined variable V (NobcV) and runoff forced with all bias corrected variables (BC), divided by the runoff of all bias corrected variables (BC). ΔRF is estimated by equation (30).

$$\Delta RF = (\text{RF from NobcV} - \text{RF from BC}) / (\text{RF from BC}) * 100\% \qquad (30)$$

Sensitivity of runoff to changes in forcing variables (S) is the fraction of runoff change over the forcing variable change and serves as a measure to assess the relative magnitude of ΔRF compared to ΔV. When ΔRF is sensitive to ΔV, relatively smaller changes in the variable should cause relatively larger changes in runoff and vice versa. Sensitivity is in general dimensionless, but for temperature has units of K^{-1}. S is estimated by equation (31):

$$S = \Delta RF / \Delta V \qquad (31)$$

In total, there are six sets of ΔVs and six sets of ΔRFs, one for each examined variable and experiment respectively, and six sets of sensitivities (S). The absolute values of ΔV, ΔRF and S denoted as |ΔV|, |ΔRF| and |S| are used to avoid dealing with the sign of the changes and rather focus on their magnitude.

As shown in Figure 9, the effect of each variable's bias (|ΔV|) on runoff (|ΔRF|) is separated into four different categories according to two rules. The first rule is the characterization of |ΔRF| among all the experiments (except ΔT) as "low" or "high" relatively to its median value, shaping the ordinate y=median(|ΔRF|). Median(|ΔRF|) is derived considering the |ΔRF| values of all land grid-boxes and for all the experiments. The second rule is the characterization of sensitivity |S| as high or low relatively to its median value. The latter forms a bisectrix s=median(|S|). Median(|S|) is, accordingly to median(|ΔRF|), derived from the |S| values of all grid-boxes and for all the

experiments-apart from temperature. In the case of temperature, median ($|S|$) is explicitly recalculated from the values of all the land grid-boxes of this specific experiment. These two rules form the four categories of Figure 9. Combinations of the two rules result to four different effect categories (ECs) presented in decreasing order of the effect of a variable's bias on runoff:

   i.   High change and high sensitivity (ECI);

  ii.   High change and low sensitivity (ECII);

 iii.   Low change and high sensitivity (ECIII); and

 iv.   Low change and low sensitivity (ECIV).
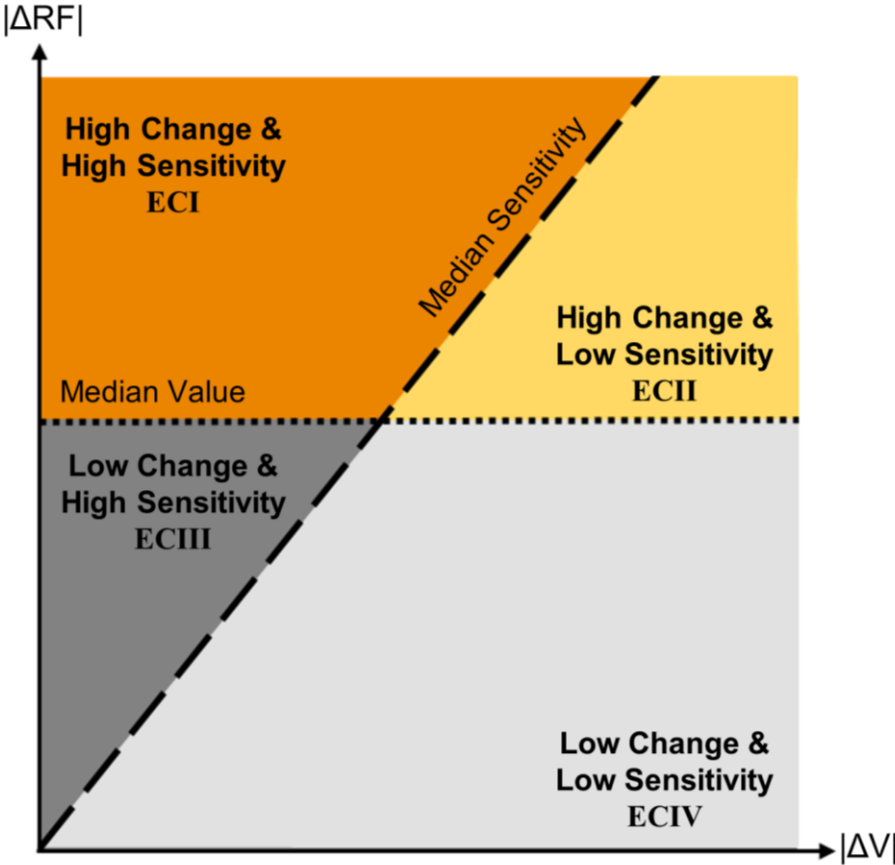
Figure 9. Categorization of the effect of changes in forcing variables (V) on runoff (RF). The four areas correspond to four defined Effect Categories. The x axis corresponds to relative changes in forcing variables and the y axis to relative changes in runoff. For all changes, the absolute value is considered.

3.5. Climate change impact assessment

3.5.1. Indicators of hydrological impact

Water availability

A number of hydrological indicators and drought indices are calculated, in order to perform a multi-faceted analysis of climate change impacts on hydrological resources. Firstly, analysis of mean precipitation gives us a metric of the total hydrological input in the examined system. Precipitation is acquired from the input meteorological data. Secondly, freshwater availability is a metric of net water that remains in the system after evaporation and infiltration losses. Freshwater availability is modelled using the runoff output of JULES. Average runoff (RFmean) is a good and widely used indicator of the mean hydrological state of a region. 10th percentile runoff (RFlow) is considered as a representative indicator of the low flow regime (Prudhomme et al., 2011). Consistent low flows (relative to the mean state) are connected with the formation of hydrological drought conditions. Thus the assessment of the changes in low flows could reveal trends towards more intense or/and often extreme lows in the future hydrological cycle.

Drought climatology

A number of methods are employed for the study of droughts. The first method is used to examine changes in drought climatology and is based on the threshold level method. The threshold level method is a widely used tool for drought identification applications (Fleig et al., 2006; Vrochidou et al., 2013). According to this method, drought conditions are characterized as the periods during which discharge falls below a pre-defined threshold level. In our application, the threshold is varying daily and is established as in Prudhomme et al. (2011): for each Julian day k, the 10th percentile of a 31-day window discharge centering at day k is derived, from data of all the years of the baseline period. The daily modelled time-series for the whole period simulated (from the start of the baseline period to the end of the projected period) is compared to the daily varying drought limit, and the number of days that fall below the threshold is summed up on an annual basis. The drought threshold is derived from the flows of the baseline period and is applied to both historical and projected flows, in order to capture the climate change induced changes in drought climatology. This method will be referred to as DVTM (Daily Varying Threshold Method).

Short- and long-term droughts

The standardized precipitation index (SPI, Mckee et al., 1993) is a widely used index for the identification of drought events' onset, intensity and duration. The calculation of the SPI is based on time series of precipitation. First the time series are fitted to a gamma distribution and then the cumulative probability of precipitation values is estimated. Finally, the cumulative probability is transformed to a standard normal deviate with zero mean and unit standard deviation (Mckee et al., 1993). Negative values of SPI indicate the existence of drought conditions. According to the SPI value, drought is grouped into one of four arbitrarily defined intensity tiers, ranging from "mild" to "extreme" (Mckee et al., 1993). This work was focused on intense drought conditions, thus only the "severe drought" ($-2 < \text{SPI} \leq -1.5$) and "extreme drought" ($\text{SPI} \leq -2$) categories were considered. Following the SPI concept, Shukla & Wood (2008) developed the standardized runoff index, which characterizes droughts by assessing modelled runoff time series. SRI has the same intensity tiers as SPI. While SPI is an indicator of meteorological drought, SRI incorporates hydrologic processes that determine seasonal lags in the influence of climate on streamflow and can serve as an indicator of hydrological drought.

For the assessment of climate change impact on droughts we used the relative versions of SPI and SRI (Dubrovsky et al., 2009). Relative indices use input data of two time periods. The first period serves as the reference period and is used for model calibration. The calibrated model is then applied to data of the second time period. This allows us to assess the drought conditions of the future compared to the benchmark drought conditions of the baseline period. The relative drought indices were calculated using two periods of temporal aggregation (6 and 48 months), in order to capture droughts of different duration. The 6-months temporal scale was selected for the examination of short-term meteorological drought associated to agricultural drought and changes to the seasonal variations. The 48-months temporal scale was employed for the description of long term droughts and effects on high capacity reservoirs related to drought indices at long time scales (Lorenzo-Lacruz et al., 2010).

3.5.2. Identifying changes in the hydrological regime

In order to identify the changes posed on the hydrological regime by the changing climate, analysis of hydrologic indicators is performed based on time-slices and time-series.

Time-slices

Climate change impacts are examined as differences between the temporal mean states of a future (projected) time-slice and the baseline period. The time-slices are comprised of thirty years. The baseline (or historical) period time-slice spans from 1976 to 2005 for the EURO-CORDEX analysis and from 1981 to 2010 for the high-resolution GCMs. The definition for determining the projected time-slices is to take a slice of thirty years, centered on the year where a Specific Warming Level (SWL) –for example 2°C- is exceeded. It is important to mention that the SWLs are defined with respect to the pre-industrial period while the baseline period corresponds to the recent past.

Throughout this work, three different SWLs are considered: +1.5°C, +2°C and +4°C. The projected time-slices corresponding to the examined SWLs are given in Table 1 and Table 3 respectively for the EURO-CORDEX and the HELIX ensembles of GCM data. For some models, the +4 SWL is achieved outside the temporal extend of the GCM input. In these cases, the last thirty-year period available is considered instead (2071-2100). For reasons of consistency in terminology the time-slice of all models describing the greater SWL achieved will be referred to as +4 SWL time-slice.

For the assessment of the impact of +1.5, +2 or +4°C warming relative to pre-industrial, the projected time-slices are compared to the baseline period in terms of both absolute and percent change. This is done for each ensemble member individually in order to check the variability of the projected changes and also for the ensemble mean.

The use of the SWL concept constitutes the results independent of the timing that the warming occurs. Although by definition of the SWL, the models reach the same level of warming in their time-slices, the different model sensitivity reflects on the evolution of temperature in the time-slice, as more sensitive models are expected to have higher rates of changes in the period before and after a specific SWL is achieved compared to the less sensitive models.

Time-series

For basin aggregates of hydrologic and drought indicators, the trend of the whole length of simulated time-series (e.g. 1981-2100) was studied. The trend of the time-series was investigated employing a linear regression analysis to estimate the sign and the average rate of the trend. The significance of the trend was tested at the 95 % confidence interval via a Student-t test.

3.6.   Summary of methodological framework

The methodological framework used in this study aims to provide a multi-faceted assessment of the effects of high-end climate change on the global hydrological regime. A graphical description of methodological framework of the present thesis can be found in Figure 10.

The first part is the historical model evaluation, which is implemented by forcing JULES with different observational datasets. Afterwards, the hydrological output is compared to a historical runoff dataset (runoff evaluation) and discharge measurements (discharge evaluation), after the newly developed routing algorithm is applied to the runoff output of the model.

The second part of the analysis is designed to assess the impact of GCM biases on hydrological simulations. To this end, JULES is forced with a combination of raw and bias corrected historical GCM data and with observational data that serve as a baseline simulation. Runoff output of the different runs participate in a newly developed methodological framework for the categorization of the effect of GCM biases.

The final part of the methodology presented in this dissertation concerns the assessment of hydrological climate change impacts. JULES is forced with historical and projected GCM data, and the assessment of hydrological impacts of climate change is done by comparing the changes of the projected simulations compared to the respective historical component. Hydrological impacts are described as effects on water availability and drought conditions, and are assessed at both the European and global scales.

Presentation of the results of this study follows the same structure as Figure 10.
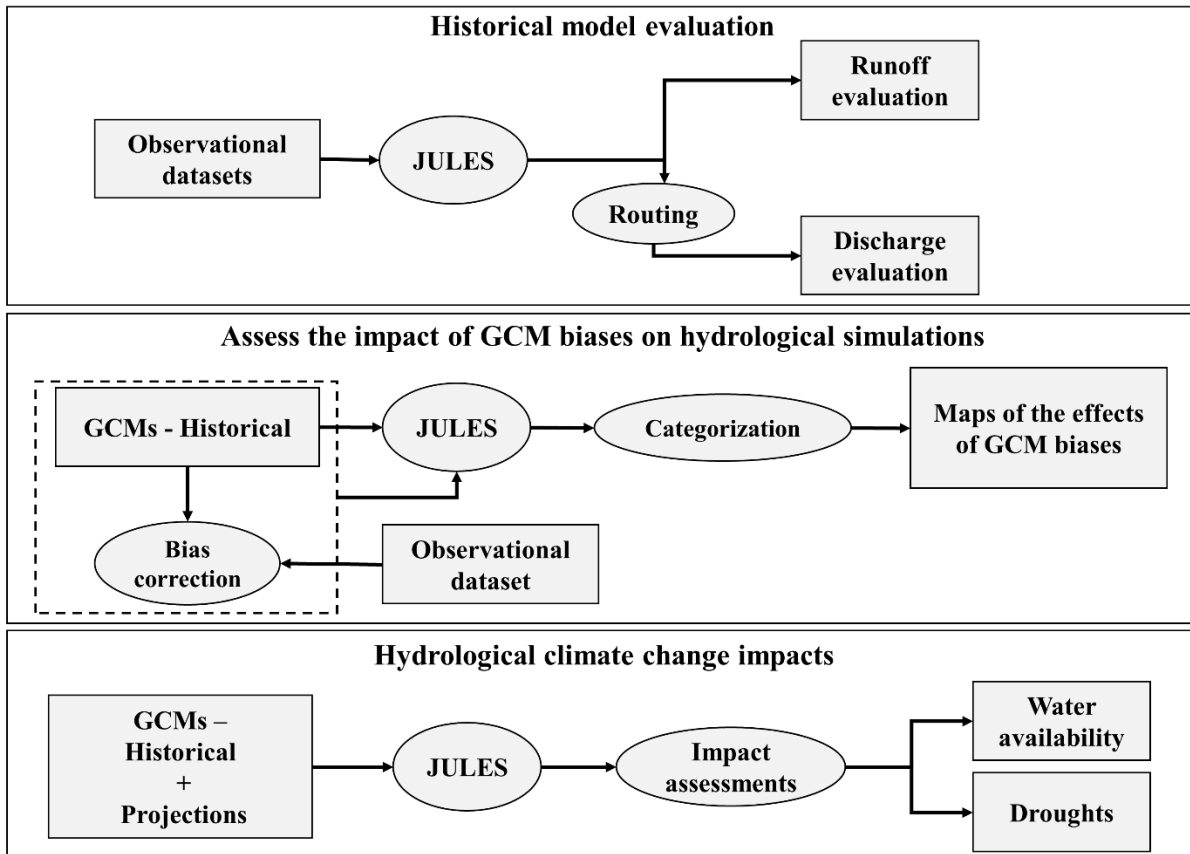
Figure 10. Schematic summary of methodological framework.

Chapter 4. Study regions

The results are firstly analysed at the whole spatial extend studied, which is the European region for the EURO-CORDEX experiments and the global scale for the rest of the runs. Focus on the European region is also given with the global high-resolution GCM data runs of the HELIX ensemble. At the global and continental scale, the spatial variation of the hydrologic indicators and their chaanges under climate change are examined, through presentation of gridded data. Moreover, spatial aggregations of hydrologic indicators are calculated and regional focus is given at hydrological basins and climatic regions around the globe.

4.1. Hydrological basins

The focus hydrological basins (shown in Figure 11), are large scale basins selected as representative of different hydro-climatic regimes, of different geographical regions and according to data availability.

Basin number	River name
1	AMAZONAS
2	CONGO
3	NILE
4	MISSISSIPPI
5	PARANA
6	LENA
7	YANGTZE
8	NIGER
9	VOLGA
10	MURRAY
11	INDUS
12	GANGES
13	ORANGE
14	DANUBE
15	HUANG HE (YELLOW RIVER)
16	SASKATCHEWAN
17	RHINE
18	ELBE
19	ODER
20	GUADIANA
21	KEMIJOKI
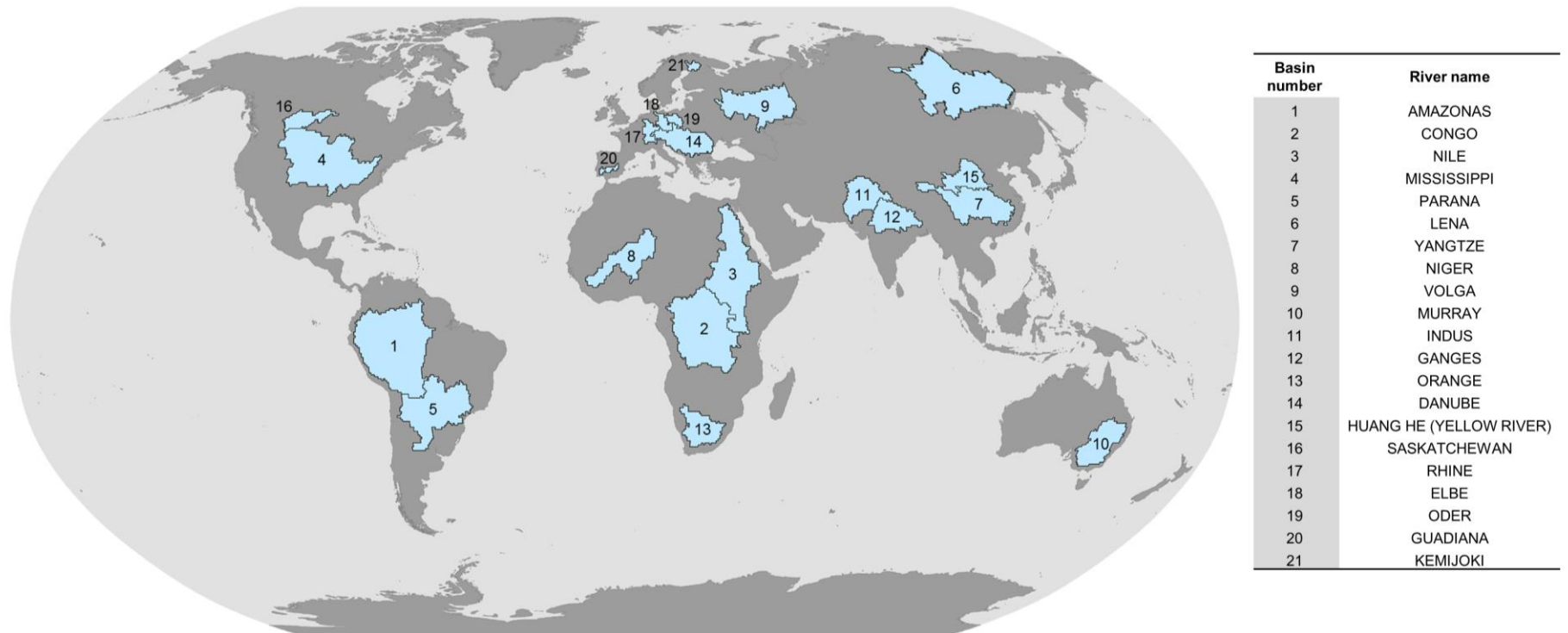
Figure 11. The 21 hydrological study basins. The basins are numbered in descending order according to their size.

4.2. Global sub-regions

Regional focus is also given at 24 regions of the globe. The examined regions were selected from the 26 regions presented in Giorgi and Bi (2005) (in our study Alaska and Greenland are excluded from the analysis), derived to express the climatic variation of the regions. The selected regions are shown in Figure 12. The abbreviations of the regions' names can be found in Table 6.
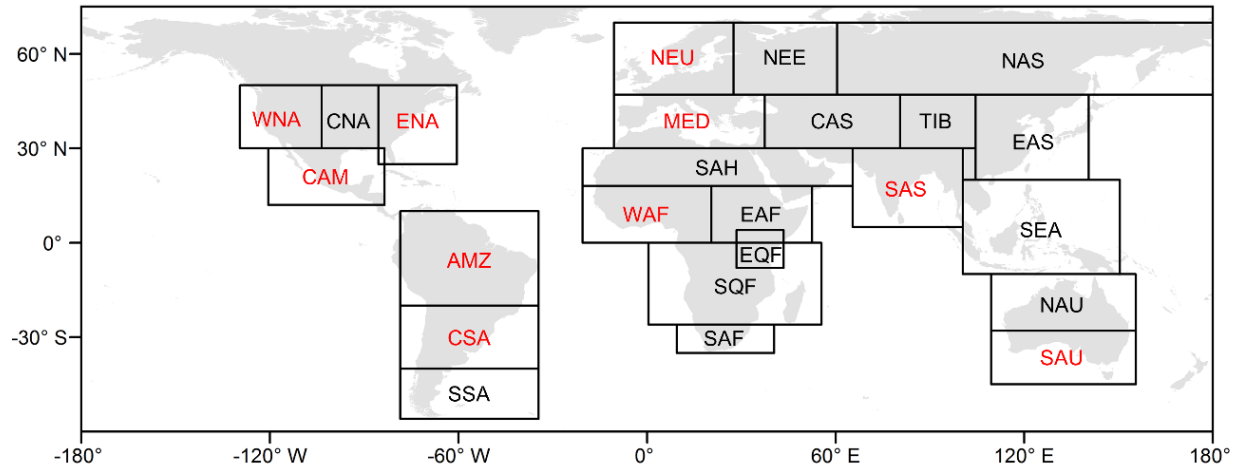
Figure 12. Outlines of study focus regions. With red colour are denoted the regions selected for more detailed analysis.

Table 6. 24 study focus regions, selected from Giorgi and Bi (2005).

Region name	Abbreviation
North Europe	NEU
Mediterranean Basin	MED
Northeast Europe	NEE
North Asia	NAS
Central Asia	CAS
Tibet	TIB
Eastern Asia	EAS
Southeast Asia	SEA
Northern Australia	NAU
Southern Australia	SAU
Sahara	SAH
Western Africa	WAF
Eastern Africa	EAF
East Equatorial Africa	EQF
South Equatorial Africa	SQF
Southern Africa	SAF
Western North America	WNA
Central North America	CNA
Eastern North America	ENA
Central America	CAM
Amazon	AMZ
Central South America	CSA
Southern South America	SSA
South Asia	SAS

4.3. European sub-regions

For the European continent, focus is given at eight sub-regions, shown in Figure 13.

Region	Short name	Full name
1	BI	British Isles
2	IP	Iberian Peninsula
3	FR	France
4	ME	Mid-Europe
5	SC	Scandinavia
6	AL	Alps
7	MD	Mediterranean
8	EA	Eastern Europe
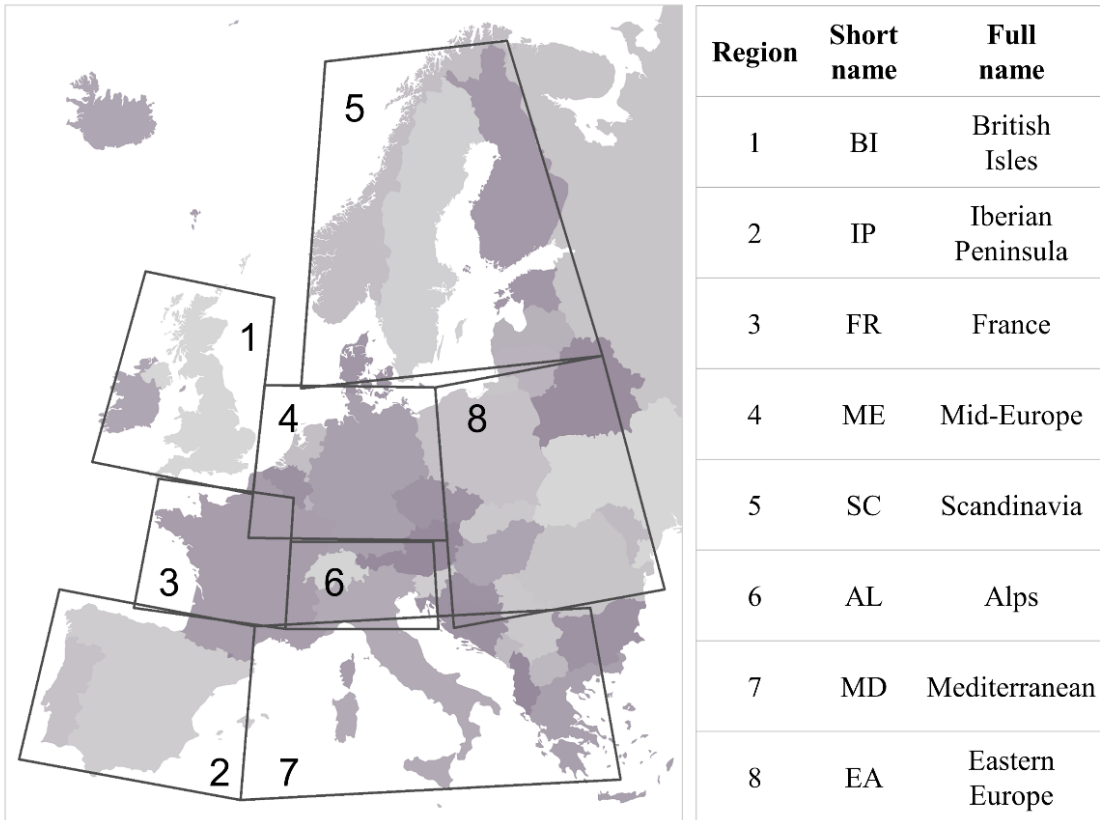
Figure 13. Studied European sub-regions (Christensen and Christensen, 2007).

Chapter 5. Results

5.1.   Model evaluation for the historical period

Model evaluation for the historical period allows the assessment of the performance of the model on the representation of mean, low and seasonal hydrological states. The first part of model evaluation is done by comparing the un-routed JULES runoff output with a Global Gridded Runoff Dataset (described in Section 2.3.1). This comparison is done both for gridded data at the global scale and for basin aggregates of the same data. The second part of model evaluation is done at the basin scale, by comparing GRDC measured discharge to the JULES simulated discharge, after the post-processing routing algorithm has been applied. In summary, the first part of model evaluation is based on runoff and aims at the evaluation of mean and low hydrological states while the second part is based on discharge, and aims at the evaluation of monthly and seasonal discharge profiles at the basin scale.

In parallel with comparing the model to observations, the sensitivity of the model to the forcing dataset is assessed, as the model has been forced by three different observational datasets (WFDEI, PGFv2 and GSWP3).

5.1.1. Runoff based evaluation

Figure 14 shows the differences in mean monthly runoff production between the JULES simulations and the observed runoff dataset. The biggest differences appear in the west and central equatorial African region and in South America, around the Amazon. Concerning the rest of the land surface, runoff underestimations of up to 25 mm/month are found at the northern regions while overestimations of the same magnitude are found in regions of central North America, Europe, east Asia and Oceania. According to Figure 15, which illustrates the differences in the lower 10th percentile of runoff between simulations and observations, low runoff is underestimated by the model in west and south equatorial Africa, east South America and Indonesia. Regions of low runoff overestimation are northern Europe and west North America, together with west South America.

For a closer insight on the differences between the simulations and the observed runoff dataset as well as on the effect of the forcing dataset on the simulations, the gridded data were spatially aggregated and compared at the basin scale. The basin aggregated mean runoff values of simulations and observations are shown in Figure 16, along with a scatterplot of simulations versus observations. Table 7 contains information on the mean runoff value of the observed dataset and simulations aggregated at the basin scale and additionally includes the range of the simulations. Respective information for low runoff can be found in Table 9. Table 8 tabulates the absolute and relative difference between simulations and observations of mean runoff aggregated at the basin scale, and Table 10 provides the respective differences for low runoff.

In general terms the deviations between observations and simulations are small and their correlation is strong (R-squared is 0.91, 0.93 and 0.85 for the WFDEI, PGFv2 and GSWP3 datasets respectively). The larger runoff underestimation is reported for Congo and overestimation for Amazon and Volga. However, this concerns the absolute difference between observed and modelled values. Expressing these deviations as relative (percent) differences (see Table 8) it is found that Amazon is one of the basins with the smaller deviations from observed runoff (5.7 % to 17.0 %). Other basins with small relative differences between simulations and observations are Mississippi, Danube and Rhine. The largest runoff underestimation in relative terms is found for Guadiana (-71.6 % to -80.2 %) followed by Niger and Congo.

The forcing dataset used has a considerable impact on mean runoff simulations. The range of the three simulations expressed as percent of the average (see Table 7) varies between 10.1% (for Amazon) to 83.5% (for Kemijoki). For some basins with large range of simulations (Lena, Oder and Kemijoki) it is observed that a single forcing dataset leads to very small values of percent difference from runoff observations while the other datasets result in large deviations from the observed values (Table 8).

The comparison and correlation between observed and simulated values of 10th percentile runoff are shown in Figure 17. Low runoff simulations are well correlated with observations, although their correlation is slightly weakened compared to the one documented for mean runoff (R-squared values are 0.86, 0.87 and 0.77 respectively for the WFDEI, PGFv2 and GSWP3 datasets). Concerning the differences of simulations from observations, they appear much smaller in absolute

terms but are significantly more pronounced in relative terms. The range of the simulations is also augmented for low runoff (21.9 % to 287.4 %).
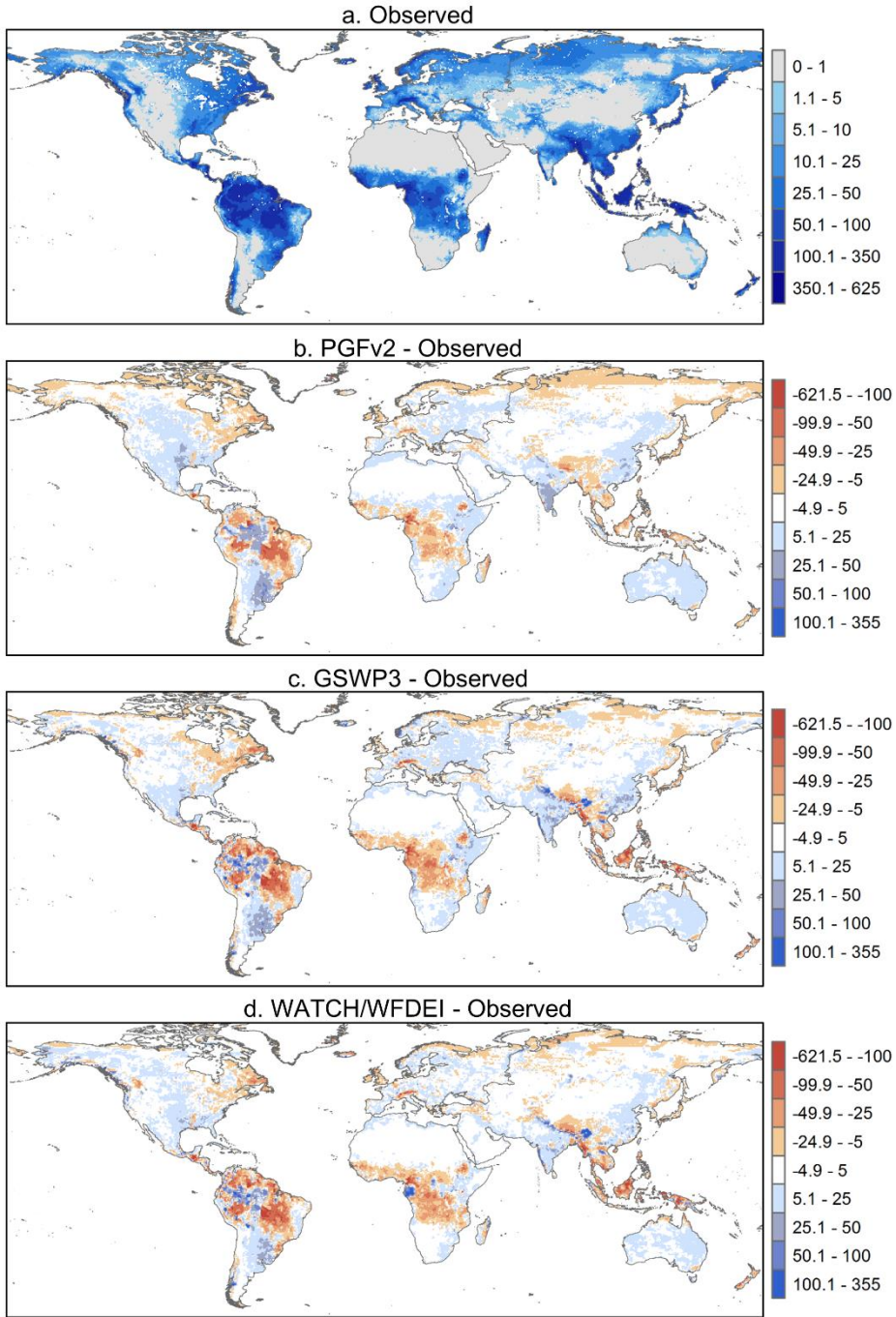
Figure 14. Mean runoff [mm/month] of the period 1986-1995, a) Observed runoff and b)-d) Difference between JULES simulated runoff for three forcing datasets and observed runoff.
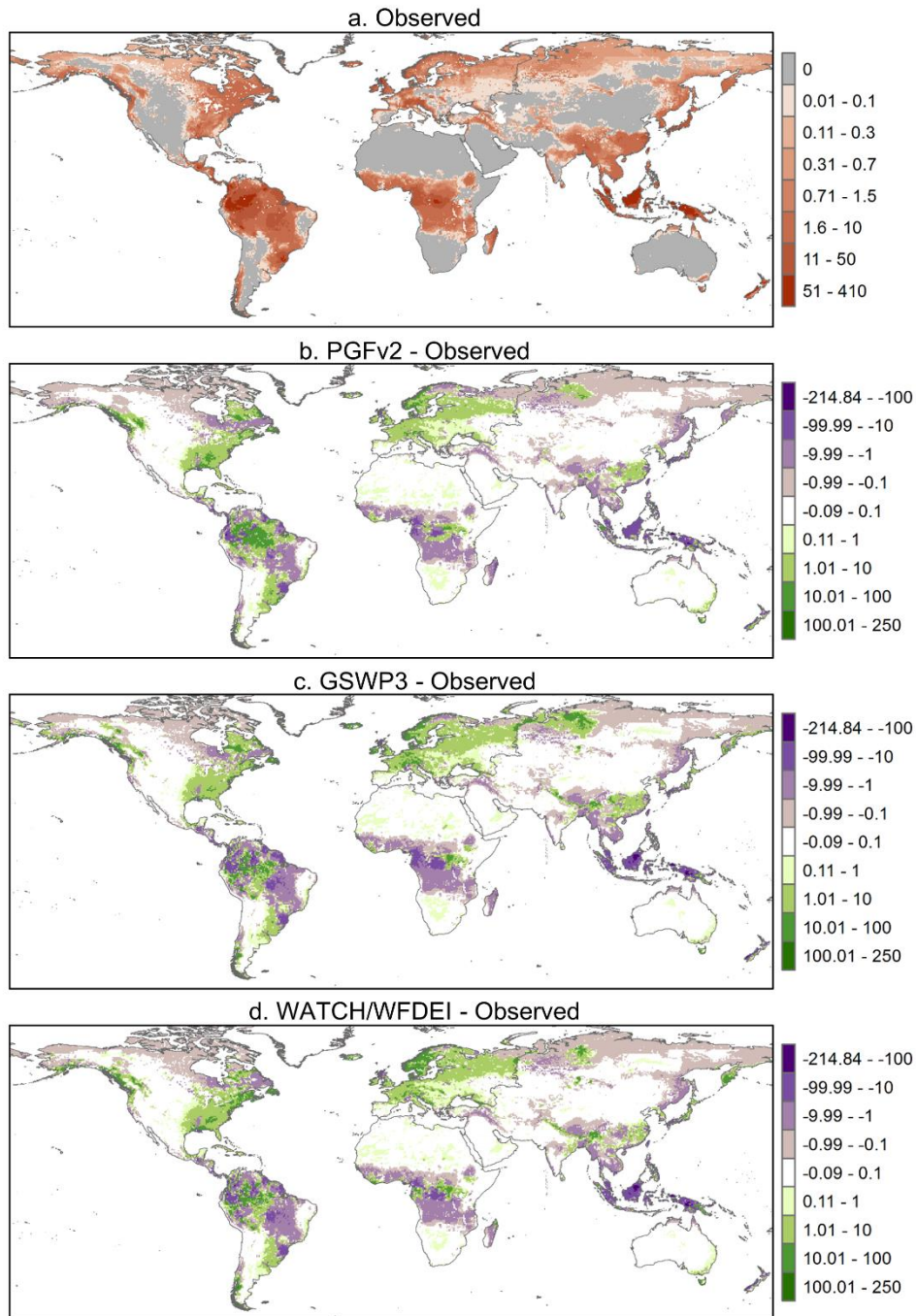
Figure 15. 10th percentile runoff [mm/month] of the period 1986-1995, a) Observed runoff and b)-d) Difference between JULES simulated runoff for three forcing datasets and observed runoff.
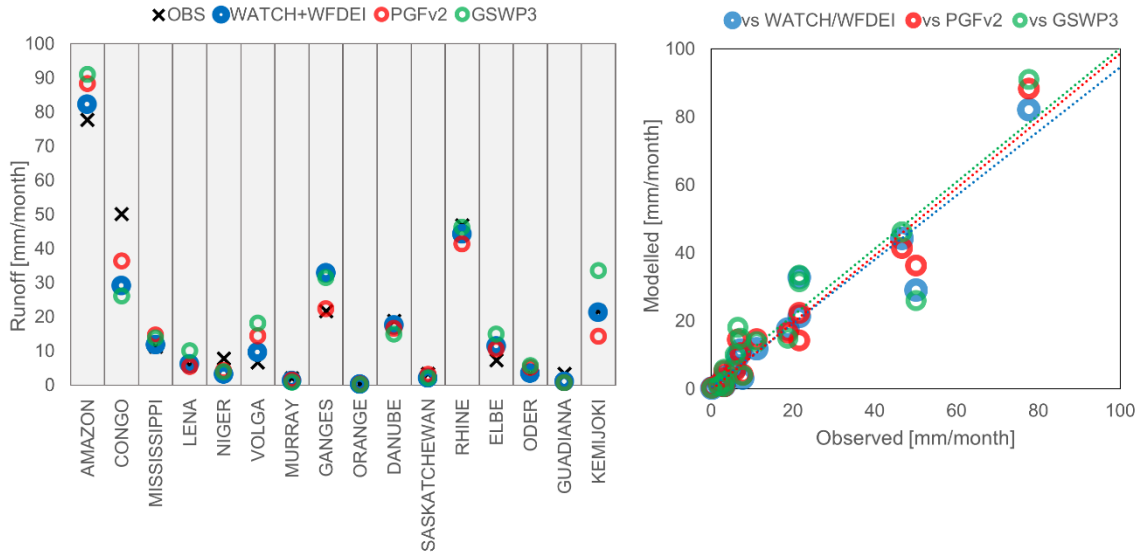
Figure 16. Basin aggregated mean runoff. Comparison between observed runoff and JULES simulated runoff for three forcing datasets.
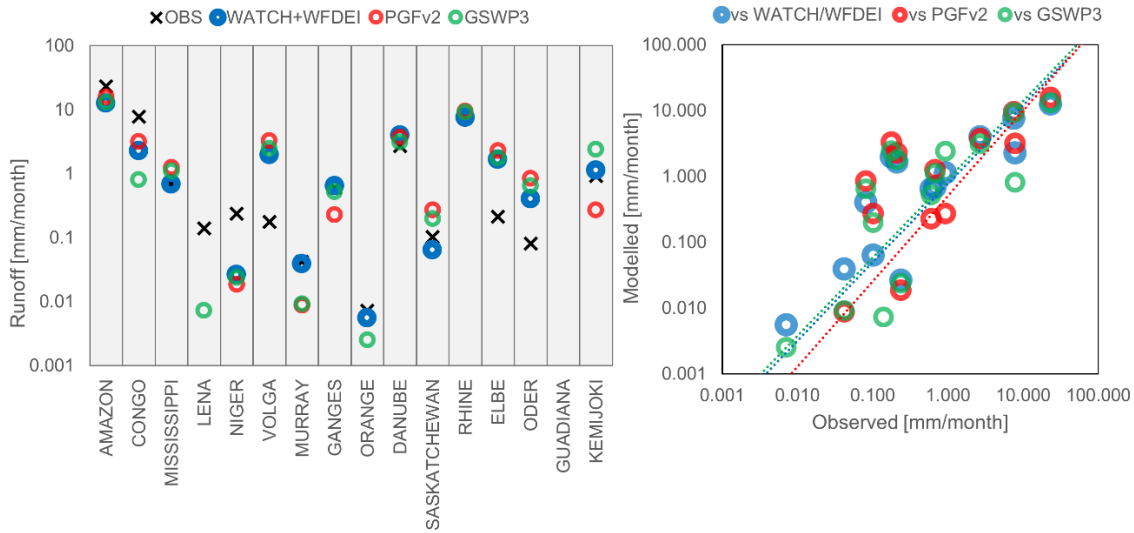
Figure 17. Basin aggregated 10th percentile runoff. Comparison between observed runoff and JULES simulated runoff for three forcing datasets.

Table 7. Basin aggregated values of mean runoff for observations and JULES simulations. The range of simulations (difference between higher and lower simulated value) and the range as percent of average value (range divided with the mean of the three simulations).

Mean runoff [mm/month]						
Basin	**OBS**	**WFDEI**	**PGFv2**	**GSWP3**	**Range of simulations**	**Range of simulations as percent of average value**
AMAZON	77.73	82.15	88.28	90.96	8.81	10.11%
CONGO	50.17	29.09	36.29	26.00	10.29	33.79%
MISSISSIPPI	11.23	11.80	14.63	13.79	2.83	21.12%
LENA	5.90	6.11	5.35	10.04	4.68	65.34%
NIGER	7.73	3.13	4.18	3.91	1.05	28.06%
VOLGA	6.56	9.50	14.44	18.10	8.59	61.33%
MURRAY	2.02	1.27	1.42	0.82	0.61	52.06%
GANGES	21.65	32.83	22.37	31.50	10.46	36.18%
ORANGE	0.30	0.18	0.30	0.15	0.15	69.04%
DANUBE	18.82	17.53	16.52	14.93	2.60	15.95%
SASKATCHEWAN	3.33	1.93	3.14	2.10	1.21	50.50%
RHINE	46.73	44.22	41.34	46.23	4.89	11.12%
ELBE	7.28	11.41	10.50	14.93	4.43	36.06%
ODER	3.29	3.43	5.18	5.70	2.27	47.58%
GUADIANA	3.28	0.93	0.71	0.65	0.28	36.78%
KEMIJOKI	21.66	21.26	14.25	33.44	19.19	83.50%

Table 8. Difference between basin aggregated mean runoff and observed mean runoff. The difference is expressed both as an absolute and as a relative difference.

Mean Runoff	**Difference from observations [Simulation – Observation] [mm/month]**			**Percent difference from observations**		
Basin	**WFDEI**	**PGFv2**	**GSWP3**	**WFDEI**	**PGFv2**	**GSWP3**
AMAZON	4.42	10.55	13.23	5.69%	13.57%	17.02%
CONGO	-21.08	-13.88	-24.17	-42.02%	-27.67%	-48.18%
MISSISSIPPI	0.56	3.40	2.56	5.02%	30.23%	22.79%
LENA	0.21	-0.54	4.14	3.61%	-9.20%	70.23%
NIGER	-4.60	-3.55	-3.83	-59.52%	-45.96%	-49.48%
VOLGA	2.94	7.88	11.53	44.77%	119.99%	175.71%
MURRAY	-0.76	-0.60	-1.21	-37.40%	-29.62%	-59.69%
GANGES	11.17	0.72	9.85	51.61%	3.32%	45.48%
ORANGE	-0.12	-0.01	-0.15	-39.27%	-1.70%	-49.84%
DANUBE	-1.29	-2.30	-3.89	-6.86%	-12.24%	-20.69%
SASKATCHEWAN	-1.40	-0.19	-1.22	-41.98%	-5.70%	-36.78%
RHINE	-2.50	-5.39	-0.50	-5.35%	-11.53%	-1.07%
ELBE	4.13	3.22	7.65	56.76%	44.27%	105.11%
ODER	0.14	1.89	2.40	4.14%	57.50%	73.09%
GUADIANA	-2.35	-2.57	-2.63	-71.61%	-78.40%	-80.17%
KEMIJOKI	-0.40	-7.41	11.79	-1.84%	-34.20%	54.43%

Table 9. Basin aggregated values of 10th percentile runoff (low runoff) for observations and JULES simulations. The range of simulations (difference between higher and lower simulated value) and the range as percent of average value (range divided with the mean of the three simulations).

	Low runoff [mm/month]					
Basin	**OBS**	**WFDEI**	**PGFv2**	**GSWP3**	**Range of simulations**	**Range of simulations as percent of average value**
AMAZON	23.09	12.55	15.71	13.07	3.16	22.94%
CONGO	7.82	2.27	3.18	0.81	2.37	113.72%
MISSISSIPPI	0.68	0.69	1.25	1.10	0.56	55.32%
LENA	0.14	0.00	0.00	0.01	0.01	287.41%
NIGER	0.24	0.03	0.02	0.02	0.01	33.78%
VOLGA	0.18	1.99	3.29	2.46	1.30	50.43%
MURRAY	0.04	0.04	0.01	0.01	0.03	159.08%
GANGES	0.60	0.64	0.23	0.52	0.41	89.58%
ORANGE	0.01	0.01	0.00	0.00	0.00	171.11%
DANUBE	2.69	3.98	3.72	3.12	0.87	24.07%
SASKATCHEWAN	0.10	0.06	0.27	0.20	0.21	116.29%
RHINE	7.50	7.56	9.47	9.22	1.91	21.86%
ELBE	0.21	1.65	2.27	1.76	0.62	32.55%
ODER	0.08	0.40	0.84	0.65	0.44	69.80%
GUADIANA	0.00	0.00	0.00	0.00	0.00	53.07%
KEMIJOKI	0.92	1.13	0.27	2.40	2.13	168.06%

Table 10. Difference between basin aggregated 10th percentile runoff (low runoff) and observed 10th percentile runoff. The difference is expressed both as an absolute and as a relative difference.

Low Runoff	Difference from observations [Simulation – Observation] [mm/month]			Percent difference from observations		
Basin	WFDEI	PGFv2	GSWP3	WFDEI	PGFv2	GSWP3
AMAZON	-10.54	-7.38	-10.02	-45.65%	-31.97%	-43.41%
CONGO	-5.55	-4.64	-7.01	-70.97%	-59.38%	-89.69%
MISSISSIPPI	0.01	0.57	0.42	1.31%	83.88%	62.54%
LENA	-0.14	-0.14	-0.13	-99.77%	-100.00%	-94.80%
NIGER	-0.21	-0.22	-0.21	-88.89%	-92.15%	-90.00%
VOLGA	1.81	3.11	2.28	1021.69%	1755.15%	1286.41%
MURRAY	0.00	-0.03	-0.03	-8.35%	-79.36%	-78.37%
GANGES	0.04	-0.38	-0.08	6.17%	-62.44%	-13.97%
ORANGE	0.00	-0.01	0.00	-23.40%	-91.85%	-64.74%
DANUBE	1.29	1.03	0.43	48.09%	38.21%	15.83%
SASKATCHEWAN	-0.04	0.17	0.10	-37.57%	164.43%	94.25%
RHINE	0.06	1.97	1.72	0.83%	26.33%	22.87%
ELBE	1.44	2.06	1.55	678.28%	968.73%	729.81%
ODER	0.32	0.76	0.57	392.87%	933.54%	697.52%
GUADIANA	0.00	0.00	0.00	-97.86%	-96.48%	-97.86%
KEMIJOKI	0.20	-0.65	1.48	22.14%	-70.59%	159.91%

5.1.2. Discharge based evaluation

Annual cycles of discharge, derived from the 1981-2010 period, for 16 examined basins are shown in Figure 18. The evaluation metrics calculated from monthly discharge are tabulated in Table 11 and a visual comparison of the difference in the achieved evaluation metrics due to the dataset used to force the discharge simulation is presented in Figure 19.

Regarding the model's performance, there are significant variations between the studied basins. The hydrological regime is well captured (NSE>0.5) regardless the forcing dataset used for Amazon, Mississippi, Lena, Ganges and Danube. For other basins the model's performance is highly dependent on the choice of the forcing dataset. For example, NSE for Kemijoki is 0.8 for the WFDEI forcing but negative for the other two datasets. Respectively, the PGFv2 dataset results in an NSE value of 0.4 for the Orange river basin while the other two forcing datasets give negative

NSE values. PBIAS values indicate that discharge is underestimated by the model for most basins, a behavior that has been identified in many LSMs and GHMs (Gudmundsson et al., 2012). However for few basins (Niger and Murray) discharge is highly overestimated (PBIAS>100 %).

Considerable variations in PBIAS are documented for the different forcing datasets. The PBIAS range spans from around 10 % to 110 %, with a mean value of 40 %. Regarding the R^2 metric, good correlations (R^2>0.5) are found for most basins. The value of R^2 for some basins is highly affected by the choice of the forcing dataset. An example is Rhine, for which GSWP3 gives very good correlation ($R^2 = 0.9$) in contrast to PGFv2 which results in a poor correlation ($R^2 < 0.1$).

Comparison of model performance with previous studies

The seasonality cycles derived in the present study resemble those found by Blyth et al. (2011), while evaluating JULES' runoff for seven large scale basins, characteristics of different hydro-climatic regimes. The R^2 values for mean and low runoff, agree with the values calculated by Gudmundsson et al. (2012) on an evaluation of JULES (together with other models) over Europe. Moreover, our results compare well with the results presented in a multi-model evaluation project performed by Hattermann et al. (2016) for a number of basins worldwide, in the context of the Inter-Sectoral Impact Model Intercomparison Project (ISIMIP). Finally, in terms of evaluation metrics, our results indicate a better model performance compared to other published studies that evaluate the hydrological performance of JULES (MacKellar et al., 2013; Zulkafli et al., 2013).

It should be noted however that it is unrealistic for a global LSM to achieve top performance around the world (Hattermann et al., 2017), as, due to its global nature, some fixes in some regions could result in deteriorations in performance in other parts of the land surface.

The shown persistent departure from the mean climatology of discharge could include three types of errors. The first is the error stemming from the insufficient description of the runoff processes by the land surface model and from the routing algorithm (Blyth et al., 2011b). The second type of error is a result of errors in the forcing datasets (either observational or GCM output) with regards to depicting the real climatic drivers (Elsner et al., 2014; Mizukami et al., 2014). A third possible error comes from the comparison of naturalized discharge of the simulations with measured discharge due to influences like abstractions and dams regulating the natural river flow (Müller

Schmied et al., 2014). An extra error component, which is not considered here, could result from the uncertainty in discharge measurements (Coxon et al., 2015).

Discussion of limitations of the modelling approach

Here we discuss the limitations of the modelling approach employed in this study. The spatial resolution used for the model runs follows the resolution of the observational datasets used as input in the model. However, a resolution of 0.5° is quite coarse to capture some of the hydrological processes that occur at the basin level. This especially applies to basins with highly variable elevation and basins of mountainous regions. Moreover, some natural processes with great significance for the hydrological regime of specific mountainous basins, like the glacier melting contribution to runoff in the case of the Indus river basin, cannot be described by JULES.
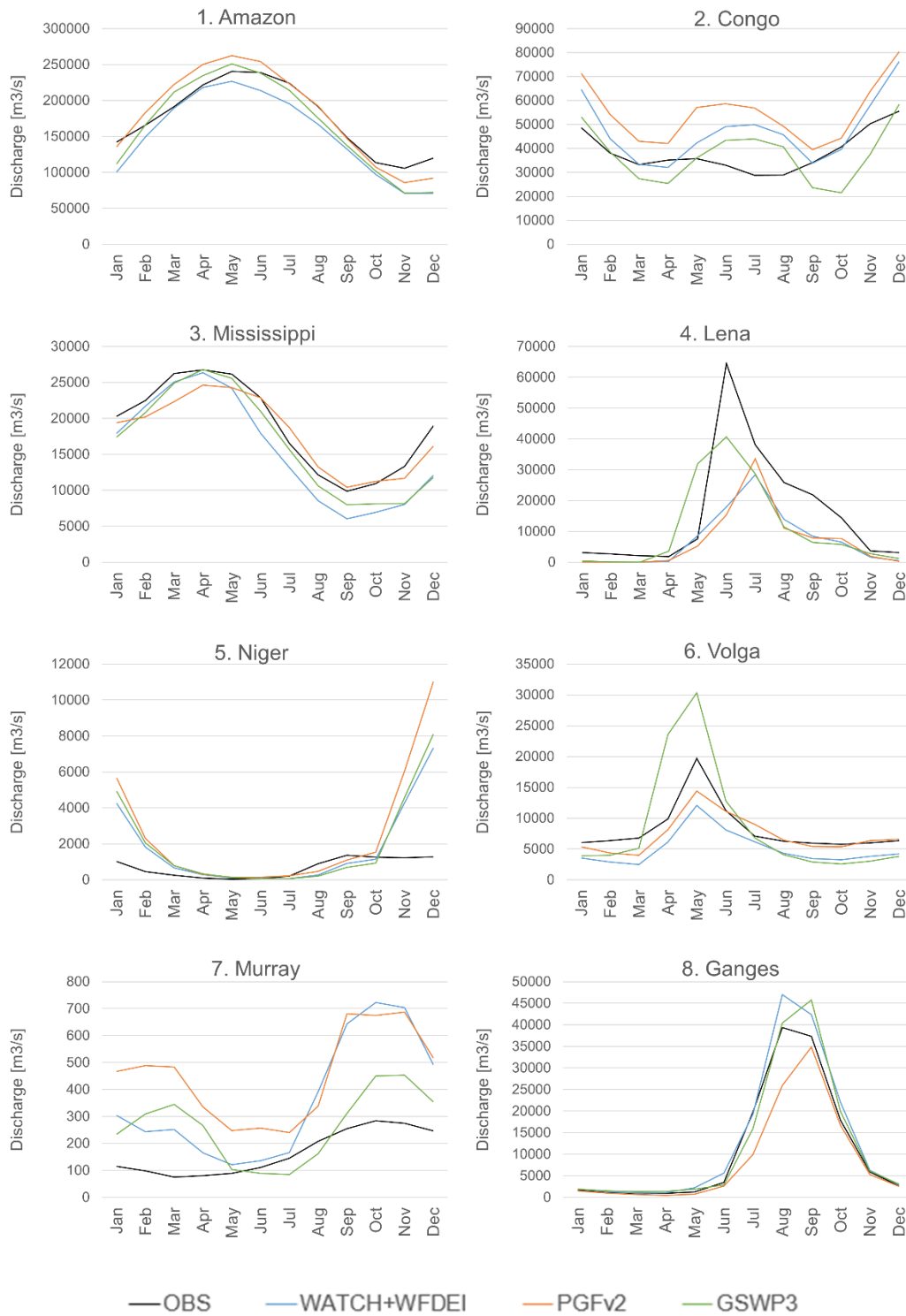
Figure 18. Observed (GRDC) and simulated discharge seasonality for 16 major hydrological study basins.

Figure 18 (continued).

Table 11. Evaluation metrics for monthly discharge, for 16 major hydrological study basins.

	Amazon			Congo			Mississippi			Lena			Niger			Volga			Murray			Ganges		
	NSE	PBIAS	R^2	NSE	PBIAS	R^2	NSE	PBIAS	R^2	NSE	PBIAS	R^2	NSE	PBIAS	R^2	NSE	PBIAS	R^2	NSE	PBIAS	R^2	NSE	PBIAS	R^2
WFDEI	0.6	-15.2	0.9	0.1	4.8	0.7	0.6	-18.3	1.0	0.3	-58.0	0.7	-15.9	137.0	0.3	-0.1	-44.7	0.9	-11.0	130.7	0.9	1.0	15.6	1.0
PGFv2	0.9	0.9	1.0	-3.5	40.6	0.6	0.9	-1.6	0.9	0.3	-58.3	0.6	-38.1	230.2	0.3	0.8	-10.2	0.8	-14.7	169.6	0.5	0.9	-13.2	1.0
GSWP3	0.8	-6.2	1.0	-0.5	-4.8	0.2	0.8	-10.6	0.9	0.6	-32.6	0.6	-27.3	194.4	0.3	-1.1	5.8	0.8	-2.1	57.4	0.4	0.9	12.9	1.0

	Orange			Danube			Saskatchewan			Rhine			Elbe			Oder			Guadiana			Kemijoki		
	NSE	PBIAS	R^2	NSE	PBIAS	R^2	NSE	PBIAS	R^2	NSE	PBIAS	R^2	NSE	PBIAS	R^2	NSE	PBIAS	R^2	NSE	PBIAS	R^2	NSE	PBIAS	R^2
WFDEI	-0.5	-63.8	0.9	0.9	-3.3	0.9	-3.2	-35.1	0.0	-3.1	28.9	0.4	0.8	-3.1	1.0	-3.9	-56.4	0.9	0.1	-59.4	0.6	0.8	-10.1	0.9
PGFv2	0.4	-34.4	0.8	0.8	-7.1	0.9	-2.2	-5.3	0.0	-4.4	23.5	0.0	0.5	-22.1	0.9	-2.6	-48.0	0.8	-0.1	-67.9	0.5	-0.6	-40.6	0.0
GSWP3	-0.8	-68.5	0.9	0.3	-13.8	0.8	-3.2	-34.1	0.1	-5.2	33.9	0.9	-0.7	23.4	0.9	-0.9	-32.4	0.9	-0.2	-71.3	0.4	-4.0	35.2	0.9

Figure 19. Comparison of monthly derived evaluation indices between discharge simulation forced with three different observational datasets, for 16 major hydrological study basins.

5.2. The effect of GCM biases on runoff

Here we investigate the effect of the biases in GCM climate variables on the historical runoff output of the large scale LSM JULES. To this end, we firstly quantify the improvements in the representation of historical modelled runoff when bias corrected variables are used as forcing. Secondly, we examine the individual effect that the bias of each climate variable can have on runoff simulations. This way we can provide an assessment of the variables beyond precipitation and temperature that may be considered as "priority" variables for bias correction, due to their possible pronounced effect on hydrological simulations.

5.2.1. Long-term annual biases in forcing variables at the global scale

Global maps of the initial and remaining biases of the forcing variables are shown in Figure 20. Respective information on the seasonal biases is presented in Figure B 1 and Figure B 2 of Appendix B. In general terms the remaining annual biases are smaller than the initial ones by one to two orders of magnitude. For precipitation (Figure 20a), the largest initial wet biases are observed for regions with high mountain ranges (the Andes in South America, the Alaska Range and the Rocky Mountains in North America and the Himalayas in Asia) and for the tropical African and Indonesian regions. Only a very small percentage (0.75%) of the land surface has small biases (-0.01 to 0.01 mm/day) while the largest biases (>5 mm/day or <-5 mm/day) occupy 31.18 % of the land surface. The remaining biases in precipitation are small (up to 0.01 mm/day in absolute terms, for 80.32 % of the land surface) and located in the tropics. The initial biases in temperature are cold biases for 57.82 % of the land surface while warm biases (mainly found in the Alaskan, Greenland, north and central Asia regions as well as in the Mediterranean and the Andes) occupy 42.12 % of the land surface (Figure 20b). Initial biases greater than 2 K in absolute terms cover approximately one third of the land surface (34.74 %). After bias adjustment, the remaining temperature bias is less than 0.1 K for the vast majority of the land surface (97.27 %).

The initial biases of longwave and shortwave radiation (Figure 20c and Figure 20d respectively) exhibit similar spatial variations but have different signs. Shortwave radiation shows a greater extent of large biases (>50 W/m^2 in absolute terms) compared to longwave radiation (8.16% as opposed to 2.95% of the land surface). Initial biases in specific humidity are greater than 10^{-3} kg/kg (1g/kg), in absolute terms, for one quarter of the land surface (23.65%) (Figure 20e). The largest

biases in surface pressure (>50 or <-50 HPa) occupy 10.01% of the land surface and are found in the areas where high mountain ranges are located (Rocky Mountains, Andes, Himalayas) (Figure 20f). The remaining bias in surface pressure is less than 0.1 HPa (in absolute terms) for most of the land surface (96.50 %). For more than half of the land surface (55.79 %) wind's initial biases are larger than 0.5 m/s or smaller than -0.5 m/s (Figure 20g). The remaining biases of the wind variable range between -0.01 and 0.01 m/s for the majority of the land surface (87.71 %).

Generally, the initial GCM biases in precipitation and temperature are more pronounced over high mountainous regions and the tropics. Recent studies argue towards a dependency between biases and altitude. According to the study of Haslinger et al. (2013), both temperature and precipitation biases of a GCM tested over the Alpine Region, show increasing trends with height. Regarding the tropics, various studies show increased GCM biases in these regions compared to model performance in other climate zones (Koutroulis et al., 2016; Randall et al., 2007; Solman et al., 2013). The initial surface pressure biases are also linked to altitude, as surface pressure heavily depends on elevation. Initial biases in surface pressure have an elevation-similar pattern and could be a result of the different spatial resolution of the elevation model in the GCMs and WFDEI. The WFDEI dataset resolution is 0.5 degrees while the original GCM spatial resolution is considerably lower (around 2.5 degrees). GCM surface pressure is simulated taking into account a relatively low resolution elevation model. Although GCM surface pressure is interpolated to the WFDEI resolution, this does not correct the elevation induced error in the GCM simulations.

The remaining biases in precipitation at the tropical regions were also identified and discussed extensively by Grillakis et al. (2013) and are related to the error in the CDF approximation during bias correction. For the rest of the variables, the remaining bias although not actually zero is very close to zero (well below the smallest positive and above the smallest negative rank in the legend, e.g. below -0.1 K and below 0.1 K for temperature). The color scale in Figure 20 was selected with the intention of showing the remaining biases, but this does not mean that their values are accountable. They are rather trace errors occurring due to truncation numerical errors during the bias correction process. Hence the remaining biases (except for precipitation) could not be attributed to a specific mechanism.
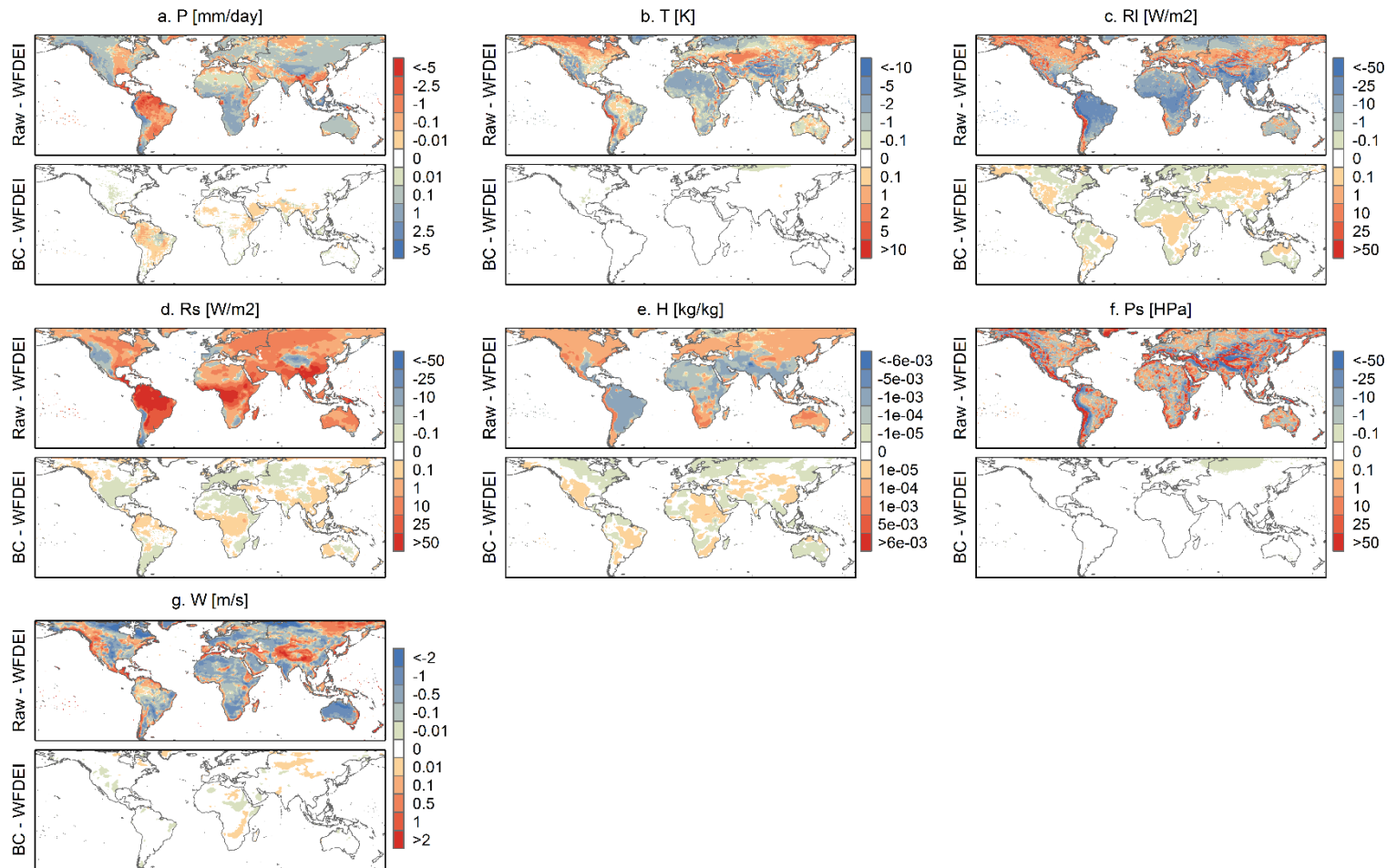
Figure 20. Difference maps, showing initial (Raw-WFDEI) and remaining (BC-WFDEI) biases of the GCM ensemble forcing variables: a. Precipitation, b. Temperature, c. Longwave downward radiation, d. Shortwave downward radiation, e. Specific humidity, h. Surface pressure, g. Wind. Differences are calculated between the long-term annual averages (ANN) of the 1981-2010 period.

5.2.2. Regional and seasonal biases in forcing variables

Figure 21 illustrates the initial biases of the GCM ensemble, spatially aggregated over 24 regions of the globe. To account for possible seasonality variations, the biases are calculated for the annual mean (ANN) and for the December-January-February (DJF) and June-July-August (JJA) means. The remaining biases are not shown because their regionally aggregated values are negligible and would be indistinguishable on the Figure. Additionally, an insight on the behavior of each ensemble member, in comparison to the ensemble mean and WFDEI is given by Table B 1 of Appendix B. Table B 1 provides the values of raw input variables for each ensemble member, the ensemble mean value and the respective WFDEI value, averaged for the 24 study regions.

Precipitation biases are less pronounced in Europe (NEU, MED, NEE) and in central and north Asian regions (CAS, NAS). The wettest precipitation biases are encountered in the equatorial and Southern Africa (EQF, SQF and SAF) and concern DJF precipitation (Figure 21). The driest biases are found for the CAM, AMZ and SAS regions, for JJA precipitation. Temperature displays cold biases in most regions. A notable exception is the warm bias in DJF temperature in the NAS region, which is the most pronounced temperature bias found. Generally the DJF temperature biases are the largest, followed by ANN, while the JJA season has the smallest temperature biases.

The two radiation components, long-wave (Rl) and short-wave (Rs) radiation, show an inverse behavior in their biases (Figure 21). That is to say, in regions where Rl has negative biases Rs exhibits positive biases and vice versa. According to Demory et al. (2014), overestimation of shortwave radiation is a common issue amongst the GCMs. Negative biases are dominant for Rl in contrast to the Rs variable, which mostly shows positive biases. Specific humidity has negative biases over the north part of the African continent (SAH, WAF, EAF, EQF), central and south America (CAM, AMZ, CSA) and south Asia (SAS). Positive humidity biases are identified in the south part of Africa (SQF and SAF) and north America (WNA, CNA and ENA).

Surface pressure shows almost exclusively positive biases (Figure 21). The regions that distinguish for the largest biases are MED, SEA, SAH, SAF, CAM, CSA and SSA. The most dominant negative wind speed bias is found in NAU. Most of the African continent (SAH, WAF, EAF, EQF, SQF) and of South America (AMZ, CSA) also have negative biases in wind. The largest positive

biases are encountered in the southern part of South America (SSA) for the JJA season and for the DJF season in regions of North America (WNA, CAM), Europe (MED) and Asia (CAS, TIB, SEA).
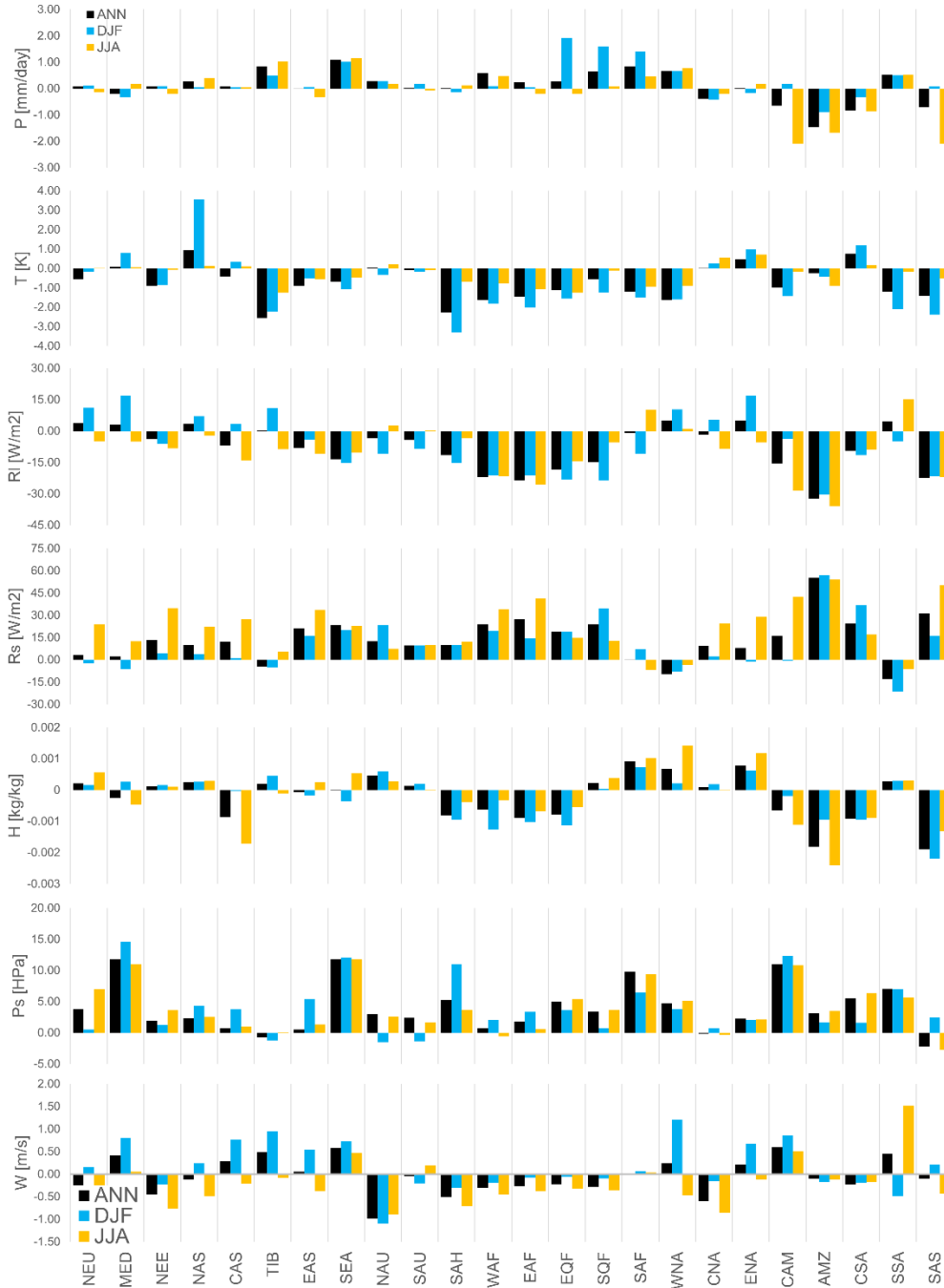
Figure 21. Initial biases (Raw-WFDEI) of the GCM ensemble forcing variables, spatially averaged for 24 Giorgi regions. Biases are calculated between long-term annual averages (ANN), December-January-February (DJF) and June-July-August (JJA) averages of the period 1981-2010.

77

5.2.3. Long-term biases in runoff at the global scale

Figure 22 shows the initial and remaining biases in runoff, derived from ANN, DJF and JJA long term means. As with the biases in the input forcing variables, the remaining bias in runoff is one to two orders of magnitude smaller than the initial bias. Hence, the use of bias corrected data led to an improved representation of runoff by the model, compared to the baseline of the WFDEI run. Accordingly, the studies of Teutschbein & Seibert (2012) and Rojas et al. (2011) found that hydrological simulations are substantially improved with the use of bias corrected forcing.

Regarding the raw GCM run, the largest runoff underestimation biases (<-5 mm/day) are encountered in central-north America, the central-east part of South America and East Asia. The most pronounced runoff overestimation biases are found in the west part of North and South America, in equatorial, south Africa, northern Europe, the Tibetan region and Indonesia. Initial runoff biases are larger than 1 mm/day in absolute terms for 16.26 %, 14.85 % and 20.18 % of the land surface respectively for ANN, DJF and JJA. The differences between the seasonal means (DJF, JJA) and the annual mean (ANN) are in general subtle. Yet, the increases in runoff overestimation biases in DJF in south equatorial Africa and in JJA in the Tibetan plateau are worth noting. Large initial biases (>5 mm/day in absolute terms) in seasonal means occupy a greater percentage of the land surface compared to annual mean (0.70 % for ANN, compared to 1.25 % and 1.97 % for DJF and JJA respectively).

The remaining biases in runoff range from -0.1 to 0.1 mm/day for the majority of the land surface (95.19 %, 87.40 % and 80.30 % for ANN, DJF and JJA respectively). Negligible biases (smaller than 0.01 mm/day in absolute terms) are found for more than one third of the land surface (specifically for 38.06 % of the land area for ANN, 37.60 % for DJF and 34.42% for JJA). The (negative) remaining bias in ANN runoff is more pronounced in the west Amazonian region. This probably corresponds to the remaining bias in precipitation identified for the Amazon region (Figure 20). In addition to the significant reduction of the biases in runoff forced with bias corrected data, it can be observed that the remaining biases have switched signs compared to the initial biases. This means that in regions where the initial bias in runoff is positive (negative), thus the raw GCM forced runoff is larger (smaller) than runoff forced with WFDEI, the use of bias corrected forcing results in runoff slightly lower (higher) than WFDEI runoff. A respective behavior was not

observed in the initial and remaining biases of the most impacting forcing variables (P and T) but it was, to an extent, present for other variables (Rl, Rs and H). Thus, the "overcorrection" manifested for bias corrected runoff compared to WFDEI runoff cannot be attributed to remaining biases in precipitation and temperature. Instead, it could plausibly be associated with the compound effect of the remaining biases in part of (or in all other) forcing variables.
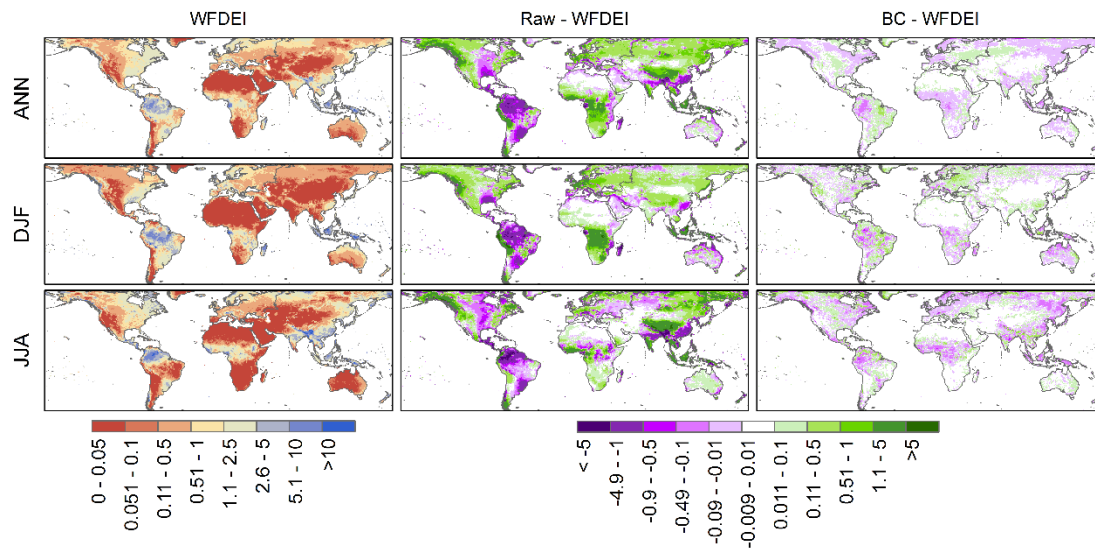
Figure 22. Runoff [mm/day], from WFDEI data (left column). Initial (Raw-WFDEI) and remaining (BC-WFDEI) biases in runoff are shown in middle and right columns respectively. Results are shown for long-term annual averages (ANN), December-January-February (DJF) and June-July-August (JJA) averages of the 1981-2010 period.

5.2.4. Effect of each forcing variable's bias on runoff

The effect that the bias of each forcing variable can have on runoff is investigated here, by comparing runoff from the bias corrected run to the partial correction assessment runs. The results are shown in Figure 23, for ANN, DJF and JJA averages.

First, we discuss the runoff differences calculated from the ANN period. Precipitation and temperature are the only two variables that cause runoff differences larger than 5 mm/day (in absolute terms) when neglected from bias correction. However, these differences regard a very small percentage of the land surface: 0.61 % for precipitation and only 0.02 % for temperature. Moreover, precipitation bias causes changes in runoff greater than 1 mm/day (in absolute terms) for 14.28 % of the land area. Such changes for the other variables occupy a significantly smaller fraction of the land area (ranging from 1.21 % for temperature to 0.05 % for wind). Based on the above it can be stated that precipitation is the variable that mostly affects runoff response. Precipitation bias causes both wet and dry biases in different regions of the land surface, with a pattern that closely resembles the effect of the initial GCMs' biases on runoff (Figure 22). A similar pattern between precipitation and runoff biases was also observed by Teng et al. (2015), who noted that precipitation errors are magnified in modelled runoff. Temperature biases result in runoff overestimation for around 60 % of the land surface (e.g. over west- and east-North America, the Amazon region, equatorial Africa, northern Europe and parts of Asia) and runoff underestimation for around 40 % (example regions: parts of central-south America and of central Asia). Temperature biases correspond with small changes in runoff (up to 0.01 mm/day in absolute terms) over about one third of the land area. Excepting the radiation components from the bias correction procedure produces negative runoff changes for the majority of the land surface (67.60 %), while for around 80 % of the land surface the differences in runoff range between -0.1 and 0.1 mm/day. The bias in the specific humidity variable corresponds to runoff overestimations for 64 % of the land area. The areas of runoff overestimation are mainly located at the higher latitudes (northern part of north America, Europe, north Asia). For 36.43 % of the land surface, changes in runoff due to specific humidity biases span between 0.1 and 0.5 in absolute terms. Surface pressure and wind are the variables that show the smaller effect on the hydrological output, as their exclusion from bias correction corresponds to small changes in runoff (less than 0.1 mm/day in absolute terms) for the vast majority of the land surface (around 94 % and 92 % of the land surface respectively for surface

pressure and wind speed). The most pronounced differences in runoff due to surface pressure biases are negative and are encountered over the high mountain ranges' regions of South America and Asia (Andes and Himalayas respectively).

The patterns of runoff changes due to the biases of the forcing variables derived from annual (ANN) and seasonal (DJF, JJA) averages show only subtle variations. In general the above analysis on the ANN runoff differences applies also to the seasonal values, with small variations on the land fractions that show a specific response to forcing biases.

From this analysis it can be deduced that apart from the main hydrological cycle drivers (precipitation and temperature), radiation and specific humidity can also pose a substantial effect on runoff, especially for specific regions. These findings will be further investigated and discussed in the following sections. Other studies also advocate towards the considerable effect that biases in radiation (Mizukami et al., 2014) and humidity (Masaki et al., 2015) can have on hydrological fluxes.
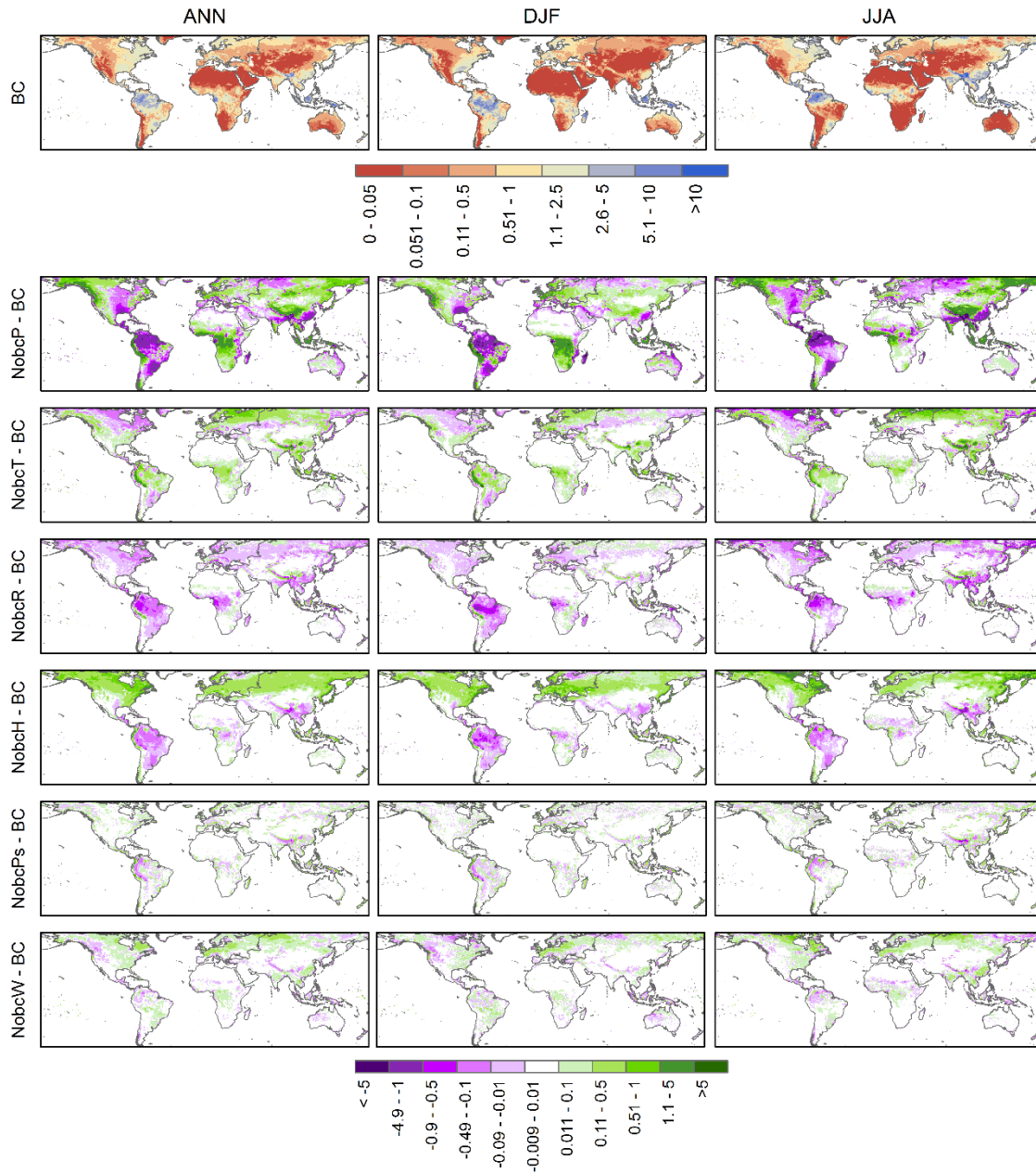
Figure 23. (top row) Runoff [mm/day], from bias corrected GCM ensemble forcing (BC), and (second to last row) runoff differences between the bias corrected run (BC) and the partially corrected runs (NobcV, where V is one of the forcing variables P, T, R, H, Ps, W). Results are shown for long-term annual averages (ANN), December-January-February (DJF) and June-July-August (JJA) averages of the 1981-2010 period.

5.2.5. Runoff sensitivities to forcing variables

Sensitivity of runoff changes to the biases of the forcing variables is examined by exploring the relationship between the input forcing biases (ΔV) and the corresponding changes in runoff (ΔRF). The regional variation of this relationship is also investigated. Figure 24 shows scatterplots of ΔRF versus ΔV for each examined variable, for 10 selected regions. The dots in each scatterplot correspond to the land grid-boxes of each region. The presented regions are selected as representative of different parts of the land surface, as the number of the regions shown in the main text had to be reduced for clarity of the results. Scatterplots of the 24 examined regions can be found in Appendix B (Figure B 3). The median values of ΔV, ΔRF and S of the land grid-boxes of each region, for the 24 examined regions, are shown in Table 12.
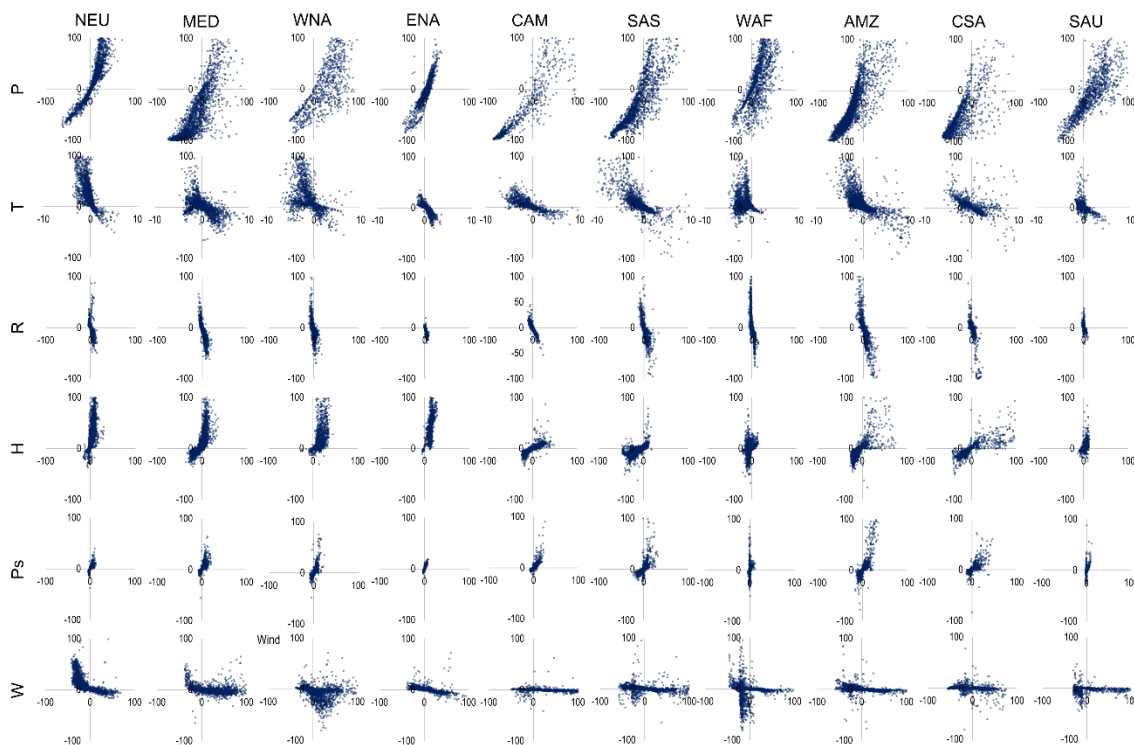
Figure 24. Scatterplots of relative changes in forcing variable (ΔV, x axis) and corresponding relative changes in runoff (ΔRF, y axis), for all the forcing variables and for selected regions. In each panel, each dot represents the $\Delta RF/ \Delta V$ relationship of each land grid-box in the examined region.

83

Table 12. Relative change (%) in forcing variable (ΔV), corresponding relative change (%) in runoff (ΔRF) and sensitivities (S= ΔRF/ ΔV) per region, for each variable. For each region, the median of the ΔV, ΔRF and S values of all land grid -boxes is shown.

	Variables	**P**	**T***	**R**	**H**	**Ps**	**W**
GLOBAL	ΔV	14.46	-0.57	1.73	0.91	-0.02	-5.86
	ΔRF	2.49	3.38	-3.71	2.04	-0.04	0.21
	S	1.76	-0.05	-2.12	0.81	1.18	-0.06
NEU	ΔV	14.6	-0.46	1.86	4.1	-0.05	-9.79
	ΔRF	27.97	22.68	-5.25	25.49	-0.02	3.62
	S	2.10	-0.31	-3.31	5.24	2.90	-0.36
MED	ΔV	-14.39	-0.15	0.55	-1.34	0.41	14.94
	ΔRF	-58.56	1.55	-1.51	4.07	0.44	-0.47
	S	2.02	-0.04	-2.52	0.77	1.08	-0.08
NEE	ΔV	4.89	-1.44	2.44	3.32	0.1	-11.77
	ΔRF	5.75	47.11	-5.39	32.73	0.26	5.98
	S	2.28	-0.32	-2.64	9.58	3.31	-0.50
NAS	ΔV	26.05	0.67	3.53	8.05	-0.06	-1.08
	ΔRF	59.36	11.8	-10.08	63.98	0.02	4.06
	S	2.35	-0.07	-2.95	7.58	2.43	-0.29
CAS	ΔV	6.44	-0.03	1.37	-13.00	-0.41	8.09
	ΔRF	-9.94	1.31	-0.44	-0.19	-0.36	-1.29
	S	2.49	-0.05	-3.50	0.31	0.88	-0.09
TIB	ΔV	128.47	-2.94	-1.14	7.69	-0.12	12.59
	ΔRF	1017.17	5.38	0.97	0.81	0.02	0.06
	S	7.27	-0.02	-2.07	0.18	0.40	0.00
EAS	ΔV	19.25	-0.94	2.51	2.92	-0.2	-3.55
	ΔRF	4.36	5.54	-2.96	3.66	-0.05	0.76
	S	1.70	-0.06	-1.53	0.82	1.07	-0.09
SEA	ΔV	19.76	-0.87	1.11	0.89	0.23	34.57
	ΔRF	43.92	5.97	-3.2	1.66	0.32	-1.04
	S	2.07	-0.08	-2.68	1.16	1.54	-0.05
NAU	ΔV	41.15	-0.04	1.43	7.71	0.1	-28.46
	ΔRF	-5.13	1.02	-1.16	1.38	0.09	-0.44
	S	0.37	-0.03	-0.75	0.31	0.56	0.00
SAU	ΔV	18.92	-0.28	0.85	2	-0.13	-11.2
	ΔRF	-9.29	1.07	-0.11	1.4	0.06	-0.49
	S	0.82	-0.05	-0.88	0.67	1.00	-0.03
SAH	ΔV	54.11	-2.73	-0.47	-8.96	0.22	-13.59
	ΔRF	-2.59	-0.68	0.64	-0.32	0	0.08
	S	0.94	0.00	-0.25	0.04	0.04	-0.01
WAF	ΔV	26.74	-1.51	-0.88	-5.79	-0.1	-15.13

	ΔRF	58.24	5.61	-1.57	-0.71	-0.13	0.09
	S	2.78	-0.04	-2.61	0.22	1.28	-0.04
EAF	ΔV	23.22	-1.68	-0.06	-5.76	-0.25	-12.11
	ΔRF	42.13	7.24	-1.51	-3.74	-0.28	0.09
	S	2.12	-0.05	-1.95	0.48	0.95	0.00
EQF	ΔV	5.64	-1.55	-0.25	-2.15	-0.2	-10.09
	ΔRF	-0.14	6.21	0.92	-1.29	0	0.07
	S	2.26	-0.05	-1.73	0.49	0.92	-0.01
SQF	ΔV	36.45	-0.9	0.9	0.89	-0.03	-15.6
	ΔRF	-73.18	-82.26	-85.07	-84.68	-84.2	-84.18
	S	2.94	-0.07	-1.91	0.59	1.10	-0.04
SAF	ΔV	89.8	-1.41	-0.38	14.28	0.68	-4.74
	ΔRF	85.47	5.5	0.54	5.33	0.42	-0.02
	S	1.35	-0.04	-1.66	0.45	0.72	-0.05
WNA	ΔV	65.92	-1.75	-1.23	13.55	0.14	10.23
	ΔRF	112.66	17.94	-0.48	9.85	0.16	-2.5
	S	2.12	-0.13	-2.01	0.77	0.98	-0.17
CNA	ΔV	-12.84	0.11	1.68	2.29	-0.08	-14.79
	ΔRF	-50.86	1.53	-2.06	6.57	-0.05	1.96
	S	2.54	-0.07	-1.47	1.08	1.09	-0.13
ENA	ΔV	4.08	0.49	2.71	13.4	0.1	5.47
	ΔRF	-0.38	-0.38	-5.18	39.72	0.13	0.86
	S	1.69	-0.07	-1.92	3.17	1.54	-0.11
CAM	ΔV	11.43	-0.98	-0.4	-6.16	0.15	25.27
	ΔRF	-7.73	3.65	-0.1	-2.55	0.14	-0.52
	S	1.32	-0.04	-1.58	0.49	0.77	-0.02
AMZ	ΔV	-26.58	-0.35	4.06	-13.19	-0.19	-4
	ΔRF	-40.52	4.88	-9.34	-6.01	-0.23	0.03
	S	1.42	-0.05	-2.37	0.53	1.44	-0.04
CSA	ΔV	-32.8	0.7	3.05	-11.53	-0.23	-7.5
	ΔRF	-63.21	-1.49	-3.22	-5.75	-0.13	0.38
	S	1.59	-0.04	-1.16	0.53	0.83	-0.04
SSA	ΔV	72.07	-1.22	-1.77	5.07	0.08	9.91
	ΔRF	84.32	10.06	-0.47	12.05	0.34	-2.44
	S	1.53	-0.09	-0.50	1.48	1.29	-0.04
SAS	ΔV	-9.19	-1.08	1.39	-13.11	-0.05	-6.81
	ΔRF	-26.35	5.2	-4.07	-2.53	-0.09	0.51
	S	1.62	-0.05	-2.46	0.29	0.90	-0.05

*ΔV for temperature is the absolute change in temperature.

The correlation between the six ΔVs and respective ΔRFs differs substantially between the examined regions. Generally, the correlations show a non-uniform behavior, identified by the highly scattered data clouds. This implies a high spatial variability of runoff sensitivity to the examined variables.

For precipitation, the ΔRF over ΔP relationship exhibits a nonlinear behavior, indicating that the relative change is runoff is not proportional to precipitation bias, but also depends on the magnitude of precipitation bias. Renner et al. (2012) also identified nonlinearities in the relationship between relative changes in streamflow and changes in precipitation and argued that nonlinear behavior is a result of the combined effects of water and energy balances. Temperature biases have an inversely proportional and highly nonlinear relationship with changes in runoff. The ΔRF over ΔT relationship is also variant for different regions. For example, the scatterplots for NEU and WNA indicate that small temperature biases may correspond with large changes in runoff. In contrast, the scatterplot for CAM indicates that larger temperature biases correspond with smaller changes in runoff compared to the other regions. Radiation biases are small but can correspond with high changes in runoff for some regions (WNA, SAS, WAF, AMZ). For specific humidity it can be observed that small positive biases correspond to high changes in runoff for some region (NEU, MED, WNA and ENA). A different behavior is observed for CAM, SAS, AMZ and CSA where the data cloud is more scattered on the x axis (meaning larger biases in specific humidity) and less scattered on the y axis (i.e. changes in runoff are smaller). Surface pressure has smaller biases compared to the other forcing variables and its effect on runoff also appears reduced. Wind has a wide range of both positive and negative biases which, however, do not seem to affect runoff accordingly.

The variation of the ΔRF over ΔV relationships across the different regions can be attributed to a number of factors. First, it depends on the magnitude and signal of the biases in the forcing variables. As previously shown, these can have significant spatial variations (Figure 20). For example, according to the median values of relative changes in Table 12, some regions are dominated by negative precipitation biases (MED, SAS, AMZ, CSA) and others by positive biases (NEU, WNA, ENA, CAM, WAF, SAU). Second, it reflects the climatology of each region. The same biases would affect differently regions with different runoff (and evapotranspiration) fractions of each region. The precipitation partitioning to runoff and evapotranspiration is a climate

86

characteristic and is controlled by either water or energy limitations depending on the region. Additionally, we should consider that although we assess the effect of long-term annual biases on long-term annual runoff, the results are still depended on the seasonal cycles of the variables and/or runoff, especially if the seasonality of precipitation in the region is strong. For example, the same annual bias in temperature would translate differently to runoff changes in a region with precipitation evenly dispersed throughout the year and in another region where most of annual precipitation happens during the summer months. Finally, as this is a model-based experiment, we should consider whether high sensitivities of some variables for specific regions are a result of over-sensitivity of the model. Vano et al. (2012) documented considerable differences in the spatial distribution of sensitivities to precipitation modelled by five LSMs.

5.2.6. Spatial distribution of bias effect categories

Figure 25 shows global maps of bias effect categories (ECs) for each forcing variable, derived according to the methodology described in Section 3.4.2. The land area fraction corresponding to each EC is tabulated in Table 13.

Precipitation is the variable whose biases have the largest effect on runoff, with the vast majority of the land surface (92 %) corresponding to the high change categories ECI (67.80 %) and ECII (24.20 %). Radiation has the second largest land fraction in ECI but temperature has the second largest land fraction in the high change categories (ECI and ECII). Radiation also has the largest land fraction in the high sensitivity categories (ECI and ECIII). This is possibly a result of combining shortwave and longwave radiation for the calculation of the radiation biases. For specific humidity, the most affected areas (ECI) show a significant spatial coherence and are clustered in the higher latitudes of the globe. Surface pressure biases belong to ECI for around one tenth of the land surface. The highly affected areas mainly correspond to regions with high mountain ranges. For wind, the majority of the land surface corresponds to ECIV. Still, around one quarter of the land surface belongs to the high change categories (ECI and ECII).
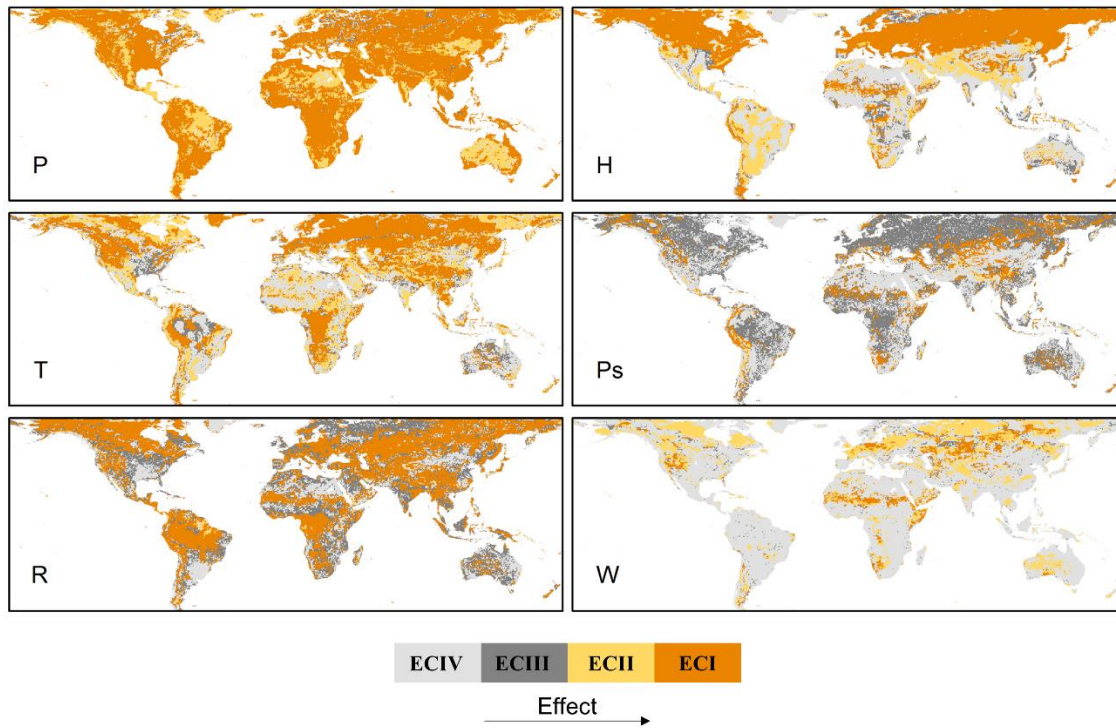
Figure 25. Global maps of bias Effect Categories (ECs) for each forcing variable.

Table 13. Percent of land area (%) under each of the four Effect Categories (ECs).

Variables / ECs	I	II	III	IV
P	67.80	24.20	1.82	6.18
T	45.15	22.03	2.46	30.35
R	48.74	1.30	26.16	23.80
H	40.80	13.76	5.58	39.86
Ps	12.17	1.83	38.48	47.52
W	6.09	19.19	2.35	72.37

5.2.7. Discussion of runoff sensitivities

Here we compare our findings to the respective literature to assess the realism of JULES' sensitivity. We use the median sensitivity value of the grid-boxes of each region (Table 12) as the representative sensitivity S for each region. Moreover, we discuss issues of possible model over-sensitivity in particular regions and the caveats of this study.

Sensitivity of runoff to precipitation

Most studies have examined the sensitivity (also reported as elasticity) of runoff (or discharge) to precipitation. A number of studies have examined sensitivity to precipitation for regions or basins in the United States. Values of runoff sensitivity (S) to precipitation between 1.5 and 2.5 were reported by Sankarasubramanian and Vogel (2003) for the US (WNA, CNA and ENA). Fu et al. (2007) reported values of 1.5 to 1.67 for the Spokane River basin (located in WNA). Vano et al. (2012) found that S to precipitation ranged from 2.2 to 3.3 for different LSMs for the Colorado River basin (also located in WNA). For the Mississippi River basin (mainly located in CNA), Renner et al. (2012) found that S of streamflow to precipitation is 2.38 and 2.55 using two different methods for sensitivity estimation. For another basin located in CNA, Brikowski (2015) reported runoff S to precipitation to be 2.64. For the US region, the S values found in this study compare very well with the literature values. Runoff S to precipitation is 2.12 for WNA, 2.54 for CNA and 1.69 for ENA. Many studies report S to precipitation for regions or basins of China. Reported values of runoff S to precipitation in the Yellow River basin (located in EAS) are 1.4 to 1.69 (Fu et al.,

2007), 1.6 to 3.9 for 89 catchments of the EAS region (Yang and Yang, 2011), 1.71 and 1.74 (estimates of two different methods) for the headwaters of the Yellow River (Renner et al., 2012). Again, the value found in our study is in good agreement with the literature (S to precipitation for EAS is 1.70).

Sensitivity of runoff to temperature and other variables

A number of studies have examined runoff sensitivity to temperature changes. Vano et al. (2012) reported S to temperature values ranging from -2 to -9 C^{-1} between 5 LSMs for the Colorado River basin (WNA) and Brikowski (2015) reported a value of -0.41 C^{-1} for S to temperature in a basin in CNA. Our values for these regions are substantially lower (-0.13 K^{-1} for WNA and -0.07 K^{-1} for CNA). This divergence could be attributed to two factors. First, to an extent it could be connected to possible non-sensitivities of our model to temperature changes for these regions. Second, the differences could arise from the inclusion (or not) of the physical link between temperature and other variables in the analysis. Vano et al. (2012) use different LSMs to calculate sensitivities by perturbing daily temperature maxima and minima. These changes also affect the downward longwave radiation and humidity, which are then used by the evapotranspiration routines of the LSMs. In our case, the change in temperature does not interact with radiation and humidity, as those are read as input variables by the model. When temperature is allowed to interact with humidity, increased temperature will increase the water vapour capacity of the air, and more water will be evaporated. The lack of this physical link in our simulations could, to an extent, explain the decreased sensitivity of runoff to temperature changes compared to Vano et al. (2012). In the analysis of Brikowski (2015), sensitivities of runoff to precipitation and temperature are derived from respective historical data. Thus, sensitivity to temperature will also include the changes caused by the interaction of temperature with other meteorological variables. In a study with a different approach, Yang and Yang (2011) separated the effect of precipitation, temperature, net radiation, relative humidity and wind speed on runoff and calculated sensitivities for each variable. They reported values of S to temperature ranging from -0.11 to -0.02 C^{-1} between 89 catchments of the EAS region. For the same region, we have computed S to temperature as -0.06 K^{-1}, which is included into the literature stated range. Moreover, our S values for radiation, humidity and wind speed are also in good agreement with Yang and Yang (2011). According to Yang and Yang (2011), S to radiation ranges from -1.9 to -0.3, S to humidity from 0.2 to 1.9 and S to wind speed from -0.8

to -0.1. The range refers to values computed for 89 catchments in the EAS region. Our respective values for this region are -1.53 for radiation, 0.82 for humidity and -0.09 for wind speed. This supports the argument that the large deviations of the sensitivity to temperature between our study and the studies of Vano et al. (2012) and Brikowski (2015), result from interactions in the forcing variables included in the referenced studies.

Sensitivity *of runoff to radiation*

The reported S to radiation values are higher in absolute terms than S to precipitation values for many of the examined regions and also globally (Table 12). However, according to the findings presented in section 5.2.4, precipitation and temperature correspond to higher changes in runoff compared to radiation. That is because high S to radiation results from relatively low ΔV values, rather than from relatively high ΔRF values (compared e.g. to precipitation). Small ΔV for radiation is possibly the consequence of combining shortwave and longwave radiation to calculate the total bias in radiation, as the two radiation components have inverse signs for most regions (Figure 21).

Sensitivity of runoff to specific humidity at high-latitude regions

Although S to humidity for EAS compares well with literature, unexpectedly high values of S to humidity are found for other regions (5.24 for NEU, 9.58 for NEE, 7.58 for NAS). We performed an extra analysis to investigate this issue and the basic findings are included in Figure 26 and Appendix B. Figure 26 examines the differences between latitudinal mean of raw and bias corrected specific humidity and the resulting runoff. Very high sensitivity of runoff to H is observed for a specific area, the zone between 70 N and 40 N latitudes. In that zone, a difference of about 10 % in H corresponds to an increase of 40 % to 60 % in runoff. Investigation of the different fluxes related to runoff production in the model revealed two mechanisms that explain this behavior. First, due to higher humidity, the water vapour deficit of the air is reduced and evapotranspiration is decreased, thus allowing more of the precipitated water available as runoff. This mechanism explains around one third of the magnitude of reported changes in runoff (Figure B 4 of Appendix B). The second mechanism happens due to super-saturation of the air, especially during the colder months of the year when the dew point is lower, and includes the condensation and deposition of water vapour (direct transition from vapour to ice). Depositioned water accumulates as snowmass. Snowmass is

higher for the raw H run (H has positive biases), which results in increased snowmelt and thus increased runoff (Figure B 5 of Appendix B).

A comparison of super-saturated air conditions for the different sets of data (WFDEI, Raw, BC and NobcH) can help us identify the origin of the aforementioned behavior. From the input specific humidity H, we estimated the respective relative humidity (this transformation also requires temperature T and surface pressure Ps as input to the Clausius-Clapeyron equation). Then we calculated the fraction of time (based on a daily timestep) that super-saturated conditions occur, for the historical period 1981-2010. The estimation was performed for a) the WFDEI H, T, Ps, b) the raw H, T, Ps, c) the bias corrected H, T, Ps and d) for a combination of data corresponding to the NobcH run (raw H combined with bias corrected T and Ps). The results are presented in Figure B 6 of Appendix B. The analysis reveals that the higher latitude regions -that display high sensitivity of runoff to H-, are under super-saturated conditions for more than 10% of the time (Figure B 6). The length of supersaturated conditions estimated for the WFDEI, Raw or BC data do not exhibit a respective spatial pattern, although super-saturation is found in all three datasets (Figure B 6). Thus, the high runoff sensitivity over the high latitude regions is not a result of supersaturated conditions in the raw GCM H and it rather stems from: 1) raw GCM H being higher than BC H and 2) the calculation of relative humidity within JULES, done by combining raw GCM H with bias corrected T and Ps. This inconsistency strengthens the argument for the need of bias correction of more forcing variables -in addition to P and T. Specific humidity is a variable that is often left uncorrected, a practice that could possibly result to runoff overestimations in the northern latitudes based on our findings, in cases that hydrological models which account for deposition and condensation are used.

Since this experiment was performed with a single LSM, it cannot be concluded whether this behavior is common between the LSMs or is an over-sensitivity of the JULES model. However, it highlights the importance of bias correction for specific humidity for specific regions, where runoff would have been highly overestimated using raw specific humidity as forcing.
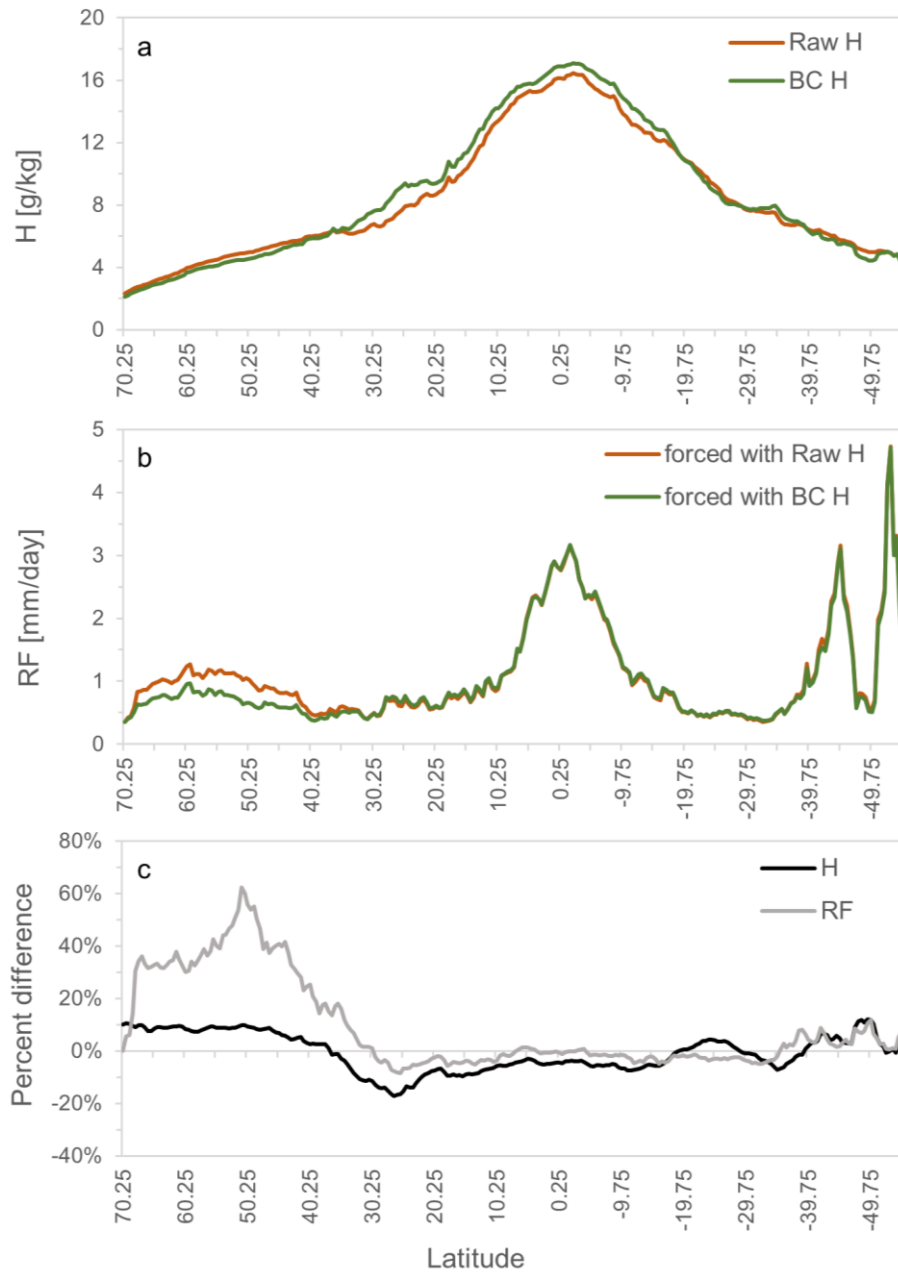
Figure 26. a. Latitudinal means of raw and bias corrected specific humidity [g/kg], b. Latitudinal means of JULES' runoff forced with raw and bias corrected specific humidity [mm/day], c. Percent differences of the latitudinal means in a (H) and b (RF). The latitudinal means are calculated from the 1981-2010 period.

Caveats

An issue that must be considered for the interpretation of the results of this study is that they have been based on a single impact model. As the uncertainty stemming from the selection of the impact model is large (Gudmundsson et al. 2012; Hagemann et al. 2013), it is preferable to use multiple models in order to capture a wide range of possible results. The effect of the meteorological forcing on a hydrological output is heavily model dependent, as different models employ different concepts and/or equations for the representation of key hydrological processes. This concern has been also discussed by other single model studies on meteorological variables' effects on hydrological outputs (Mizukami et al. 2014; Masaki et al. 2015). Nonetheless, the results of single model studies are useful in giving indicative answers on the issues they examine and set a basis for the methodology needed for respective multi-model applications.

5.3. Projections of hydrological impacts under high-end climate change – European scale

Here, transient hydrological simulations for the period 1971 to 2100 performed by forcing the JULES model with five Euro-CORDEX (Coordinated Downscaling Experiment over Europe) climate projections are analyzed. The scope of this part of the results is to assess future water availability and identify drought conditions in the European region under high-end scenarios of climate change. To this end, the following points are studied. Firstly, changes posed on the hydrological cycle (mean state and lower extremes) at +4 °C global warming compared to a baseline situation, and relative to the target of 2 °C warming are identified. Secondly, the effect of bias correction on projected hydrological simulations is analyzed. To achieve this, both raw and bias corrected Euro-CORDEX data were used as input forcing in the impact model. Thirdly, climate change induced changes in drought climatology at the basin scale are examined and finally, the effect of the observational dataset used for bias correction on the projection is assessed.

5.3.1. Hydrological simulation at Pan-European scale with raw Euro-CORDEX forcing data

Figure 27 shows the average runoff production estimated by JULES forced with the five participating EURO-CORDEX dynamically downscaled GCMs, for each model separately and for the ensemble mean. Measures of model agreement (coefficient of variation between the ensemble members and model agreement on a wetter change in the projected time-slice) are also shown in Figure 27. The change in runoff in the +4 SWL projected time-slice with respect to the baseline period is expressed as both absolute and percent relative difference. It is interesting to observe the variations between the models for the historical time-slice, with the low climate sensitivity GFDL and NorESM1 exhibiting generally wetter patterns for northern Europe and Scandinavian Peninsula, and with IPSL describing drier patterns, especially for southern Europe. Concerning the overall agreement of the ensemble members in the baseline period the coefficient of variation is below 0.5 for most of the European region (Figure 27, bottom), indicating a good agreement of the models. In more detail, the coefficient of variation is lower for the Scandinavian region and is reduced towards the lower latitudes.

For the projected time-slice, all models agree in a general pattern of increased runoff production in northern Europe and a small part in central Europe and decreased runoff production in Spain, Greece and parts of Italy. Especially for the negative trends shown in southern Europe it is important that though small in absolute terms they increase in magnitude when expressed as a percentage, meaning that small negative changes can pose severe stress in regions where water availability is already an issue.

Concerning the ensemble mean, smoothing of the projected changes due to averaging has revealed clear patterns of change, which however have to be interpreted considering the full spread of the GCM-forced outcomes and the agreement between them in order to avoid misguided conclusions. Less extreme values are encountered in the ensemble mean of projected changes in runoff, compared to the change projected by each ensemble member individually (Figure 27). Especially for percent change a clear trend of runoff increase is revealed in northern Europe and decrease in southern Europe, with a mixed pattern for central Europe. Four or five out of the five ensemble members agree on the wetter response in the northern regions and the drier response in the southern part of Europe. The smaller cv value (cv<0.1) for the southern regions indicates that the models

agree more on the value of the change compared to the changes in the Scandinavian region (0.11<cv<0.75). For central Europe there are areas of reduced agreement, with two models showing a change different in sign than the other three of the ensemble. For the same areas cv has values greater than 1, marking a large spread between the values of the five ensemble members.

Figure 28 has the same features as Figure 27 but concerns the 10th percentile runoff production instead of the average. The 10th percentile limit is used to describe low flows that are related to the creation of hydrological drought conditions. For 10th percentile runoff, model agreement in the baseline period is notably reduced compared to agreement for average runoff, with the coefficient of variation for most regions exceeding 0.5 while it exceeds the unity for a large part of Europe. For the +4 SWL projected time-slice, according to Figure 28, all models agree in relative decreases in runoff production in western and southern Europe which are specifically pronounced in the western Iberian and Balkan Peninsulas. Another common trend between the models is the significant increase in runoff production in the Scandinavian Peninsula, with MIROC5 and HadGEM2 being the two ensemble member that expand this wetter climate down to central Europe.

Regarding the ensemble mean changes, percent change in 10th percentile runoff (Figure 28) shows more significant reductions (up to 100 %) compared to average runoff (for which changes range between -50 % and 50 %). It is thus deduced that the changes in low flows are more pronounced than the changes in the mean, a conclusion that points towards the overall intensification of the water cycle. The decreasing trend in 10th percentile runoff covers most of the west and south European area (with 80 % to 100 % agreement on the sign of the change) while all models agree in an increase in 10th percentile runoff in the Scandinavian region.
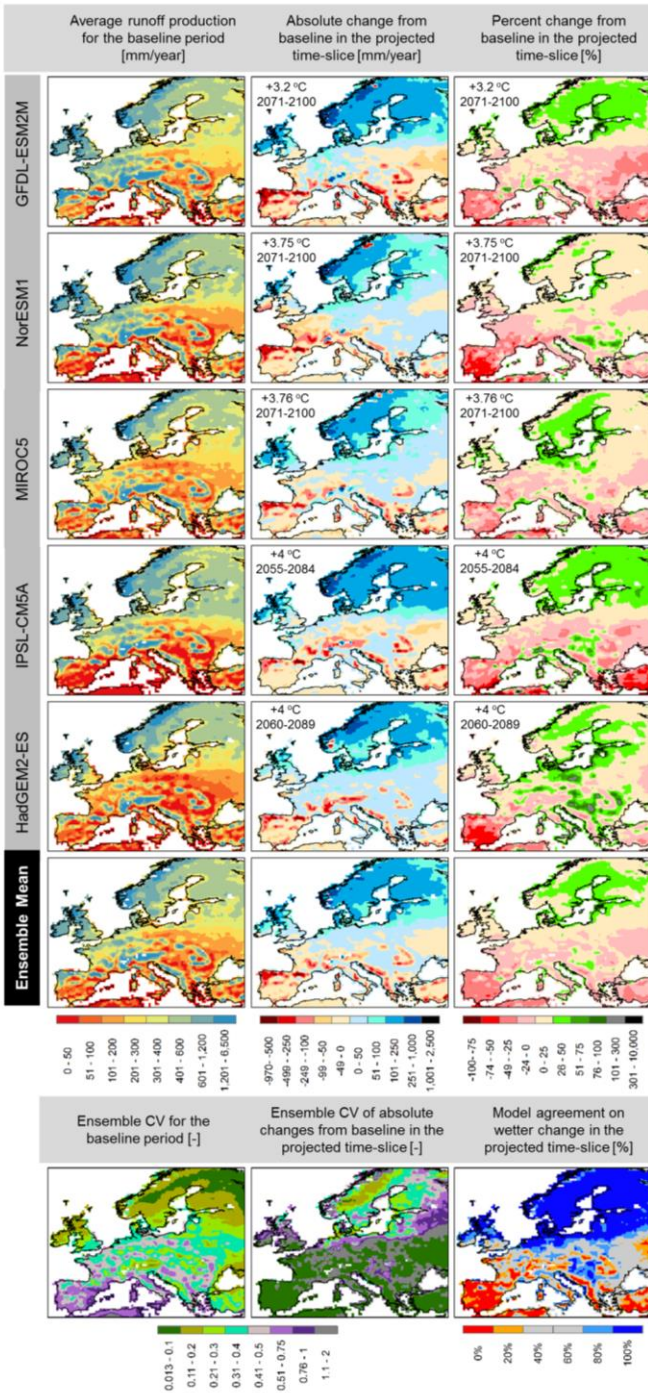
Figure 27. Average runoff production from raw Euro-CORDEX data for all dynamical downscaled GCMs and their ensemble mean. Runoff production averaged over the baseline period (1976-2005) (left column), absolute change in runoff in the +4 SWL projected time-slice (middle column) and percent change in the +4 SWL projected time-slice (right column). Bottom row: coefficient of variation of the ensemble members for the baseline period (left column), coefficient of variation of the projected absolute changes in the +4SWL projected time-slice (middle column) and model agreement towards a wetter change in the +4 SWL projected time-slice.
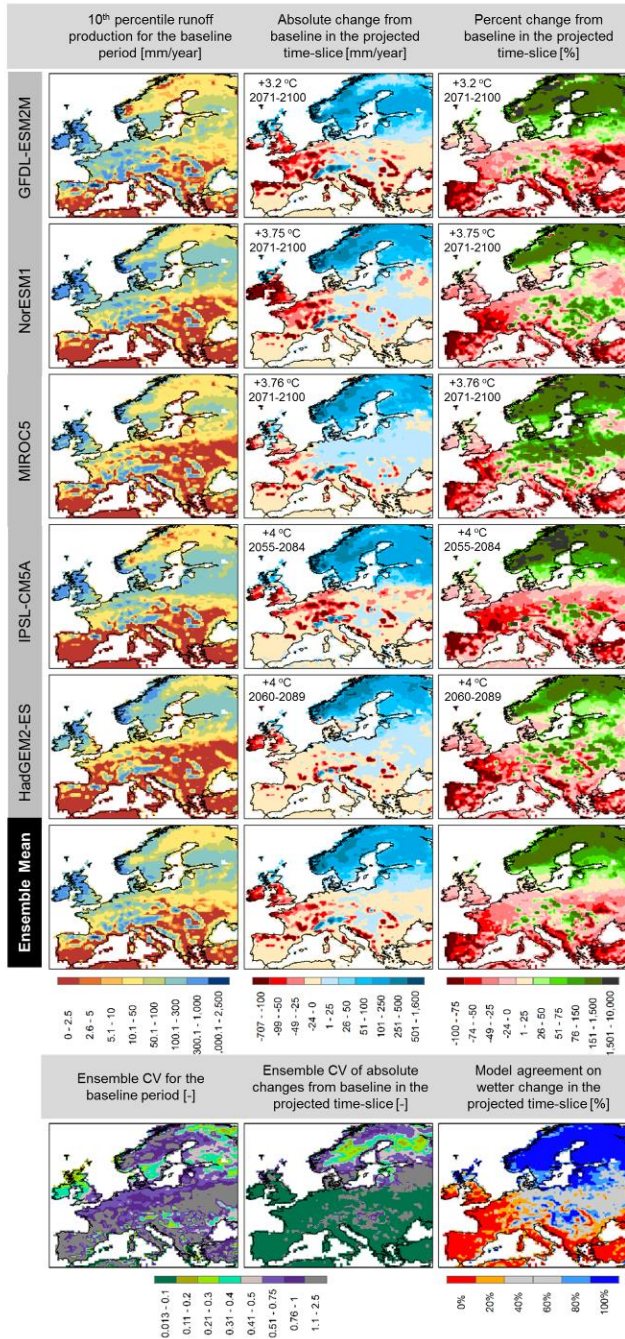
Figure 28. 10th percentile of runoff production from raw Euro-CORDEX data for all dynamical downscaled GCMs and their ensemble mean. 10th percentile runoff production derived on an annual basis and averaged over the baseline period (1976–2005), absolute change in 10th percentile runoff in the +4 SWL projected time-slice (middle column) and percent change in the +4 SWL projected time-slice (right column). Bottom row: coefficient of variation of the ensemble members for the baseline period (left column), coefficient of variation of the projected absolute changes in the +4SWL projected time-slice (middle column) and model agreement towards a wetter change in the +4 SWL projected time-slice.

5.3.2. Hydrological simulation at Pan-European scale with bias adjusted Euro-CORDEX forcing data

The ensemble mean of average runoff derived from the five participating EURO-CORDEX downscaled GCMs, whose temperature and precipitation were bias adjusted according to the WFDEI dataset is presented in Figure 29. Bias adjustment of the forcing data resulted in a drier ensemble mean runoff for the baseline period for 70.40 % of the pan-European land surface, in comparison to 26.01 % of the land area that had a wetter response after bias adjustment. The remaining 3.59 % of the European area had changes that were classified as insignificant (see Figure B 7 of Appendix B for details). Projected changes from bias adjusted data exhibit very similar patterns and magnitudes with the raw data derived changes. For some regions in central Europe, where a small negative change is reported by the raw data run, a sign change of the projected difference is documented after bias correction. Lastly, bias correction has a strong positive effect on model agreement as it can be documented from the low values of the coefficient of determination all over Europe, with the exception of the Scandinavian Peninsula where model disagreement appears increased after bias correction.

In Figure 30, the effect of bias correction on the representation of the 10th percentile runoff is shown. Some hotspots of pronounced negative changes in western Europe have been eliminated and replaced with milder projected absolute changes. There are areas where sign change is observed (central and central-west Europe) however it is difficult to interpret this result and correlate it with bias correction as these are also the areas where models show the lowest agreement (coefficient of variation exceeding one and agreement towards wetter change 40 %-60 %). Although the coefficient of variation for the baseline period is considerably reduced compared to the raw data runs, there are still areas of high model uncertainty in the representation of lower flows.
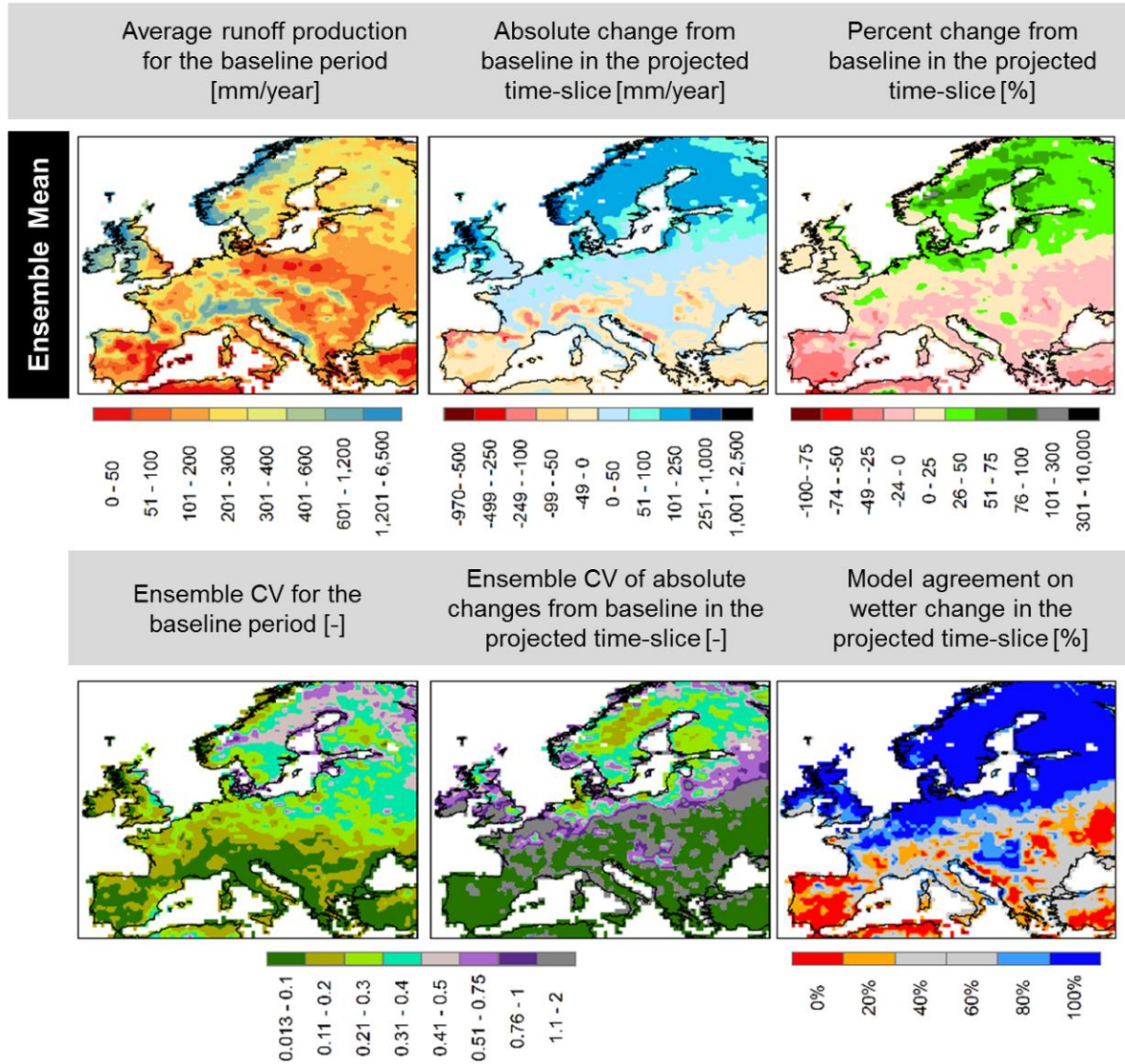
Figure 29. Ensemble mean of average runoff production from Euro-CORDEX data bias adjusted against the WFDEI dataset. Top row: Runoff production averaged over the baseline period (1976-2005) (top row), absolute (middle row) and percent change (bottom row) in ensemble mean runoff in the +4 SWL projected time-slice. Bottom row: coefficient of variation of the ensemble members for the baseline period (left column), coefficient of variation of the projected absolute changes in the +4 SWL projected time-slice (middle column) and model agreement towards a wetter change in the +4 SWL projected time-slice.
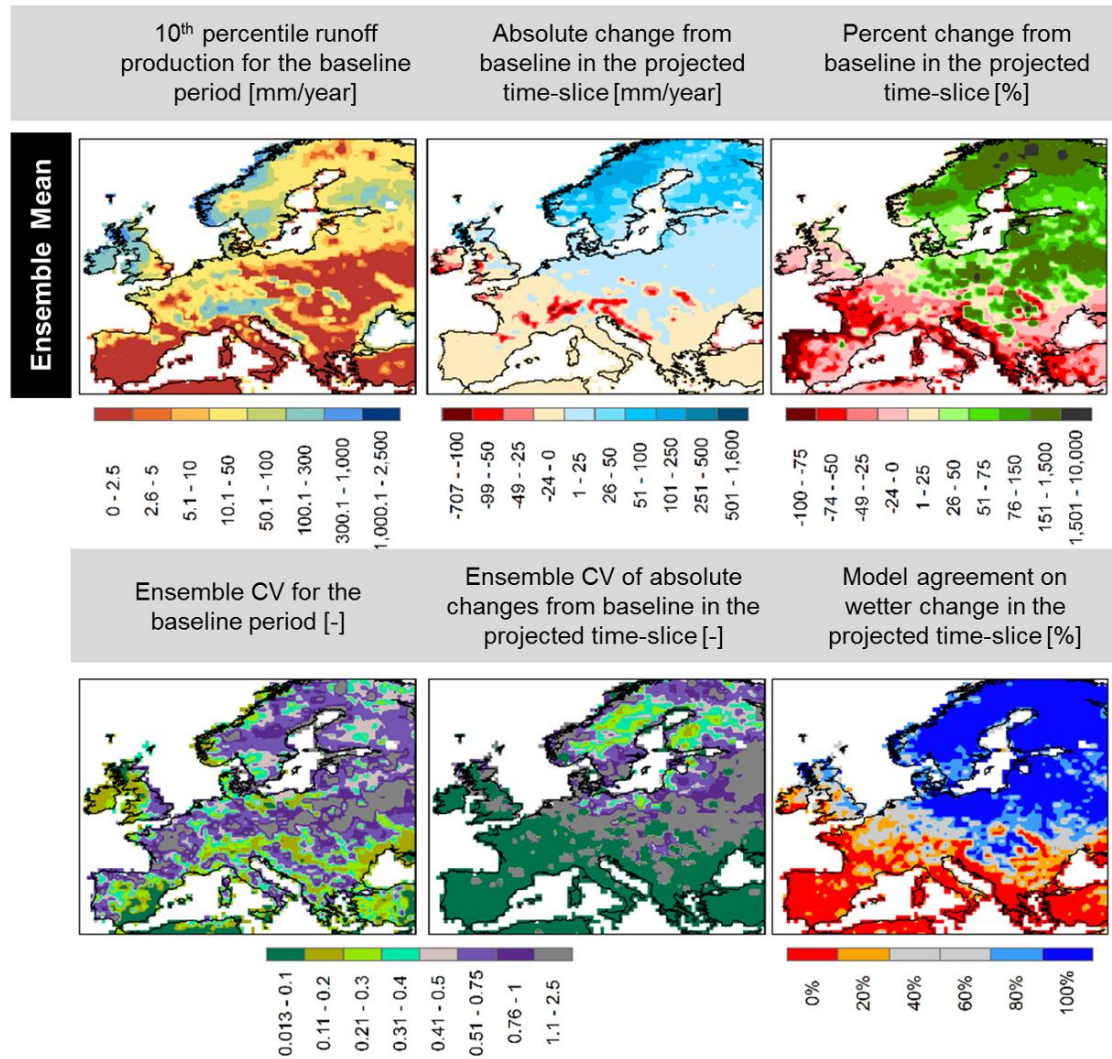
Figure 30. Ensemble mean of 10th percentile runoff production from Euro-CORDEX data bias adjusted against the WFDEI dataset. Top row: 10th percentile runoff production derived on an annual basis averaged over the baseline period (1976-2005) (top row), absolute (middle row) and percent change (bottom row) in ensemble mean runoff in the +4 SWL projected time-slice. Bottom row: coefficient of variation of the ensemble members for the baseline period (left column), coefficient of variation of the projected absolute changes in the +4 SWL projected time-slice (middle column) and model agreement towards a wetter change in the +4 SWL projected time-slice.

5.3.3. Basin averaged runoff regime

In Figure 31, annual time-series of basin averaged runoff production (average and 10th percentile) for five European basins are shown. These cover the whole length of historical and projected years simulated (1971-2100) in an attempt to identify general trends in average and low runoff, calculating 10-year moving averages from the ensemble mean. Results in Figure 31include both raw and bias adjusted output, thus an assessment of the effect of the bias correction on the basin scale hydrology can be made. A common observation for all the basins is that runoff decreases considerably for bias adjusted input forcing.

For Danube and Guadiana, significantly important negative trends are identified for average runoff (-0.24 mm/year and -0.35 mm/year respectively for raw output, -0.11 mm/year and -0.31 mm/year respectively for bias adjusted output) which are more pronounced for the 10th percentile runoff. For Rhine, the identified trends in average runoff production of both raw and bias corrected forcing are not statistically significant. In contrast, the 10th percentile runoff production in Rhine exhibits statistically significant decreasing trends, for both raw (-0.74 mm/year) and bias corrected (-0.50 mm/year) outputs. For Elbe, raw output gives an insignificant trend in average runoff and a slight decreasing trend for 10th percentile runoff. Bias corrected data result in a small but statistically significant increasing trend (0.18 mm/year) in annual average runoff while for 10th percentile runoff the trend is decreasing (-0.06 mm/year, statistically significant). For Kemijoki average and low flows, of raw and bias adjusted forcing, are all exhibiting statistically significant increasing trends.

Basin scale average annual runoff production for raw and bias adjusted Euro-CORDEX data as well as the +4°C absolute and percent change for each ensemble member and ensemble mean is included in Table 14. Similar information but for low flows (10th percentile) are presented in Table 15. In Table B 2 and Table B 3 of Appendix B, the results of the linear regression applied to the average and 10th percentile runoff time-series for the estimation of the trend and its significance can be found.
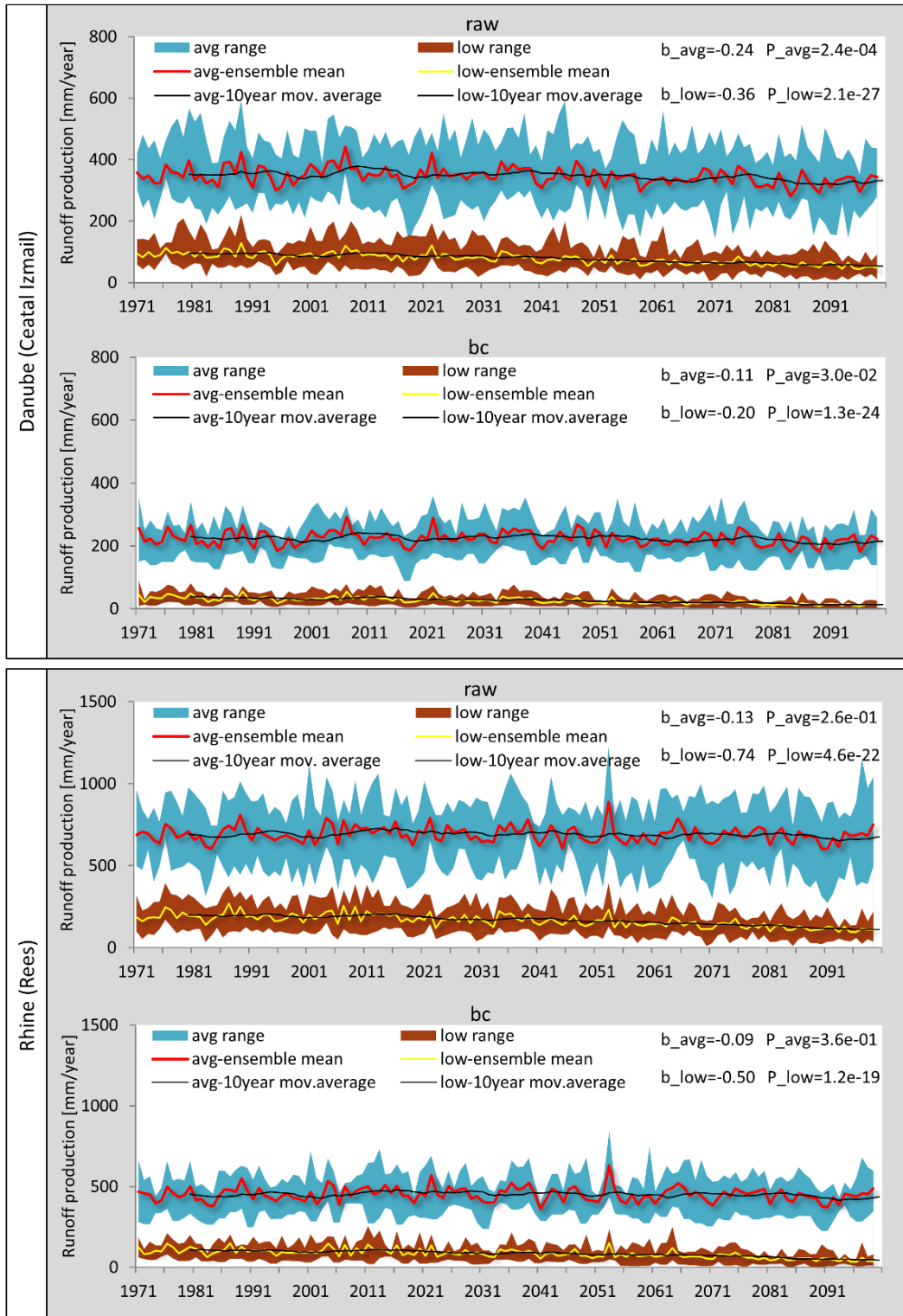
Figure 31. Annual time-series of basin averaged runoff production (average and 10th percentile of annual runoff) for raw and bias adjusted Euro-CORDEX data. For both average and 10th percentile time-series, the ensemble range, mean and 10-year moving average is shown.
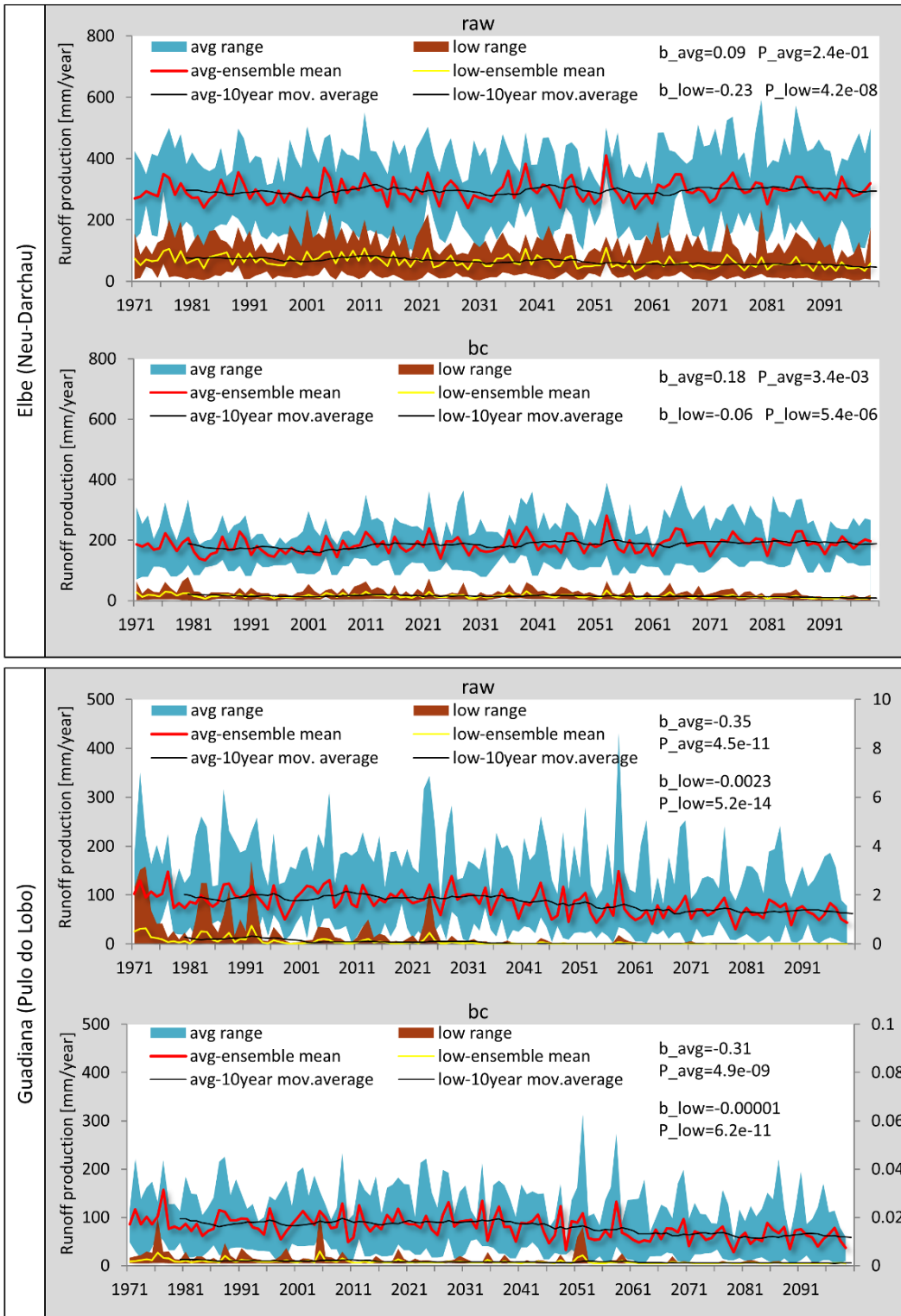
Figure 31 (continued).
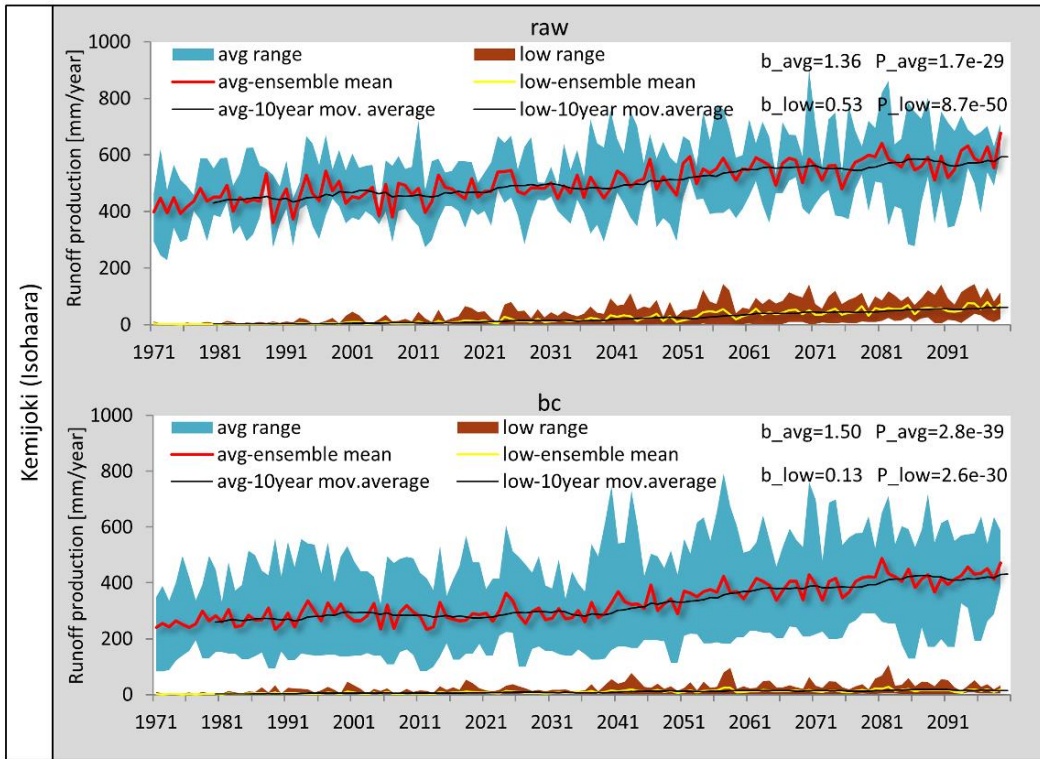
Figure 31 (continued).

Table 14. Basin's annual average runoff production for raw and bias adjusted Euro-CORDEX data.

	Basin's Annual Average Runoff Production [mm/year]											
	Raw						Bias Corrected					
	Historical average 1976-2005						Historical average 1976-2005					
Danube	462.05	362.35	383.78	304.02	266.21	355.68	219.37	249.80	201.95	226.70	229.00	225.36
Rhine	794.21	845.83	616.94	710.16	495.99	692.63	426.67	503.68	415.00	439.11	470.29	450.95
Elbe	371.88	356.72	219.68	337.42	174.41	292.02	148.70	203.39	135.98	174.79	202.12	173.00
Guadiana	166.13	71.44	116.14	46.60	81.51	96.36	93.14	96.42	90.06	79.22	89.82	89.73
Kemijoki	428.17	482.28	427.95	418.03	507.48	452.78	174.68	327.78	197.30	238.28	450.70	277.75
CM-GCM	RCA4-GFDL-ESM2M +3.2 (2071-2100)	RCA4-NorESM1 +3.75 (2071-2100)	RCA4-MIROC5 +3.76 (2071-2100)	RCA4-IPSL-CM5A +4 (2055-2084)	RCA4-HadGEM2-ES +4 (2060-2089)	MEAN	RCA4-GFDL-ESM2M +3.2 (2071-2100)	RCA4-NorESM1 +3.75 (2071-2100)	RCA4-MIROC5 +3.76 (2071-2100)	RCA4-IPSL-CM5A +4 (2055-2084)	RCA4-HadGEM2-ES +4 (2060-2089)	MEAN
	Absolute change from baseline in the projected time-slice						Absolute change from baseline in the projected time-slice					
Danube	-54.57	3.36	-13.20	-42.04	-14.96	-24.28	-11.83	-1.38	3.61	-30.04	-11.48	-10.22
Rhine	59.95	-19.81	-13.23	-39.31	-20.14	-6.51	53.83	-5.91	6.09	-44.17	-21.73	-2.37
Elbe	2.05	33.91	30.00	-28.39	19.05	11.32	22.81	33.28	31.55	-5.57	25.71	21.55
Guadiana	-55.70	-37.02	-17.16	-14.09	-46.16	-34.03	-26.23	-48.81	-10.37	-28.52	-45.23	-31.83
Kemijoki	146.86	67.46	67.48	174.94	108.26	113.00	149.69	97.38	89.71	179.15	119.97	127.18
	Percent change from baseline in the projected time-slice						Percent change from baseline in the projected time-slice					
Danube	-11.81	0.93	-3.44	-13.83	-5.62	-6.83	-5.39	-0.55	1.79	-13.25	-5.01	-4.54
Rhine	7.55	-2.34	-2.14	-5.54	-4.06	-0.94	12.62	-1.17	1.47	-10.06	-4.62	-0.53
Elbe	0.55	9.51	13.66	-8.42	10.92	3.88	15.34	16.36	23.20	-3.19	12.72	12.46
Guadiana	-33.53	-51.82	-14.78	-30.24	-56.63	-35.31	-28.16	-50.63	-11.51	-36.00	-50.35	-35.47
Kemijoki	34.30	13.99	15.77	41.85	21.33	24.96	85.69	29.71	45.47	75.19	26.62	45.79

Table 15. Basin's 10th percentile of runoff production, derived on an annual basis, for raw and bias adjusted Euro-CORDEX data.

	Basin's 10th percentile on annual basis [mm/year]											
	Raw						Bias Corrected					
	Historical average 1976-2005						Historical average 1976-2005					
Danube	146.63	96.81	80.55	79.71	58.69	92.48	31.49	41.73	28.54	30.32	37.94	34.00
Rhine	250.22	258.37	162.58	200.59	109.23	196.20	98.23	120.41	93.24	101.58	107.68	104.23
Elbe	118.79	99.15	29.98	98.30	28.95	75.04	10.22	20.08	11.23	16.75	22.14	16.08
Guadiana	0.74	0.00	0.12	0.00	0.00	0.17	0.00	0.00	0.00	0.00	0.00	0.00
Kemijoki	0.80	4.50	1.10	1.47	10.79	3.73	0.25	5.91	0.53	1.00	11.60	3.86

CM-GCM	RCA4-GFDL-ESM2M +3.2 (2071-2100)	RCA4-NorESM1 +3.75 (2071-2100)	RCA4-MIROC 5 +3.76 (2071-2100)	RCA4-IPSL-CM5A +4 (2055-2084)	RCA4-HadGEM2-ES +4 (2060-2089)	MEAN	RCA4-GFDL-ESM2M +3.2 (2071-2100)	RCA4-NorESM1 +3.75 (2071-2100)	RCA4-MIROC 5 +3.76 (2071-2100)	RCA4-IPSL-CM5A +4 (2055-2084)	RCA4-HadGEM2-ES +4 (2060-2089)	MEAN
	Absolute change from baseline in the projected time-slice						Absolute change from baseline in the projected time-slice					
Danube	-53.89	-23.89	-18.83	-38.22	-27.41	-32.45	-18.03	-15.89	-9.68	-22.28	-24.37	-18.05
Rhine	-89.38	-87.03	-20.39	-103.94	-43.25	-68.80	-31.43	-49.93	-19.49	-69.92	-52.57	-44.67
Elbe	-29.14	-21.01	1.21	-44.80	-9.96	-20.74	-2.03	-2.73	-0.91	-8.90	-8.52	-4.62
Guadiana	-0.73	0.00	-0.11	0.00	0.00	-0.17	0.00	0.00	0.00	0.00	0.00	0.00
Kemijoki	16.77	53.16	36.71	56.80	72.44	47.18	3.24	3.12	5.05	22.55	16.79	10.15
	Percent change from baseline in the projected time-slice						Percent change from baseline in the projected time-slice					
Danube	-36.75	-24.68	-23.38	-47.95	-46.71	-35.09	-57.26	-38.07	-33.90	-73.50	-64.22	-53.08
Rhine	-35.72	-33.68	-12.54	-51.82	-39.59	-35.07	-32.00	-41.46	-20.91	-68.83	-48.82	-42.86
Elbe	-24.53	-21.19	4.04	-45.57	-34.41	-27.64	-19.86	-13.58	-8.11	-53.15	-38.47	-28.71
Guadiana	-98.67	-73.37	-96.24	-26.22	-76.38	-98.01	-48.53	-50.67	-65.42	-32.31	-56.63	-53.36
Kemijoki	2088.40	1181.25	3328.72	3877.01	671.51	1264.16	1283.66	52.88	946.08	2265.11	144.71	263.09

5.3.4. Drought climatology at basin scale

Figure 32 shows the results of the drought threshold level method analysis for the five study basins, for raw and bias corrected output. For each year, the number of days under the historical drought threshold has been counted. This allows a comparison of the tendency towards the formation of drought conditions between the historical period and the projected period. As this is a statistically oriented interpretation of our data, we can see that the differences between raw and bias corrected time-series are very small, especially compared to the difference in the magnitude of their absolute values. For Danube, Rhine and Guadiana strong rising trends (all statistically significant) were identified in the time-series of ensemble mean of days under threshold per year. Before bias correction these were 0.43, 0.37 and 0.52 days/year for the three basins respectively and changed to 0.39, 0.39 and 0.38 days/year respectively after bias correction. For Elbe, non-bias corrected data give a slight but statistically significant increasing trend (0.14 days/year) in contrast to bias corrected output that shows a statistically insignificant trend. For Kemijoki strong decreasing (statistically significant) trends are found for both for raw (-0.20 days/year) and bias corrected (-0.18 days/year) data.
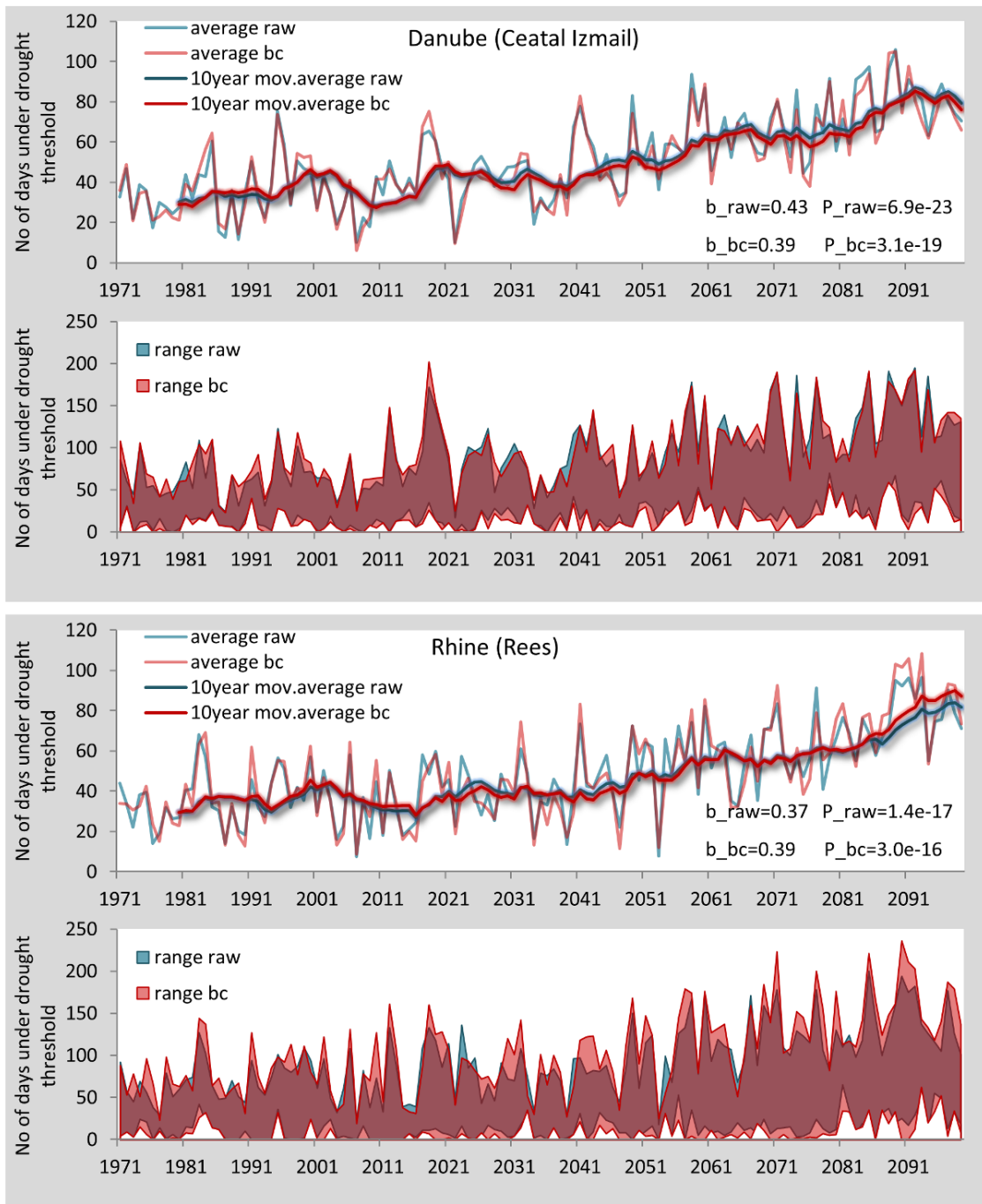
Figure 32. Number of days under drought threshold per year for raw and bias adjusted Euro-CORDEX data. Ensemble mean and 10-year moving average of the ensemble mean (top), ensemble range (bottom).

109
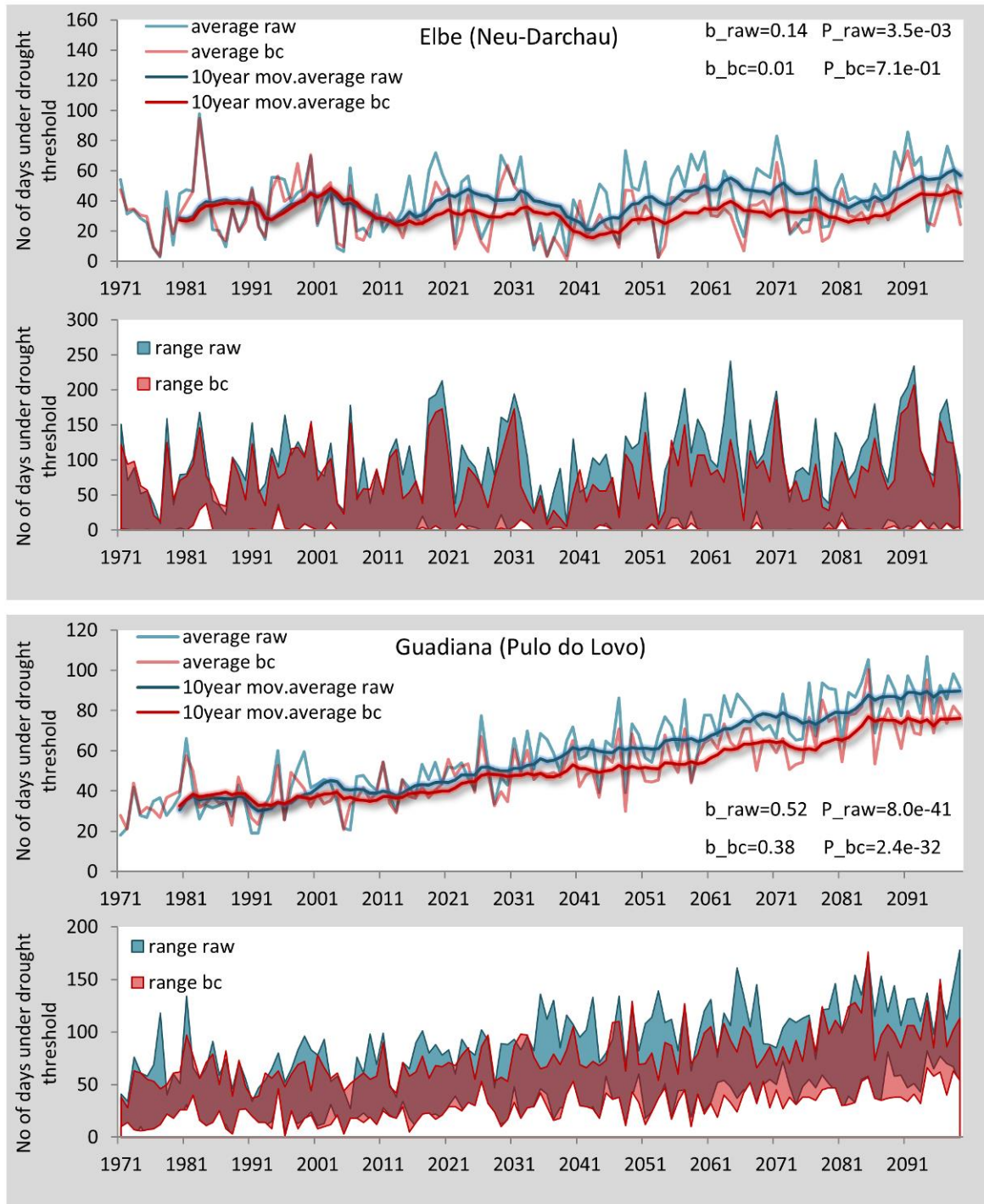
Figure 32 (continued).
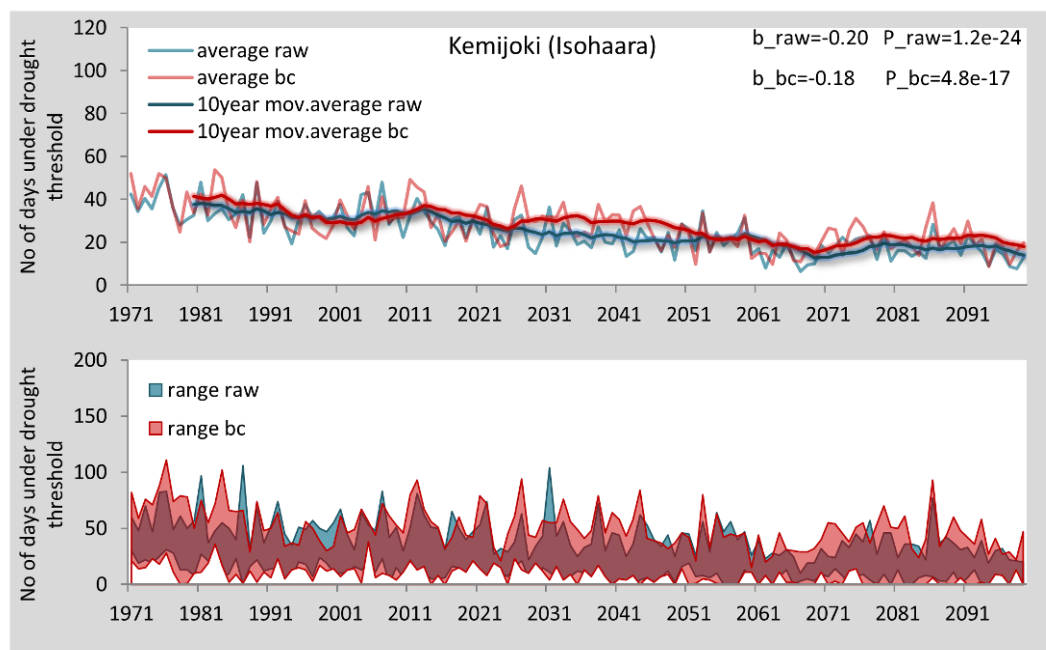
Figure 32 (continued).

5.3.5. Impacts of +4ºC warming relative to +2ºC warming

Figure 33 shows the basin average runoff production for raw and bias corrected Euro-CORDEX data with respect to the corresponding SWL in degrees Celsius. This analysis considers the runoff values corresponding to the +2ºC and +4ºC SWLs, the latter ranging from 3.2 to 4 between the GCMs, and also the SWL achieved by each participating GCM in the baseline period (0.3 - 0.5ºC). It is thus allowing us to examine the changes in basin runoff as temperature increases and to compare the effect of different SWLs.

Comparing the annual average runoff production for raw and bias corrected input forcing it is clear that bias corrected output exhibits a considerably reduced range, which translates in increased model agreement for the basins of Danube, Rhine, Elbe and Guadiana. In Kemijoki basin the bias adjusted output has a greater range than the raw output. Concerning the range of the low flows, an increase in model agreement for the bias corrected forcing is observed for all basins.

111

Examining the changes in annual average runoff, a slight decreasing trend can be identified for Danube and a slight increasing trend for Elbe while for Rhine there is not a clear trend present. In contrast, Guadiana and Kemijoki exhibit strong decreasing and increasing trends respectively. The falling trend in Guadiana is marginally intensified between +2 and +4 SWL compared to 0 to +2 SWL. The rising trend in Kemijoki does not have evident differences between +2°C and +4°C.

According to the results in Figure 33, the 10th percentile runoff in Danube and Rhine decreases as SWLs increase while the opposite trend is observed for the low flows in Kemijoki. For Elbe the raw results show an intense decreasing trend up to +2 SWL which continues more moderately until +4 SWL, in contrast with the bias corrected output that shows milder changes with temperature increase . For Guadiana it is difficult to observe a trend in the bias corrected low percentile runoff as the values are already very low. For the raw output however there is an abrupt decrease from 0 to +2°C which continues with a milder trend up to +4°C.

Figure 34 illustrates the correlation between the percent projected change in annual average and 10th percentile runoff production from bias corrected and raw forcing, for the +2 and +4 SWLs.

Concerning the effect of bias adjustment it can be observed that regardless the significant differences in magnitude between runoff from raw and bias corrected data discussed before, the projected change in average flow by the two forcings almost coincide for the +2 SWL. For the +4 SWL the GCM range has increased for Kemijoki after bias adjustment while for the rest of the basins raw and bias corrected data result in very similar levels of same percent change. For the projected change in 10th percentile runoff, the larger spreading of the values in Figure 34 (right column) shows that the GCM uncertainty on this field is higher. Guadiana is the only basin where bias corrected data result in an improvement in GCM agreement, probably due to its very low values of 10th percentile runoff. Kemijoki is not included in the 10th percentile scatterplots as its projected increase far exceeds the 100 % limit selected. For the rest of the basins, the effect of the bias correction on the change of the 10th percentile runoff is not constant. For Guadiana and Elbe bias adjustment mostly increases percent change while for Rhine and Danube percent change is in general terms decreased after bias correction.

Comparing the difference on percent projected change in average annual runoff from +2 to +4 SWL it can be observed that temperature increase results in a slight decline in percent change for basins

with small absolute values of change, causing sign changes for Danube and Rhine, and it intensifies the negative and positive changes of Guadiana and Kemijoki respectively. For the 10th percentile runoff there is a similar response to temperature increase. For Elbe there is positive percent change at +2 SWL which falls below zero at +4 SWL while for Danube, Rhine and Guadiana the already declining projected changes present are further intensified.
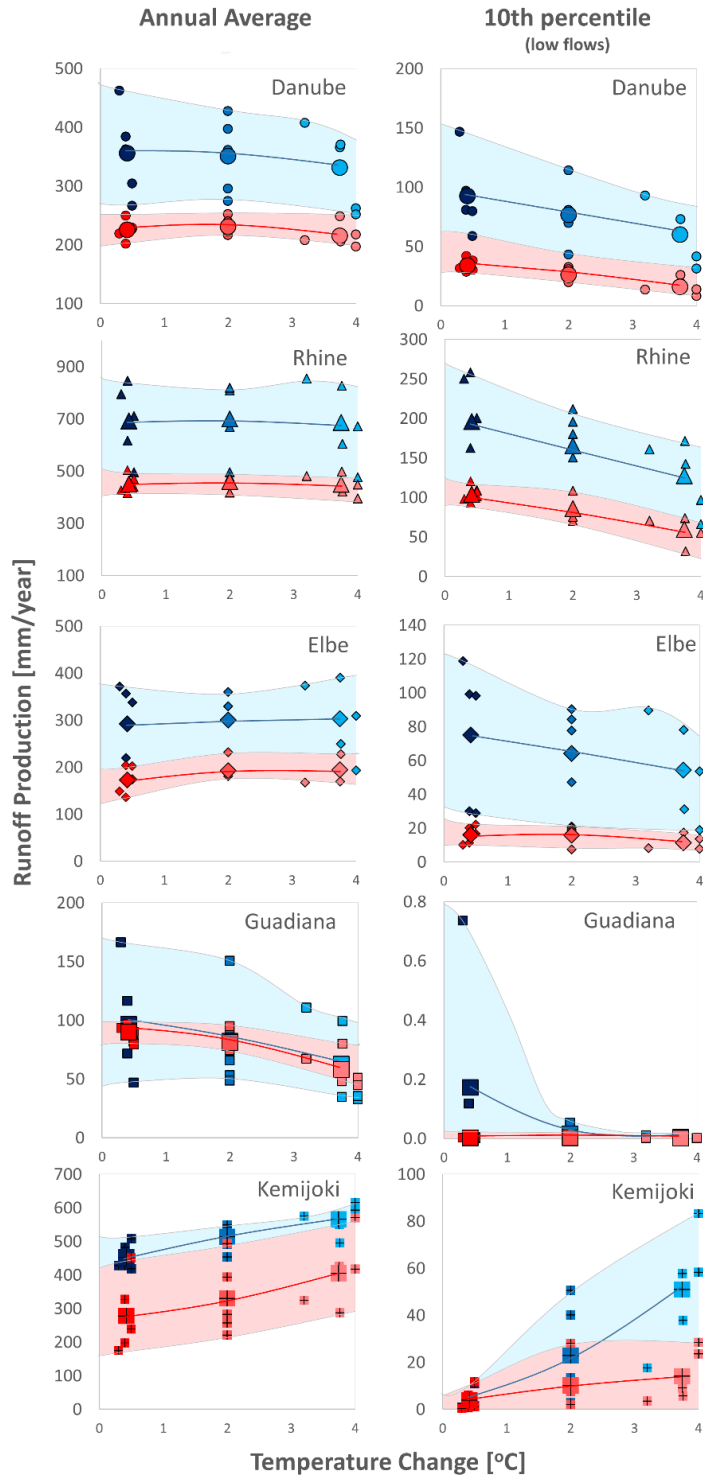
Figure 33. Variation of runoff production with respect to temperature change (+2 and +4 SWLs) for raw (light blue) and bias adjusted (light red) Euro-CORDEX data, for both annual average (left column) and 10th percentile (right column) runoff production. Small markers represent the value of each individual model and bigger markers correspond to ensemble mean value.

114
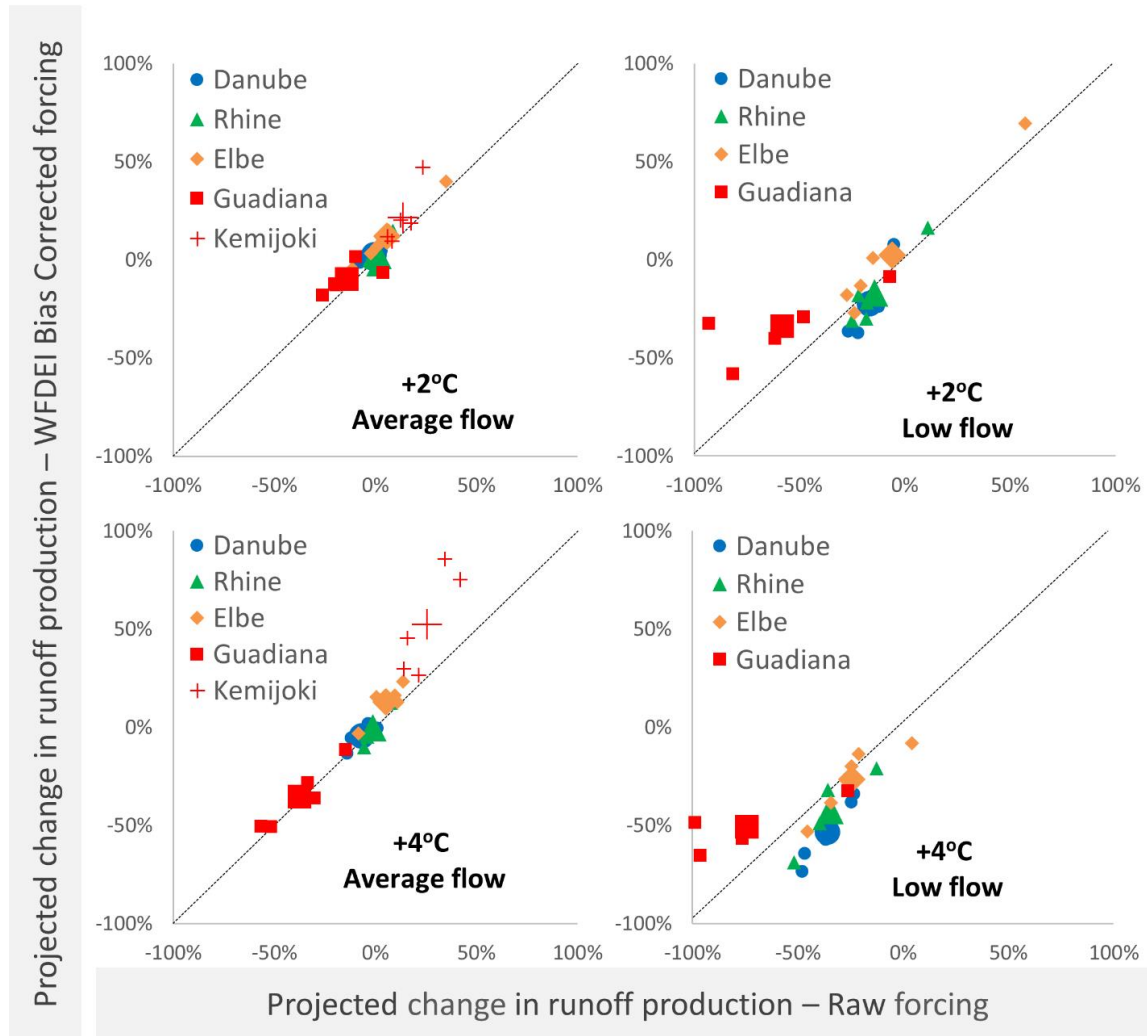
Figure 34. Correlation between projected change in basin averaged runoff production derived from WFDEI-bias adjusted and raw Euro-CORDEX data, for both annual average (left) and 10th percentile (right) runoff production. Correlation is examined at +2°C SWL (top) and at +4°C SWL (bottom). Small markers represent the value of each individual model and bigger markers correspond to ensemble mean value.

5.3.6. Effect of observational datasets for bias correction on the output of the hydrological model

The aspect of the impact posed by the observational dataset used for bias correction to the results of the hydrological simulations is introduced in this part of our analysis. Additional model runs performed with bias adjusted Euro-CORDEX precipitation and temperature, corrected against the E-OBS (instead of the WFDEI) dataset participate in a comprehensive comparison between all the outputs used in this study. The results are illustrated in Figure 35. Three different sets of outputs are compared: one driven by raw downscaled and two driven by Euro-CORDEX data bias corrected against two different datasets. The comparison considers both the mean and range of the ensembles and results are presented as basin aggregates. The first part of the comparison concerns the long-term annual average for the period 1976 to 2005 (Figure 35, top row) and apart from the model results includes values corresponding to observations, derived from GRDC discharge measurements. Observations can serve as a baseline for this comparison, allowing us to evaluate which configuration can better simulate "true" water budget numbers and the effect of bias correction with respect to this baseline.

For all basins the raw data result in overestimates of runoff production which is though significantly reduced after bias correction. E-OBS corrected data however produce values lower than the observations (with the exception of Guadiana) while the WFDEI-corrected data produce the best simulation in terms of approximating the observed values. From Figure B 8 and Figure B 9 of Appendix B (showing the effect of bias correction on the forcing variables of precipitation and temperature) it can be deduced that that E-OBS corrected precipitation has lower values than precipitation adjusted against the WFDEI dataset. This explains the lower runoff produced by the E-OBS bias adjusted dataset, as it is reasonable for the differences in precipitation to reflect on the output of the hydrological model. As already has been revealed in previous stages of this analysis, it is again clear the positive impact that bias adjustment has on the increase of model agreement. The only exception is Kemijoki basin due to its high latitude position (coefficient of variation was increased after bias correction for the high latitude areas).

Changes in annual average runoff production at the +4 SWL appear to be more intensified compared to the +2 SWL (Figure 35, middle and bottom). Although for percent change the

differences of the distinctive configurations are less pronounced, variations can be observed between the two bias corrected data driven simulations. It is also interesting that the effect of bias correction on reducing the uncertainty is not that strong when looking the results from the more statistical perspective of percent projected change. The improvements in model agreement after bias adjustment however are still pronounced for all basins except for Rhine.

From the application of the same analysis on 10th percentile runoff production (Figure B 10 of Appendix B), it is deduced that for the low flows the E-OBS corrected data again produce lower values of runoff compared to WFDEI. In this case, however, even the raw forced output (which is wetter than the bias corrected) underestimates the observed 10th percentile runoff values. Regarding the percent projected changes, results from bias corrected data produce smaller values compared to the raw data while E-OBS adjusted data result in decreased changes compared to output from WFDEI adjusted forcing.
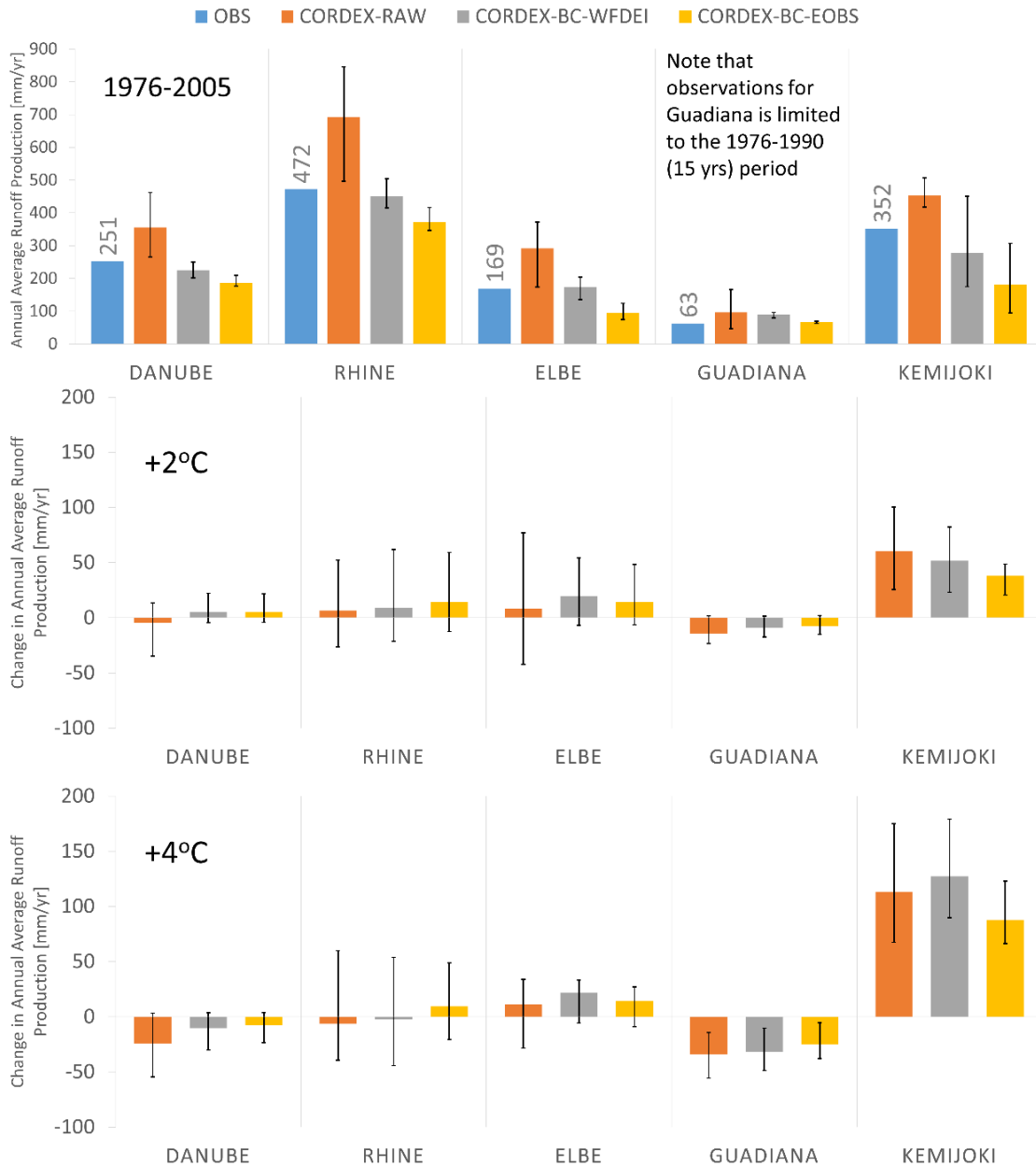
Figure 35. Comparison between the simulations of raw Euro-CORDEX data and bias adjusted against two different datasets (WFDEI and E-OBS) for five study basins. Bars show the ensemble means and error bars the minimum and maximum ensemble member values. (Top row) Annual average runoff production for the period 1976 to 2005.OBS values are derived from GRDC discharge measurements converted to basin averages at the annual time-scale. (Middle row) Percent change in annual average runoff production at the +2 SWL and (bottom row) at the +4 SWL.

5.3.7. Hydrological response to +4°C global warming

In our analysis we investigated the effects of climate change on the European hydrological resources, extracting time periods that correspond to an increase of 4°C of the global temperature, rather than using pre-defined time-slices. The same approach was followed by Vautard et al. (2013), stating that reduced GCM induced uncertainty is achieved with this method and thus the regional patterns of change in the variables of study are strengthened.

In our study only one impact model (JULES) was used. Hagemann et al. (2013) argue that impact model induced uncertainty in future hydrological simulations is larger than that of the GCMS for some regions of the land surface and suggest using multi-impact model ensembles to deal with this issue. However useful conclusions can be drawn also from studies employing a single GHM/LSM. Examples of such single model climate change impact assessments performed recently are the studies of Schneider et al. (2013) and Laizé et al. (2013) with the WaterGAP GHM, the studies of Arnell and Gosling (2013), Gosling and Arnell (2013) and Arnell et al. (2013) with the GHM MacPDM and of Hanasaki et al. (2010) using the H08 LSM.

The findings of the study regarding the climate changed induced alterations of the mean hydrological state in Europe show decreasing trends for southern Europe, including the Mediterranean region, and strong increasing trends for northern and north-eastern Europe. These follow the same patterns as identified by previous studies. Schneider et al. (2013) found that the most pronounced changes in the magnitude of European river flows are projected for the Mediterranean region and the northern part of the continent. Hagemann et al. (2013) reported positive changes in projected runoff for the high latitudes and negative changes for southern Europe. For central Europe the projected changes are smaller (mostly in the range of -25 % to 25 %) and thus more easily obscured by GCM and bias correction uncertainty. Arnell & Lloyd-Hughes (2014) report that the main source of uncertainty in the projected climate impact stems from the GCMs, with a range of uncertainty for the CMIP5 ensemble that is similar to that of older climate model experiments.

The projected relative changes found for 10th percentile runoff are far more pronounced than the changes in average, even for the regions where changes in average-state annual runoff were negligible. This finding implies that seasonality in runoff is likely to intensify under climate change

and is in accordance with the results of Fung et al. (2011) and Van Vliet et al. (2013) who also reported pronounced seasonality in their projected simulations. This may translate to increased dry spells and thus elevated drought risks in the future. Under the light of these findings (mean-state runoff changing slightly and low-state changing significantly), more extreme hydrological droughts are expected in the future. It should be noted however that projections of low flow bear higher uncertainty compared to average-state, as indicated by the higher values of the coefficient of variation. Similar results of increased model spread expressed as cv for low flows compared to average state flows were found by Koirala et al., (2014).

Specifically for the Guadiana River, the close to zero values of 10th percentile runoff encountered even in the historical period indicate that the river exhibits intermittent flow regime. This is relevant for this particular river, as it is located in a semi-arid region and intermittent flows typically characterize its hydrological regime (Collares-Pereira et al., 2000; Filipe et al., 2002; Pires et al., 1999). Given the changes that are projected for the Iberian Peninsula at +4 SWL, it is expected that the intermittent flow regime in Guadiana might intensify.

Concerning the effects of a $+4^oC$ temperature increase on the European hydrological regime compared to a $+2\ ^oC$ increase, significant alterations posed by the +2 degrees of global warming are identified for south Europe and northern and north-eastern Europe, where the respective decreasing and rising trends are intensified. Fung et al. (2011) also found that changes in mean annual runoff identified at +2 are intensified at +4. More specifically, their study reports that regions where decreasing runoff trends have been found become even drier and, in contrast, areas where runoff is projected to increase are getting wetter. For most of the river basins examined by Fung et al. (2011), water stress is increased at +4 compared to +2, with the exception of a few basins where an increase in rainfall is projected thus decreasing water stress. In our study, the basins located at central Europe (Danube, Rhine and Elbe) do not exhibit significant changes in their annual average runoff values due to temperature increase from +2 to +4. For 10th percentile runoff, however, a temperature increase of $+4^oC$ from the pre-industrial baseline results in an aggravation of the lowering trends that are already significantly affecting the low runoff regime at $+2^oC$.

Our analysis of drought climatology at the basin scale was based on the total number of days under a predefined daily varying drought threshold. We did not employ any buffering criterion for the

days under threshold to be accounted for in the total sum (as discussed for example by Sung and Chung (2014) and Tallaksen et al. (1997)). The use of such a criterion would have decreased the calculated dry days. However, as the interpretation of the results of this study is mostly oriented in identifying trends of change rather than absolute numbers describing the future regime, the lack of a buffering criterion is not supposed to notably affect the extracted conclusions. Wanders et al. (2015) employed a transient variable threshold for the assessment of the drought conditions under climate change, considering a gradual adaptation of the ecosystem on the altered hydrological regime. This is an interesting alternative, especially for climate change mitigation and adaptation studies. In our study we aimed to identify global warming induced changes in the future hydrological state without considering adaptation, thus the same historically derived threshold was applied to the whole length of the simulated runoff time-series.

From the analysis performed on drought climatology, increased number of days per year under the historically defined drought threshold are found for the basins of Danube, Rhine and Guadiana. Our results correspond with the findings of previous studies about drought regime under climate change. Giuntoli et al. (2015), investigating future high and low flow regimes at the global scale, using multiple impact models and climate scenarios, found increased number of low flow days in Southern Europe. In the study of Wanders & Van Lanen (2015) the impact of climate change on the hydrological drought regime of different climate regions was assessed, using a conceptual hydrological model forced with 3 GCMs. The study findings describe a decrease in the frequency of drought events in the future, which however does not point towards drought alleviation. In contrast, it relates to increased drought event duration and deficit volume. These effects are more pronounced for the arid climates that already face problems of water availability.

5.3.8. The effect of bias correction

As proposed by Ehret et al. (2012), both raw and bias corrected data driven simulations are presented in our study, in order to comprehensively assess the effect of bias correction on our results. In four of the five study basins, raw data driven simulated runoff overestimates the corresponding observed values. After bias correction, the modelled results represent more accurately the past hydrological regime. Similar improvements in the bias corrected output have been reported by Hagemann et al. (2011), Muerth et al. (2013) and Harding et al. (2014).

For some regions, the sign of the projected change in runoff shifted after bias correction. This finding was also encountered in the study of Hagemann et al. (2011). Hagemann et al. (2011) underline that these changes in the climate signal reveal another uncertainty aspect of the GCM to GHM modelling procedure, that is inherent to the GCM but becomes apparent after the bias adjustment of the climate model output. Teng et al. (2015) argue that signal changes are produced by bias correction errors in higher percentiles' precipitation, thus adding another factor to the uncertainty of the runoff projections.

Although the absolute values of raw and bias corrected simulations differ significantly, this does not apply to the projected relative changes. Liu et al. (2014) also found that raw and bias corrected data resulted in similar estimations of relative changes for a series a variables, including ET and runoff. The study of Muerth et al. (2013) investigates the effect of bias adjustment on hydrological simulations and their climate change induced alterations. Concerning the relative changes between baseline and future time-slices, it is reported that bias correction does not influence notably the hydrologic indicators, apart from the one describing flow seasonality.

Chen et al. (2011) identify three uncertainty components in bias correction applications: the uncertainty of: the different GCM, the variable emission scenarios and that of the decade used for bias adjustment. From a comparison of the latter uncertainty source with the two former, concluded that the choice of correction decade has the smallest contribution to total uncertainty. In the present study we address another uncertainty source; that of the dataset used for correction. It was found that the WFDEI-bias corrected simulation captured better the past hydrological regime compared to the E-OBS-bias corrected configuration. The differences between the two simulations abate when results are expressed as percent change but still their variation are of the same magnitude as that between raw and bias corrected data. This implies that the selection of the observational dataset used for bias correction is not a trivial step of the modelling procedure and it should be treated as an extra factor that causes the uncertainty window of the projected hydrologic conditions to further open.

5.4. Projections of hydrological impacts under high-end climate change – Global scale

This section presents hydrological projections forced with the 13 models of the HELIX ensemble and run by the JULES model. The analysis is based on transient hydrological simulations for the period 1971 to 2100. In this part, water availability and droughts are studied at the global scale, under high-end scenarios of climate change. A first aim is to assess the changes on mean and low runoff and droughts of different types and durations, due to high-end climate. Secondly, the progression of the changes as the level of warming increases is assessed. Thirdly, the uncertainty in the projections is estimated by considering the agreement of the ensemble members and the values of each individual member. Climate change induced changes in mean and low runoff and drought climatology are also assessed at the basin scale level.

5.4.1. Hydrological projections at the global scale

Figure 36 shows the ensemble mean of percent changes in mean runoff per SWL and the associated model agreement, based on JULES' runoff simulations forced by the HELIX ensemble. Mean runoff is projected to increase for the majority of the land surface, with the increase intensifying for higher SWLs. Regions with decreased projected mean runoff, especially at SWL4, are the Mediterranean, north Africa and parts of central and south America. Model agreement is high (80 to 100 %) for the regions with large changes in mean runoff, especially at SWL4. Respective projected changes for low runoff are shown in Figure 37. The areas where low runoff of the baseline period is zero have been masked out from the relative changes' panel (shown with black colour). Large increases in low runoff are projected for the majority of the land surface with high model agreement. However, low agreement of the ensemble members is observed for the projected changes over Europe, which means that the ensemble mean climate change signal for this region should be interpreted with particular caution.

Figure B 11 of Appendix B shows the relative changes in mean annual precipitation per SWL. Mean annual precipitation is projected to increase for a largest part of the land surface. Thus the positive signal in runoff projections stems, to a degree, from the increased precipitation but it could also be attributed, to the stomatal closure due to increased CO_2 in the atmosphere – a plant

mechanism that reduces evapotranspiration losses and consequently leaves more of the precipitated water available as runoff.

RFmean

Relative change [%]

+ 1.5 °C   + 2 °C   + 4 °C

-75   -50   -25   -5   5   25   50   75

Model agreement on sign of change[%]

+ 1.5 °C   + 2 °C   + 4 °C

50   60   80   100
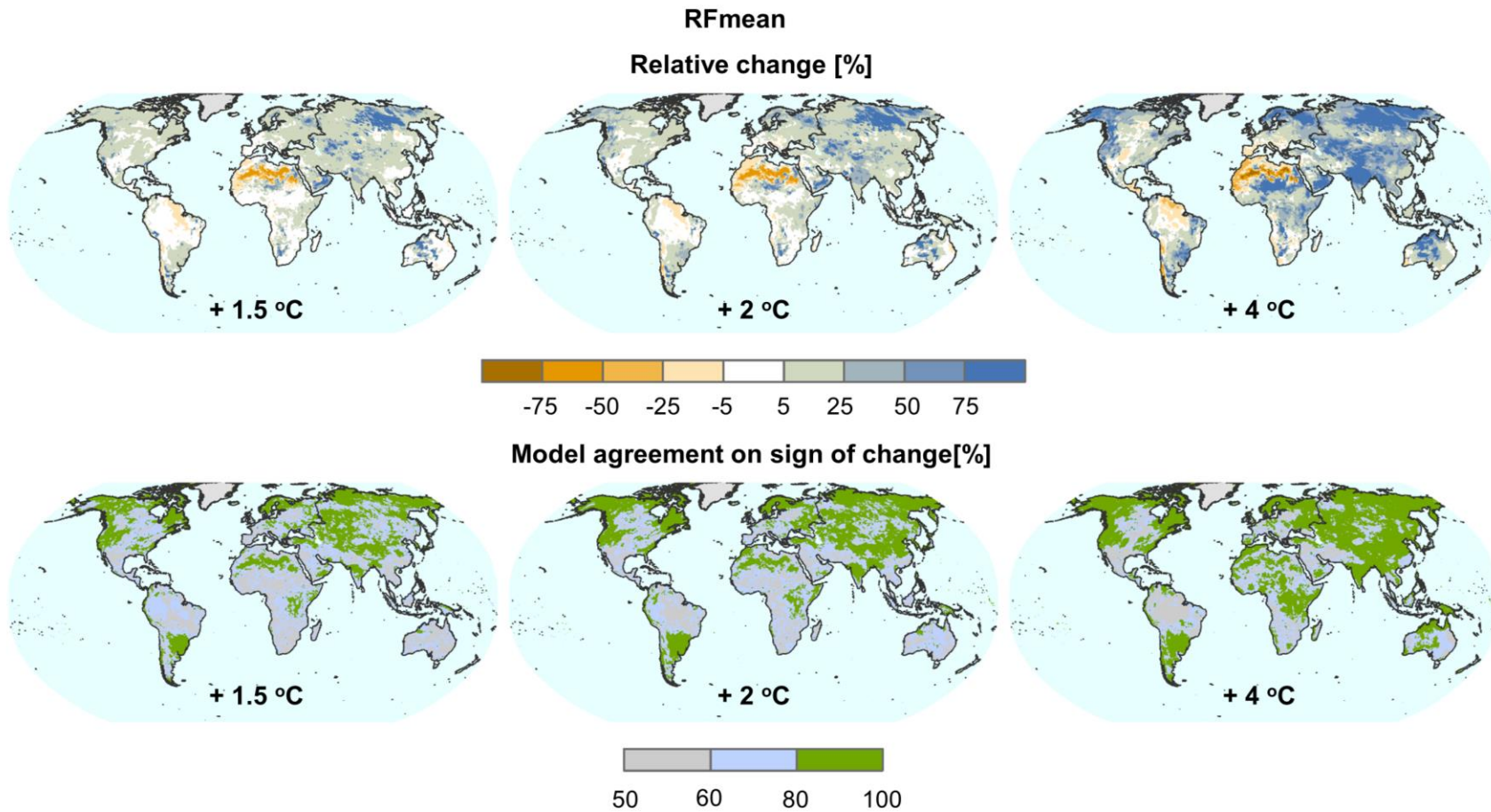
Figure 36. (top) Percent change in mean annual runoff (RFmean) per SWL compared to the baseline period, derived from the HELIX ensemble and (bottom) the respective agreement of the ensemble members on the sign of the change.
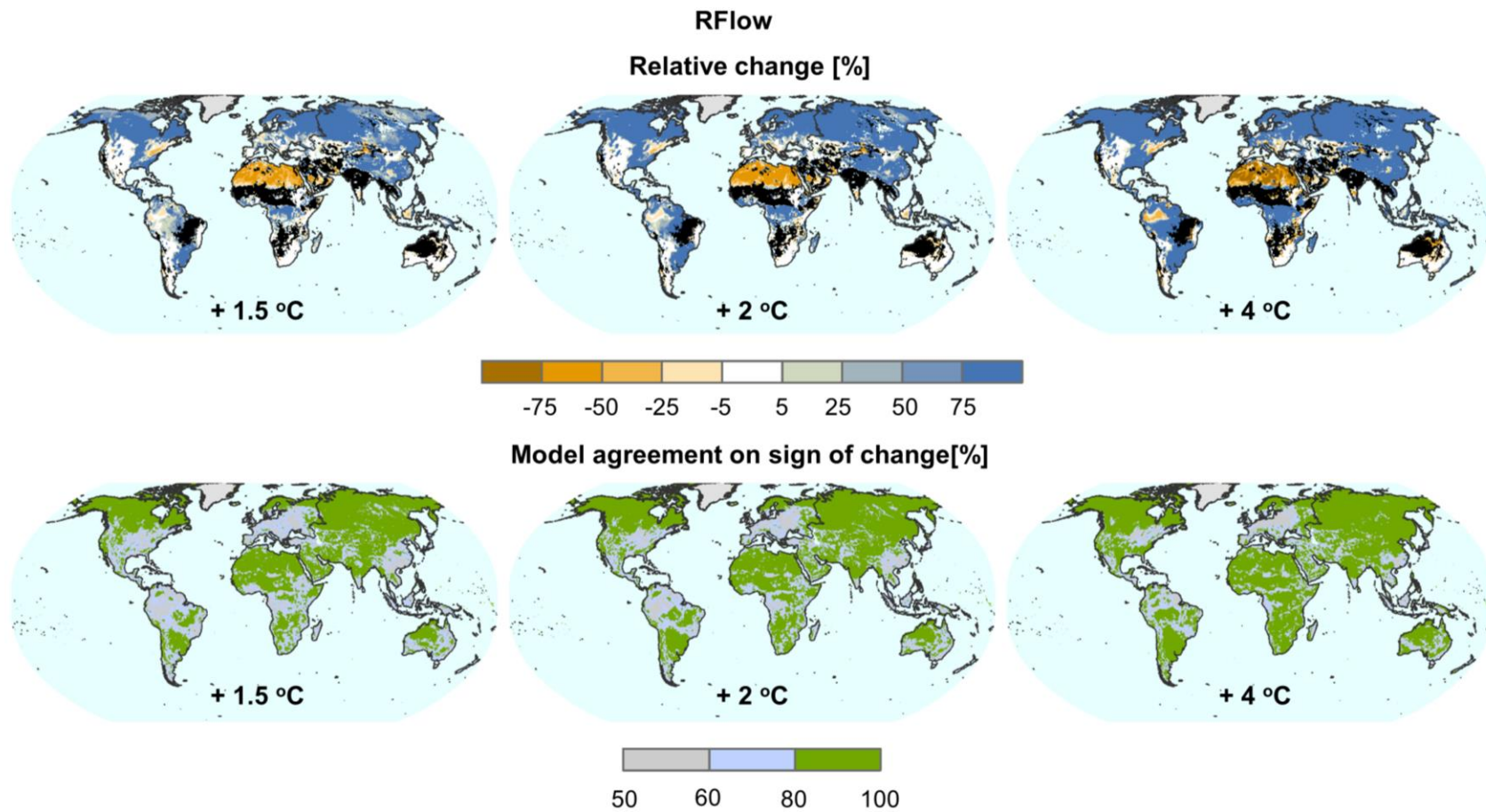
Figure 37. (top) Percent change in 10th percentile runoff (RFlow) per SWL compared to the baseline period, derived from the HELIX ensemble and (bottom) the respective agreement of the ensemble members on the sign of the change. The black areas in the relative change panels correspond to regions of zero historical low runoff values.

5.4.2. Projections of extreme drought duration at the global scale

Figure 38 and Figure 39 present the projected changes in drought duration and the respective model agreement derived based on 6- and 48-month SPI and SRI indices. For short-term extreme droughts, modelled with SPI6 and SRI6 (shown in Figure 38 and Figure 39 respectively), increased drought duration by 10-25 % is found for regions of Europe (west Europe and the Mediterranean) at +4°C of warming and less intense increases (5 to 10%) are found for small areas over north and south America and Australia. For long-term extreme droughts, modelled with SPI48 and SRI48 (Figure 38 and Figure 39respectively) increases in drought duration are more pronounced and apparent even from +1.5°C of warming. Under the highest examined level of warming (+4°C), the areas with the largest increases in drought duration are the Mediterranean, the north part of South America and south Africa. Increased drought duration is also projected for regions extended over central North America, north Africa, the middle East and Australia. Both short- and long-term SRI drought calculations show increases of more than 50% in drought duration for the Sahara region. However, this does not mean that the Sahara region should be regarded as the most affected area, as the large computed increase in drought duration is probably virtual due to the arid climate of this region and the percent calculation of changes in drought duration.
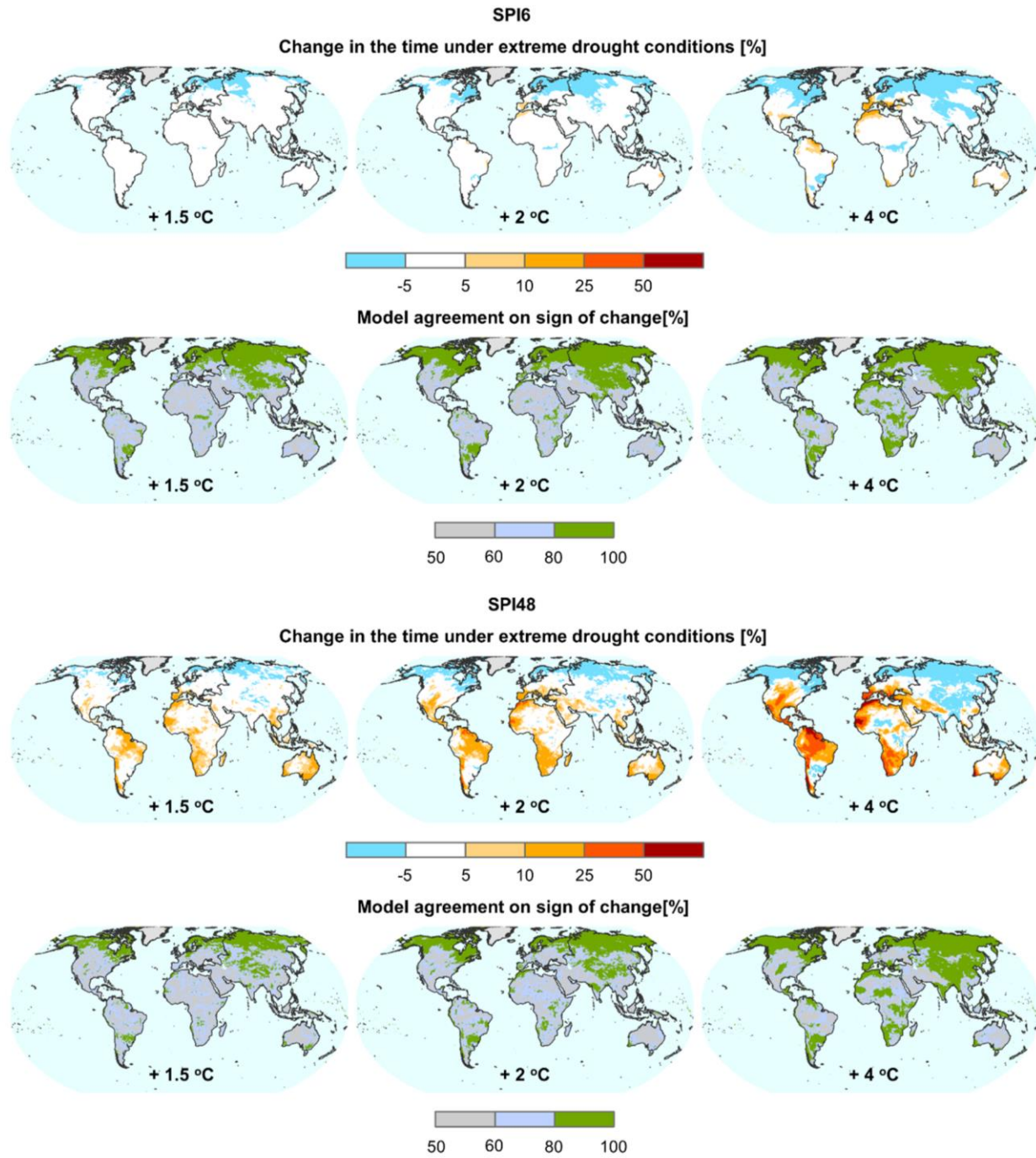
Figure 38. Ensemble mean change in time under extreme drought duration [%] based on SPI6 and SPI48, derived from the HELIX ensemble, and respective model agreement of the ensemble members on the sign of change per SWL.
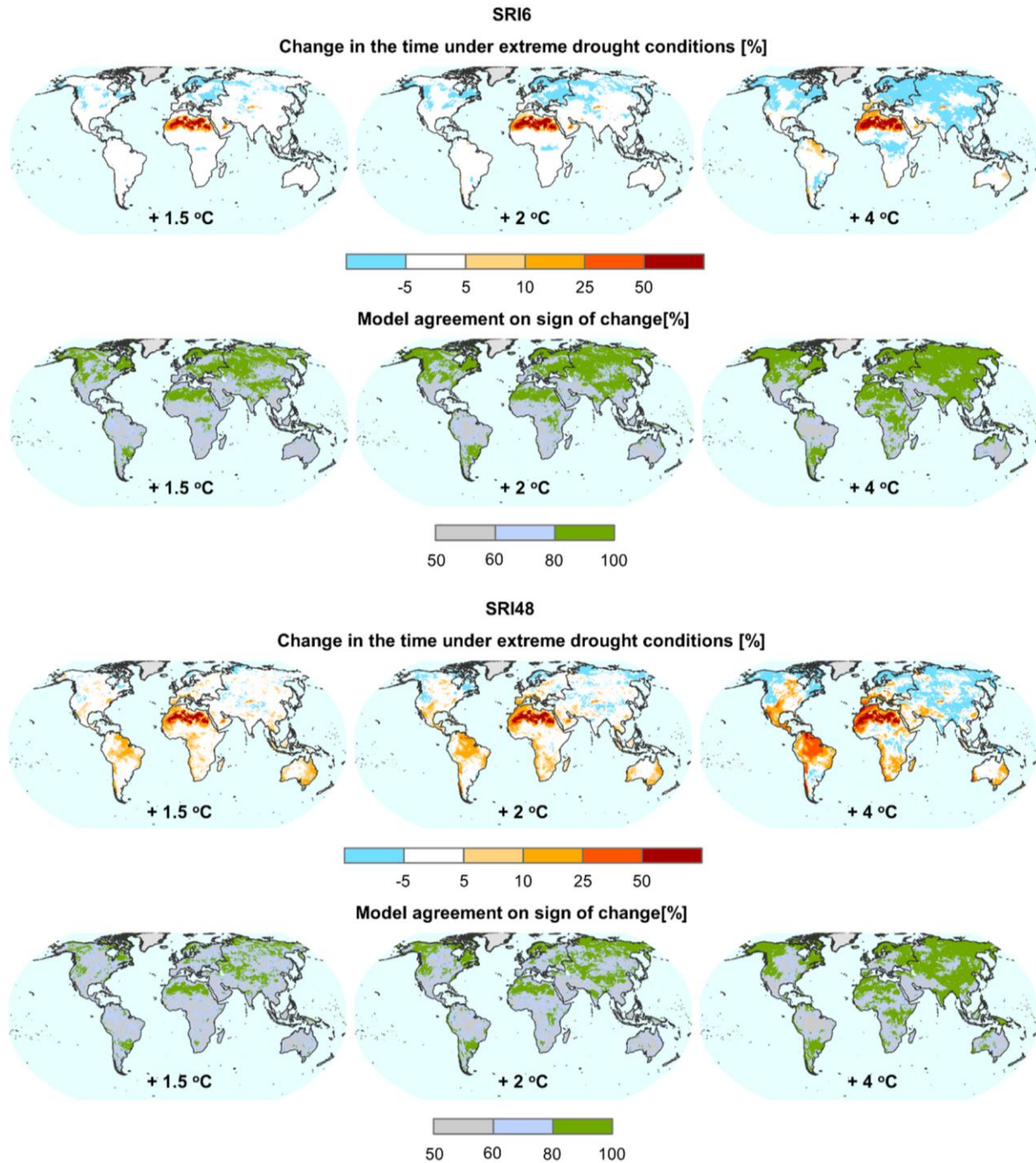
Figure 39. Ensemble mean change in time under extreme drought duration [%] based on SRI6 and SRI48, derived from the HELIX ensemble, and respective model agreement of the ensemble members on the sign of change per SWL.

5.4.3. Basin averaged runoff regime

Changes in basin aggregated mean and low runoff per SWL for the basins of study are shown in Figure 40 and Figure 41 respectively. Increases in mean runoff are projected for 19 out of the 21 basins. The two basins with projected decreases in mean runoff are both located in Europe (Danube and Guadiana). For most of the basins, the range of the ensemble members increases at SWL4 compared to the lower levels of warming. Another important observation is that the range of projected changes between the ensemble members is large and for some basins it spans through negative and positive values.

Low runoff is also projected to increase for the majority of the examined basins and especially for those located in the northern latitudes. Projected decreases in low runoff are found for 6 basins. The largest decreases concern the Guadiana basin, located in the Mediterranean region that has been identified as a hotspot for increased extreme drought duration from the global maps in Figure 38 and Figure 39. The range of the ensemble members at SWL4 is remarkably reduced, highlighting the agreement of the models towards low runoff decrease in this basin. A decreasing signal in low runoff is found for Amazon, which intensifies at higher warming levels. Negative signals for low runoff are also encountered in the Orange, Murray, Danube and Rhine basins. For some basins, particularly the largest ones, the projected changes are small because there are regions of both positive and negative signals in the domain of the basin.
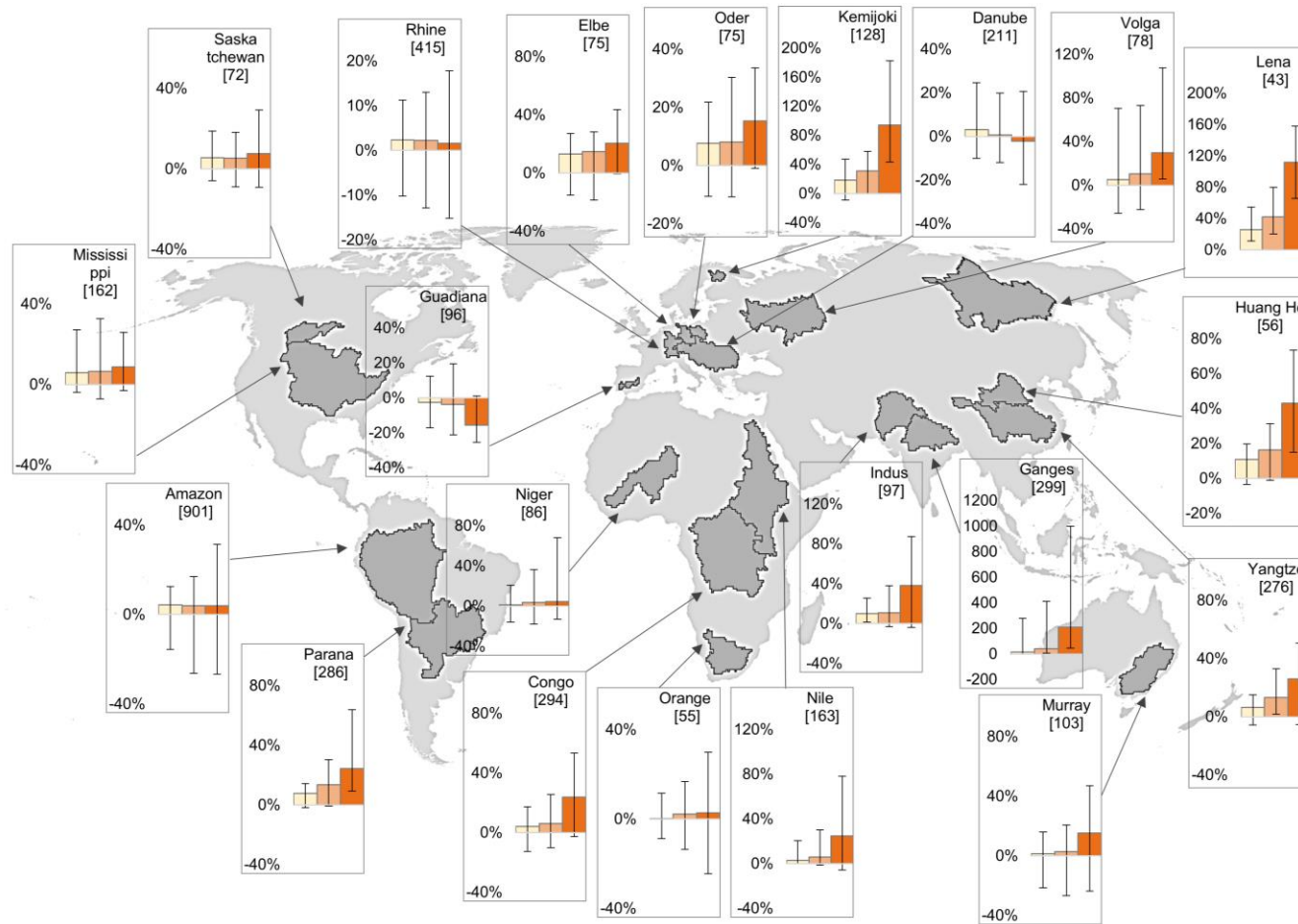
Figure 40. Changes in basin aggregated mean runoff per SWL compared to the baseline period, derived from the HELIX ensemble. Column bars show the ensemble median changes and the error bars the range of the ensemble members. The number in brackets [] corresponds to the basin aggregated mean runoff of the baseline period in mm/year. Changes are shown as percentages [%]. For the basins that changes exceed 200% the absolute differences (in mm/year) are shown instead.

131
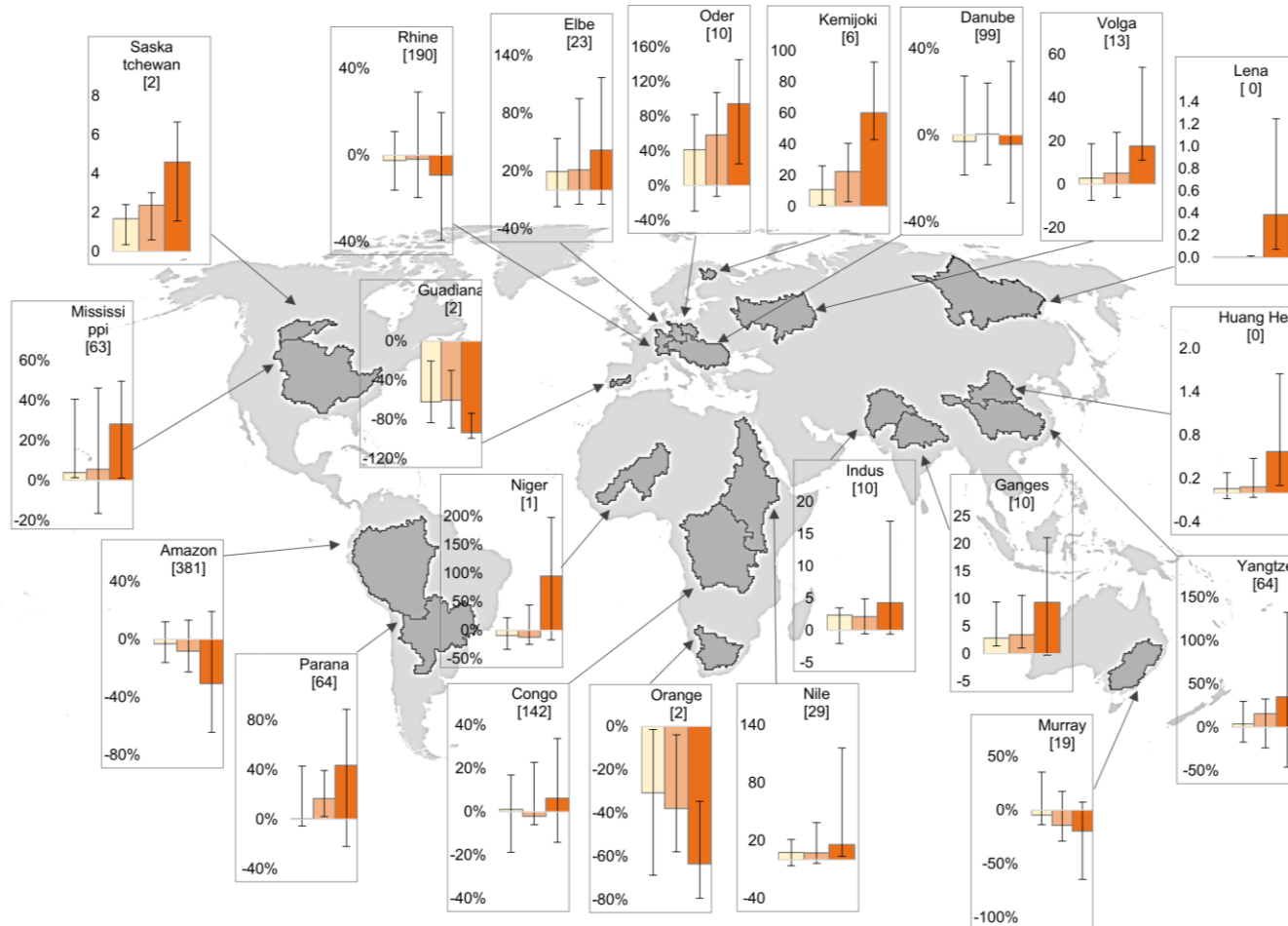
Figure 41. Changes in basin aggregated low runoff per SWL compared to the baseline period, derived from the HELIX ensemble. Column bars show the ensemble median changes and the error bars the range of the ensemble members. The number in brackets [] corresponds to the basin aggregated mean runoff of the baseline period in mm/year. Changes are shown as percentages [%]. For the basins that changes exceed 200% the absolute differences (in mm/year) are shown instead.

5.4.4. Drought climatology at the basin scale

DVTM is implemented to the ensemble mean daily runoff of the HELIX ensemble and a linear regression is then employed to examine the trend of the annual time series of drought days per years and its statistical significance. The regression results for the 21 examined basins are presented in Table 16. Increased drought days per year are found for eight basins, with the largest positive statistical significant trends reported for Rhine and Danube (0.80 and 0.60 days/year respectively). A decrease in drought days is found for 10 basins, with the largest negative statistically significant trend found for Congo (-0.33 days/year) and the smallest for Volga (-0.12 days/year). For three remaining basins (Lena, Elbe and Oder), the calculated trends were evaluated as statistically insignificant.

Table 16. Linear regression analysis' results for drought days per years, according to the daily varying threshold level method, per basin. Results are derived from the mean of the HELIX ensemble. Statistical significance is tested at the 95% confidence interval.

Basin	beta (trend) (days/year)	p	Statistical significance of the trend
Amazon	0.46	9.25E-14	YES
Congo	-0.33	5.57E-15	YES
Nile	-0.27	1.77E-20	YES
Mississippi	0.06	0.048827	YES
Parana	-0.31	5.62E-24	YES
Lena	-0.05	0.075708	NO
Yangtze	-0.30	2.31E-18	YES
Niger	-0.13	5.92E-11	YES
Volga	-0.12	0.001648	YES
Murray	0.24	2.19E-11	YES
Indus	-0.28	1.59E-26	YES
Ganges	-0.25	2.97E-20	YES
Orange	0.31	3.67E-24	YES
Danube	0.60	9.14E-24	YES
Huang He	-0.27	6.20E-17	YES
Saskatchewan	0.12	1.35E-07	YES
Rhine	0.80	3.02E-27	YES
Elbe	-0.05	0.098452	NO
Oder	-0.01	0.668181	NO
Guadiana	0.35	2.68E-18	YES
Kemijoki	-0.18	1.55E-07	YES

5.5. Comparison of hydrological projections from different forcing data

Here we compare the hydrological projections derived from the HELIX ensemble to EURO-CORDEX projections and simulations of the ISIMIP ensemble. The HELIX and EURO-CORDEX are of higher spatial resolution compared to ISIMIP. The aim posed in this section is to explore the differences and similarities between the projections of the three ensembles and assess possible added value provided by the higher resolution simulations. This analysis focuses on the European

region, as it the common domain of all the three ensembles (HELIX and ISIMIP cover the global domain but EURO-CORDEX only the European area).

5.5.1. General comparison between three ensembles

Figure 42 to Figure 49 provide a comparison between the projected changes in hydrologic indicators and drought indices derived from the three examined ensembles (ISIMIP, EURO-CORDEX and HELIX). Figure 42 and Figure 44 show the projected changes per SWL in mean and low runoff respectively and Figure 43 and Figure 45 show the model agreement on the sign of change of mean and low runoff respectively. Moreover, spatially aggregated relative projected changes in the two runoff indicators for each single ensemble member, for eight European sub-regions can be found in Appendix B (Table B 4, Table B 5 and Table B 6).

The projections of the eight ensembles exhibit a considerably different behavior. The ISIMIP projections are far less detailed than the other two, due to the lower resolution of the ISIMIP ensemble. In contrast, EURO-CORDEX projections show more variant spatial patterns than the HELIX ensemble, although the two ensembles have a similar resolution. A common pattern on the projected changes in mean runoff between the three ensembles (Figure 42) is the increasing signal in north and north-eastern Europe and the decreasing signal in the south part of the continent. Northern and southern Europe are regions with higher agreement on the sign of mean annual runoff change, while agreement is lower for central Europe (Figure 43).

Projected changes in low runoff by the ISIMIP and EURO-CORDEX ensembles show similar patterns of increased low runoff in the north-east and decreased low runoff in the south-west, although the latter ensemble projects greater changes (Figure 44). The HELIX ensemble has quite a distinguished behavior of projected increases in low runoff over the majority of the continent. Concerning model agreement on the signal of low runoff projections (Figure 45), the HELIX ensemble has the lower extent of high model agreement (80-100%), mainly at the Scandinavian Peninsula. The ISIMIP ensemble has higher agreement for the increasing changes in Scandinavian countries and the decreasing signal in the Mediterranean while EURO-CORDEX projections highly agree (80-100% of the models) on the sign of changes in low runoff over the majority of the continent.

The comparison of the projected changes in hydrologic indicators of the three examined ensembles reveals remarkably diverse patterns between the ensembles. A greater similarity can be observed between the spatial patterns of projected changes in extreme drought duration of the three ensembles. For short-term droughts (modelled with SPI6), all the ensembles project increases in drought duration in the Mediterranean region at SWL4, while only ISIMIP shows spatially coherent regions of increased drought duration at lower levels of warming (SWL1.5 and 2) (Figure 46). Especially at SWL4, the regions of increased drought duration are also regions with high model agreement on the sign of the change of short term drought duration (Figure 47). The projected changes in time under long term extreme drought conditions (modelled with SPI48) are more intense and spatially extended compared to short term droughts (Figure 48). Again, similar patterns can be found between the three ensembles. Under +4 °C of warming, increased drought duration is projected for south Europe by all the ensembles. The agreement of the models is less uniform between the three ensembles (Figure 49). At SWL4, the ISIMIP ensemble exhibits high agreement over the whole south-European region, EURO-CORDEX shows patches of high agreement all over south Europe while the HELIX ensemble shows high agreement on increased drought duration only for the south Iberian Peninsula, Sardinia and south Italy.
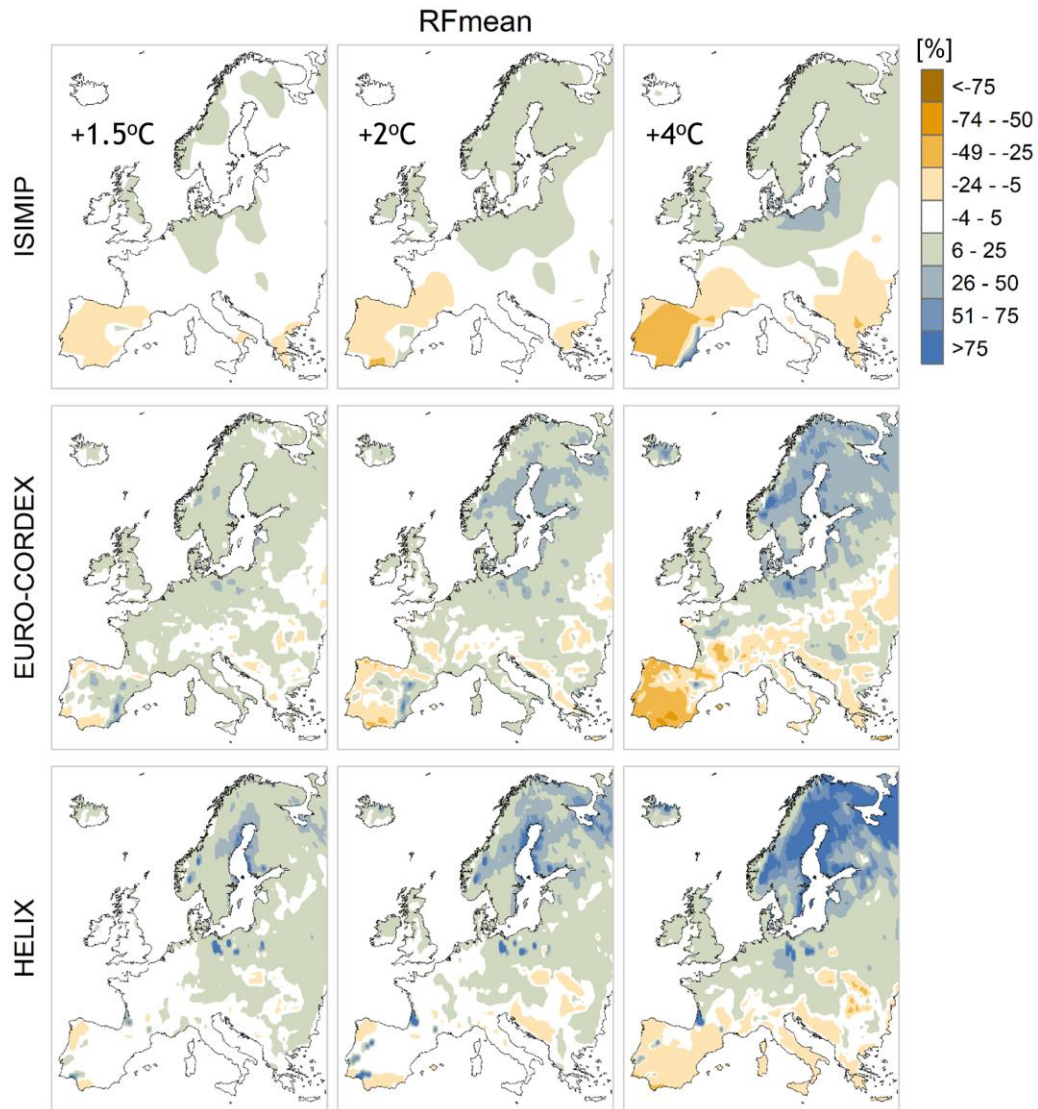
Figure 42. Relative change in mean annual runoff (RFmean) per SWL, simulated by the three different ensembles: ISIMIP (top), EURO-CORDEX (middle) and HELIX (bottom).
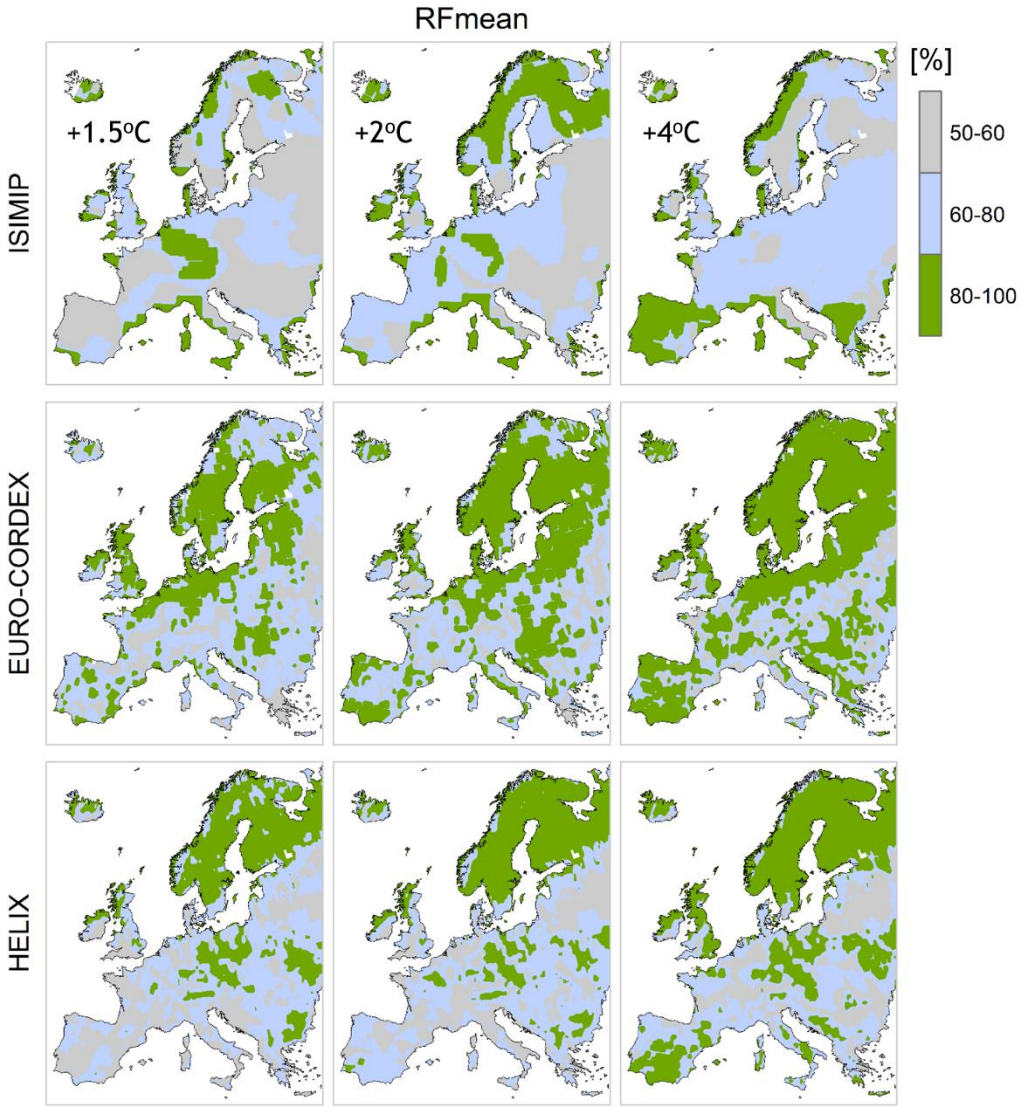
Figure 43. Model agreement on the sign of change in mean annual runoff (RFmean) per SWL, simulated by the three different ensembles: ISIMIP (top), EURO-CORDEX (middle) and HELIX (bottom).
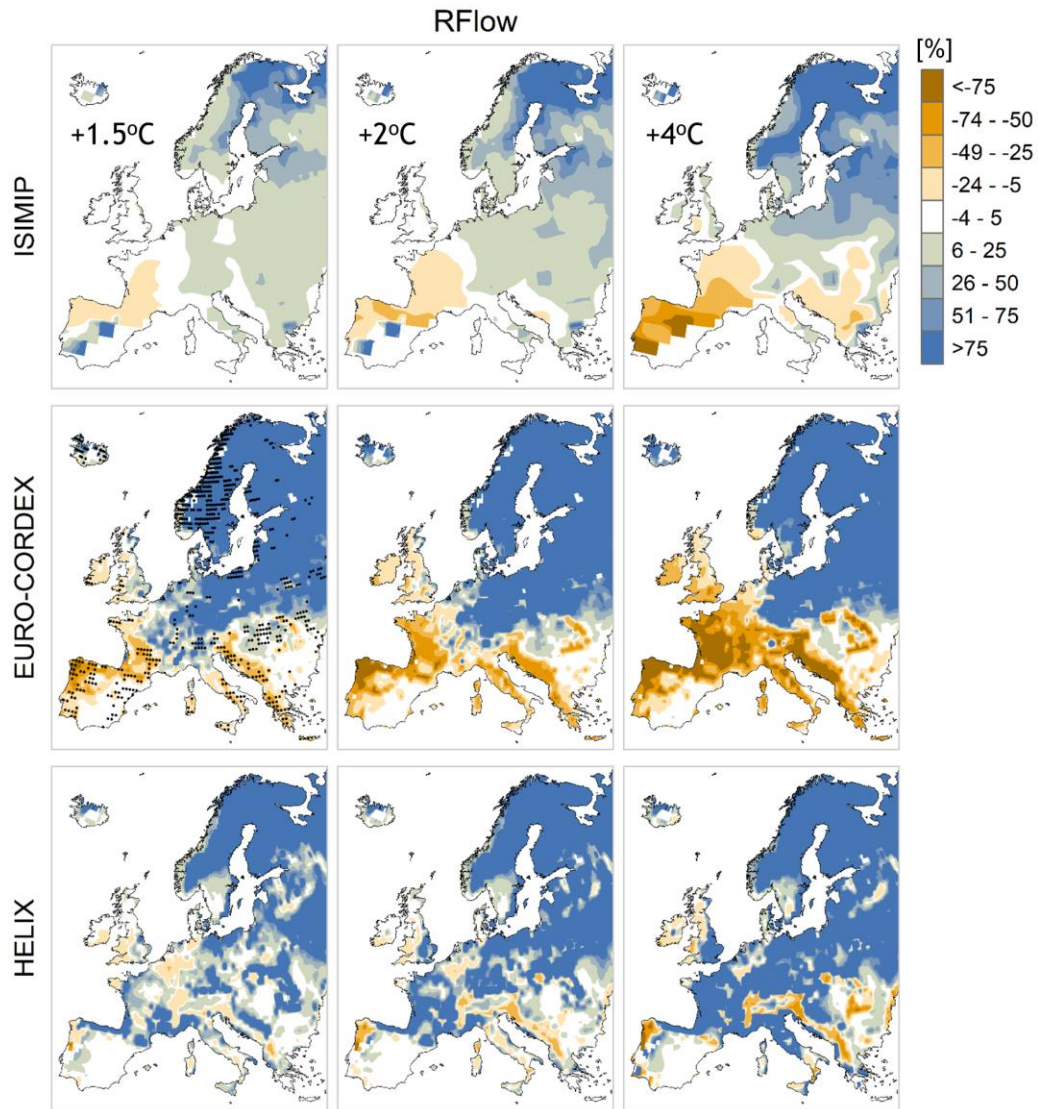
Figure 44. Relative change in 10th percentile runoff (RFlow) per SWL, simulated by the three different ensembles: ISIMIP (top), EURO-CORDEX (middle) and HELIX (bottom).
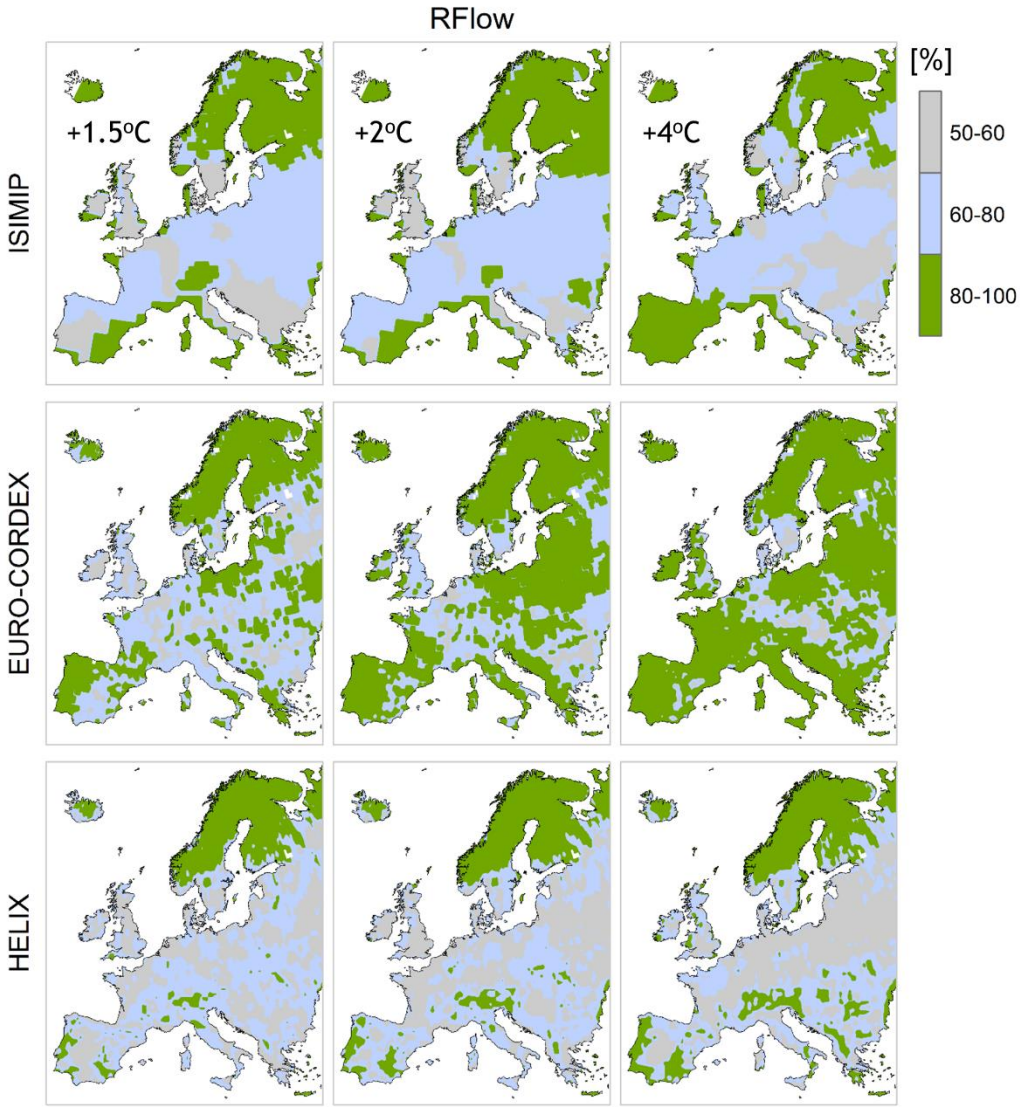
Figure 45. Model agreement on the sign of change in 10th percentile runoff (RFlow) per SWL, simulated by the three different ensembles: ISIMIP (top), EURO-CORDEX (middle) and HELIX (bottom).

5.5.2. Evaluation of a combined ensemble

So far we have examined differences in the projected changes in runoff indicators and duration of drought conditions derived by three different ensembles. Here we combine the three ensembles (ISIMIP, EURO-CORDEX and HELIX) into one, and examine the projected changes in short and long term drought conditions (Figure 50 and Figure 51 respectively) along with the model agreement of the extended ensemble on the sign of change of drought duration.

The combined ensemble shows virtually no change in short term drought duration at SWL1.5, small increases in short term drought duration over regions of the Iberia Peninsula at SWL2 and increases ranging from 5 to 25 % for the Mediterranean region at SWL4 (Figure 50). It is important to note that the aforementioned regions of drought duration increases in the Mediterranean, also show a high level of model agreement.

Regarding long term droughts (Figure 51), the combined ensemble shows increases of 5 to 25 % in duration over the Iberian Peninsula, west France, Italy and Greece at SWLs 1.5 and 2. However the confidence on these changes is debatable, as only 60-80 % of the combined ensemble members agree on the sign of the changes. At SWL4, the combined ensemble shows increases in long term drought conditions up to 50 %, affecting all the south part of Europe and even regions of central Europe. Nonetheless, regions of high agreement (80-100 %) on these changes, are only the Mediterranean regions.

5.5.3. Ensemble differences and attributions

The comparison of the different model ensembles revealed large differences in the projected hydrological impacts, with conflicting signs of change for some runoff metrics. In summary, the highest level of consensus between the ensembles was observed for changes in mean runoff. The climate change signal for mean runoff regards increases in the north of Europe, decreases in the south and only small changes with lower model agreement for central Europe. For low runoff, the HELIX ensemble shows increased response over most of Europe, but also exhibits low model agreement on the sign of change for most of the European area. The other two ensembles show a different response of low runoff to climate change, as both consent on increased low runoff in the north-eastern part of Europe and decreased low runoff over the south-western part of the continent.

The three examined ensembles show a markedly more similar response regarding the drought duration projections. For short-term droughts, all the ensembles show increased drought duration over the Mediterranean while for long-term droughts the region of increased drought duration extents to the whole of southern Europe. Moreover, the projected increase in drought duration is larger for long-term compared to short-term droughts.

In a set of figures provided in Appendix B (Figure B 12 to Figure B 15), an examination of the differences in the projected changes caused by the selection of the HELIX model (EC-EARTH of HadGEM) is attempted. Only the ensemble members forced with common driving models participate in this comparison. Examination of the role of the HELIX model for the hydrological simulations reveals that the two HELIX models project very different futures of conflicting climate change signals. Specifically, HadGEM projects a dramatically drier future while EC-EARTH projects a wetter future in terms of runoff production metrics. Regarding the drought analysis, HadGEM shows increased drought duration for a considerably larger part of Europe compared to EC-EARTH. The projected climate change signal is determined by the HELIX model rather than by the SST driving model.

The combined ensemble shows that spatially coherent regions of increased drought duration and high model agreement appear under +4°C of warming over the Mediterranean region.
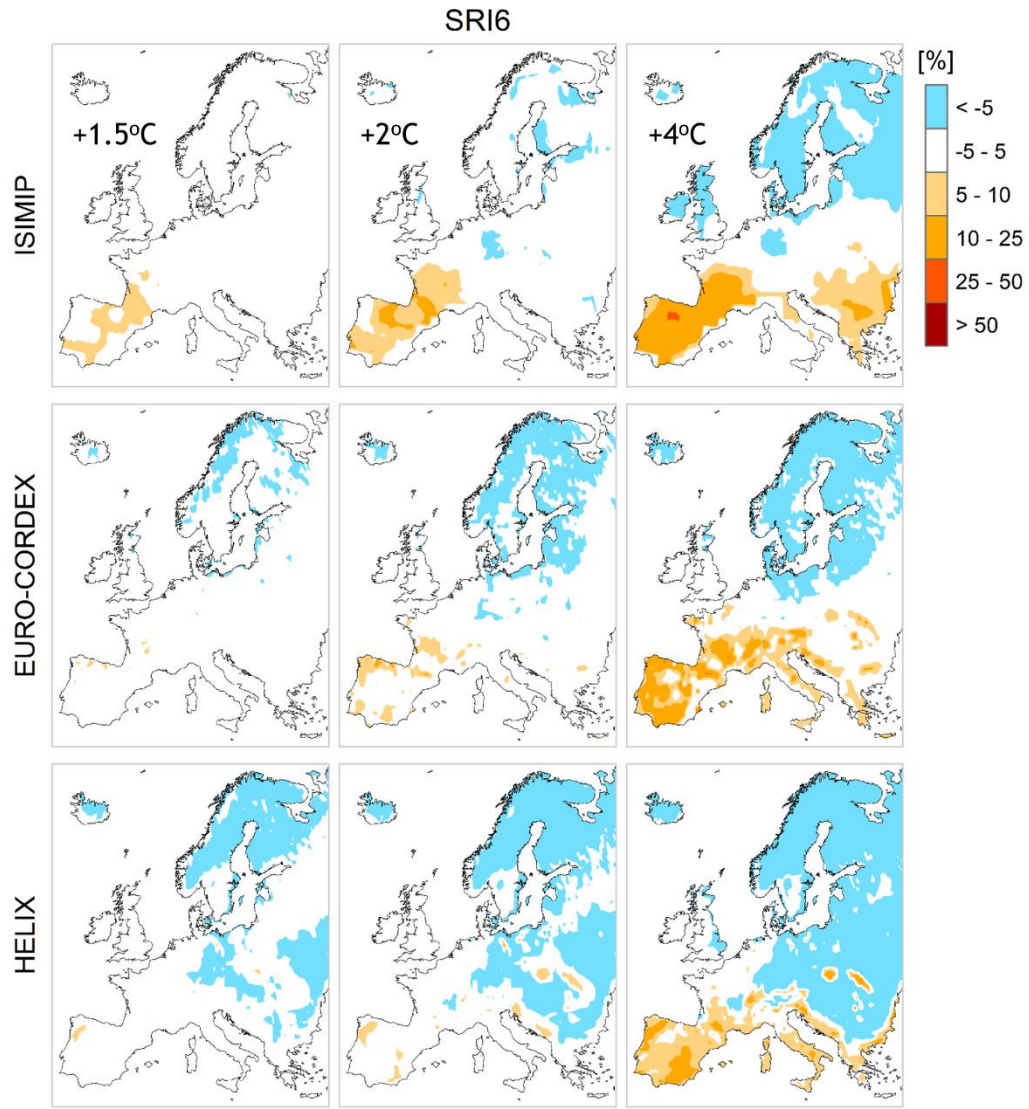
Figure 46. Relative change in extreme short term drought (SRI<=-1.5) duration per SWL, simulated by the three different ensembles: ISIMIP (top), EURO-CORDEX (middle) and HELIX (bottom).
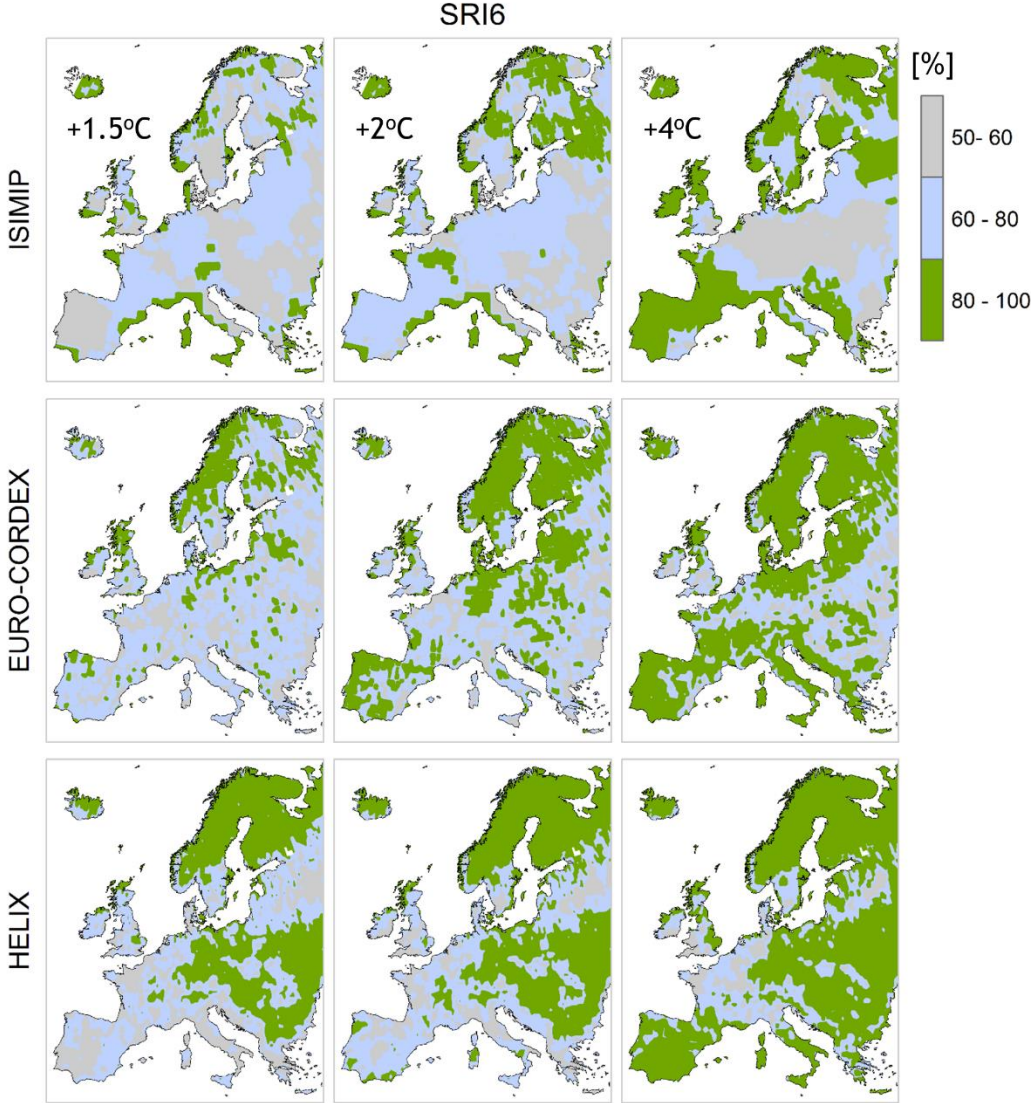
Figure 47. Model agreement on the sign of change in extreme short term drought duration per SWL, simulated by the three different ensembles: ISIMIP (top), EURO-CORDEX (middle) and HELIX (bottom).
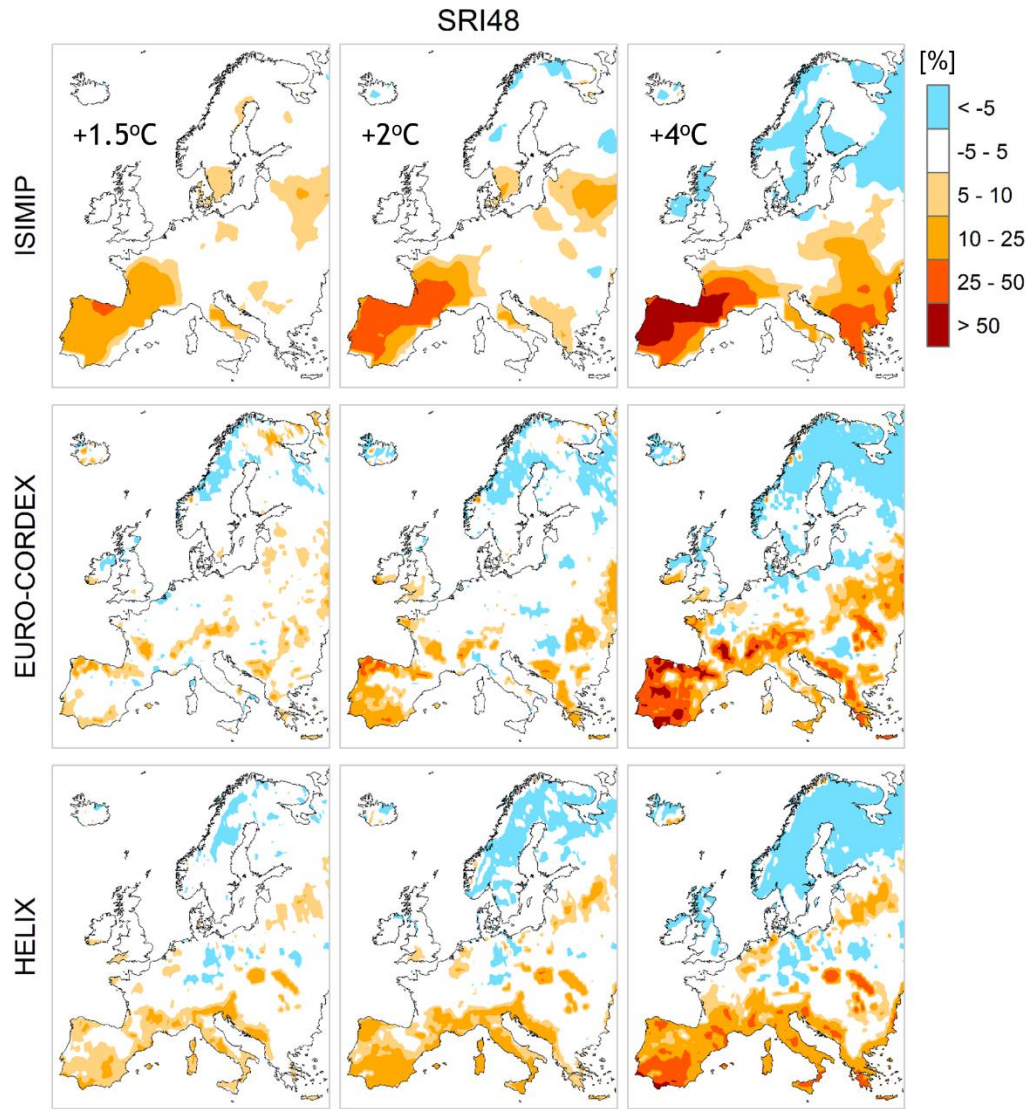
Figure 48. Relative change in extreme long term drought (SRI<=-1.5) duration per SWL, simulated by the three different ensembles: ISIMIP (top), EURO-CORDEX (middle) and HELIX (bottom).
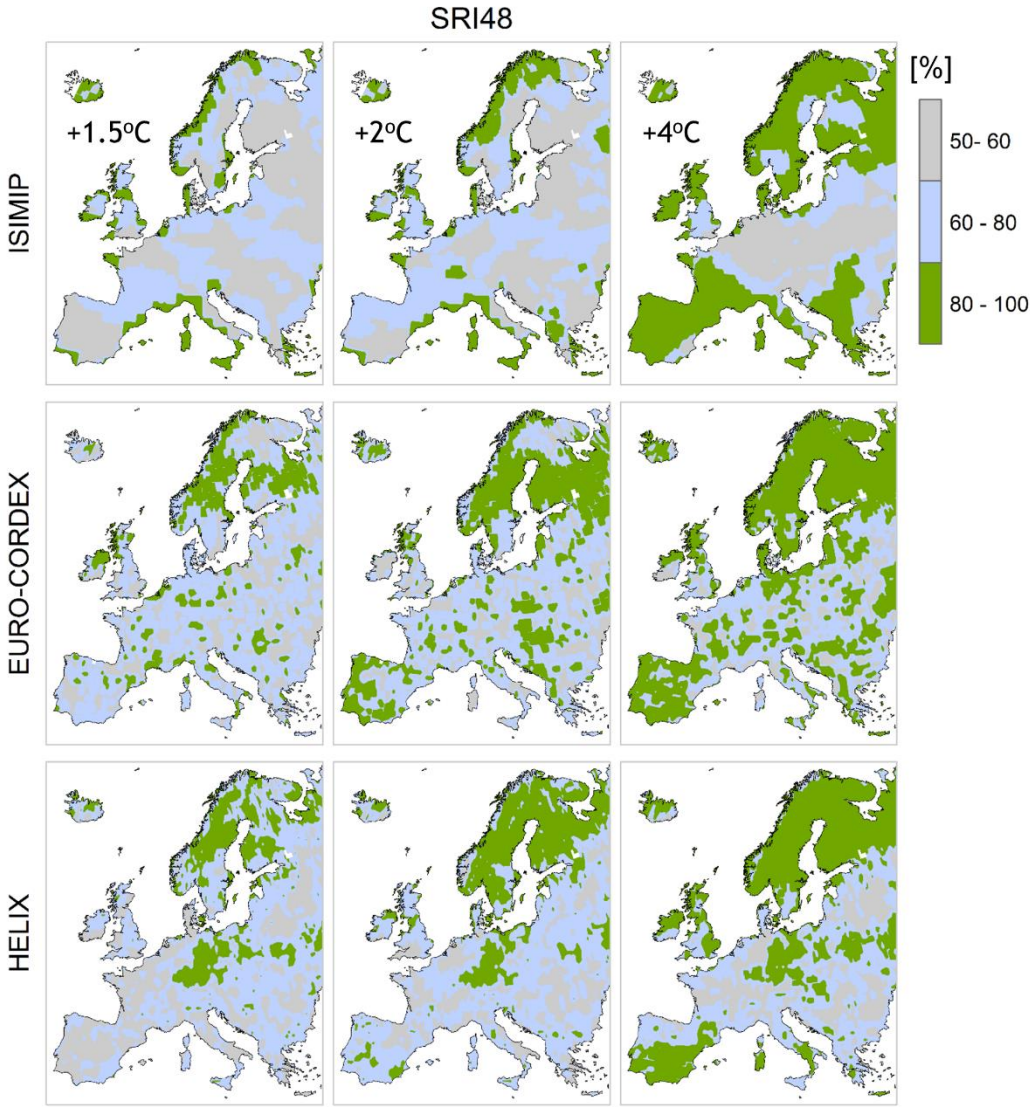
Figure 49. Model agreement on the sign of change in extreme long term drought duration per SWL, simulated by the three different ensembles: ISIMIP (top), EURO-CORDEX (middle) and HELIX (bottom).
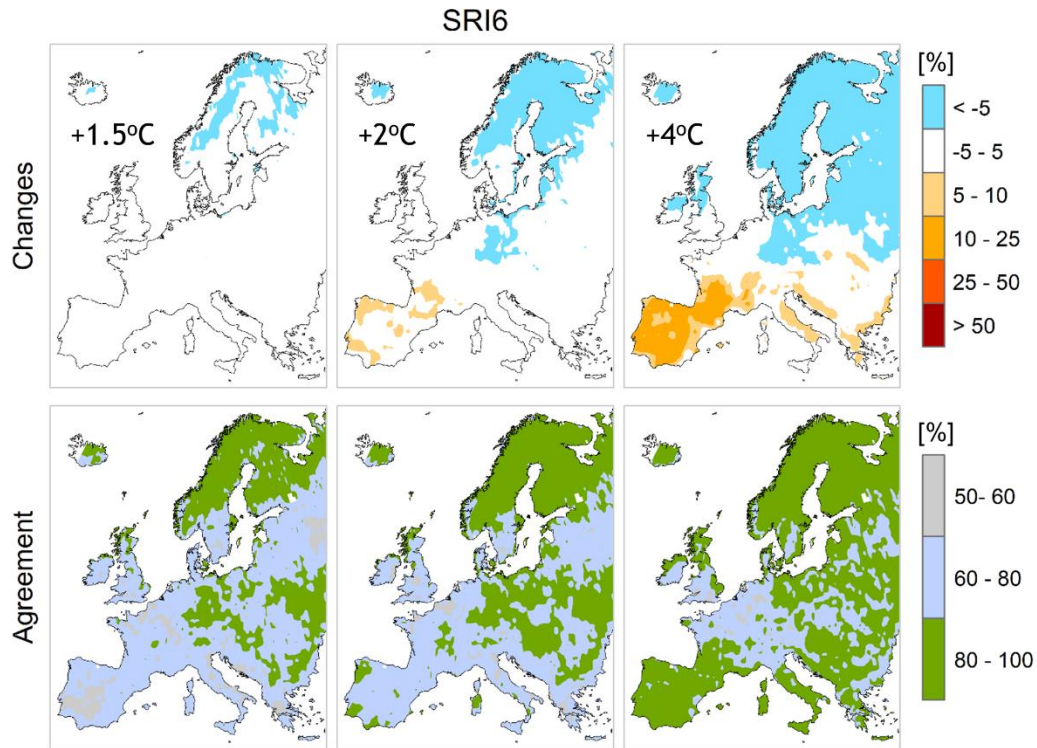
Figure 50. Relative change in extreme short term drought (SRI<=-1.5) duration per SWL, simulated by the three the combined ensemble (top), and model agreement on the sign of change (bottom).
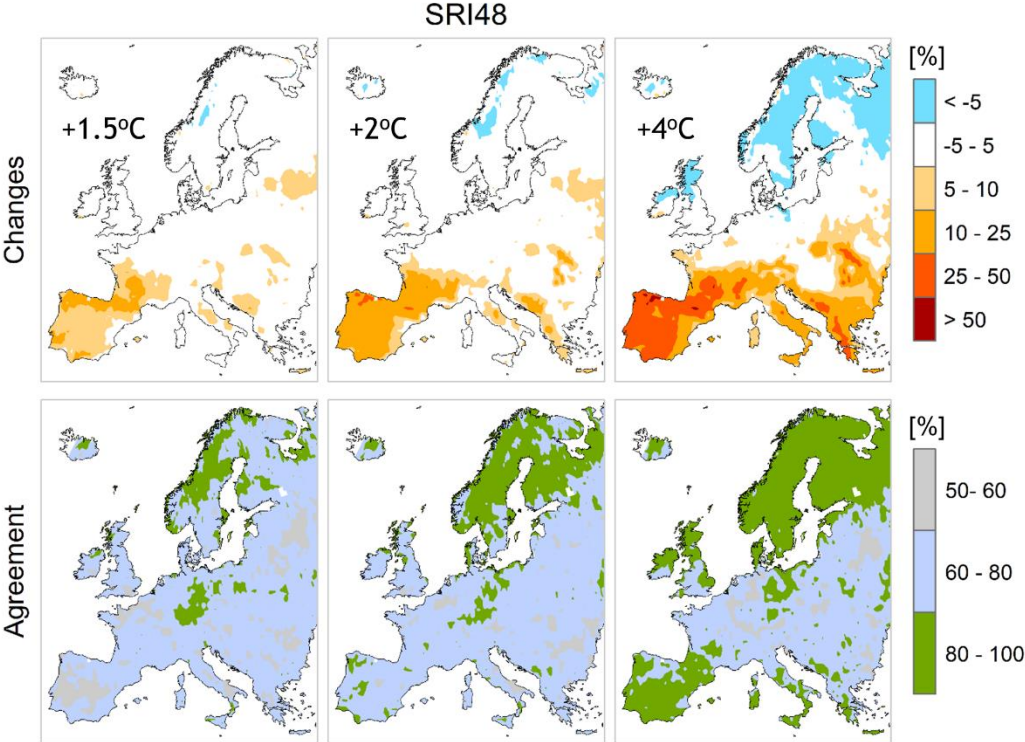
Figure 51. Relative change in extreme long term drought (SRI<=-1.5) duration per SWL, simulated by the three the combined ensemble (top), and model agreement on the sign of change (bottom).

Chapter 6. Conclusions

6.1. Summary and concluding remarks

In this section, a summary of the thesis is presented, the main findings are highlighted and conclusions are drawn. The present thesis provides a complete methodological framework for a detailed assessment of the effects of high-end climate change on hydrological resources at the regional, European and global scale. Hydrological simulations are performed with the large scale LSM JULES. JULES, as a physically based model, provides an advantage to our impact assessment compared to assessments established on pure hydrological models, as it can account for the effects of rising atmospheric CO_2 on plant physiology.

Model evaluation for the historical period

The first step in our methodological framework is the evaluation of the JULES model for the historical period and the assessment of the model's sensitivity to the observational dataset used as forcing. The evaluation of the hydrological performance of the JULES model is done in two stages. The first part of model evaluation is based on runoff and aims at the evaluation of mean and low hydrological states while the second part is based on discharge, and aims at the evaluation of monthly and seasonal discharge profiles at the basin scale. To implement the second stage of model evaluation, a routing algorithm was developed and applied to the model output, to convert the vertical runoff production flux to discharge at the basin outlet. The algorithm uses a conceptual semi-distributed model based on time of concentration, following a source-to-sink routing approach. Meanwhile, the sensitivity of the model to the forcing dataset is assessed by comparing model runs of the same model configuration forced by three different observational datasets (WFDEI, PGFv2 and GSWP3).

From the analysis described above it can be concluded that JULES can capture well the shape of the annual discharge cycle for most of the examined basins, although a tendency towards discharge underestimation by the model was identified. The use of different forcing datasets produces considerable changes in the results for some regions (especially in the African continent). For the studied basins the different forcing results in at least 10 % difference in the magnitude of simulated

discharge, while the median range of PBIAS is 30 % and the average range 40 %. It can thus be stated that JULES exhibits high sensitivity to the climate drivers.

The effect of GCM biases on runoff

The second step of the methodological framework presented in this thesis concerns the examination of GCM biases and their effect on hydrological simulations. More specifically, the present study examined the effect of the biases in GCM output variables on historical runoff simulations, using the JULES LSM. The effects of biases were studied for each forcing variable separately, for six meteorological variables (precipitation, temperature, radiation, specific humidity, surface pressure and wind speed) in total. Biases of each variable and the respective effect of runoff were quantified at the global and regional scale. A framework for the categorization of the effects of biases of the different variables was developed and implemented, leading to global maps of bias ECs.

According to the findings of this study, bias correction of GCM outputs results to substantially improved representation of historical runoff. For this reason, the present study adds to the numerous studies that advocate on the use of some kind of bias correction of GCM data prior to their use as impact model forcing. Precipitation and temperature biases were identified to cause the largest changes in runoff. Radiation and specific humidity can also pose a substantial effect on runoff, especially for specific regions. The sensitivity of runoff to the different forcing variables exhibits a high spatial variability. Depending on the region, runoff can be more sensitive to radiation or humidity compared to precipitation or temperature. The produced EC maps show that all variables can potentially affect runoff to a high extent depending on the region. The fraction of the land surface occupied by the high effect category ECI (high changes in runoff and high sensitivity of runoff to the variable's changes) ranges between the variables from 67.80 % for precipitation to 6.09 % for wind.

The produced maps of ECs aid the identification of the regions mostly affected by the bias of each variable. Thus, they could serve as a decision tool in cases when an informed decision needs to be made on the variables that would need to be bias corrected or could be neglected from bias correction, according the planned model application. Moreover, when raw forcing is used in model applications, EC maps could provide a guidance towards the areas where the results would need a more careful interpretation.

Based on the findings of this study it is suggested that the widely used concept of bias correcting precipitation and temperature should be extended to include more input variables. Radiation and specific humidity should be added to the priority variables for bias correction in hydrological applications, along with precipitation and temperature.

Due to the heavily model dependent nature of runoff sensitivity to forcing variables, generalized conclusions for the behavior of other impact models to GCM biases cannot be drawn from the present single model assessment. Nevertheless, this study aims to initiate a discussion on the effect of GCM biases on hydrological output, as the consideration of these sensitivities is crucial to understand the uncertainty spectrum of hydrologically relevant climate change assessments.

Projections of hydrological impacts under high-end climate change – European scale

The next step of our methodological framework includes the projections of hydrological impacts of high-end climate change. The first set of hydrological projections concerns the European region and is forced by the novel dataset of the Euro-CORDEX climate projections. The spatial patterns of changes in future mean- and low- hydrological states under +4°C of global warming are assessed and an analysis of the changes in future drought climatology is performed for five major European basins. Moreover, the impact of +2°C versus +4°C global warming is estimated. Concurrently, the effect of bias correction of the climate model outputs on the projected climate and the role of the observational dataset used for bias correction are also evaluated.

Projections show an intensification of the water cycle at +4 SWL, as even for areas where the average state is not considerably affected, there are remarkable projected decreases of low flows. With the exception of the Scandinavian Peninsula and some small areas in central Europe, 10th percentile runoff production is projected to reduce all over Europe. This favours the formation of extreme hydrological events, thus more droughts compared to the current state could be expected in the future due to the warming climate.

Drought climatology is projected to change to more dry days per year for the Danube, Rhine and Guadiana basins. Thus these areas are projected to experience more usual and more intense drought events in the future.

For the areas where clear decreasing or increasing runoff trends are projected, the changes are considerably intensified when moving from the +2 SWL to the +4 SWL. Decreasing trends apply to southern Europe, including the Mediterranean region, while strong increasing trends are projected for northern and north-eastern Europe. For the rest of the European region where trends are not clear or ensemble members do not agree towards the change, the effect of the further warming from +2 SWL to +4 SWL, does not seem to severely affect the hydrological state, which is however already significantly altered at +2 SWL compared to pre-industrial.

Bias correction results in an improved representation of the historical hydrological conditions. However, raw and bias corrected simulations exhibit minor variations for results of statistical interpretation (in our study: percent change, number of days under drought threshold).

The dataset used for bias correction can affect the quality of the projections in absolute terms to a great extent. The comparison performed here showed that the WFDEI-corrected dataset produces simulations that capture better the past observed hydrologic state compared to the E-OBS-corrected dataset and should thus be preferred for bias correction applications over Europe. The selection of the "correct" dataset is an added uncertainty to the climate impact modelling chain, with magnitude similar to that of the bias correction procedure itself.

Projections of hydrological impacts under high-end climate change – Global scale

The second set of hydrological projections regards the global scale. The global hydrological projections are forced with the thirteen models of the HELIX ensemble and run by the JULES model. Here only bias corrected data of the HELIX GCM ensemble are included in the analysis. In this part, the water availability and drought duration analysis under high-end scenarios of climate change of the previous section is extended to the global scale. In addition, the study of droughts is approached with different methods (SPI and SRI) and different types of drought (short- and long-term) are examined. While our first aim is to assess the changes on mean and low runoff and droughts of different types and durations due to high-end climate, concurrently, the progression of the changes as the level of warming increases is assessed (from +1.5, to +2, to +4ºC). Climate change induced changes in mean and low runoff and drought climatology are also assessed at the basin scale level. Finally, estimation of the uncertainty in the projected impacts is also integrated in this part of the study.

The global scale analysis provides information on the regions of the globe that are projected to have increased or decreased mean and low runoff in a future under high-end climate change. Runoff indicators (mean and low runoff) are projected to increase for the majority of the land surface. However, there are areas (the European region included in these) that model agreement on the sign of change is low and thus we cannot be definitive on the impacts projected for these regions. The global scale drought analysis revealed regions with projected increases in extreme drought duration. Increased short-term extreme drought duration is mainly projected for the Mediterranean region while for long-term extreme droughts, the regions that are expected to experience increases in the events' duration are located in the Mediterranean, central North America, north Africa, the middle East and Australia.

The basin scale drought analysis concluded in eight basins that are expected to experience increased days per year under drought conditions in the future. The mean and low runoff regime analysis at the basin scale showed that the impacts are exacerbated as the level of warming increases for most basins. An important finding is that the range of the projections is very large and for many basins spans through both negative and positive changes. In these cases, the use of the ensemble mean may not be a particularly useful indicator of the projected changes. Moreover, since there is not a way to favour or reject a projected response, policy makers and adaptation strategies should account and prepare for both possible outcomes.

Comparison of hydrological projections from different forcing data

In this final section, the EURO-CORDEX- and HELIX- driven hydrological projection are inter-compared and also examined in contrast to respective simulations of the former GCM ensemble generation (denoted ISIMIP) which has a lower spatial resolution. This analysis is limited to European region, as the common domain of all the three ensembles. Generally there are large differences between the projected impacts for mean and low runoff, and a greater consensus on the projected changes in drought duration. For the HELIX ensemble specifically, it has been revealed that the projected climate change signal is determined by the HELIX model rather than by the SST driving model. Finally, combination of three ensembles into one highlights the Mediterranean region as a hotspot of increased drought duration.

6.2.   Innovation and contribution

The present thesis contributes to the basic science with two newly developed methodologies. The first contribution is the development of a routing algorithm, which allows the comparison of the gridded JULES output to observed discharge, thus allowing the evaluation of the model against actual discharge measurements. The second contribution is the new methodology for the categorization of the effects of GCM biases.

Regarding applied science, the present thesis contributes providing maps of effect categories of GCM biases, which can be a very useful tool for scientists planning climate change impacts' studies. Moreover, the contribution to applied research lies in the use of state-of-the art GCM data of the highest available spatial resolution to produce a detailed and multi-faceted assessment of the effects of high-end climate change on hydrological regime. Many different methodologies were combined to provide the assessment of impacts for mean and low state hydrological states and drought conditions. The output of the climate change impacts' study is important to policy makers at the inter-governmental level in order to plan relevant legislations and adaptation practices.

For the implementation of the routing algorithm, the methodologies described in this thesis and the processing of GCM data and JULES' outputs, an extensive number of coding scripts were produced in the MATLAB programming language. The total volume of data processed for the purposes of this thesis is close to nine T (a detailed description of the size of inputs and outputs of the JULES model is presented in Table 17). The JULES' simulations performed in the context of the present thesis correspond to around 6730 years in total, and were produced in a computational time of around 350 days.

Table 17. Size of input and output JULES' data used in the present thesis.

	Input	Output
Historical	1 T	128 GB
Europe Ensemble	32 GB	200 GB
Global Ensemble 1	908 GB	2.28 T
Global Ensemble 2	2.9 T	1.45 T
Total	~5 T	~4 T

6.3. Recommendations for future research

Future development of the JULES model, and of other similar models, should focus on the depiction of hydrological processes of the basin level. Firstly, parameterizations of regional scale processes (such as contributions from glaciers for mountainous basins) should be added in the models. Secondly, in order for the models to give simulations of higher spatial resolution, forcing data of respective higher resolution are also required.

Regarding the evaluation of the model, the development of a more complicated routing scheme and the integration of human impacts (such as dams and abstractions) in the JULES model are proposed as future research steps. The need for inclusion of more processes in the models highlights the scientific community's request for more data to be used for model evaluation and development, such as information on dams and abstractions, water management, agricultural and irrigated areas, etc.

The present study could be complemented by using more than one hydrological impact models for the assessment of both the effects of GCM biases and the effects of climate change on the hydrological regime. Multi-impact model assessments provide the opportunity to assess the uncertainty of the impact model component of the modelling chain.

Although a considerable number of GCMs was used in the present thesis, an extension of the used GCMs should be a goal for future assessments, as the uncertainty component due to the GCM choice is an important factor that defines the assessed climate change signal.

In future research, the assessment of climate change impacts should be accompanied by scenarios of changes in land use and agricultural practices. Finally, the next proposed research step after climate change impacts' studies is to study the effects of climate change adaptation and mitigation practices. Such studies are of particular importance for policy makers who need to assess the level of action needed to avoid adverse effects of climate change, and the possible synergies and trade-offs between adaptation and mitigation actions.

List of references

Alfieri, L., Burek, P., Feyen, L. and Forzieri, G.: Global warming increases the frequency of river floods in Europe, Hydrol. Earth Syst. Sci. Discuss., 12, 1119–1152, doi:doi:10.5194/hessd-12-1119-2015, 2015.

Arnell, N. W. and Gosling, S. N.: The impacts of climate change on river flow regimes at the global scale, J. Hydrol., 486, 351–364, doi:10.1016/j.jhydrol.2013.02.010, 2013.

Arnell, N. W. and Lloyd-Hughes, B.: The global-scale impacts of climate change on water resources and flooding under new climate and socio-economic scenarios, Clim. Change, 122(1–2), 127–140, doi:10.1007/s10584-013-0948-4, 2014.

Arnell, N. W., Lowe, J. A., Brown, S., Gosling, S. N., Gottschalk, P., Hinkel, J., Lloyd-Hughes, B., Nicholls, R. J., Osborn, T. J., Osborne, T. M., Rose, G. A., Smith, P. and Warren, R. F.: A global assessment of the effects of climate policy on the impacts of climate change, Nat. Clim. Chang., 3(5), 512–519, doi:10.1038/nclimate1793, 2013.

Best, M. J., Pryor, M., Clark, D. B., Rooney, G. G., Essery, R. L. H., Menard, C. B., Edwards, J. M., Hendry, M. a., Porson, A., Gedney, N., Mercado, L. M., Sitch, S., Blyth, E., Boucher, O., Cox, P. M., Grimmond, C. S. B. and Harding, R. J.: The Joint UK Land Environment Simulator (JULES), model description. Part 1: Energy and water fluxes, Geosci. Model Dev., 4(3), 677–699, doi:10.5194/gmd-4-677-2011, 2011.

Betts, R. A., Golding, N., Gonzalez, P., Gornall, J., Kahana, R., Kay, G., Mitchell, L. and Wiltshire, A.: Climate and land use change impacts on global terrestrial ecosystems and river flows in the HadGEM2-ES Earth System Model using the Representative Concentration Pathways, Biogeosciences Discuss., 10(4), 6171–6223, doi:10.5194/bg-12-1317-2015, 2015.

Blyth, E., Clark, D. B., Ellis, R., Huntingford, C., Los, S., Pryor, M., Best, M. and Sitch, S.: A comprehensive set of benchmark tests for a land surface model of simultaneous fluxes of water and carbon at both the global and seasonal scale, Geosci. Model Dev., 4(2), 255–269, doi:10.5194/gmd-4-255-2011, 2011a.

Blyth, E., Clark, D. B., Ellis, R., Huntingford, C., Los, S., Pryor, M., Best, M. and Sitch, S.: A

comprehensive set of benchmark tests for a land surface model of simultaneous fluxes of water and carbon at both the global and seasonal scale, Geosci. Model Dev., 4(2), 255–269, doi:10.5194/gmd-4-255-2011, 2011b.

Bonaccorso, B., Peres, D. J., Cancelliere, A. and Rossi, G.: Large Scale Probabilistic Drought Characterization Over Europe, Water Resour. Manag., 27(6), 1675–1692, doi:10.1007/s11269-012-0177-z, 2013.

Bowman, J.: The greenhouse effect, Land use policy, 7(2), 101–108, doi:10.1016/0264-8377(90)90002-G, 1990.

Brikowski, T. H.: Applying multi-parameter runoff elasticity to assess water availability in a changing climate: An example from Texas, USA, Hydrol. Process., 29(7), 1746–1756, doi:10.1002/hyp.10297, 2015.

Bromwich, D. H., Otieno, F. O., Hines, K. M., Manning, K. W. and Shilo, E.: Comprehensive evaluation of polar weather research and forecasting model performance in the Antarctic, J. Geophys. Res. Atmos., 118(2), 274–292, doi:10.1029/2012JD018139, 2013.

Brooks, R. H. and Corey, A. T.: Hydraulic properties of porous media and their relation to drainage design, Trans. ASAE, 7(1), 26–28, 1964.

Carrão, H., Naumann, G. and Barbosa, P.: Mapping global patterns of drought risk: An empirical framework based on sub-national estimates of hazard, exposure and vulnerability, Glob. Environ. Chang., 39, 108–124, doi:10.1016/j.gloenvcha.2016.04.012, 2016.

Chen, C., Haerter, J. O., Hagemann, S. and Piani, C.: On the contribution of statistical bias correction to the uncertainty in the projected hydrological cycle, Geophys. Res. Lett., 38(20), 1–6, doi:10.1029/2011GL049318, 2011.

Christensen, H. J. and Christensen, B. O.: A summary of the PRUDENCE model projections of changes in European climate by the end of this century, Clim. Res., 81, 7–30, doi:10.1007/s10584-006-9210-7, 2007.

Christensen, J. H., Boberg, F., Christensen, O. B. and Lucas-Picher, P.: On the need for bias

correction of regional climate change projections of temperature and precipitation, Geophys. Res. Lett., 35(20), L20709, doi:10.1029/2008GL035694, 2008.

Ciscar, J.-C., Feyen, L., Soria, A., Lavalle, C., Raes, F., Perry, M., Nemry, F., Demirel, H., Rozsai, M., Dosio, A. and others: Climate Impacts in Europe-The JRC PESETA II project, 2014.

Clark, D. B., Mercado, L. M., Sitch, S., Jones, C. D., Gedney, N., Best, M. J., Pryor, M., Rooney, G. G., Essery, R. L. H., Blyth, E., Boucher, O., Harding, R. J., Huntingford, C. and Cox, P. M.: The Joint UK Land Environment Simulator (JULES), model description – Part 2: Carbon fluxes and vegetation dynamics, Geosci. Model Dev., 4(3), 701–722, doi:10.5194/gmd-4-701-2011, 2011.

Collares-Pereira, M. J., Cowx, I. G., Ribeiro, F., Rodrigues, J. A. and Rogado, L.: Threats imposed by water resource development schemes on the conservation of endangered fish species in the Guadiana River basin in Portugal, Fish. Manag. Ecol., 7(1–2), 167–178, doi:10.1046/j.1365-2400.2000.00202.x, 2000.

Cox, P. ., Huntingford, C. and Harding, R. .: A canopy conductance and photosynthesis model for use in a GCM land surface scheme, J. Hydrol., 212–213, 79–94, doi:10.1016/S0022-1694(98)00203-0, 1998.

Cox, P. M.: Description of the " TRIFFID " Dynamic Global Vegetation Model, 2001.

Coxon, G., Freer, J., Westerberg, I. K., Wagener, T., Woods, R. and Smith, P. J.: A novel framework for discharge uncertainty quantification applied to 500 UK gauging stations, Water Resour. Res., 51(7), 5531–5546, doi:10.1002/2014WR016532, 2015.

Dai, A.: Drought under global warming: A review, Wiley Interdiscip. Rev. Clim. Chang., 2(1), 45–65, doi:10.1002/wcc.81, 2011.

Dankers, R., Arnell, N. W., Clark, D. B., Falloon, P. D., Fekete, B. M., Gosling, S. N., Heinke, J., Kim, H., Masaki, Y., Satoh, Y., Stacke, T., Wada, Y. and Wisser, D.: First look at changes in flood hazard in the Inter-Sectoral Impact Model Intercomparison Project ensemble., Proc. Natl. Acad. Sci. U. S. A., 1–5, doi:10.1073/pnas.1302078110, 2013.

Demory, M. E., Vidale, P. L., Roberts, M. J., Berrisford, P., Strachan, J., Schiemann, R. and

Mizielinski, M. S.: The role of horizontal resolution in simulating drivers of the global hydrological cycle, Clim. Dyn., 42(7–8), 2201–2225, doi:10.1007/s00382-013-1924-4, 2014.

Denman, K. L., Brasseur, G. P., Chidthaisong, A., Ciais, P., Cox, P. M., Dickinson, R. E., Hauglustaine, D. A., Heinze, C., Holland, E. A., Jacob, D. J. and others: Couplings between changes in the climate system and biogeochemistry, in Climate change 2007: The physical science basis, Cambridge University Press., 2007.

Dirmeyer, P. A.: A History and Review of the Global Soil Wetness Project (GSWP), J. Hydrometeorol., 12(5), 729–749, doi:10.1175/JHM-D-10-05010.1, 2011.

Dirmeyer, P. A., Gao, X., Zhao, M., Guo, Z., Oki, T. and Hanasaki, N.: GSWP-2 Multimodel Analysis and Implications for Our Perception of the Land Surface, , (OCTOBER), 1381–1397, doi:10.1175/BAMS-87-10-1381, 2006.

Döll, P. and Schmied, H. M.: How is the impact of climate change on river flow regimes related to the impact on mean annual runoff? A global-scale analysis, Environ. Res. Lett., 7(1), 14037, doi:10.1088/1748-9326/7/1/014037, 2012.

Dubrovsky, M., Svoboda, M. D., Trnka, M., Hayes, M. J., Wilhite, D. A., Zalud, Z. and Hlavinka, P.: Application of relative drought indices in assessing climate-change impacts on drought conditions in Czechia, Theor. Appl. Climatol., 96(1–2), 155–171, doi:10.1007/s00704-008-0020-x, 2009.

Ehret, U., Zehe, E., Wulfmeyer, V., Warrach-Sagi, K. and Liebert, J.: HESS Opinions "should we apply bias correction to global and regional climate model data?," Hydrol. Earth Syst. Sci., 16(9), 3391–3404, doi:10.5194/hess-16-3391-2012, 2012.

Elsner, M. M., Gangopadhyay, S., Pruitt, T., Brekke, L. D., Mizukami, N., Clark, M. P., Elsner, M. M., Gangopadhyay, S., Pruitt, T., Brekke, L. D., Mizukami, N. and Clark, M. P.: How Does the Choice of Distributed Meteorological Data Affect Hydrologic Model Calibration and Streamflow Simulations?, J. Hydrometeorol., 15(4), 1384–1403, doi:10.1175/JHM-D-13-083.1, 2014.

Fekete, B. and Vorosmarty, C. J.: ISLSCP II UNH/GRDC Composite Monthly Runoff, ISLSCP Initiat. II Collect. Ed. by Hall, FG, Collat. G., Meeson, B., Los, S., Brown Colstoun, E., Landis, D.,

Data set, available http//daac. ornl. go v/, from Oak Ridge Natl. Lab. Distrib. Act. Arch. Center, Oak Ridg, 10, 2011.

Filipe, A. F., Cowx, I. G. and Collares-Pereira, M. J.: Spatial modelling of freshwater fish in semi-arid river systems: A tool for conservation, River Res. Appl., 18(2), 123–136, doi:10.1002/rra.638, 2002.

Fischer, E. M. and Knutti, R.: Anthropogenic contribution to global occurrence of heavy-precipitation and high-temperature extremes, Nat. Clim. Chang., (April), 1–6, doi:10.1038/nclimate2617, 2015.

Fleig, A. K., Tallaksen, L. M., Hisdal, H. and Demuth, S.: Sciences A global evaluation of streamflow drought characteristics, , (2002), 535–552, 2006.

Forzieri, G., Feyen, L., Rojas, R., Flörke, M., Wimmer, F. and Bianchi, a.: Ensemble projections of future streamflow droughts in Europe, Hydrol. Earth Syst. Sci., 18(1), 85–108, doi:10.5194/hess-18-85-2014, 2014.

Fu, G., Charles, S. P. and Chiew, F. H. S.: A two-parameter climate elasticity of streamflow index to assess climate change effects on annual streamflow, Water Resour. Res., 43(11), 1–12, doi:10.1029/2007WR005890, 2007.

Fung, F., Lopez, A. and New, M.: Water availability in +2°C and +4°C worlds., Philos. Trans. A. Math. Phys. Eng. Sci., 369(1934), 99–116, doi:10.1098/rsta.2010.0293, 2011.

Van Genuchten, M. T.: A closed-form equation for predicting the hydraulic conductivity of unsaturated soils, Soil Sci. Soc. Am. J., 44(5), 892–898, 1980.

Giorgi, F. and Bi, X.: Updated regional precipitation and temperature changes for the 21st century from ensembles of recent AOGCM simulations, Geophys. Res. Lett., 32(21), L21715, doi:10.1029/2005GL024288, 2005.

Giuntoli, I., Vidal, J., Prudhomme, C. and Hannah, D. M.: Future hydrological extremes : the uncertainty from multiple global climate and global hydrological models, Earth Syst. Dyn., 1–30, doi:10.5194/esdd-6-1-2015, 2015.

Goose, H., Barriat, P. Y., Lefebvre, W., Loutre, M. F. and Zunz, V.: Introduction to climate dynamics and climate modelling. [online] Available from: http://www.climate.be/textbook, 2010.

Gosling, S. N. and Arnell, N. W.: A global assessment of the impact of climate change on water scarcity, Clim. Change, doi:10.1007/s10584-013-0853-x, 2013.

Grillakis, M. G., Koutroulis, A. G. and Tsanis, I. K.: Multisegment statistical bias correction of daily GCM precipitation output, J. Geophys. Res. Atmos., 118(8), 3150–3162, doi:10.1002/jgrd.50323, 2013.

Gudmundsson, L. and Seneviratne, S. I.: Towards observation-based gridded runoff estimates for Europe, , 2859–2879, doi:10.5194/hess-19-2859-2015, 2015.

Gudmundsson, L., Tallaksen, L. M., Stahl, K., Clark, D. B., Dumont, E., Hagemann, S., Bertrand, N., Gerten, D., Heinke, J., Hanasaki, N., Voss, F. and Koirala, S.: Comparing large-scale hydrological model simulations to observed runoff percentiles in Europe, J. Hydrometeorol., 13, doi:10.1175/JHM-D-11-083.1, 2012a.

Gudmundsson, L., Tallaksen, L. M., Stahl, K., Clark, D. B., Dumont, E., Hagemann, S., Bertrand, N., Gerten, D., Heinke, J., Hanasaki, N., Voss, F. and Koirala, S.: Comparing Large-Scale Hydrological Model Simulations to Observed Runoff Percentiles in Europe, J. Hydrometeorol., 13(2), 604–620, doi:10.1175/JHM-D-11-083.1, 2012b.

Gudmundsson, L., Wagener, T., Tallaksen, L. M. and Engeland, K.: Evaluation of nine large-scale hydrological models with respect to the seasonal runoff climatology in Europe, , 48(October), 1–20, doi:10.1029/2011WR010911, 2012c.

Haddeland, I., Clark, D. B., Franssen, W., Ludwig, F., Voß, F., Arnell, N. W., Bertrand, N., Best, M., Folwell, S., Gerten, D., Gomes, S., Gosling, S. N., Hagemann, S., Hanasaki, N., Harding, R., Heinke, J., Kabat, P., Koirala, S., Oki, T., Polcher, J., Stacke, T., Viterbo, P., Weedon, G. P. and Yeh, P.: Multimodel Estimate of the Global Terrestrial Water Balance: Setup and First Results, J. Hydrometeorol., 12(5), 869–884, doi:10.1175/2011JHM1324.1, 2011.

Haddeland, I., Heinke, J., Voß, F., Eisner, S., Chen, C., Hagemann, S. and Ludwig, F.: Effects of climate model radiation, humidity and wind estimates on hydrological simulations, Hydrol. Earth

Syst. Sci., 16(2), 305–318, doi:10.5194/hess-16-305-2012, 2012.

Hagemann, S., Chen, C., Haerter, J. O., Heinke, J., Gerten, D. and Piani, C.: Impact of a Statistical Bias Correction on the Projected Hydrological Changes Obtained from Three GCMs and Two Hydrology Models, J. Hydrometeorol., 12(4), 556–578, doi:10.1175/2011JHM1336.1, 2011a.

Hagemann, S., Chen, C., Haerter, J. O., Heinke, J., Gerten, D. and Piani, C.: Impact of a Statistical Bias Correction on the Projected Hydrological Changes Obtained from Three GCMs and Two Hydrology Models, J. Hydrometeorol., 12(4), 556–578, doi:10.1175/2011JHM1336.1, 2011b.

Hagemann, S., Chen, C., Clark, D. B., Folwell, S., Gosling, S. N., Haddeland, I., Hanasaki, N., Heinke, J., Ludwig, F., Voss, F. and Wiltshire, A. J.: Climate change impact on available water resources obtained using multiple global climate and hydrology models, Earth Syst. Dyn., 4(1), 129–144, doi:10.5194/esd-4-129-2013, 2013.

Hanasaki, N., Inuzuka, T., Kanae, S. and Oki, T.: An estimation of global virtual water flow and sources of water withdrawal for major crops and livestock products using a global hydrological model, J. Hydrol., 384(3–4), 232–244, doi:10.1016/j.jhydrol.2009.09.028, 2010.

Hansen, J. W., Challinor, A., Ines, A. V. M., Wheeler, T. and Moron, V.: Translating climate forecasts into agricultural terms: advances and challenges, Clim. Res., 33(1), 27–41, 2006.

Harding, R. J., Weedon, G. P., van Lanen, H. a. J. and Clark, D. B.: The future for Global Water Assessment, J. Hydrol., 518, 186–193, doi:10.1016/j.jhydrol.2014.05.014, 2014.

Haslinger, K., Anders, I. and Hofstätter, M.: Regional climate modelling over complex terrain: an evaluation study of COSMO-CLM hindcast model runs for the Greater Alpine Region, Clim. Dyn., 40(1–2), 511–529, doi:10.1007/s00382-012-1452-7, 2013.

Hattermann, F., Krysanova, V., Gosling, S. N., Dankers, R., Daggupati, P., Donnelly, C., Flörke, M., Huang, S., Motovilov, Y., Buda, S., Yang, T., Muller, C., Leng, G., Tang, Q., Portmann, F. T., Hagemann, S., Gerten, D., Wada, Y., Masaki, Y., Alemayehu, T., Satoh, Y. and Samaniego, L.: Cross-scale intercomparison of climate change impacts simulated by regional and global hydrological models in eleven large river basins, Clim. Change, 141(3), 561–576, doi:10.1007/s10584-016-1829-4, 2017.

Haylock, M. R., Hofstra, N., Klein Tank, A. M. G., Klok, E. J., Jones, P. D. and New, M.: A European daily high-resolution gridded data set of surface temperature and precipitation for 1950-2006, J. Geophys. Res. Atmos., 113(20), D20119, doi:10.1029/2008JD010201, 2008.

Hempel, S., Frieler, K., Warszawski, L., Schewe, J. and Piontek, F.: A trend-preserving bias correction – the ISI-MIP approach, Earth Syst. Dyn., 4, 219–236, doi:10.5194/esd-4-219-2013, 2013.

van Huijgevoort, M. H. J., Hazenberg, P., van Lanen, H. a. J., Teuling, a. J., Clark, D. B., Folwell, S., Gosling, S. N., Hanasaki, N., Heinke, J., Koirala, S., Stacke, T., Voss, F., Sheffield, J. and Uijlenhoet, R.: Global Multimodel Analysis of Drought in Runoff for the Second Half of the Twentieth Century, J. Hydrometeorol., 14(5), 1535–1552, doi:10.1175/JHM-D-12-0186.1, 2013.

Jacob, D., Petersen, J., Eggert, B., Alias, A., Christensen, O. B., Bouwer, L. M., Braun, A., Colette, A., Déqué, M., Georgievski, G., Georgopoulou, E., Gobiet, A., Menut, L., Nikulin, G., Haensler, A., Hempelmann, N., Jones, C., Keuler, K., Kovats, S., Kröner, N., Kotlarski, S., Kriegsmann, A., Martin, E., van Meijgaard, E., Moseley, C., Pfeifer, S., Preuschmann, S., Radermacher, C., Radtke, K., Rechid, D., Rounsevell, M., Samuelsson, P., Somot, S., Soussana, J. F., Teichmann, C., Valentini, R., Vautard, R., Weber, B. and Yiou, P.: EURO-CORDEX: New high-resolution climate change projections for European impact research, Reg. Environ. Chang., 14(2), 563–578, doi:10.1007/s10113-013-0499-2, 2014.

Jain, P. C.: Greenhouse effect and climate change: scientific basis and overview, Renew. Energy, 3(4–5), 403–420, doi:10.1016/0960-1481(93)90108-S, 1993.

Katzav, J. and Parker, W. S.: The future of climate modeling, Clim. Change, 132(4), 475–487, doi:10.1007/s10584-015-1435-x, 2015.

Koirala, S., Hirabayashi, Y., Mahendran, R. and Kanae, S.: Global assessment of agreement among streamflow projections using CMIP5 model outputs, Environ. Res. Lett., 9(6), 64017, doi:10.1088/1748-9326/9/6/064017, 2014.

Koutroulis, A. G., Grillakis, M. G., Tsanis, I. K. and Papadimitriou, L.: Evaluation of precipitation and temperature simulation performance of the CMIP3 and CMIP5 historical experiments, Clim.

Dyn., 47(5–6), 1881–1898, doi:10.1007/s00382-015-2938-x, 2016.

Laizé, C. L. R., Acreman, M. C., Schneider, C., Dunbar, M. J., Houghton-Carr, H. A., Florke, M. and Hannah, D. M.: Projected flow alteration and ecological risk for pan-european rivers, River Res. Appl., 2013.

Li, H., Sheffield, J. and Wood, E. F.: Bias correction of monthly precipitation and temperature fields from Intergovernmental Panel on Climate Change AR4 models using equidistant quantile matching, J. Geophys. Res., 115(D10), D10101, doi:10.1029/2009JD012882, 2010.

Liu, M., Rajagopalan, K., Chung, S. H., Jiang, X., Harrison, J., Nergui, T., Guenther, a., Miller, C., Reyes, J., Tague, C., Choate, J., Salathé, E. P., Stöckle, C. O. and Adam, J. C.: What is the importance of climate model bias when projecting the impacts of climate change on land surface processes?, Biogeosciences, 11(10), 2601–2622, doi:10.5194/bg-11-2601-2014, 2014.

Lorenzo-Lacruz, J., Vicente-Serrano, S. M., López-Moreno, J. I., Beguería, S., García-Ruiz, J. M. and Cuadrat, J. M.: The impact of droughts and water management on various hydrological systems in the headwaters of the Tagus River (central Spain), J. Hydrol., 386(1), 13–26, doi:10.1016/j.jhydrol.2010.01.001, 2010.

MacKellar, N. C., Dadson, S. J., New, M. and Wolski, P.: Evaluation of the JULES land surface model in simulating catchment hydrology in Southern Africa, Hydrol. Earth Syst. Sci. Discuss., 10(8), 11093–11128, doi:10.5194/hessd-10-11093-2013, 2013.

Maraun, D.: Nonstationarities of regional climate model biases in European seasonal mean temperature and precipitation sums, Geophys. Res. Lett., 39(6), L06706, doi:10.1029/2012GL051210, 2012.

Masaki, Y., Hanasaki, N., Takahashi, K. and Hijioka, Y.: Propagation of biases in humidity in the estimation of global irrigation water, Earth Syst. Dynam, 6, 461–484, doi:10.5194/esd-6-461-2015, 2015.

Mckee, T. B., Doesken, N. J. and Kleist, J.: The relationship of drought frequency and duration to time scales, AMS 8th Conf. Appl. Climatol., (January), 179–184, doi:citeulike-article-id:10490403, 1993.

Miao, C., Su, L., Sun, Q. and Duan, Q.: A nonstationary bias-correction technique to remove bias in GCM simulations, J. Geophys. Res. Atmos., 121, 5718–5735, doi:10.1002/2015JD024159, 2016.

Mishra, A. K. and Singh, V. P.: Drought modeling - A review, J. Hydrol., 403(1–2), 157–175, doi:10.1016/j.jhydrol.2011.03.049, 2011.

Mizukami, N., Clark, M. P., Slater, A. G., Brekke, L. D., Elsner, M. M., Arnold, J. R. and Gangopadhyay, S.: Hydrologic Implications of Different Large-Scale Meteorological Model Forcing Datasets in Mountainous Regions, J. Hydrometeorol., 15(1), 474–488, doi:10.1175/JHM-D-13-036.1, 2014.

Muerth, M. J., Gauvin St-Denis, B., Ricard, S., Velázquez, J. a., Schmid, J., Minville, M., Caya, D., Chaumont, D., Ludwig, R. and Turcotte, R.: On the need for bias correction in regional climate scenarios to assess climate change impacts on river runoff, Hydrol. Earth Syst. Sci., 17(3), 1189–1204, doi:10.5194/hess-17-1189-2013, 2013.

Müller Schmied, H., Eisner, S., Franz, D., Wattenbach, M., Portmann, F. T., Flörke, M. and Döll, P.: Sensitivity of simulated global-scale freshwater fluxes and storages to input data, hydrological model structure, human water use and calibration, Hydrol. Earth Syst. Sci., 18(9), 3511–3538, doi:10.5194/hess-18-3511-2014, 2014.

Oki, T. and Sud, Y. C.: Design of Total Runoff Integrating Pathways (TRIP)— A Global River Channel Network, , 2(1), 7–22, 1998.

Parry, S., Hannaford, J., Lloyd-Hughes, B. and Prudhomme, C.: Multi-year droughts in Europe: analysis of development and causes, Hydrol. Res., 43(5), 689–706, 2012.

Photiadou, C., van den Hurk, B., van Delden, A. and Weerts, A.: Incorporating circulation statistics in bias correction of GCM ensembles: hydrological application for the Rhine basin, Clim. Dyn., 46(1–2), 187–203, doi:10.1007/s00382-015-2578-1, 2016.

Piani, C., Weedon, G. P., Best, M., Gomes, S. M., Viterbo, P., Hagemann, S. and Haerter, J. O.: Statistical bias correction of global simulated daily precipitation and temperature for the application of hydrological models, J. Hydrol., 395(3), 199–215, doi:10.1016/j.jhydrol.2010.10.024, 2010.

Pires, A., Cowx, I. and Coelho, M.: Seasonal changes in fish community structure of intermittent streams in the middle reaches of the Guadiana basin, Portugal, J. Fish Biol., 54, 235–249, doi:10.1006/jfbi.1998.0860, 1999.

Prudhomme, C., Parry, S., Hannaford, J., Clark, D. B., Hagemann, S. and Voss, F.: How Well Do Large-Scale Models Reproduce Regional Hydrological Extremes in Europe?, J. Hydrometeorol., 12(6), 1181–1204, doi:10.1175/2011JHM1387.1, 2011.

Prudhomme, C., Giuntoli, I., Robinson, E. L., Clark, D. B., Arnell, N. W., Dankers, R., Fekete, B. M., Franssen, W., Gerten, D., Gosling, S. N., Hagemann, S., Hannah, D. M., Kim, H., Masaki, Y., Satoh, Y., Stacke, T., Wada, Y. and Wisser, D.: Hydrological droughts in the 21st century, hotspots and uncertainties from a global multimodel ensemble experiment., Proc. Natl. Acad. Sci. U. S. A., 111(9), 3262–7, doi:10.1073/pnas.1222473110, 2014.

Pryor, M., Clark, D., Harris, P. and Hendry, M.: Joint UK Land Environment Simulator (JULES) Version 3.2 User Manual, 2012.

Randall, D. A., Wood, R. A., Bony, S., Colman, R., Fichefet, T., Fyfe, J., Kattsov, V., Pitman, A., Shukla, J., Srinivasan, J., Stouffer, R. J., Sumi, A. and Tayler, K. E.: Climate Models and Their Evaluation, Clim. Chang. 2007 Phys. Sci. Basis. S. Solomon al., Eds., Cambridge Univ. Press, 589–662, 2007.

Renner, M., Seppelt, R. and Bernhofer, C.: Evaluation of water-energy balance frameworks to predict the sensitivity of streamflow to climate change, Hydrol. Earth Syst. Sci., 16(5), 1419–1433, doi:10.5194/hess-16-1419-2012, 2012.

Ridgwell, A. and Valdes, P. J.: Climate and climate change., Curr. Biol., 19(14), R563-6, doi:10.1016/j.cub.2009.05.014, 2009.

Rojas, R., Feyen, L., Dosio, A. and Bavera, D.: Improving pan-European hydrological simulation of extreme events through statistical bias correction of RCM-driven climate simulations, Hydrol. Earth Syst. Sci., 15(8), 2599–2620, doi:10.5194/hess-15-2599-2011, 2011.

Sankarasubramanian, A. and Vogel, R. M.: Hydroclimatology of the continental United States, Geophys. Res. Lett., 30(7), 1–4, doi:10.1029/2002GL015937, 2003.

Schewe, J., Heinke, J., Gerten, D., Haddeland, I., Arnell, N. W., Clark, D. B., Dankers, R., Eisner, S., Fekete, B. M., Colón-González, F. J., Gosling, S. N., Kim, H., Liu, X., Masaki, Y., Portmann, F. T., Satoh, Y., Stacke, T., Tang, Q., Wada, Y., Wisser, D., Albrecht, T., Frieler, K., Piontek, F., Warszawski, L. and Kabat, P.: Multimodel assessment of water scarcity under climate change., Proc. Natl. Acad. Sci. U. S. A., 111(9), 3245–3250, doi:10.1073/pnas.1222460110, 2014.

Schneider, C., Laizé, C. L. R., Acreman, M. C. and Flörke, M.: How will climate change modify river flow regimes in Europe?, Hydrol. Earth Syst. Sci., 17(1), 325–339, doi:10.5194/hess-17-325-2013, 2013.

Sharma, D., Das Gupta, a. and Babel, M. S.: Spatial disaggregation of bias-corrected GCM precipitation for improved hydrologic simulation: Ping River Basin, Thailand, Hydrol. Earth Syst. Sci. Discuss., 4(1), 35–74, doi:10.5194/hessd-4-35-2007, 2007.

Sheffield, J., Goteti, G. and Wood, E. F.: Development of a 50-Year High-Resolution Global Dataset of Meteorological Forcings for Land Surface Modeling, , 3088–3111, 2006.

Shukla, S. and Wood, A. W.: Use of a standardized runoff index for characterizing hydrologic drought, Geophys. Res. Lett., 35(2), L02405, doi:10.1029/2007GL032487, 2008.

Solman, S. A., Sanchez, E., Samuelsson, P., da Rocha, R. P., Li, L., Marengo, J., Pessacg, N. L., Remedio, A. R. C., Chou, S. C., Berbery, H., Le Treut, H., de Castro, M. and Jacob, D.: Evaluation of an ensemble of regional climate model simulations over South America driven by the ERA-Interim reanalysis: model performance and uncertainties, Clim. Dyn., 41(5–6), 1139–1157, doi:10.1007/s00382-013-1667-2, 2013.

Sung, J. H. and Chung, E.-S.: Development of streamflow drought severity&ndash;duration&ndash;frequency curves using the threshold level method, Hydrol. Earth Syst. Sci., 18(9), 3341–3351, doi:10.5194/hess-18-3341-2014, 2014.

Tallaksen, L., Madsen, H. and Clausen, B.: On the definition and modelling of streamflow drought duration and deficit volume, Hydrol. Sci. J., 42(1), 15–33, doi:10.1080/02626669709492003, 1997.

Taylor, K. E., Stouffer, R. J. and Meehl, G. A.: An Overview of CMIP5 and the Experiment Design, Bull. Am. Meteorol. Soc., 93(4), 485–498, doi:10.1175/BAMS-D-11-00094.1, 2012.

Teng, J., Potter, N. J., Chiew, F. H. S., Zhang, L., Wang, B., Vaze, J. and Evans, J. P.: How does bias correction of regional climate model precipitation affect modelled runoff?, Hydrol. Earth Syst. Sci., 19(2), 711–728, doi:10.5194/hess-19-711-2015, 2015.

Teutschbein, C. and Seibert, J.: Bias correction of regional climate model simulations for hydrological climate-change impact studies: Review and evaluation of different methods, J. Hydrol., 456–457, 12–29, doi:10.1016/j.jhydrol.2012.05.052, 2012.

Trenberth, K. E., Smith, L., Qian, T., Dai, A. and Fasullo, J.: Estimates of the Global Water Budget and Its Annual Cycle Using Observational and Model Data, J. Hydrometeorol., 8(4), 758–769, doi:10.1175/JHM600.1, 2007.

Trenberth, K. E., Fasullo, J. T. and Kiehl, J.: Earth's global energy budget, Bull. Am. Meteorol. Soc., 90(3), 311–323, doi:10.1175/2008BAMS2634.1, 2009.

Uppala, S. M., KÅllberg, P. W., Simmons, A. J., Andrae, U., Bechtold, V. D. C., Fiorino, M., Gibson, J. K., Haseler, J., Hernandez, A., Kelly, G. A., Li, X., Onogi, K., Saarinen, S., Sokka, N., Allan, R. P., Andersson, E., Arpe, K., Balmaseda, M. A., Beljaars, A. C. M., Berg, L. Van De, Bidlot, J., Bormann, N., Caires, S., Chevallier, F., Dethof, A., Dragosavac, M., Fisher, M., Fuentes, M., Hagemann, S., Hólm, E., Hoskins, B. J., Isaksen, L., Janssen, P. A. E. M., Jenne, R., Mcnally, A. P., Mahfouf, J. -F., Morcrette, J. -J., Rayner, N. A., Saunders, R. W., Simon, P., Sterl, A., Trenberth, K. E., Untch, A., Vasiljevic, D., Viterbo, P. and Woollen, J.: The ERA-40 re-analysis, Q. J. R. Meteorol. Soc., 131(612), 2961–3012, doi:10.1256/QJ.04.176, 2005.

Vano, J. A., Das, T. and Lettenmaier, D. P.: Hydrologic Sensitivities of Colorado River Runoff to Changes in Precipitation and Temperature, J. Hydrometeorol., 13(3), 932–949, doi:10.1175/JHM-D-11-069.1, 2012.

Vautard, R., Gobiet, A., Jacob, D., Belda, M., Colette, A., Déqué, M., Fernández, J., García-Díez, M., Goergen, K., Güttler, I., Halenka, T., Karacostas, T., Katragkou, E., Keuler, K., Kotlarski, S., Mayer, S., van Meijgaard, E., Nikulin, G., Patarčić, M., Scinocca, J., Sobolowski, S., Suklitsch, M., Teichmann, C., Warrach-Sagi, K., Wulfmeyer, V. and Yiou, P.: The simulation of European heat waves from an ensemble of regional climate models within the EURO-CORDEX project, Clim. Dyn., 41(9–10), 2555–2575, doi:10.1007/s00382-013-1714-z, 2013.

169

Vicente-Serrano, S. M., Lopez-Moreno, J.-I., Beguería, S., Lorenzo-Lacruz, J., Sanchez-Lorenzo, A., García-Ruiz, J. M., Azorin-Molina, C., Morán-Tejeda, E., Revuelto, J., Trigo, R., Coelho, F. and Espejo, F.: Evidence of increasing drought severity caused by temperature rise in southern Europe, Environ. Res. Lett., 9(4), 44001, doi:10.1088/1748-9326/9/4/044001, 2014.

Van Vliet, M. T. H., Franssen, W. H. P., Yearsley, J. R., Ludwig, F., Haddeland, I., Lettenmaier, D. P. and Kabat, P.: Global river discharge and water temperature under climate change, Glob. Environ. Chang., 23(2), 450–464, doi:10.1016/j.gloenvcha.2012.11.002, 2013.

Vrochidou, a. E. K., Tsanis, I. K., Grillakis, M. G. and Koutroulis, a. G.: The impact of climate change on hydrometeorological droughts at a basin scale, J. Hydrol., 476, 290–301, doi:10.1016/j.jhydrol.2012.10.046, 2013.

van Vuuren, D. P., Edmonds, J., Kainuma, M., Riahi, K., Thomson, A., Hibbard, K., Hurtt, G. C., Kram, T., Krey, V., Lamarque, J. F., Masui, T., Meinshausen, M., Nakicenovic, N., Smith, S. J. and Rose, S. K.: The representative concentration pathways: An overview, Clim. Change, 109(1), 5–31, doi:10.1007/s10584-011-0148-z, 2011.

Wanders, N. and Van Lanen, H. a. J.: Future discharge drought across climate regions around the world modelled with a synthetic hydrological modelling approach forced by three general circulation models, Nat. Hazards Earth Syst. Sci., 15(3), 487–504, doi:10.5194/nhess-15-487-2015, 2015.

Wanders, N., Wada, Y. and Van Lanen, H. A. J.: Global hydrological droughts in the 21st century under a changing hydrological regime, Earth Syst. Dyn., 6(1), 1–15, doi:10.5194/esd-6-1-2015, 2015.

Weedon, G., P., Balsamo, G., Bellouin, N., Gomes, S., Best, M. J. and Viterbo, P.: The WFDEI meteorological forcing data set: WATCH Forcing Data methodology applied to ERA-Interim reanalysis data, Water Resour. Res., 50((9)), 7505–7514, doi:10.1002/2014WR015638.Received, 2014.

Weedon, G. P., Gomes, S., Viterbo, P., Österle, H., Adam, J. C., Bellouin, N., Boucher, O. and Best, M.: The WATCH forcing data 1958--2001: A meteorological forcing dataset for land surface

and hydrological models, Watch. Ed. Watch Tech. Rep., 22, 2010.

Weedon, G. P., Prudhomme, C., Crooks, S., Ellis, R. J., Folwell, S. S. and Best, M. J.: Evaluating the Performance of Hydrological Models via Cross-Spectral Analysis: Case Study of the Thames Basin, United Kingdom, J. Hydrometeorol., 16(1), 214–231, doi:10.1175/JHM-D-14-0021.1, 2015.

Yang, H. and Yang, D.: Derivation of climate elasticity of runoff to assess the effects of climate change on annual runoff, Water Resour. Res., 47(7), 1–12, doi:10.1029/2010WR009287, 2011.

Zulkafli, Z., Buytaert, W., Onof, C., Lavado, W. and Guyot, J.-L.: A critical assessment of the JULES land surface model hydrology for humid tropical environments, Hydrol. Earth Syst. Sci., 17(3), 1113–1132, 2013.

Appendix A

Definition of symbols

Symbol	Units	Definition
A	mol CO_2 m^{-2} s^{-1}	Net photosynthesis uptake
A_m	kg m^{-2}	Puddling of water on soil surface and interception by leafless vegetation
B_L	kg C m^{-2}	Leaf biomass
B_m	kg C m^{-2}	Rate of change of water holding capacity with leaf area index
B_w	kg C m^{-2}	Woody biomass
C	kg m^{-2}	Canopy water
C_c	Pa	Leaf surface carbon dioxide concentration
C_i	Pa	Internal leaf carbon dioxide concentration
C_L	J kg^{-1} K^{-1}	Specific heat capacity of leaves
C_m	kg m^{-2}	Vegetation canopy water holding capacity
C_s	J m^{-2} K^{-1}	Areal heat capacity associated with the surface material
c_p	J kg^{-1} K^{-1}	Specific heat capacity of air
C_w	J kg^{-1} K^{-1}	Specific heat capacity of wood
C_{water}	J kg^{-1} K^{-1}	Specific heat capacity of water
C_a	J m^{-3} K^{-1}	Volumetric heat capacity of the soil
d_r	m	Root depth
d_s	m	Snow depth
D_f	m^2 s^{-1}	Diffusivity of water vapour in air
E	Kg m^{-2} s^{-1}	Turbulent moisture flux
ET	kg m^{-2} s^{-1}	Evapotranspiration rate
G	W m^{-2}	Surface/Soil heat flux
G_{in}	kg m^{-2} s^{-1}	Groundwater inflow
G_{out}	kg m^{-2} s^{-1}	Groundwater outflow
g_s	m s^{-1}	Leaf level stomatal conductance
g_{soil}	m s^{-1}	Bare soil surface conductance
H_s	W m^{-2}	Sensible heat flux
$H_{sat}(T)$	kg kg^{-1}	Saturated specific humidity at the temperature T
H_1	kg kg^{-1}	Specific humidity at the reference atmospheric level
I	kg m^{-2}	Intercepted snow load
I_{max}	m^{-2}	Snow interception canopy capacity
J	W m^{-3}	Vertical advective flux for soil moisture
K	kg m^{-2} s^{-1}	Surface infiltration rate
K_h	m s^{-1}	Hydraulic conductivity
K_{hs}	m s^{-1}	Hydraulic conductivity for saturated soil
L	m^2 m^{-2}	Leaf area index
L_c	J kg^{-1}	Latent heat of condensation of water at 0 °C
$L_{w\downarrow}$	W m^{-2}	Downward longwave radiation
$L_{w\uparrow}$	W m^{-2}	Upward longwave radiation
P	kg m^{-2} s^{-1}	Precipitation rate

Ps	Pa	Surface air pressure
Q	kg m^{-2} s^{-1}	Discharge rate
r	μm	Snow grain size
r_a	s m^{-1}	Aerodynamic resistance
$r_{a_{can}}$	s m^{-1}	Aerodynamic resistance between the surface canopy of vegetation and the underlying soil
r_k	-	Fraction of roots in the k-th soil layer
r_s	s m^{-1}	Stomatal or surface moisture resistance
R_n	W m^{-2}	Net radiation
RF	kg m^{-2} s^{-1}	Total runoff
RF_s	kg m^{-2} s^{-1}	Surface runoff
S_m	kg m^{-2} s^{-2}	Snowmelt
$S_{w\downarrow}$	W m^{-2}	Downward shortwave radiation
T_A	K	Reference level atmospheric temperature
T_F	kg m^{-2} s^{-1}	Throughfall rate
T_s	K	Soil temperature
T_{s1}	K	Temperature of the first soil level
T_{sk}	K	Temperature of the k-th soil level
T_*	K	Surface temperature
W	m s^{-1}	Atmospheric wind speed
W_0	kg m^{-2} s^{-1}	Infiltration rate into the soil
W'	kg m^{-2} s^{-1}	Vertical flux of soil water
a	-	Surface albedo
β	-	Soil moisture factor
ΔS	kg m^{-2} s^{-1}	Change in storage in a basin
Δz_i	m	Thickness of the i-th soil layer
ϵ	-	Surface emissivity
$\in_r$	-	Fraction of gridcell occupied by convective precipitation
ϵ_s	-	Emissivity of the underlying soil surface
θ	m^3 m^{-3}	Soil moisture concentration
θ_1	m^3 m^{-3}	Soil moisture concentration in the top soil layer
θ_c	m^3 m^{-3}	Soil moisture concentration at critical point
λ	W m^{-1} K^{-1}	Thermal conductivity
λE	W m^{-2}	Latent heat flux
λ_{snow}	W m^{-1} K^{-1}	Thermal conductivity of the snow
λ_{soil}	W m^{-1} K^{-1}	Thermal conductivity of the soil
v_j	-	Fraction of gridbox covered by surface type j
ρ	Kg m^{-3}	Density of air
ρ_i	kg m^{-3}	Density of ice
σ	W m^{-2} K^{-4}	Stefan Boltzmann constant
Ψ	m	Soil water suction

Appendix B

Supplementary information and results
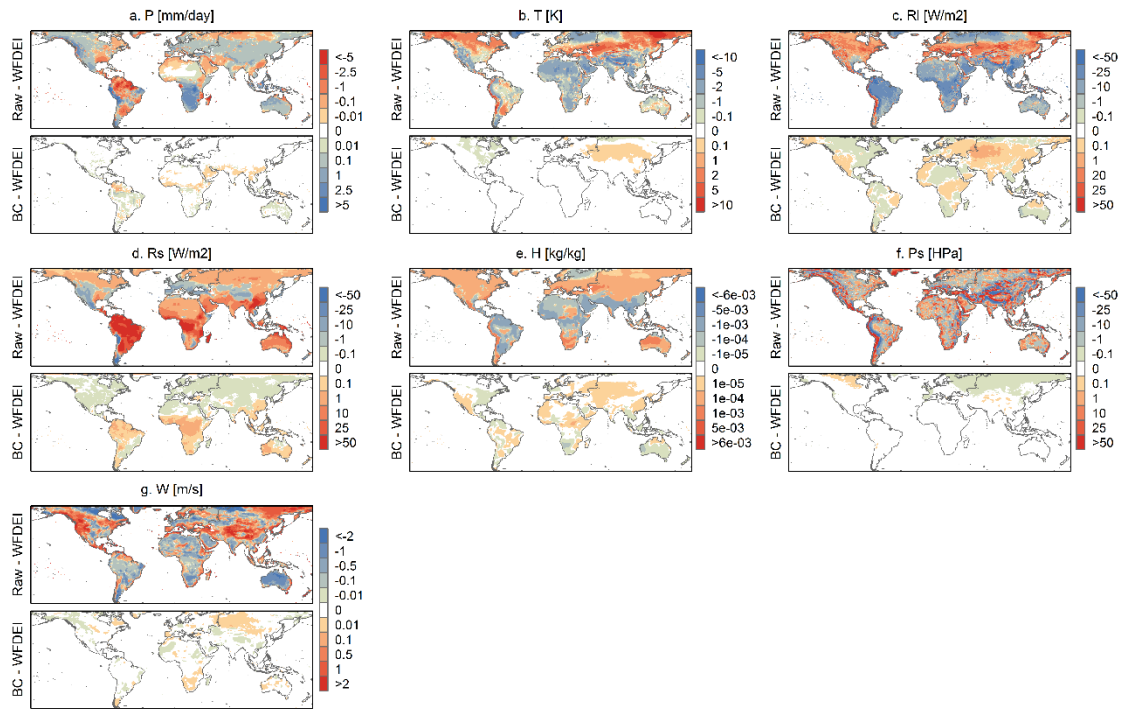
Figure B 1. Difference maps, showing initial (Raw-WFDEI) and remaining (BC-WFDEI) biases of the GCM ensemble forcing variables: a.Precipitation, b.Temperature, c.Longwave downward radiation, d.Shortwave downward radiation, e.Specific humidity, h.Surface pressure, g.Wind. Differences are calculated between the December-January-February averages (DJF) of the 1981-2010 period.
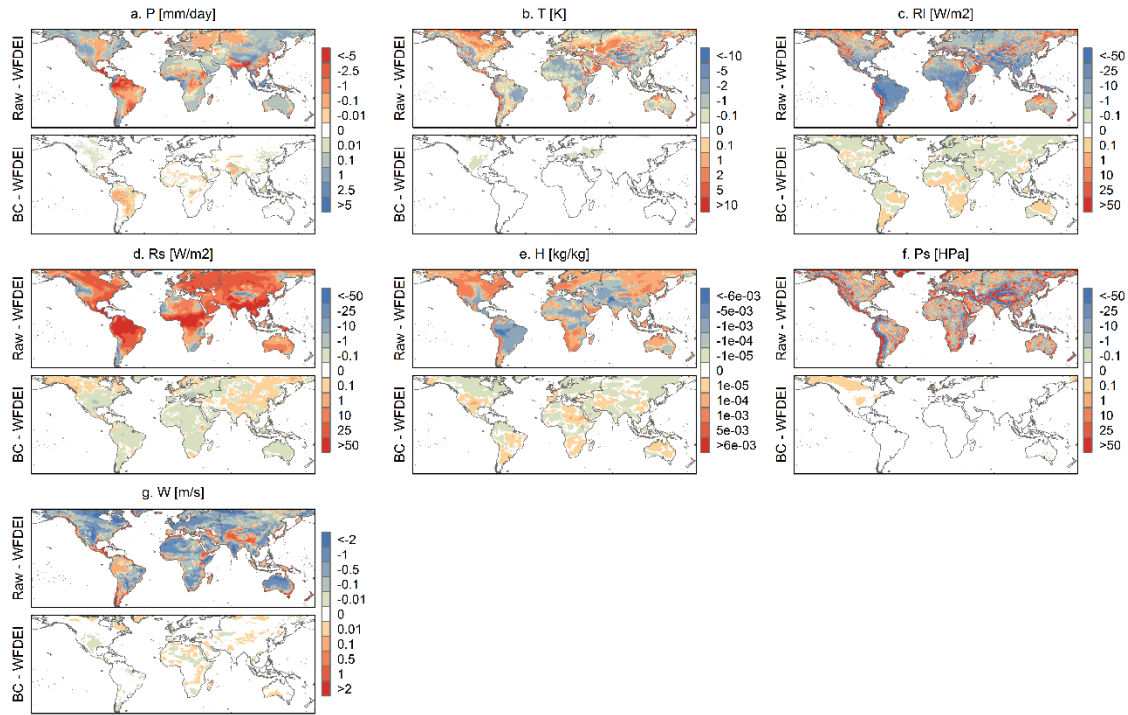
Figure B 2. Difference maps, showing initial (Raw-WFDEI) and remaining (BC-WFDEI) biases of the GCM ensemble forcing variables: a.Precipitation, b.Temperature, c.Longwave downward radiation, d.Shortwave downward radiation, e.Specific humidity, h.Surface pressure, g.Wind. Differences are calculated between the June-July-August averages (JJA) of the 1981-2010 period.

Table B 1. Values of input variables, for each GCM (GFDL, IPSL and MIROC), the ensemble mean (Ens.Mean) and WFDEI data, spatially averaged for 24 Giorgi regions.

	P [mm/day]					T [K]				
	GFDL	IPSL	MIROC	Ens.Mean	WFDEI	GFDL	IPSL	MIROC	Ens.Mean	WFDEI
NEU	2.61	2.30	2.53	2.48	2.43	277.90	277.15	281.16	278.74	279.50
MED	1.44	1.08	1.44	1.32	1.56	288.73	287.57	290.13	288.81	288.26
NEE	1.71	1.67	1.79	1.72	1.67	274.42	274.15	277.89	275.49	276.75
NAS	1.59	1.66	1.78	1.68	1.25	267.91	269.70	270.71	269.44	267.53
CAS	0.92	0.79	1.36	1.02	0.93	284.84	284.00	287.60	285.48	285.79
TIB	1.36	1.05	1.99	1.47	0.63	274.44	271.79	273.20	273.14	275.70
EAS	2.96	2.88	2.96	2.94	2.57	286.26	285.73	288.39	286.79	284.48
SEA	8.77	6.74	6.80	7.44	6.96	299.45	299.15	298.99	299.19	299.21
NAU	2.97	1.37	3.46	2.60	1.65	297.80	297.47	298.36	297.87	297.40
SAU	1.79	1.60	2.28	1.89	1.28	289.28	286.59	287.49	287.79	290.68
SAH	0.22	0.06	0.35	0.21	0.15	297.02	294.15	296.73	295.97	298.18
WAF	4.60	2.92	4.02	3.85	2.86	298.65	298.50	299.70	298.95	300.57
EAF	2.15	1.52	2.87	2.18	1.99	297.86	297.14	298.09	297.69	298.99
EQF	2.87	3.34	2.80	3.00	2.67	295.21	295.47	295.61	295.43	296.00
SQF	3.33	3.18	2.79	3.10	3.04	295.89	295.95	296.37	296.07	295.96
SAF	2.37	1.62	2.20	2.06	1.27	291.60	290.33	290.83	290.92	290.89
WNA	1.92	1.88	2.32	2.04	1.49	282.01	282.41	284.29	282.90	282.96
CNA	2.48	2.11	2.12	2.23	2.62	283.22	283.91	286.66	284.59	284.58
ENA	3.53	3.49	3.77	3.60	3.20	286.57	287.57	289.45	287.86	282.26
CAM	3.43	2.17	2.22	2.60	2.84	295.70	295.89	297.40	296.33	295.32
AMZ	3.57	3.55	4.06	3.72	5.32	297.74	297.44	297.66	297.61	297.94
CSA	2.37	1.71	2.20	2.09	2.83	291.79	290.06	291.07	290.97	290.61
SSA	2.58	2.76	2.70	2.68	2.57	281.71	278.10	279.75	279.85	281.32
SAS	3.61	2.94	4.76	3.77	3.75	296.89	296.78	297.21	296.96	296.36
	Rl [W/m2]					Rs [W/m2]				
	GFDL	IPSL	MIROC	Ens.Mean	WFDEI	GFDL	IPSL	MIROC	Ens.Mean	WFDEI
NEU	298.76	289.91	313.39	300.69	295.33	106.90	113.95	105.91	108.92	115.03
MED	325.96	306.36	328.73	320.35	314.19	194.08	207.62	202.13	201.27	199.11
NEE	283.96	268.51	293.05	281.84	286.82	113.46	130.74	131.76	125.32	113.86
NAS	255.12	250.35	261.36	255.61	245.13	115.27	125.07	132.40	124.24	117.66
CAS	294.43	276.17	300.68	290.43	295.95	208.62	212.39	224.00	215.01	204.59
TIB	254.00	226.63	239.74	240.12	239.85	193.41	203.32	238.30	211.68	216.40
EAS	330.69	311.34	329.96	324.00	310.11	175.70	203.77	197.67	192.38	171.51
SEA	412.92	398.55	404.30	405.26	415.89	217.69	235.62	220.55	224.62	194.56
NAU	375.94	353.13	375.57	368.22	357.89	245.74	275.31	245.39	255.48	248.10
SAU	330.27	314.19	326.86	323.77	326.54	197.93	190.86	185.11	191.30	216.98

177

SAH	337.31	309.98	339.92	329.07	337.15	262.15	275.38	277.74	271.75	264.56
WAF	384.32	363.56	388.70	378.86	392.92	230.64	281.46	240.12	250.74	231.51
EAF	371.89	347.30	372.53	363.91	384.45	251.09	292.60	247.54	263.74	237.33
EQF	372.31	356.07	365.27	364.55	377.08	240.21	278.16	231.80	250.05	232.56
SQF	378.02	362.43	370.00	370.15	373.27	234.04	268.65	237.10	246.60	223.85
SAF	344.64	323.67	334.37	334.23	321.71	217.70	237.28	219.01	224.66	232.14
WNA	296.89	293.37	302.39	297.55	281.30	196.70	183.22	195.71	191.87	205.10
CNA	311.69	298.60	310.79	307.03	308.70	178.09	198.56	207.13	194.59	185.28
ENA	339.03	327.43	341.57	336.01	305.46	171.46	189.71	187.69	182.95	164.46
CAM	377.27	360.63	370.16	369.35	366.67	229.89	252.57	248.63	243.70	229.00
AMZ	386.81	370.84	385.43	381.03	410.20	236.57	276.72	229.83	247.71	195.18
CSA	345.94	327.65	331.53	335.04	336.63	213.80	221.64	223.21	219.55	210.34
SSA	306.49	300.96	309.79	305.75	296.61	143.79	119.23	129.33	130.78	149.19
SAS	376.44	362.65	375.76	371.62	373.47	232.43	252.54	230.45	238.47	207.03

	H [kg/kg]					Ps [HPa]				
	GFDL	IPSL	MIROC	Ens.Mean	WFDEI	GFDL	IPSL	MIROC	Ens.Mean	WFDEI
NEU	0.0051	0.0048	0.0066	0.0055	0.0055	995.14	994.72	992.99	994.28	983.13
MED	0.0075	0.0075	0.0087	0.0079	0.0076	981.06	979.10	980.40	980.19	958.26
NEE	0.0042	0.0041	0.0054	0.0046	0.0045	998.58	997.13	995.35	997.02	994.48
NAS	0.0031	0.0036	0.0042	0.0037	0.0033	966.94	964.29	964.13	965.12	955.25
CAS	0.0044	0.0044	0.0057	0.0048	0.0055	900.50	896.25	899.36	898.70	893.06
TIB	0.0033	0.0034	0.0042	0.0036	0.0034	735.65	728.50	736.90	733.68	734.45
EAS	0.0090	0.0089	0.0108	0.0096	0.0078	974.67	969.55	973.25	972.49	947.43
SEA	0.0176	0.0178	0.0186	0.0180	0.0176	1000.13	1001.34	1003.18	1001.55	977.85
NAU	0.0121	0.0117	0.0140	0.0126	0.0096	991.65	994.78	994.03	993.49	978.92
SAU	0.0079	0.0068	0.0081	0.0076	0.0071	1004.23	1001.10	1002.27	1002.53	988.15
SAH	0.0061	0.0055	0.0068	0.0061	0.0061	965.67	965.58	966.70	965.98	955.18
WAF	0.0132	0.0123	0.0145	0.0133	0.0124	982.76	982.58	982.96	982.77	970.86
EAF	0.0113	0.0112	0.0130	0.0118	0.0122	939.81	936.28	940.58	938.89	928.97
EQF	0.0126	0.0135	0.0132	0.0131	0.0131	927.28	923.68	927.22	926.06	897.12
SQF	0.0134	0.0136	0.0144	0.0138	0.0123	964.04	963.95	964.50	964.16	924.14
SAF	0.0104	0.0094	0.0104	0.0101	0.0077	970.87	970.37	970.88	970.71	909.10
WNA	0.0059	0.0062	0.0074	0.0065	0.0051	908.11	909.20	907.96	908.42	867.44
CNA	0.0071	0.0067	0.0078	0.0072	0.0071	970.30	967.75	964.45	967.50	967.64
ENA	0.0092	0.0097	0.0113	0.0101	0.0068	1005.31	1003.65	1001.77	1003.58	986.35
CAM	0.0135	0.0136	0.0147	0.0140	0.0122	983.62	983.88	982.98	983.49	928.03
AMZ	0.0135	0.0140	0.0158	0.0144	0.0158	969.59	970.66	970.49	970.25	956.50
CSA	0.0100	0.0091	0.0096	0.0096	0.0095	976.00	975.62	973.88	975.17	935.84
SSA	0.0060	0.0047	0.0057	0.0055	0.0050	997.59	994.17	993.09	994.95	957.83
SAS	0.0134	0.0136	0.0152	0.0141	0.0132	965.75	965.46	965.67	965.63	932.59
	W [m/s]									

	GFDL	IPSL	MIROC	Ens.Mean	WFDEI
NEU	5.50	4.47	4.10	4.69	3.64
MED	4.02	3.99	4.32	4.11	3.17
NEE	3.61	2.93	3.01	3.18	3.56
NAS	3.57	3.46	3.85	3.63	3.05
CAS	2.85	3.64	4.33	3.61	3.27
TIB	2.46	3.98	5.50	3.98	3.49
EAS	4.54	4.39	4.18	4.37	3.15
SEA	5.09	3.75	3.89	4.24	1.83
NAU	4.48	3.93	4.24	4.22	4.24
SAU	6.46	6.87	7.14	6.83	4.16
SAH	3.59	4.12	4.53	4.08	4.33
WAF	2.84	2.54	3.12	2.83	2.77
EAF	2.95	3.23	3.85	3.34	3.24
EQF	3.08	2.75	3.19	3.01	2.68
SQF	3.82	3.55	4.01	3.79	2.49
SAF	5.15	5.40	5.78	5.44	3.79
WNA	3.88	3.50	4.78	4.05	3.06
CNA	3.29	3.28	3.34	3.30	3.90
ENA	5.22	4.72	4.46	4.80	2.86
CAM	4.48	3.89	4.55	4.31	2.50
AMZ	2.91	2.73	2.10	2.58	1.71
CSA	4.68	4.83	5.11	4.87	3.24
SSA	7.94	7.90	8.54	8.12	5.14
SAS	4.31	3.56	3.13	3.67	2.49
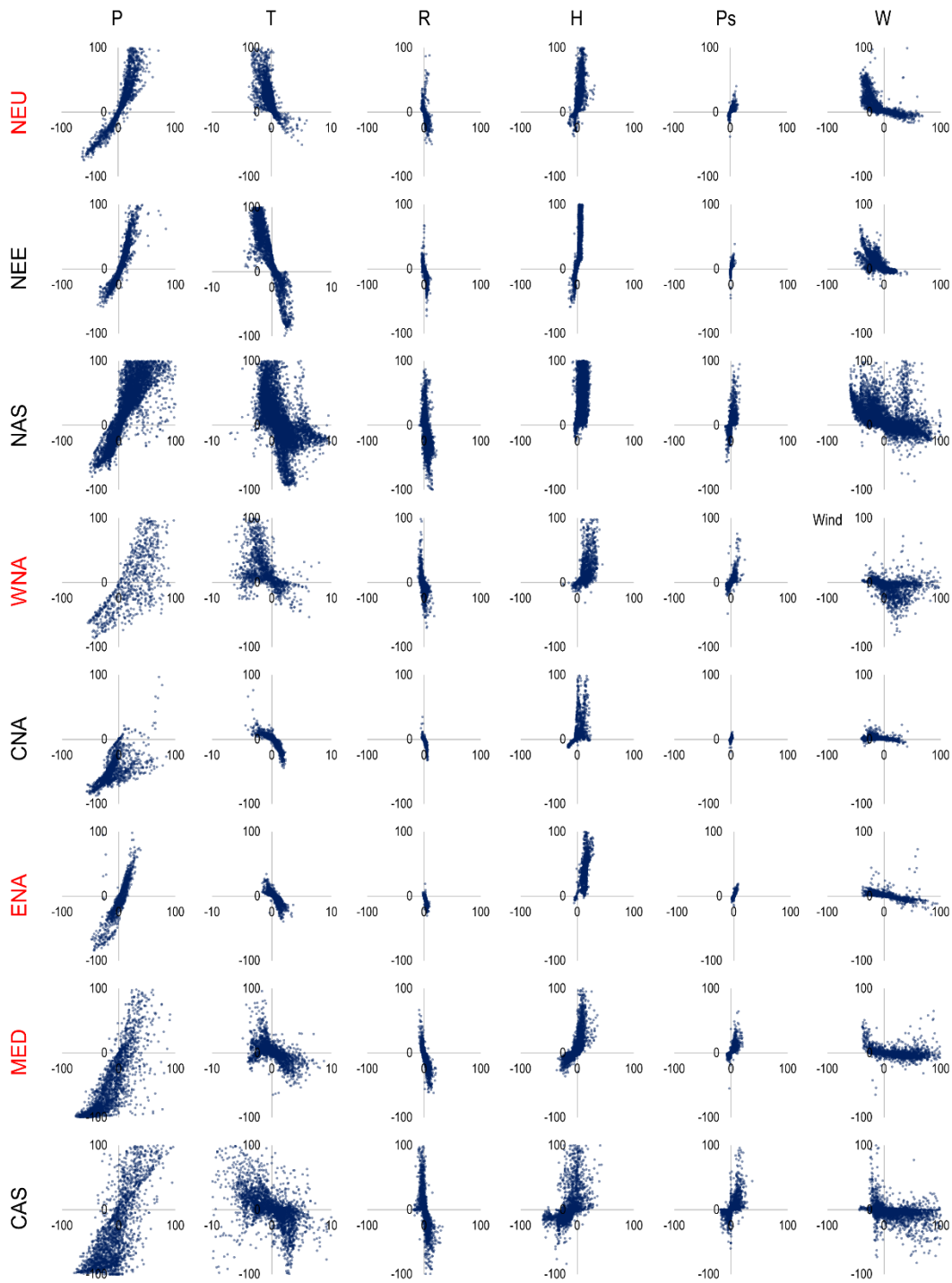
Figure B 3. Scatterplots of relative changes in forcing variable (ΔV, x axis) and corresponding relative changes in runoff (ΔRF, y axis), for all the forcing variables and for the 24 regions. In each panel, each dot represents the ΔRF/ ΔV relationship of each land grid-box in the examined region. The regions names in red colour correspond to the selected focus regions that are presented in the main text.

180

Figure B 3 (continued).

181
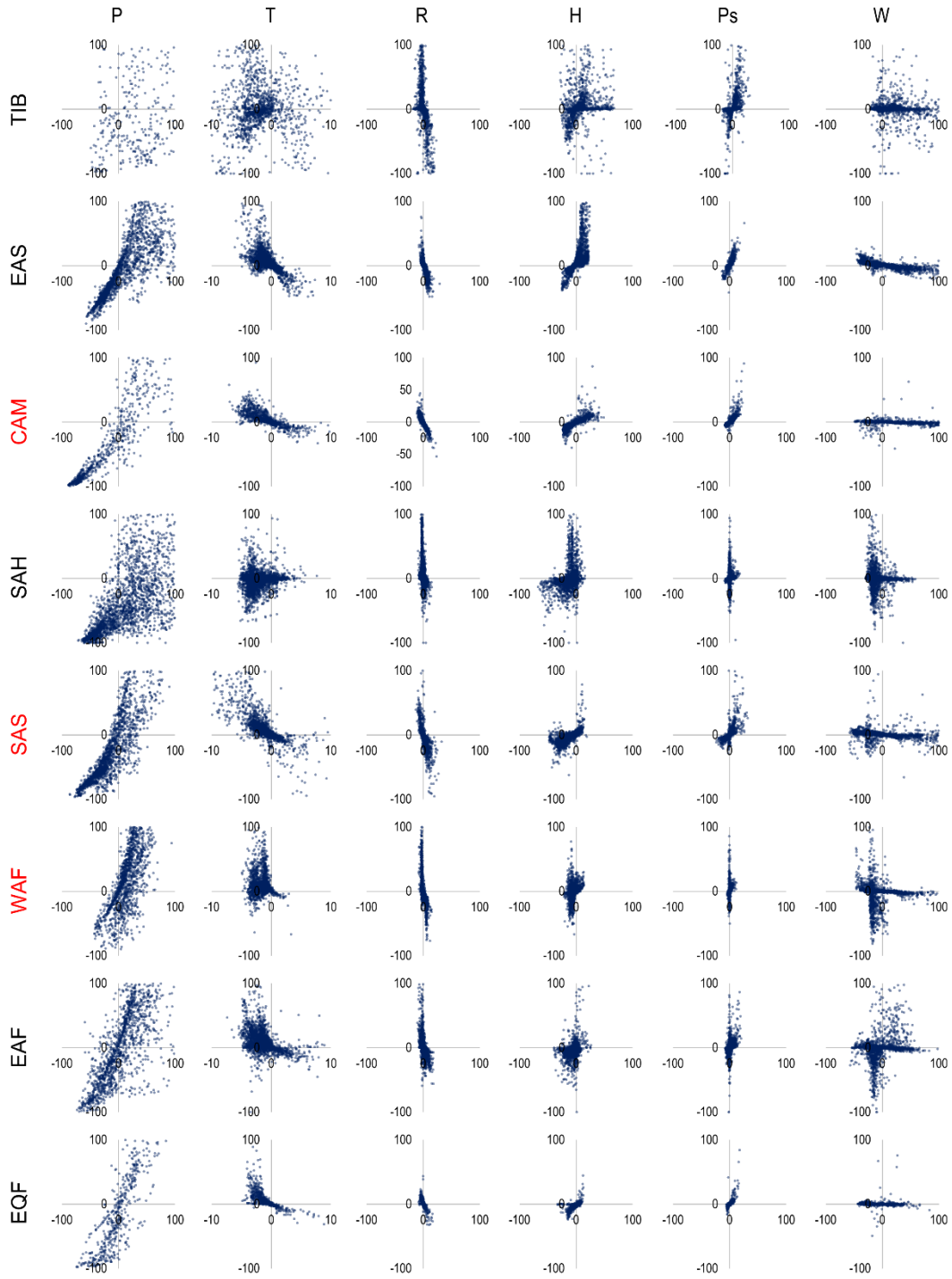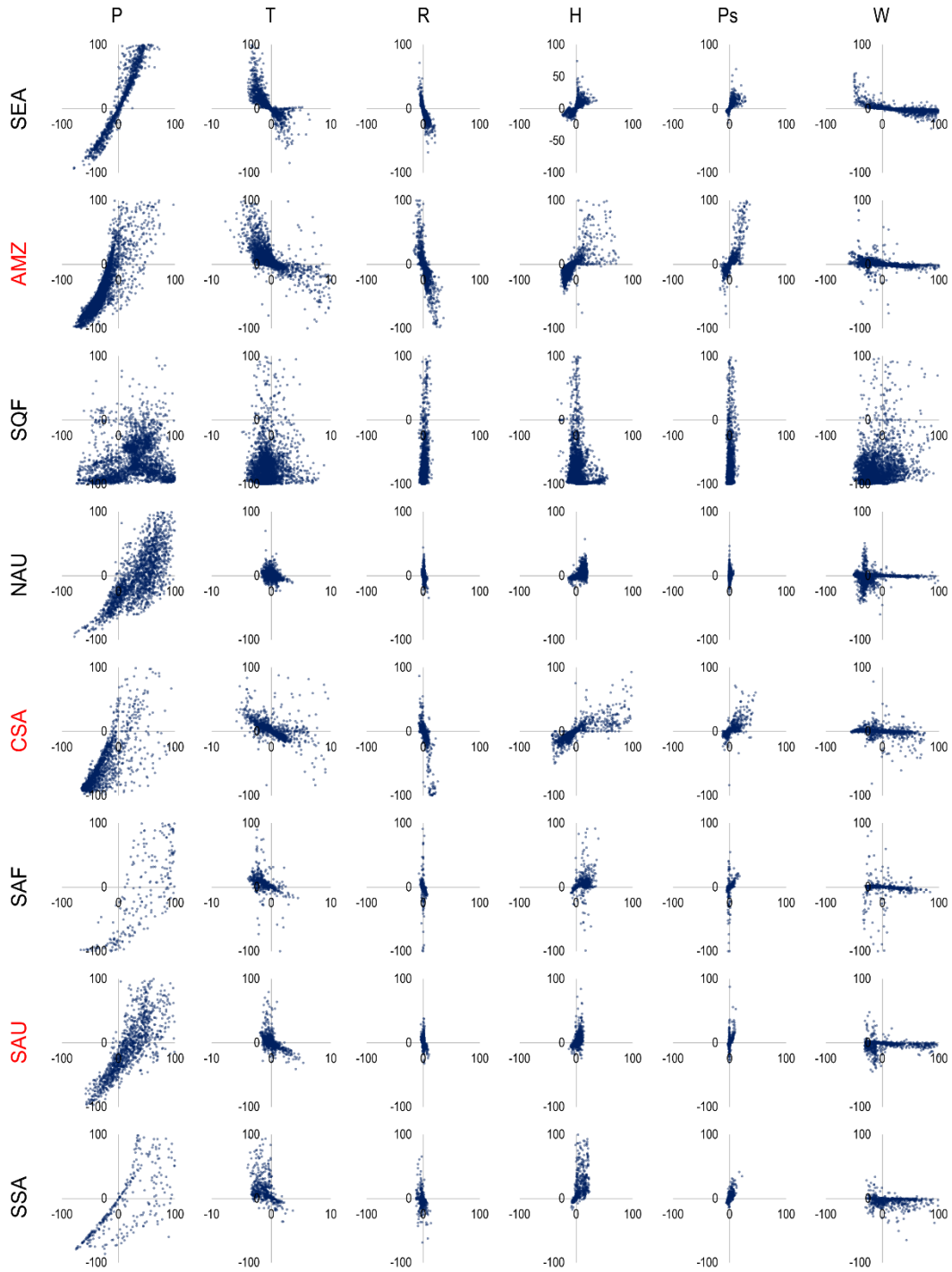
Figure B 3 (continued).
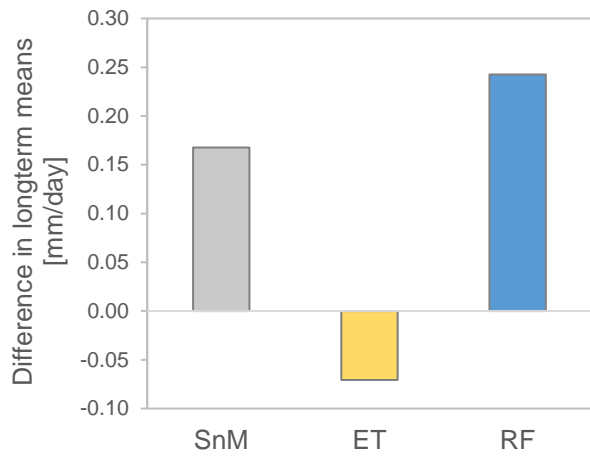
Figure B 4. Difference between the long term means (of the 1981-2010 period) of three fluxes (SnM:snowmelt, ET: evapotranspiration and RF:runoff), forced with raw and bias corrected humidity (forced with Raw H- forced with BC H). The fluxes are calculated for a representative grid-box with center location at 60.25 Longitude and 60.25 Latitude.
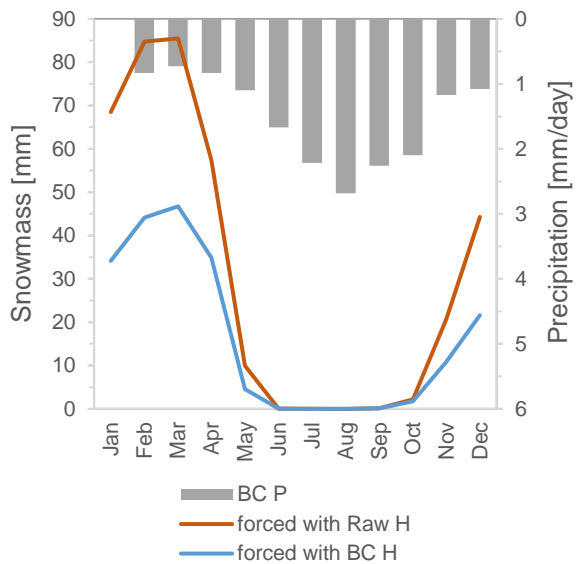
Figure B 5. Annual cycle of JULES' snowmass, forced with raw and bias corrected humidity [mm/day] and bias corrected precipitation (common forcing for both runs). Annual cycles are calculated from the 1981-2010 period, for a representative grid-box with center location at 60.25 Longitude and 60.25 Latitude.
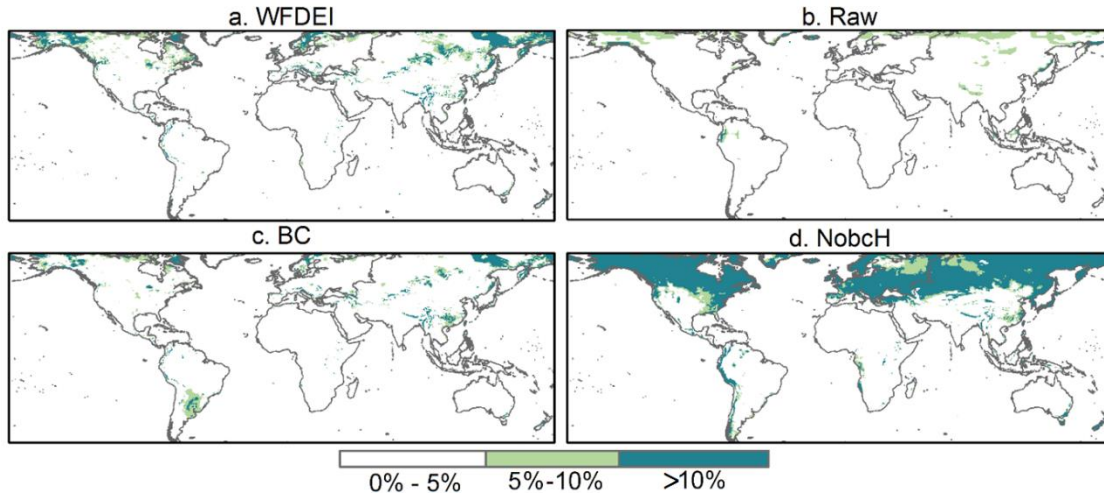
Figure B 6. Fraction of time under supersaturated air conditions (Relative humidity>100%), calculated from specific humidity H, temperature T and surface pressure Ps for: a. WFDEI data, b. Raw GCM data, c. BC GCM data and d. data corresponding to NobcH (raw H, BC T and BC Ps). Calculation of relative humidity uses the Clausius-Clapeyron equation. Fraction of time refers to the historical period 1981-2010.

	Bias Corrected with WFDEI			Bias Corrected with E-OBS		
	Drier output	Wetter output	Insignificant change	Drier output	Wetter output	Insignificant change
Percent of pan-European land area	70.40%	26.01%	3.59%	83.62%	14.67%	1.70%
Average percent change	-44.15%	148.77%	-0.53%	-56.10%	215.33%	-0.87%
Average absolute change [mm/year]	-231.44	159.37	-2.96	-285.70	131.97	1.49
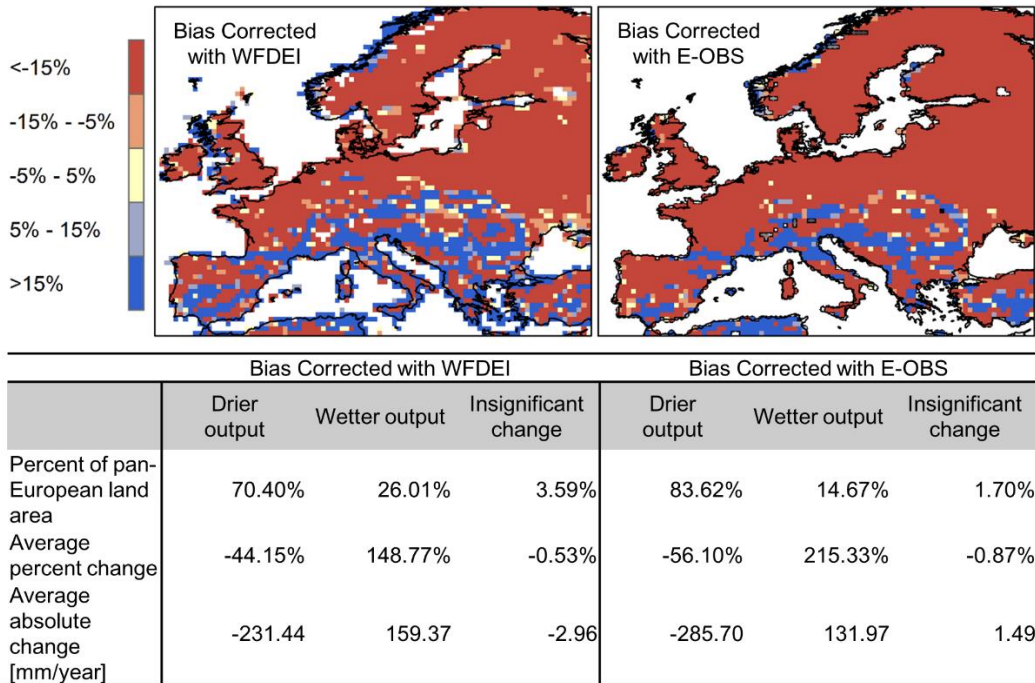
Figure B 7. The effect of bias correction on the ensemble mean of average runoff production for the baseline period. Figures: Relative difference between the ensemble means of bias corrected (left:with WFDEI, right:with E-OBS) and raw forcing data. Differences between -5% and 5% are classified as insignificant, differences <-5% as drier output and differences >5% as wetter output after bias correction. Table: percent of land area that falls into each category of change and average of the changes

Table B 2. Results of linear regression applied to basin aggregated annual average runoff production for raw and bias adjusted Euro- CORDEX data.

		Basin's Annual Average Runoff Production [mm/year]											
		Raw						Bias Corrected					
Danube		Coeff.	St. Error	tStat	P-value	r	0.32		Coeff.	St. Error	tStat	P-value	r	0.19
	Interc.	829.12	127.91	6.48	1.82E-09	R^2	0.10	Interc.	451.47	104.08	4.34	2.91E-05	R^2	0.04
	X	-0.24	0.06	-3.77	2.45E-04	Adj. R^2	0.09	X	-0.11	0.05	-2.19	3.02E-02	Adj. R^2	0.03
Rhine		Coeff.	St. Error	tStat	P-value	r	0.10		Coeff.	St. Error	tStat	P-value	r	0.08
	Interc.	950.24	228.55	4.16	5.87E-05	R^2	0.01	Interc.	640.82	204.57	3.13	2.15E-03	R^2	0.01
	X	-0.13	0.11	-1.14	2.58E-01	Adj. R^2	0.00	X	-0.09	0.10	-0.93	3.56E-01	Adj. R^2	0.00
Elbe		Coeff.	St. Error	tStat	P-value	r	0.10		Coeff.	St. Error	tStat	P-value	r	0.26
	Interc.	112.23	155.05	0.72	4.70E-01	R^2	0.01	Interc.	-171.71	119.48	-1.44	1.53E-01	R^2	0.07
	X	0.09	0.08	1.18	2.39E-01	Adj. R^2	0.00	X	0.18	0.06	2.99	3.38E-03	Adj. R^2	0.06
Guadiana		Coeff.	St. Error	tStat	P-value	r	0.54		Coeff.	St. Error	tStat	P-value	r	0.49
	Interc.	794.88	98.58	8.06	4.76E-13	R^2	0.29	Interc.	713.59	100.97	7.07	9.31E-11	R^2	0.24
	X	-0.35	0.05	-7.21	4.46E-11	Adj. R^2	0.28	X	-0.31	0.05	-6.28	4.87E-09	Adj. R^2	0.23
Kemijoki		Coeff.	St. Error	tStat	P-value	r	0.80		Coeff.	St. Error	tStat	P-value	r	0.86
	Interc.	-2257.94	186.45	-12.11	6.46E-23	R^2	0.63	Interc.	-2717.09	159.07	-17.08	1.06E-34	R^2	0.74
	X	1.36	0.09	14.83	1.72E-29	Adj. R^2	0.63	X	1.50	0.08	19.16	2.81E-39	Adj. R^2	0.74

Table B 3. Results of linear regression applied to basin aggregated annual 10th percentile runoff production for raw and bias adjusted Euro- CORDEX data.

Basin's Annual 10th percentile Runoff Production [mm/year]													
		Raw							Bias Corrected				
Danube		Coeff.	St. Error	tStat	P-value	r	0.78		Coeff.	St. Error	tStat	P-value	r	0.75
	Interc.	817.99	53.05	15.42	6.94E-31	R2	0.61	Interc.	442.02	32.50	13.60	1.49E-26	R2	0.56
	X	-0.36	0.03	-13.96	2.09E-27	Adj. R2	0.60	X	-0.20	0.02	-12.80	1.29E-24	Adj. R2	0.56
Rhine		Coeff.	St. Error	tStat	P-value	r	0.72		Coeff.	St. Error	tStat	P-value	r	0.69
	Interc.	1665.80	127.58	13.06	3.13E-25	R2	0.52	Interc.	1102.30	94.45	11.67	7.82E-22	R2	0.48
	X	-0.74	0.06	-11.76	4.59E-22	Adj. R2	0.52	X	-0.50	0.05	-10.78	1.21E-19	Adj. R2	0.47
Elbe		Coeff.	St. Error	tStat	P-value	r	0.46		Coeff.	St. Error	tStat	P-value	r	0.39
	Interc.	530.57	79.89	6.64	8.18E-10	R2	0.21	Interc.	139.24	26.24	5.31	4.84E-07	R2	0.15
	X	-0.23	0.04	-5.84	4.19E-08	Adj. R2	0.21	X	-0.06	0.01	-4.75	5.40E-06	Adj. R2	0.14
Guadiana		Coeff.	St. Error	tStat	P-value	r	0.60		Coeff.	St. Error	tStat	P-value	r	0.54
	Interc.	4.70	0.55	8.61	2.35E-14	R2	0.36	Interc.	0.02	0.00	7.63	4.97E-12	R2	0.29
	X	0.00	0.00	-8.47	5.23E-14	Adj. R2	0.36	X	0.00	0.00	-7.15	6.16E-11	Adj. R2	0.28
Kemijoki		Coeff.	St. Error	tStat	P-value	r	0.91		Coeff.	St. Error	tStat	P-value	r	0.80
	Interc.	-1048.22	43.96	-23.85	9.80E-49	R2	0.82	Interc.	-247.59	16.93	-14.62	5.35E-29	R2	0.64
	X	0.53	0.02	24.41	8.67E-50	Adj. R2	0.82	X	0.13	0.01	15.18	2.62E-30	Adj. R2	0.64
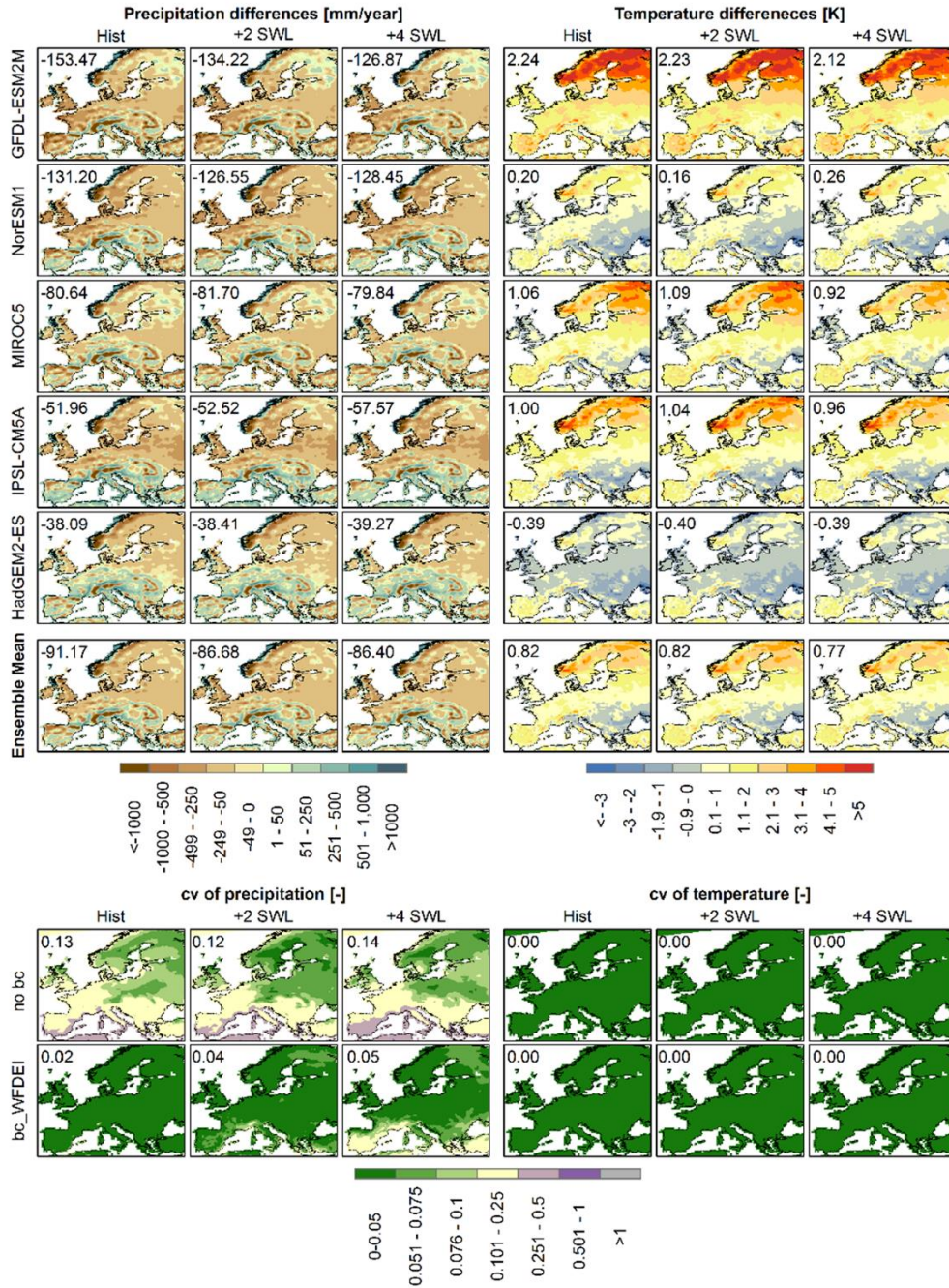
Figure B 8. Absolute differences between Euro-CORDEX data bias adjusted against the WFDEI dataset and raw Euro-CORDEX data, for the variables of precipitation (right block) and temperature (left block). Differences are calculated from the historical, +2 SWL and +4 SWL time-slice averages, for all dynamical downscaled GCMs and their ensemble mean. Bottom block: Coefficient of variation between the ensemble members, for raw and bias corrected against the WFDEI dataset precipitation and temperature forcing variables, for the historical, +2 SWL and +4 SWL time-slices. The average value for the pan-European area is shown in each sub-figure.
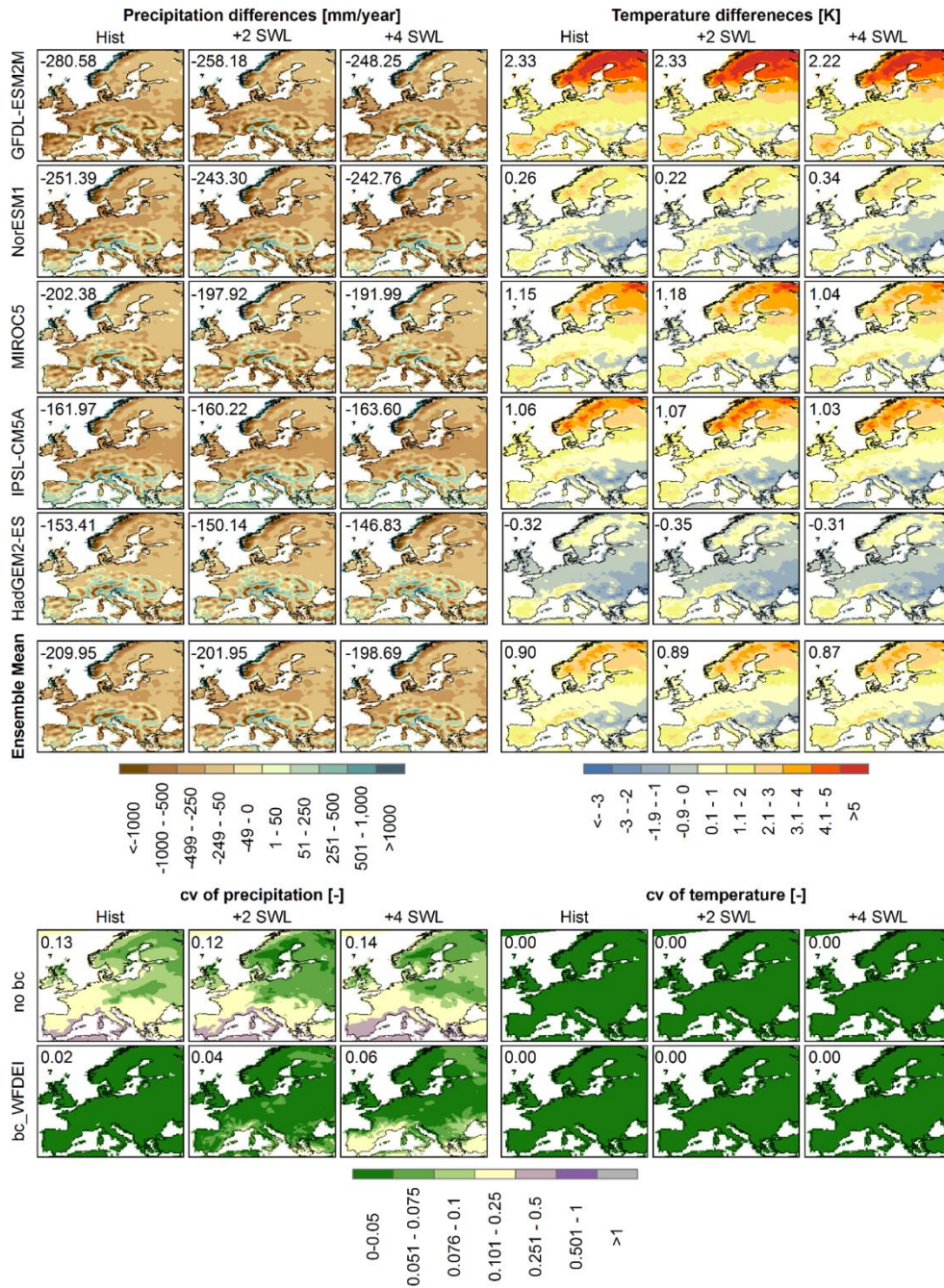
Figure B 9. Absolute differences between Euro-CORDEX data bias adjusted against the E-OBS dataset and raw Euro-CORDEX data, for the variables of precipitation (right block) and temperature (left block). Differences are calculated from the historical, +2 SWL and +4 SWL time-slice averages, for all dynamical downscaled GCMs and their ensemble mean. Bottom block: Coefficient of variation between the ensemble members, for raw and bias corrected against the E-OBS dataset precipitation and temperature forcing variables, for the historical, +2 SWL and +4 SWL time-slices. The average value for the pan-European area is shown in each sub-figure.
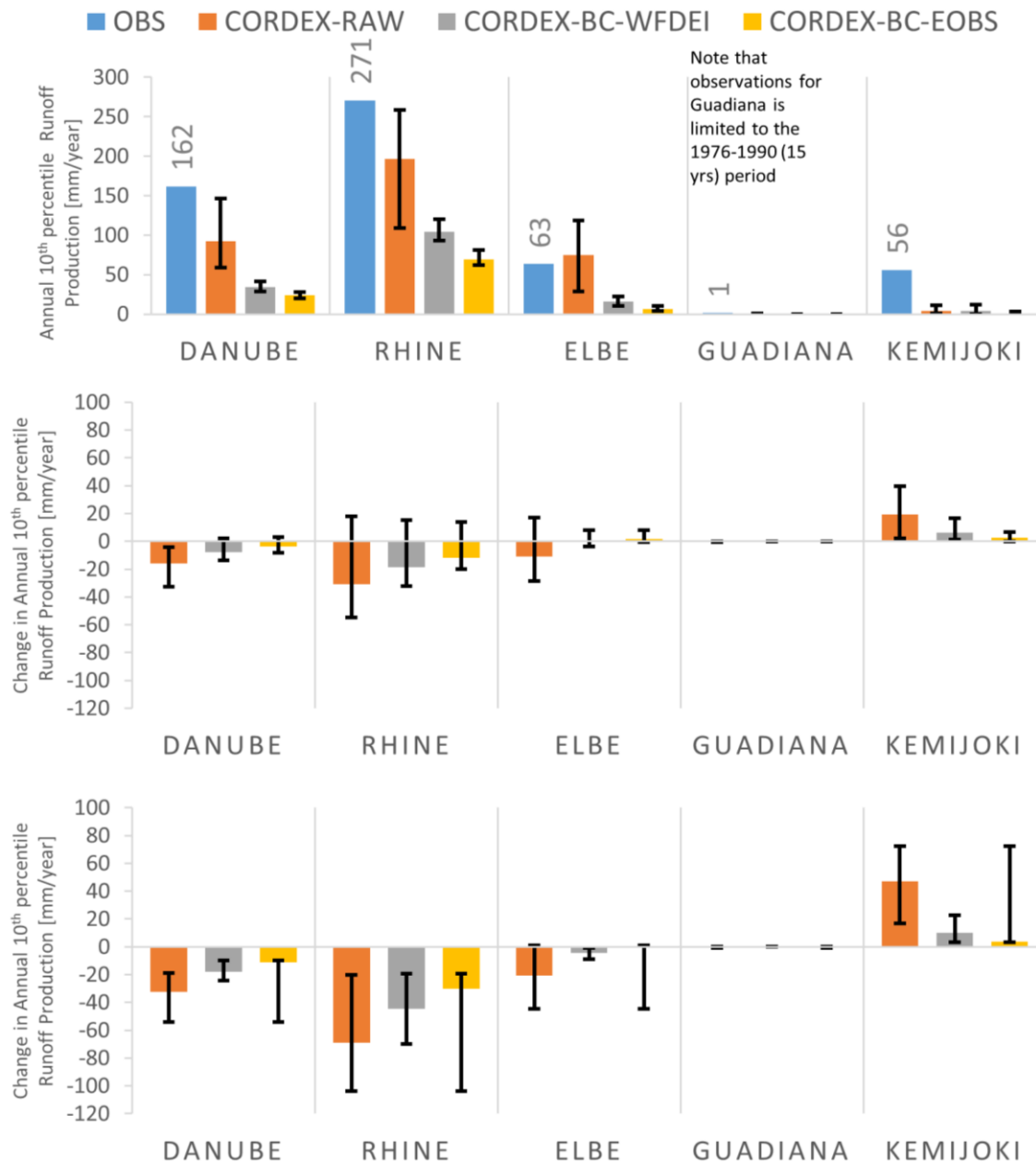
Figure B 10. Comparison between the simulations of raw Euro-CORDEX data and bias adjusted against two different datasets (WFDEI and E-OBS) for five study basins. Bars show the ensemble means and error bars the minimum and maximum ensemble member values. (Top row) Annual 10th percentile runoff production for the historical period.OBS values are derived from GRDC discharge measurements converted to basin averages at the annual time-scale. (Middle row) Percent change in annual 10th percentile runoff production at the +2 SWL and (bottom row) at the +4 SWL.

189
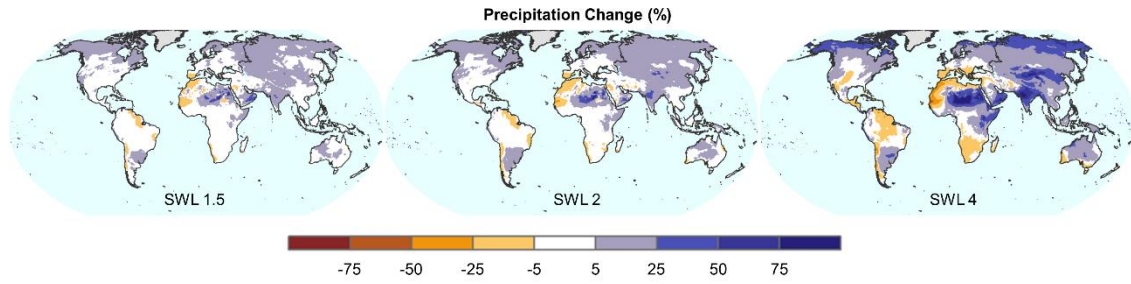
Figure B 11. Percent change in mean annual precipitation per SWL compared to the baseline period, derived from the HELIX ensemble

Table B 4. Relative changes in mean and low and high runoff, per SWL, for each ensemble member of the ISIMIP ensemble, aggregated for 8 European sub-regions.

ISIMIP	RF_mean							
SWL1.5	BI	IP	FR	ME	SC	AL	MD	EA
GFDL	13.59%	12.02%	11.98%	8.31%	0.46%	12.01%	3.42%	-3.29%
NorESM	4.37%	1.64%	1.54%	-2.61%	-5.98%	-1.57%	-5.52%	-6.53%
MIROC	7.42%	8.08%	10.69%	11.70%	4.22%	13.67%	5.28%	0.23%
IPSL	-1.31%	-1.97%	-3.09%	0.10%	6.64%	0.43%	5.32%	7.48%
HadGEM	3.73%	4.13%	1.98%	-3.48%	-1.35%	-6.15%	-1.84%	-0.28%
EnsMean	5.88%	5.24%	5.12%	3.64%	0.90%	4.74%	1.59%	-0.55%
SWL2	BI	IP	FR	ME	SC	AL	MD	EA
GFDL	16.96%	15.86%	16.00%	12.61%	-0.23%	16.42%	3.49%	-7.41%
NorESM	5.88%	4.20%	2.26%	-2.02%	-4.99%	-2.00%	-5.03%	-6.79%
MIROC	12.41%	11.92%	18.65%	20.47%	6.46%	23.73%	8.83%	-1.96%
IPSL	1.88%	1.40%	-0.07%	0.32%	5.72%	-0.86%	3.82%	4.30%
HadGEM	4.43%	4.84%	2.94%	-5.44%	-3.00%	-8.31%	-4.50%	-2.75%
EnsMean	8.74%	8.20%	8.68%	6.49%	0.96%	7.42%	1.73%	-2.99%
SWL4	BI	IP	FR	ME	SC	AL	MD	EA
GFDL								
NorESM	12.78%	8.29%	11.83%	4.77%	-3.36%	5.12%	-2.69%	-5.88%
MIROC	32.75%	32.14%	40.74%	33.31%	11.71%	34.39%	15.62%	-4.27%
IPSL	18.42%	17.53%	18.45%	7.70%	-3.76%	6.06%	-0.06%	-11.27%
HadGEM	8.24%	7.60%	5.75%	0.71%	-4.57%	-1.72%	-4.45%	-7.18%
EnsMean	14.76%	12.31%	15.73%	8.54%	-1.58%	8.20%	0.60%	-7.44%
ISIMIP	RF_low							
SWL1.5	BI	IP	FR	ME	SC	AL	MD	EA
GFDL	40.95%	55.05%	36.19%	24.03%	9.39%	28.29%	11.62%	3.61%
NorESM	18.21%	11.22%	11.22%	3.59%	-3.15%	4.83%	-2.66%	-4.42%
MIROC	27.92%	34.27%	32.08%	21.39%	10.93%	23.31%	11.94%	5.42%
IPSL	4.41%	15.31%	4.40%	9.32%	15.90%	7.31%	13.36%	14.61%
HadGEM	8.92%	16.35%	5.17%	-10.01%	-11.45%	-15.93%	-9.26%	-9.52%
EnsMean	21.23%	28.25%	19.11%	12.15%	5.23%	13.05%	5.97%	2.06%
SWL2	BI	IP	FR	ME	SC	AL	MD	EA
GFDL	49.51%	67.09%	46.65%	35.02%	10.48%	40.00%	14.41%	-1.73%
NorESM	27.12%	23.46%	19.17%	13.20%	0.97%	12.04%	1.09%	-3.17%
MIROC	40.94%	47.06%	46.62%	33.54%	12.56%	36.86%	14.45%	0.02%

IPSL	7.94%	28.87%	4.48%	10.69%	13.81%	7.26%	11.93%	9.40%
HadGEM	12.75%	21.73%	7.81%	-11.09%	-14.51%	-14.79%	-12.82%	-15.37%
EnsMean	28.79%	39.43%	26.53%	19.66%	5.78%	20.90%	7.06%	-2.07%
SWL4	BI	IP	FR	ME	SC	AL	MD	EA
GFDL								
NorESM	41.77%	33.25%	38.21%	26.30%	8.30%	28.78%	6.98%	3.26%
MIROC	93.47%	93.69%	96.53%	54.05%	19.29%	53.83%	23.31%	-1.77%
IPSL	57.87%	95.19%	51.00%	24.34%	-6.92%	20.29%	0.09%	-19.27%
HadGEM	18.63%	27.50%	8.22%	-6.98%	-17.30%	-5.24%	-16.11%	-23.96%
EnsMean	43.47%	56.74%	43.07%	25.66%	1.95%	25.62%	5.04%	-9.00%

Table B 5. Relative changes in mean and low runoff, per SWL, for each ensemble member of the EURO-CORDEX ensemble, aggregated for 8 European sub-regions.

EURO-CORDEX	**RF_mean**							
SWL1.5	BI	IP	FR	ME	SC	AL	MD	EA
GFDL	12.89%	-2.34%	22.22%	12.37%	23.39%	7.32%	-5.32%	-1.92%
NorESM	5.34%	-10.36%	-1.59%	8.29%	7.63%	-5.44%	-4.99%	6.36%
MIROC5	2.23%	2.70%	4.52%	6.08%	3.51%	11.02%	11.36%	7.24%
IPSL	5.71%	-4.23%	-2.82%	8.25%	10.10%	-2.83%	8.00%	3.41%
HadGEM2	6.66%	7.83%	12.65%	14.87%	8.92%	3.57%	9.06%	9.10%
EnsMean	6.33%	-1.45%	6.72%	10.00%	9.93%	2.64%	3.42%	5.05%
SWL2	BI	IP	FR	ME	SC	AL	MD	EA
GFDL	11.56%	-3.11%	17.13%	5.11%	28.31%	4.62%	-2.01%	-0.90%
NorESM	2.52%	-11.78%	0.22%	9.32%	10.68%	-2.81%	0.80%	5.38%
MIROC5	6.45%	-12.44%	7.56%	19.55%	13.32%	10.29%	2.26%	14.15%
IPSL	6.56%	-14.04%	-8.32%	8.13%	13.64%	-6.40%	3.84%	7.39%
HadGEM2	3.69%	-7.89%	-2.88%	17.26%	11.59%	-1.51%	9.47%	13.04%
EnsMean	5.90%	-9.79%	2.77%	11.99%	14.46%	0.82%	2.78%	7.84%
SWL4	BI	IP	FR	ME	SC	AL	MD	EA
GFDL								
NorESM	8.58%	-37.80%	-9.65%	15.15%	20.30%	-10.77%	-10.31%	3.77%
MIROC5	13.69%	-14.18%	4.52%	7.48%	26.73%	-1.29%	-4.33%	5.28%
IPSL	16.40%	-28.02%	7.10%	10.62%	39.41%	-12.55%	-11.55%	0.34%
HadGEM2	8.12%	-30.99%	-6.93%	20.30%	21.10%	-8.25%	0.40%	4.17%

EnsMean	15.49%	-28.38%	-0.71%	17.96%	34.83%	-7.81%	-7.20%	6.74%

EURO-CORDEX				**RF_low**				
SWL1.5	BI	IP	FR	ME	SC	AL	MD	EA
GFDL	4.04%	-39.52%	14.50%	48.54%	84.00%	17.42%	-23.01%	-36.47%
NorESM	-12.79%	-49.00%	-33.82%	4.09%	33.49%	-1.57%	-18.19%	3.85%
MIROC5	-16.53%	-27.12%	-36.25%	9.73%	46.49%	45.28%	6.33%	67.87%
IPSL	15.30%	-31.05%	-4.77%	20.63%	61.90%	-10.01%	-4.81%	-20.35%
HadGEM2	-10.59%	-46.46%	-24.97%	-3.90%	43.17%	-2.38%	-20.20%	-34.70%
EnsMean	-5.93%	-40.50%	-21.06%	11.52%	49.01%	8.50%	-12.77%	-11.29%
SWL2	BI	IP	FR	ME	SC	AL	MD	EA
GFDL	-6.83%	-67.03%	-15.98%	9.57%	101.94%	-7.03%	-32.02%	-54.98%
NorESM	-25.19%	-62.95%	-42.50%	-8.58%	53.62%	2.20%	-25.92%	-2.98%
MIROC5	-19.07%	-60.15%	-43.69%	54.27%	76.68%	50.31%	-16.31%	154.01%
IPSL	7.32%	-50.15%	-25.52%	22.84%	96.95%	-17.56%	-19.71%	17.30%
HadGEM2	-15.58%	-71.14%	-47.20%	2.86%	51.61%	-13.06%	-23.17%	-11.96%
EnsMean	-13.40%	-63.97%	-36.98%	9.97%	69.75%	2.05%	-23.82%	3.20%
SWL4	BI	IP	FR	ME	SC	AL	MD	EA
GFDL								
NorESM	-28.05%	-92.04%	-69.23%	-23.88%	63.72%	-31.22%	-53.01%	-27.68%
MIROC5	-20.92%	-82.25%	-69.06%	-10.14%	93.02%	-12.64%	-41.45%	2.89%
IPSL	-9.84%	-75.02%	-55.61%	-24.65%	151.22%	-70.38%	-46.55%	-41.36%
HadGEM2	-20.71%	-89.96%	-69.43%	-24.91%	78.99%	-67.74%	-47.67%	-47.45%
EnsMean	-15.78%	-87.39%	-66.07%	-14.83%	112.70%	-44.76%	-48.69%	-28.35%

Table B 6. Relative changes in mean, low and high runoff, per SWL, for each ensemble member of the HELIX ensemble, aggregated for 8 European sub-regions.

HELIX				**RF_mean**				
SWL1.5	BI	IP	FR	ME	SC	AL	MD	EA
EC_EARTH_r1	3.06%	-5.74%	-0.93%	9.18%	16.94%	1.92%	6.45%	20.84%
EC_EARTH_r2	5.19%	10.71%	3.02%	8.98%	13.53%	6.47%	0.73%	6.72%
EC_EARTH_r3	6.17%	8.69%	5.76%	4.01%	6.90%	-0.32%	6.01%	8.20%
EC_EARTH_r4	1.08%	-13.51%	-1.92%	15.41%	12.45%	7.01%	7.78%	40.03%
EC_EARTH_r5	5.37%	2.16%	12.09%	24.68%	19.58%	12.30%	-1.03%	8.91%
EC_EARTH_r6	5.92%	7.23%	9.38%	8.40%	11.61%	14.01%	19.92%	13.35%

	BI	IP	FR	ME	SC	AL	MD	EA
EC_EARTH_r7	6.26%	-3.57%	5.12%	12.35%	16.41%	-4.19%	-15.38%	2.41%
HadGEM_r1	2.79%	-15.38%	-7.83%	-1.34%	15.34%	-3.48%	-10.86%	-8.14%
HadGEM_r2	1.09%	-5.80%	-5.29%	-2.16%	9.76%	-2.07%	-0.86%	-2.90%
HadGEM_r3	3.61%	-9.04%	-7.15%	-13.13%	3.15%	-9.94%	0.45%	-10.73%
HadGEM_r6	-1.59%	4.20%	1.25%	-4.03%	4.94%	9.49%	6.59%	0.47%
HadGEM_r8	1.34%	6.50%	-0.10%	-5.34%	9.59%	-1.87%	-1.82%	-5.35%
HadGEM_r9	2.70%	-16.34%	2.81%	5.30%	8.44%	1.96%	1.33%	-12.56%
EnsMean	3.35%	-2.30%	1.34%	4.54%	11.10%	2.25%	1.44%	4.30%
SWL2	BI	IP	FR	ME	SC	AL	MD	EA
EC_EARTH_r1	8.75%	8.26%	9.96%	7.99%	23.31%	4.03%	3.69%	12.79%
EC_EARTH_r2	6.71%	19.03%	12.03%	10.27%	17.19%	12.28%	7.22%	13.52%
EC_EARTH_r3	4.99%	14.48%	9.12%	1.86%	11.71%	0.92%	7.84%	6.56%
EC_EARTH_r4	8.47%	-15.36%	3.42%	24.81%	27.69%	11.94%	-1.00%	33.32%
EC_EARTH_r5	12.77%	-3.06%	11.64%	26.33%	28.20%	9.45%	-8.33%	4.74%
EC_EARTH_r6	8.61%	-0.31%	11.72%	18.65%	13.63%	15.27%	13.39%	14.69%
EC_EARTH_r7	11.66%	-5.41%	8.11%	20.55%	30.79%	-5.26%	-18.37%	7.12%
HadGEM_r1	-0.12%	-11.66%	-3.37%	-1.60%	14.41%	-3.37%	-8.55%	-10.37%
HadGEM_r2	4.48%	-12.83%	-7.58%	-1.35%	12.45%	-4.31%	-5.90%	-6.78%
HadGEM_r3	3.91%	-7.53%	-10.28%	-17.40%	5.86%	-11.27%	0.83%	-14.20%
HadGEM_r6	-3.57%	-1.10%	-0.06%	-7.07%	5.56%	3.80%	-0.80%	-9.80%
HadGEM_r8	0.91%	-5.63%	-9.14%	-7.25%	17.58%	-8.55%	-5.65%	-6.33%
HadGEM_r9	2.72%	-23.22%	-2.07%	2.42%	13.55%	-4.31%	0.63%	-15.45%
EnsMean	5.44%	-3.60%	2.40%	5.67%	16.91%	1.24%	-1.21%	1.90%
SWL4	BI	IP	FR	ME	SC	AL	MD	EA
EC_EARTH_r1	17.08%	5.12%	26.98%	36.96%	62.97%	17.47%	-2.14%	24.80%
EC_EARTH_r2								
EC_EARTH_r3	13.96%	-4.20%	2.04%	6.56%	43.05%	0.53%	3.12%	8.12%
EC_EARTH_r4	19.03%	-16.79%	8.90%	35.43%	48.84%	9.34%	-4.59%	26.89%
EC_EARTH_r5								
EC_EARTH_r6	13.79%	-15.59%	16.59%	30.72%	51.22%	16.57%	8.96%	25.85%
EC_EARTH_r7	22.95%	0.19%	27.36%	38.28%	49.15%	9.05%	-8.82%	17.44%
HadGEM_r1	4.10%	-19.09%	-6.30%	-3.83%	42.40%	-11.22%	-15.83%	-10.86%
HadGEM_r2								
HadGEM_r3	1.91%	-16.81%	-13.77%	-17.06%	10.55%	-11.75%	-3.71%	-8.91%
HadGEM_r6	11.22%	-16.13%	5.13%	3.72%	23.32%	0.53%	-16.87%	-11.31%
HadGEM_r8	6.68%	-9.04%	-7.04%	-8.56%	21.57%	-19.69%	-16.27%	-20.86%
HadGEM_r9	5.22%	-22.28%	-2.06%	8.84%	23.58%	-5.64%	-2.82%	-13.26%

EnsMean	11.32%	-12.05%	5.24%	13.51%	39.53%	0.23%	-5.88%	4.04%
HELIX				**RF_low**				
SWL1.5	BI	IP	FR	ME	SC	AL	MD	EA
EC_EARTH_r1	11.85%	-18.98%	-19.40%	-31.40%	63.65%	-7.57%	68.31%	71.66%
EC_EARTH_r2	7.19%	17.68%	-7.53%	-3.37%	33.68%	16.02%	3.35%	-23.59%
EC_EARTH_r3	5.28%	-13.99%	-2.28%	7.05%	21.59%	-0.90%	-3.01%	-6.21%
EC_EARTH_r4	2.49%	-60.97%	-7.35%	38.86%	28.83%	24.68%	9.88%	146.34%
EC_EARTH_r5	1.66%	6.53%	19.00%	39.79%	57.81%	14.79%	16.33%	-5.20%
EC_EARTH_r6	3.70%	169.88%	39.99%	-1.41%	33.28%	16.15%	91.26%	8.55%
EC_EARTH_r7	-1.45%	-35.60%	4.57%	16.63%	34.39%	-3.60%	-59.85%	-15.58%
HadGEM_r1	-7.48%	-66.96%	-39.05%	-38.70%	29.31%	-1.64%	-43.70%	-40.51%
HadGEM_r2	-12.90%	-35.36%	-13.13%	-11.61%	15.94%	-11.96%	-43.20%	-47.26%
HadGEM_r3	8.02%	-54.93%	-29.70%	-45.84%	10.62%	-21.62%	-29.63%	-62.51%
HadGEM_r6	-11.81%	6.42%	-9.67%	-28.55%	21.58%	2.14%	-11.40%	-54.08%
HadGEM_r8	-9.58%	7.76%	-31.17%	-45.53%	16.00%	-8.02%	-24.32%	-52.97%
HadGEM_r9	-6.15%	-51.24%	-11.83%	-3.92%	12.21%	4.14%	-26.63%	-51.57%
EnsMean	-0.67%	-20.14%	-7.18%	-7.72%	26.33%	1.15%	-9.66%	-21.19%
SWL2	BI	IP	FR	ME	SC	AL	MD	EA
EC_EARTH_r1	20.33%	-1.27%	-5.92%	-33.88%	87.25%	-5.23%	39.07%	10.58%
EC_EARTH_r2	11.37%	98.44%	25.10%	12.32%	37.83%	24.47%	26.93%	4.67%
EC_EARTH_r3	5.72%	-25.83%	-2.04%	-6.12%	38.18%	-0.13%	-11.28%	-24.44%
EC_EARTH_r4	14.06%	-39.66%	23.87%	93.24%	73.12%	25.30%	-17.06%	144.88%
EC_EARTH_r5	0.78%	4.79%	14.57%	54.37%	83.17%	14.09%	-14.99%	-17.49%
EC_EARTH_r6	5.36%	77.83%	40.48%	24.68%	51.03%	17.15%	55.88%	9.40%
EC_EARTH_r7	2.96%	-22.55%	37.75%	28.47%	67.77%	10.65%	-75.04%	-15.22%
HadGEM_r1	-11.56%	-62.60%	-16.01%	-39.77%	36.68%	1.71%	-49.60%	-46.32%
HadGEM_r2	-13.36%	-46.06%	-11.34%	0.64%	19.72%	-9.76%	-55.30%	-49.96%
HadGEM_r3	3.01%	-68.29%	-40.12%	-57.25%	15.00%	-24.01%	-57.41%	-75.62%
HadGEM_r6	-17.61%	-21.95%	-21.97%	-45.50%	30.68%	-14.99%	-27.83%	-75.86%
HadGEM_r8	-18.24%	-38.50%	-43.98%	-48.63%	28.71%	-15.06%	-36.84%	-57.82%
HadGEM_r9	-5.13%	-77.46%	-24.93%	-17.57%	26.92%	-15.54%	-32.42%	-59.85%
EnsMean	-0.22%	-25.84%	-2.40%	-4.67%	42.70%	-0.39%	-24.82%	-29.54%
SWL4	BI	IP	FR	ME	SC	AL	MD	EA
EC_EARTH_r1	19.36%	37.68%	60.35%	69.00%	224.62%	20.78%	8.75%	7.02%
EC_EARTH_r2								
EC_EARTH_r3	-1.20%	-45.77%	-10.06%	-17.95%	117.94%	-8.65%	-20.14%	-40.50%
EC_EARTH_r4	22.16%	-17.97%	72.23%	118.88%	159.41%	21.11%	-0.44%	34.51%

|								
EC_EARTH_r5								
EC_EARTH_r6	13.64%	82.26%	75.20%	67.28%	148.32%	5.20%	75.36%	-7.99%
EC_EARTH_r7	-5.35%	9.60%	84.69%	59.78%	118.17%	-2.55%	-13.57%	25.12%
HadGEM_r1	-19.72%	-78.36%	-20.98%	-43.00%	101.46%	-29.18%	-58.82%	-60.24%
HadGEM_r2								
HadGEM_r3	-16.67%	-82.68%	-44.19%	-58.80%	32.09%	-29.93%	-42.03%	-72.73%
HadGEM_r6	-10.01%	-63.96%	-4.99%	-19.45%	57.52%	-33.28%	-60.79%	-77.25%
HadGEM_r8	-23.64%	-77.99%	-41.33%	-52.36%	34.45%	-53.51%	-65.30%	-77.93%
HadGEM_r9	-17.50%	-66.56%	-11.33%	-7.52%	55.17%	-21.19%	-10.67%	-56.48%
EnsMean	-5.19%	-43.73%	9.20%	6.21%	101.17%	-15.63%	-22.96%	-39.09%
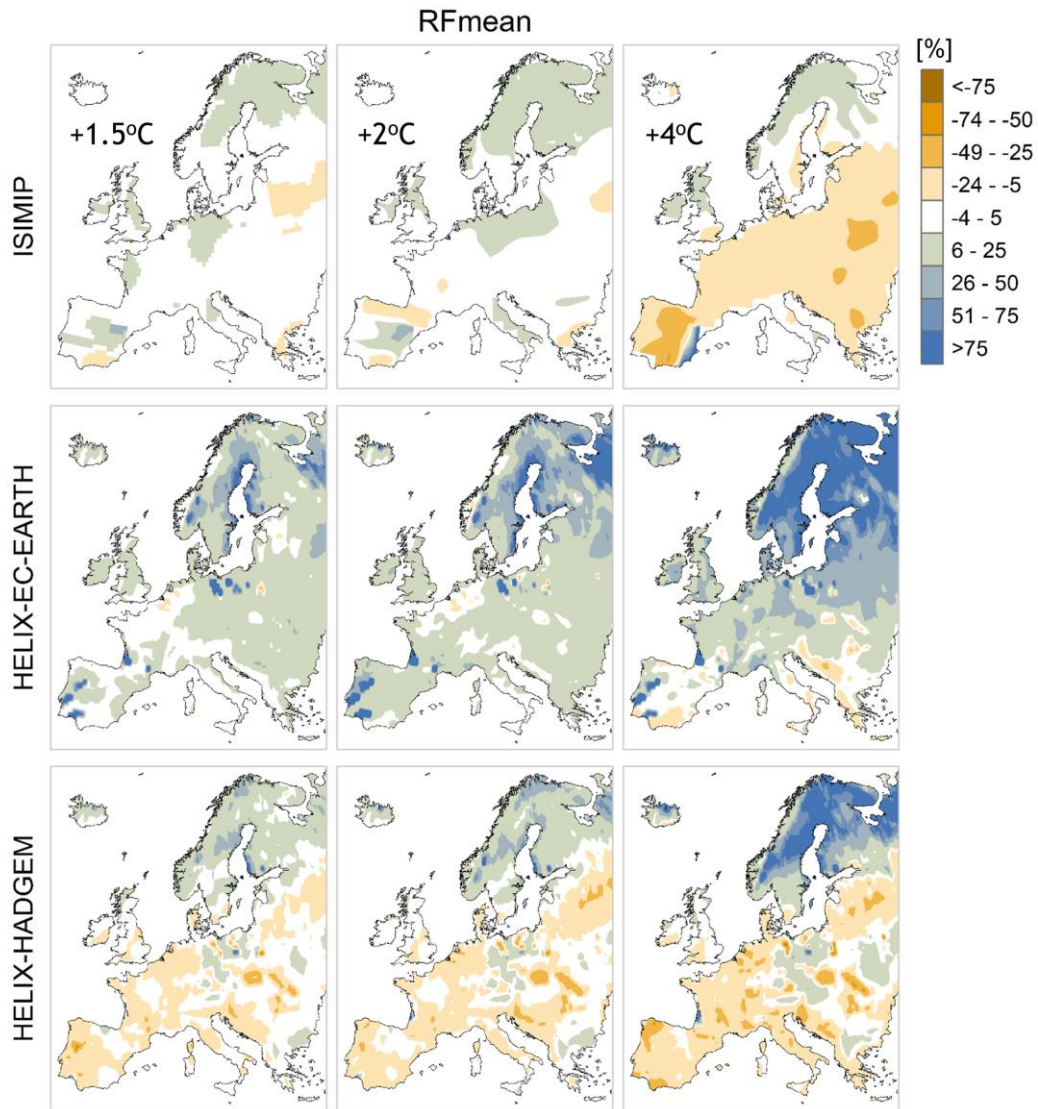
Figure B 12. Relative change in mean annual runoff (RFmean) per SWL, simulated by the three different sub-ensembles with common forcing models: ISIMIP (top), HELIX-EC-EARTH (middle) and HELIX-HADGEM (bottom).
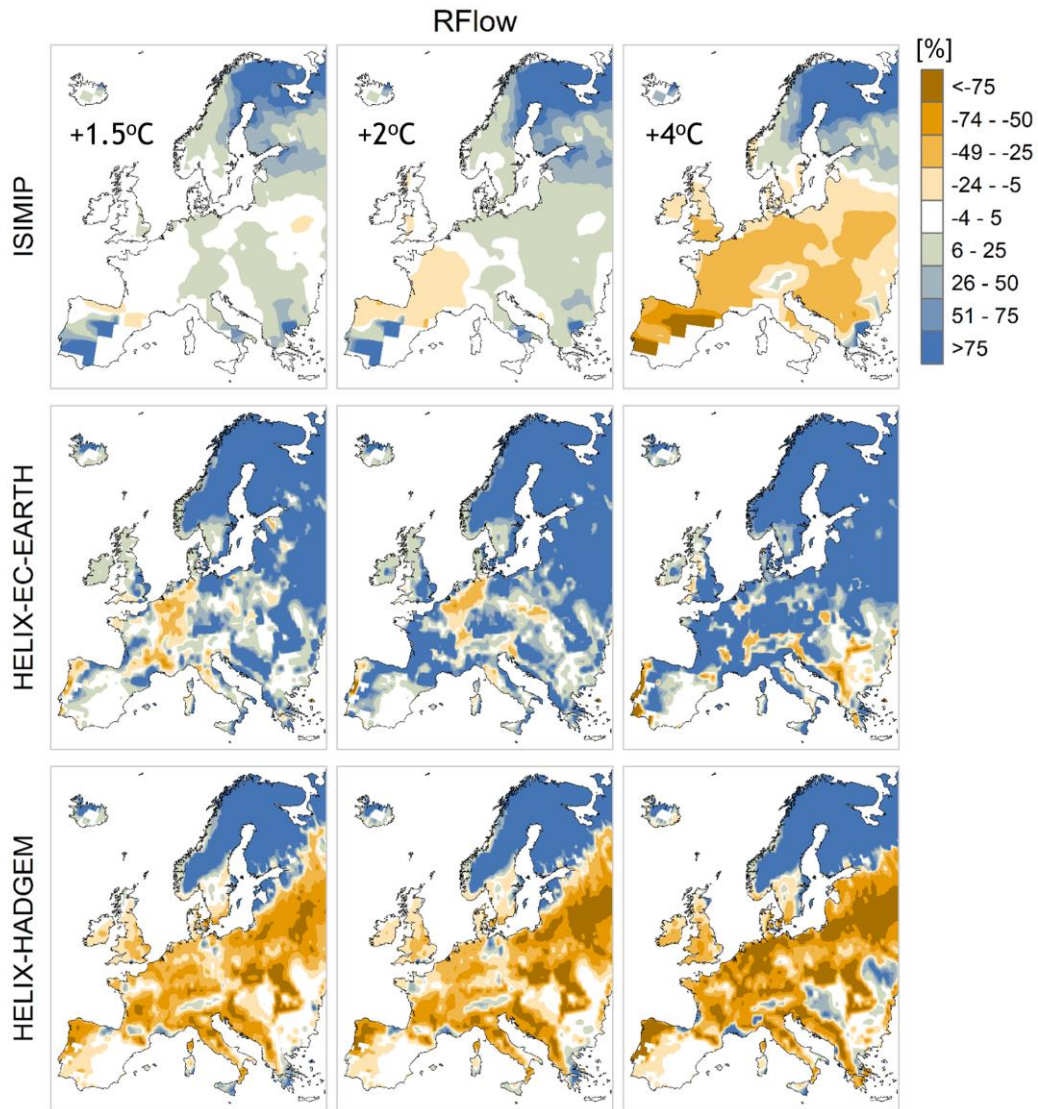
Figure B 13. Relative change in 10th percentile runoff (RFlow) per SWL, simulated by the three different sub-ensembles with common forcing models: ISIMIP (top), HELIX-EC-EARTH (middle) and HELIX-HADGEM (bottom).
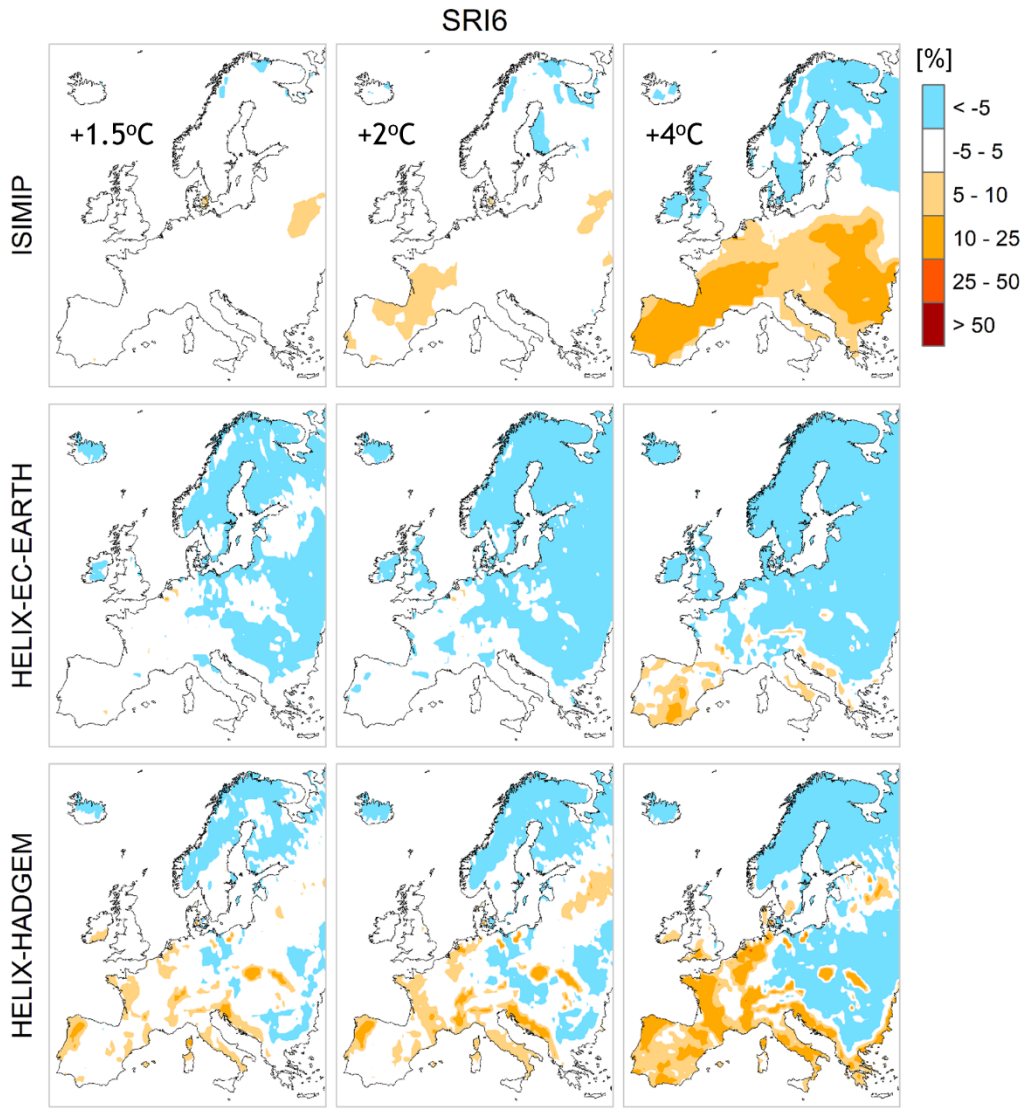
Figure B 14. Relative change in extreme short term drought (SRI<=-1.5) duration per SWL, simulated by the three different sub-ensembles with common forcing models: ISIMIP (top), HELIX-EC-EARTH (middle) and HELIX-HADGEM (bottom).
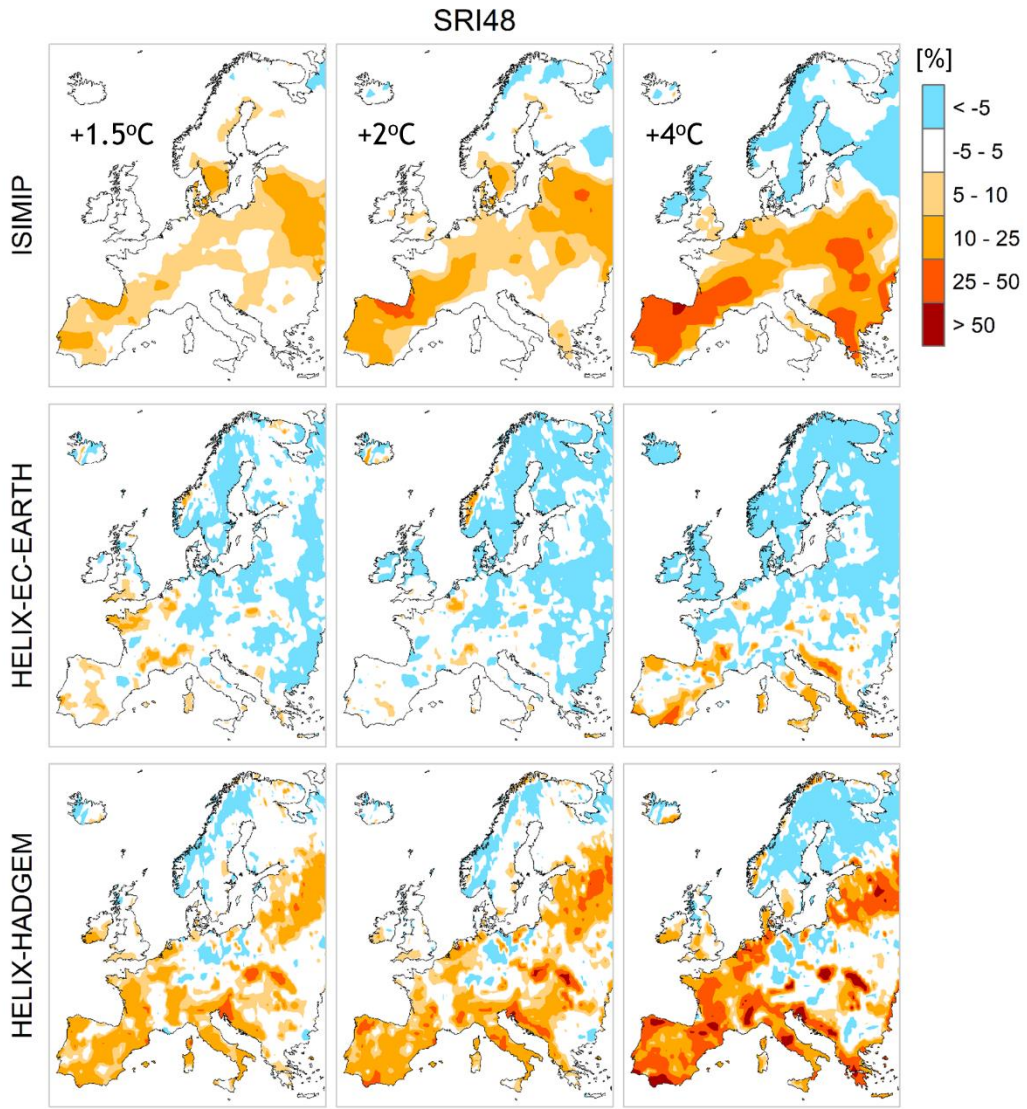
Figure B 15. Relative change in extreme long term drought (SRI<=-1.5) duration per SWL, simulated by the three different sub-ensembles with common forcing models: ISIMIP (top), HELIX-EC-EARTH (middle) and HELIX-HADGEM (bottom).